

INFORMATION TO USERS

This manuscript has been reproduced from the microfilm master. UMI films the text directly from the original or copy submitted. Thus, some thesis and dissertation copies are in typewriter face, while others may be from any type of computer printer.

The quality of this reproduction is dependent upon the quality of the copy submitted. Broken or indistinct print, colored or poor quality illustrations and photographs, print bleedthrough, substandard margins, and improper alignment can adversely affect reproduction.

In the unlikely event that the author did not send UMI a complete manuscript and there are missing pages, these will be noted. Also, if unauthorized copyright material had to be removed, a note will indicate the deletion.

Oversize materials (e.g., maps, drawings, charts) are reproduced by sectioning the original, beginning at the upper left-hand corner and continuing from left to right in equal sections with small overlaps. Each original is also photographed in one exposure and is included in reduced form at the back of the book.

Photographs included in the original manuscript have been reproduced xerographically in this copy. Higher quality 6" x 9" black and white photographic prints are available for any photographs or illustrations appearing in this copy for an additional charge. Contact UMI directly to order.

UMI

A Bell & Howell Information Company
300 North Zeeb Road, Ann Arbor MI 48106-1346 USA
313/761-4700 800/521-0600

UNIVERSITY OF ALBERTA

**POLARIZED ELECTROCHEMICAL VAPOR DEPOSITION (PEVD)
AND ITS APPLICATIONS**

by

(Eric) Zheng Tang ©

A thesis submitted to the Faculty of Graduate Studies and Research in partial fulfillment
of the requirements for the degree of DOCTOR OF PHILOSOPHY

in

MATERIALS ENGINEERING

DEPARTMENT OF CHEMICAL AND MATERIALS ENGINEERING

EDMONTON, ALBERTA, CANADA

Fall, 1998



National Library
of Canada

Acquisitions and
Bibliographic Services

395 Wellington Street
Ottawa ON K1A 0N4
Canada

Bibliothèque nationale
du Canada

Acquisitions et
services bibliographiques

395, rue Wellington
Ottawa ON K1A 0N4
Canada

Your file Votre référence

Our file Notre référence

The author has granted a non-exclusive licence allowing the National Library of Canada to reproduce, loan, distribute or sell copies of this thesis in microform, paper or electronic formats.

The author retains ownership of the copyright in this thesis. Neither the thesis nor substantial extracts from it may be printed or otherwise reproduced without the author's permission.

L'auteur a accordé une licence non exclusive permettant à la Bibliothèque nationale du Canada de reproduire, prêter, distribuer ou vendre des copies de cette thèse sous la forme de microfiche/film, de reproduction sur papier ou sur format électronique.

L'auteur conserve la propriété du droit d'auteur qui protège cette thèse. Ni la thèse ni des extraits substantiels de celle-ci ne doivent être imprimés ou autrement reproduits sans son autorisation.

0-612-34846-6

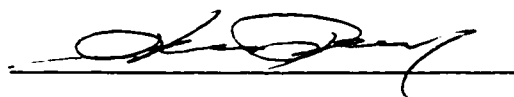
UNIVERSITY OF ALBERTA

Library Release Form

NAME OF AUTHER: **(ERIC) ZHENG TANG**
TITLE OF THESIS: **Polarized Electrochemical Vapor Deposition (PEVD)
and Its Applications**
DEGREE: **Doctor of Philosophy**
YEAR THIS DEGREE GRANTED: **1998**

Permission is hereby granted to the University of Alberta Library to reproduce single copies of this thesis, and to lend or sell such copies for private, scholarly or scientific research purposes only.

The author reserves all other publication and other rights in association with the copyright in the thesis, and except as hereinbefore provided neither the thesis nor any substantial portion thereof may be printed or otherwise reproduced in any material form whatever without the author's prior written permission.



(Eric) Zheng Tang
c/o. Mr. Rongling Tang
P.O. Box 72
China Agriculture University (East)
Qinghua Dong Road, Beijing,
P. R. China

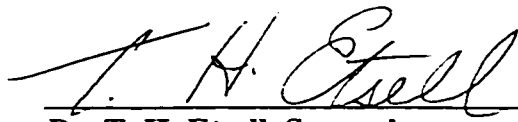
Date:

July 10, 1998

UNIVERSITY OF ALBERTA

FACULTY OF GRADUATE STUDIES AND RESEARCH

The undersigned certify that they have read, and recommend to the Faculty of Graduate Studies and Research for acceptance, a thesis entitled **POLARIZED ELECTROCHEMICAL VAPOR DEPOSITION (PEVD) AND ITS APPLICATIONS** submitted by (ERIC) **ZHENG TANG** in partial fulfillment of the requirement for the degree of **DOCTOR OF PHILOSOPHY** in **MATERIALS ENGINEERING**.



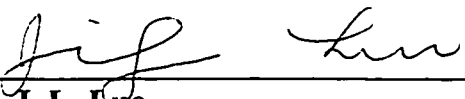
Dr. T. H. Etsell, Supervisor



Dr. D. G. Ivey, Co-supervisor




Dr. S. A. Bradford



Dr. J. L. Luo



Dr. S. Dew



Dr. P. Sarkar



Dr. A. Petric

DATE:

June 30/98

ABSTRACT

The interfacing of thin film vapor deposition technologies and solid state ionic technologies has led to the development of polarized electrochemical vapor deposition (PEVD) in this study. PEVD utilizes a solid state electrochemical cell, which can transport one or more reactants in the ionic state. Thus, under an electrochemical potential gradient, which is mainly provided by a dc potential, ionic reactants travel from the source side of a solid substrate to the sink side and react electrochemically with the surrounding vapor to form the desired solid product. PEVD has brought Wagner's scaling tarnishing theory to a new field for making man-made products under well-defined thermodynamic and kinetic conditions. The immediate advantages of using a closed-circuit electrochemical cell in PEVD include easy control and monitoring. Furthermore, the PEVD product is capable of modifying the solid electrolyte/electrode interface both physically and chemically due to its unique crystallization and growth behavior.

PEVD has been applied to deposit auxiliary phases (Na_2CO_3 , NaNO_3 and Na_2SO_4) for solid potentiometric gaseous oxide (CO_2 , NO_2 and SO_2) sensors, as well as an yttria stabilized zirconia (YSZ) ceramic phase to form composite anodes for solid oxide fuel cells. In both cases, the theoretically ideal interfacial microstructures were realized. The performances of these solid state ionic devices improved significantly. Furthermore, in order to set the foundation for future PEVD applications, a well-defined PEVD system has been studied both thermodynamically and kinetically in the current thesis, indicating that PEVD shows promise for a wide range of potential technological applications.

To my beloved grandma

ACKNOWLEDGEMENTS

The author is deeply grateful to Dr. T. H. Etsell and Dr. D. G. Ivey for their supervision, guidance, and encouragement extended throughout the course of this study.

Special thanks are extended to Dr. J. L. Luo, Dr. R. F. Egerton, Dr. R. L. Eadie, Dr. R. J. Mikula, Mr. R. Roy, Mr. C. D. Eastman and Mr. G. H. McKinnon for their stimulating and greatly helpful suggestions during the progress of this research, and their kindness in enabling the author to conduct a substantial part of the work using their facilities.

The author would also wishes to thank Ms. T. Barker and Mr. S. Merali for the assistance they provided in scanning electron microscopy and x-ray diffraction analysis; also Mr. B. Konzuk and Mr. W. Boddez for their help in setting up experiments and obtaining supplies.

Finally, the author would like to thank his wife, Brenda Li, for her selfless support.

TABLE OF CONTENTS

1. Introduction	1
2. Literature Review	4
2.1. Solid State Ionics	4
2.1.1. The Development of Solid State Ionics	5
2.1.2. Solid State Physics	6
2.1.2.1. Defects in Solids	6
2.1.2.2. Ionic Transport in Solids	8
2.1.2.3. The Structure of Solid State Ionic Materials	9
2.1.2.4. Ionic Transport in Solid State Ionic Materials	11
2.1.3. Defect Chemistry	11
2.1.4. Conductivities in Solid State Ionic Materials	18
2.1.4.1. Partial Conductivity	18
2.1.4.2. Partial Pressure Dependence of Partial Conductivities	19
2.1.4.3. Temperature and Partial Pressure Dependence of Partial Conductivities	20
2.1.4.4. Classification of solids and solid electrolyte domains	21
2.2. Solid Electrolytes	24
2.2.1. General Features of Solid Electrolytes	24
2.2.2. Classification of Solid Electrolytes	26
2.2.3. β -alumina	29
2.2.4. Stabilized Zirconia	31
2.3. Solid State Electrochemistry	34
2.3.1. The Development of Solid State Electrochemistry – From Wagner's Electrochemical Tarnishing Theory	34
2.3.2. Solid Electrochemical Systems	37
2.3.3. Energy Transfer in Solid Electrochemical Cells	40
2.3.4. Material Transport in Solid Electrochemical Cells	43

2.3.4.1. Transport in a Solid Electrolyte	45
2.3.4.2. Transport in a Mixed Conductor	46
2.3.5. Interface Effects in Solid Electrochemical Cells	47
2.3.5.1. Interface Polarization in Solid Electrochemical Cells	48
2.3.5.2. Current Conservation in Solid Electrochemical Cells	49
2.3.6. Solid State Electrochemistry for Theoretical Studies	50
2.3.6.1. Solid State Ionics Technology for Thermodynamic Studies	51
2.3.6.2. Solid State Ionics Technology for Kinetic Studies	52
2.4. Solid State Ionic Technology	53
2.4.1. Solid State Ionic Technology for Solid State Ionic Devices	54
2.4.1.1. Basic Devices	55
2.4.1.2. Solid Potentiometric Sensors – Open Circuit SSI Devices	56
2.4.1.3. Solid Oxide Fuel Cells – Closed Circuit SSI Devices	60
2.4.1.4. The Major Problems with Current SSI Devices	63
2.4.2. Solid State Ionic Technology for SSI Device Fabrication – Solid Electrochemical Deposition (SED)	63
3. Polarized Electrochemical Vapor Deposition Fundamentals	70
3.1. Introduction	70
3.2. PEVD system basics	73
3.3. Mass and charge transport in a PEVD system	77
3.3.1. Open circuit condition and equilibrium potentials of the PEVD system	79
3.3.2. Closed circuit condition and steady-state potentials in a PEVD system	81
3.4. Electrochemical control and monitoring of a PEVD process through the solid electrochemical cell of a PEVD system	88
3.4.1. PEVD process monitoring	88
3.4.2. Process control via the applied dc electric potential	89
3.5. General product deposition behavior in PEVD	92
3.5.1. Selective deposition	93
3.5.2. Growth on electrically shorted surfaces	93

3.5.3. Self-leveling effect	96
4. Applying Polarized Electrochemical Vapor Deposition (PEVD) for Auxiliary Phase Deposition at Working Electrodes of Gaseous Oxide Sensors	98
4.1. Gaseous oxide sensors and corresponding kinetics	98
4.1.1. The development of solid-state potentiometric gaseous oxide sensors	100
4.1.2. Gas electrode reactions in type III potentiometric CO ₂ sensors	105
4.1.2.1 A kinetic gas sensing model for type III potentiometric CO ₂ sensors	105
4.1.2.2. Geometric criteria for the best auxiliary phases for CO ₂ sensors	110
4.1.2.3. Previous auxiliary phase preparation techniques and their problems	111
4.2. Polarized electrochemical vapor deposition to deposit auxiliary phases at the working electrode of type III potentiometric CO ₂ sensors	112
4.2.1. PEVD process design	112
4.2.2. Experimental procedure	116
4.2.2.1. PEVD system setup	116
4.2.2.2. PEVD process	119
4.2.2.3. PEVD product microstructure studies	121
4.2.3. Results	122
4.2.3.1. Microanalysis of the PEVD deposit	122
4.2.3.2. Current and flux during PEVD	127
4.2.4. Discussion	129
4.2.4.1. Formation of Na ₂ CO ₃ by PEVD	129
4.2.4.2. Selective deposition in PEVD	130
4.2.4.3. PEVD product phase growth behavior	131
4.2.4.4. PEVD current	133
4.2.4.5. PEVD auxiliary phases	135
4.3. Sensor response behavior testing	136
4.3.1. Experimental procedure	136

4.3.2. Results	140
4.3.2.1. PEVD auxiliary phase step coverage at the working electrode	140
4.3.2.2. Sensor response	141
4.3.3. Discussion	146
4.4. Conclusions	150
5. Applying Polarized Electrochemical Vapor Deposition to Composite Anode Fabrication for Solid Oxide Fuel Cells	151
5.1. Introduction	151
5.2. SOFC anodes	152
5.2.1. Previous investigations of SOFC anodes	152
5.2.2. The criteria for a theoretically ideal SOFC anode	155
5.2.3. PEVD composite anode design	156
5.3. Experimental aspects	161
5.3.1 PEVD sample preparation	161
5.3.2. PEVD system setup	161
5.3.3 PEVD procedure	163
5.3.4 Microstructure studies	164
5.4. Results	164
5.5. Discussion	174
5.6. Conclusions	176
6. PEVD Process Electrochemical Studies	177
6.1. Introduction	177
6.2. Theoretical considerations	178
6.2.1. Overpotential in a PEVD system	178
6.2.2. Working electrode overpotential in a PEVD system	180
6.2.2.1. Activation overpotential	182
6.2.2.2. Resistance overpotential	183
6.2.2.3. Concentration overpotential	184
6.2.2.4. Crystallization overpotential	185
6.3. PEVD system for electrochemical studies	186

6.3.1. PEVD system setup	186
6.3.2. PEVD reaction rate limiting steps at the working electrode	189
6.4. Steady-state potentiostatic studies	192
6.4.1. Experimental Methods	193
6.4.2. Results	195
6.4.2.1. Current-overpotential behavior	195
6.4.2.2. Activation energy of PEVD reaction	197
6.4.2.3. Exchange current for the PEVD system	200
6.4.3. Summary	201
6.5. Cyclic voltammetry studies	202
6.5.1. Experimental Setup	203
6.5.2. Results and discussion for stage II of PEVD	204
6.5.2.1. General features of an SECV spectrum	204
6.5.2.2. Effects of sweep rate	205
6.5.2.3. Effect of holding time	209
6.5.2.4. Summary	211
6.5.3. Application of SECV to the study of stage I of PEVD	211
6.5.3.1. Spectra at lower temperatures	211
6.5.3.2. Spectra at higher temperatures	215
6.5.3.3. Summary	218
7. Conclusions and recommendations	219
References	222

LIST OF TABLES

2-1. Principal equilibrium defects in solids and symbols used for their identification, according to Kroger and Vink.	14
2-2. Classification of disorder and conductivity types for an MX compound with Frenkel disorder.	16
2-3. Classification of solid state ionic materials.	22
2-4. List of selected solid electrolytes for each type of mobile ionic species.	27
2-5. Classification of solid potentiometric sensors.	59
4-1. Gaseous oxides in environment and current detection methods.	99
4-2. The current during a 50-hour potentiostatic PEVD process.	128
4-3. Geometric properties of auxiliary phases deposited by various techniques.	135
4-4. PEVD processing time at each step for both samples at the same gas flow rate.	140
4-5. The response and recovery times for sample #1 with increasing PEVD auxiliary phase coverage at the working electrode.	143
4-6. The response and recovery times for sample #2 with increasing PEVD auxiliary phase coverage at the working electrode.	145
6-1. The overpotential and corresponding current during the second stage of growth.	195
6-2. Temperature dependence of exchange current and cathodic transfer coefficient	201
6-3. Stage II PEVD steady-state potentiostatic study results.	202
6-4. Comparison of the cathodic and anodic transfer coefficients from the two stages.	214

LIST OF FIGURES

2-1. (a) A Schottky pair (a cationic and anionic vacancy) in a MX type of ionic compound; (b) A Frenkel pair (a cation interstitial and a cation vacancy) in a MX type of ionic compound.	7
2-2. Defect (Brouwer) diagram of pure compound of MX with Frenkel disorder. Dotted lines represent electronic defects; solid lines represent ionic defects.	17
2-3. Conductivity diagram of pure compound MX with Frenkel disorder. Electrolytic domain boundaries are within the range of ionic disorder.	20
2-4. Minimum value of band gap for good electrolytes as a function of temperature (Curve I). A safety margin with a factor 100 is used for Curve II.	23
2-5. Temperature dependence of the conductivity of some solid electrolytes; comparison with the conductivity of concentrated H ₂ SO ₄ (37 wt.%) is also shown.	25
2-6. Oxide ion packing arrangement in β -alumina (a) and β'' -alumina (b). (Note: letters refer to stacking arrangement in spinel block, where ABC represents face-centered cubic packing while ABAB would represent hexagonal packing.)	30
2-7. Two dimensional conduction in Na ⁺ - β / β'' -alumina.	31
2-8. Schematic of one half of the unit cell of the fluorite structure of a ZrO ₂ doped with a divalent (Ca ²⁺) or trivalent (Y ³⁺) cation.	33
2-9. Variation of ionic conductivity of stabilized ZrO ₂ with dopant concentration (T = 1080 K).	34
2-10. Physical arrangement of a metal (M) undergoing scaling at ambient atmosphere of X to form scaling product MX.	35
2-11. Illustration of the influencing parameters in a solid electrochemical cell.	39
2-12. Schematic construction of basic SSI devices.	55
2-13. Solid potentiometric gas sensor.	57

2-14. The working principle of a solid oxide fuel cell.	62
2-15. CVD/EVD process to deposit a YSZ thin film on a porous substrate.	65
3-1. Comparison of PEVD and CVD processes.	71
3-2. Comparison of EVD and PEVD processes.	72
3-3. Schematic of a fundamental PEVD system.	74
3-4. The potential profiles in the PEVD system under open circuit conditions.	81
3-5. Potential profiles inside the solid electrolyte (E) and product (D) under closed-circuit conditions.	83
3-6. Ideal current-applied potential behavior of a PEVD system.	91
3-7. The initial PEVD reaction and product nucleation occurs at the three-phase boundary of solid electrolyte (E), working electrode (W) and the sink vapor phase (S).	93
3-8. PEVD product growth on both ionically and electronically shorted surfaces.	94
3-9. Plot of PEVD product thickness vs. electronic transference number for varying lengths (y) of the product.	96
3-10. The step by step increase of PEVD product (D) thickness which reduces the aspect ratio at the working electrode. From t_1 to t_4 , the deposition time increases.	97
4-1. A type II potentiometric sensor for CO ₂ detection.	100
4-2. A type III potentiometric sensor for CO ₂ gas detection.	103
4-3. Gas electrode reaction model for type III CO ₂ potentiometric sensors.	107
4-4. Comparison of geometric structure of an ideal auxiliary phase (a) with those prepared by current techniques, such as in-situ formation (b), mechanically pressed discs (c), physical vapor deposition (d), and melting and quenching (e).	112
4-5. Schematic cross-section of a Pt thick film electrode on a Na ⁺ -β-alumina solid electrolyte of a type III potentiometric CO ₂ sensor.	114
4-6. PEVD process design for applying an auxiliary phase (Na ₂ CO ₃) at the working electrode of a type III potentiometric CO ₂ gas sensor.	115
4-7. The PEVD system and sample holder.	117

4-8. Sintering procedure for the Pt thick film working electrode.	118
4-9. PEVD apparatus for Na ₂ CO ₃ formation at the working electrode.	119
4-11. SEM SE plan-view images of the working electrode (a) before and (b) after a PEVD process.	122
4-12. XRD spectra at the working electrode of the PEVD system; Spectrum (a) before PEVD; and spectrum (b) after PEVD.	123
4-13. Selective deposition: (A) continuous Pt thick film area; (B) discontinuous Pt thick film area.	124
4-14. Cross section micrograph from a cleaved sample. Area (A) is the Na ⁺ -β-alumina solid electrolyte; area (B) is the Pt thick film electrode; and area (C) is the PEVD product Na ₂ CO ₃ .	125
4-15. EDX spectra (a), (b) and (c) of areas (A), (B) and (C) in Figure 4-14.	126
4-16. (a) Cross section picture from a polished sample, the average thickness of Na ₂ CO ₃ layer is 2.5 μm according to the measurements along arrows a, b and c; (b) X-ray maps of the same area.	126
4-17. Current – time curve for a 50-hour PEVD process.	129
4-18. Potential profiles in the PEVD system.	130
4-19. The nucleation and growth of Na ₂ CO ₃ at the working electrode of a type III potentiometric sensor.	131
4-20. PEVD auxiliary phase deposition and sensor testing procedure.	137
4-21. Schematic of (a) sample holder; (b) a joint PEVD and sensor testing facility.	139
4-22 (a-f). SEM SE images of the working electrode: (a) before PEVD; (b) first stable EMF response; (c) when the response time of the sensor just passed the minimum point; (d) when the recovery time of the sensor just passed the minimum point; (e) final auxiliary phase coverage (plan view); (f) final auxiliary phase coverage (cross-section).	142
4-23. A typical EMF response curve for a type III CO ₂ potentiometric sensor.	143
4-24. The response (curve 1) and recovery (curve 2) behavior of the type III potentiometric CO ₂ sensor (sample #1) with increasing PEVD auxiliary phase at the working electrode.	144

4-25. The response time (a) and recovery time (b) of sample #2 at various gas flow rates (curve (A) at 40 sccm and curve (B) at 80 sccm).	146
4-26. Comparison of the response time (a) and recovery time (b) for the two sensors at the same working electrode flow rate of 40 sccm.	147
4-27. Response and recovery times vs. the thickness of the auxiliary phase.	148
5-1. Two-dimensional schematic of the microstructure of a pure metallic SOFC anode.	153
5-2. Two-dimensional schematic of the microstructure of a slurry coated cermet anode.	154
5-3. Two dimensional schematic of the microstructure of the theoretically ideal composite anode.	156
5-4. PEVD process for fabricating a composite SOFC anode.	157
5-5. The calculated equilibrium vapor pressures of $ZrCl_4$ and YCl_3 .	159
5-6. Comparison of EVD and PEVD processes.	160
5-7. PEVD sample system.	161
5-8. PEVD reactor setup.	162
5-9(a) and (b). SEM SE plan-view images of the anode of the sample before (a) and after (b) PEVD.	166
5-10. XRD spectrum of the anode of the sample after PEVD. Also shown are representative spectrum from standard $Y_2O_3-ZrO_2$, ZrO_2 and Pt specimens.	167
5-11. SEM BSE image of the anode/solid electrolyte interfacial region.	169
5-12. SEM SE image of the anode/solid electrolyte interfacial region.	170
5-13. EDX spectra of areas A, B and C in Figure 5-12.	171
5-14 (a) and (b). EDX line scan from point A to point C. (a) gray level; (b) $Yb\ L\alpha$ intensity.	172
5-15. SEM SE plan-view image of an anode after a longer PEVD time.	173
5-16. PEVD preferred growth of an ionic conducting layer on an electronically shorted surface (metallic electrode surface).	175
6-1. The PEVD system setup.	187
6-2. The kinetic steps for PEVD reaction at the working electrode.	190
6-3. Current decay during the charging process.	194

6-4. Current-overpotential behavior (I - η curves) of a stage II PEVD process at various temperatures.	196
6-5. Tafel plot ($\ln(I)$ vs. η) of the current-overpotential behavior in Figure 6-4.	196
6-6. Arrhenius plot at $\eta = 100$ mV.	198
6-7. Arrhenius plot at $\eta = 400$ mV.	199
6-8. Arrhenius plot of the slope of the I - η curves at lower temperatures.	200
6-9. Activation energy of the exchange current.	201
6-10. A three-dimensional SECV spectrum and its projection planes for a stage II PEVD sample at 550°C.	204
6-11. Cyclic voltammograms at various sweep rates during stage II PEVD (550°C).	206
6-12. Cathodic and anodic peak currents in Figure 6-9 vs. the square root of the sweep rates.	207
6-13. Linear regression of cathodic overpotential vs. logarithm of sweep rate.	207
6-14. The linear regression of anodic overpotential vs. logarithm of sweep rate.	208
6-15. Cyclic voltammetric curves at various holding times.	210
6-16. Cathodic peak shift at various holding times.	210
6-17. (a) Cyclic voltammetric curves at 450°C; (b) cathodic coefficient; (c) anodic coefficient.	212
6-18. (a) Cyclic voltammetric curves at 475°C; (b) cathodic coefficient; (c) anodic coefficient.	213
6-19. (a) Cyclic voltammetric curves at 500°C; (b) cathodic coefficient; (c) anodic coefficient.	214
6-20. Cyclic voltammetric curves at 525°C.	216
6-21. Cyclic voltammetric curves at 550°C.	216
6-22. The effect of holding time on cyclic voltammetric curves during the first stage of PEVD at 550°C.	218

LIST OF SYMBOLS

a	Activity
a'	Constant
a''	Constant
(A)	Reactant A
A_D	The surface area of PEVD product
A_E	The surface area of solid electrolyte
A^{z+}	Ionic reactant
(B)	Reactant B
b	General mobility
c	Concentration
(C)	Counter electrode
(D)	PEVD deposit
D	Self diffusion coefficient
D^*	Tracer diffusion coefficient
d	Constant (a ratio of small integers)
(E)	Solid electrolyte
E_a	Activation energy
E_F	Fermi level
E_g	Bandgap
E_l	Internal electric field
$E_{p,a}$	The anodic peak potential
$E_{p,c}$	The cathodic peak potential
EMF	Electrochemical motive force
e	Electron
(F)	Other PEVD products
F	Faraday's constant
f	Haven ratio
G	Gibbs free energy

G_D	Conductance of PEVD product
G_E	Conductance of solid electrolyte
G_t	Total conduction of PEVD system
ΔG	Gibbs free energy of formation
h	Electron-hole
ΔH	Reaction enthalpy
I	Current
I_0	Exchange current
I_p	The peak current
i	Current density
i_0	Exchange current density
i_+	Anodic current
i_-	Cathodic current
k	Boltzmann constant
k_p	Parabolic constant
l	Jumping distance
L_D	The thickness of the deposit
L_E	The thickness of the solid electrolyte
M	The amount of product formed
M_i^\bullet	Cation in interstitial position
M_M	Cation in lattice
N	The mole number
n	The concentration of electrons
n_r	The number of reactant
n_0	Constant
(O)	Source of a PEVD system
P	Partial pressure
p	The concentration of electron holes
q	Electronic charge
(R)	Reference electrode
ΔS	Reaction entropy

(S)	Sink of a PEVD system
T	Temperature in Kelvin
t	Time
t_e	Transference number of electron
t_i	Transference number of ions
t_s	The starting time
(W)	Working electrode
u	Mobility
V	Molar volume of the PEVD product
V_a	Applied dc electric potential
V_i	Vacancy in interstitial position
V_M'	Ionized cationic vacancy
V_{stop}	Stop potential
V_{WC}	The potential difference between the working and counter electrode
V_{WC}°	The equilibrium potential difference between the working and counter electrode
V_{WR}	The potential difference between the working and reference electrode
W	Enhancement factor
x	A position in the deposit
z	Valence of ions
Z	Atomic number
α_a	Anodic coefficient
α_c	Cathodic coefficient
δ	Thickness of the product
η	Overpotential
η_w	Overpotential at the working electrode
η_c	Overpotential at the counter electrode
η_R	Overpotential at the reference electrode
$\eta_{E,WC}$	Overpotential at the solid electrolyte between the working and the counter electrode

$\eta_{E,WR}$	Overpotential at the solid electrolyte between the working and the reference electrode
η_a	Activation overpotential
η_Ω	Resistance overpotential
η_c	Concentration overpotential
η_y	Crystallization overpotential
η_d	Diffusion overpotential
η_r	Reaction overpotential
η_{WC}	Overpotential between the working and the counter electrode
μ	Chemical potential
μ°	The chemical potential in the standard state.
$\bar{\mu}$	Electrochemical potential
v	The product formation rate
v_0	Constant
σ	Conductivity
σ_e	Conductivity of electron
σ_e°	Intrinsic conductivity of electron
σ_h	Conductivity of hole
σ_j	Conductivity of j – ion
σ_j°	Intrinsic conductivity of j – ion
σ_t	Total conductivity
ν	Frequency of ionic jump
ν'	Sweep rate
τ	The time for one scan in SECV
ϕ	Inner electric potential
ϕ_w	Inner potential of the working electrode
ϕ_w°	Equilibrium inner potential of the working electrode

ABBREVIATIONS

BSE	Back scattered electron
Cermet	Ceramic – metal composite
CV	Cyclic Voltammetry
CLD	Chemical liquid deposition
CVD	Chemical vapor deposition
EDX	Energy dispersive x-ray
ELD	Electrochemical liquid deposition
EMF	Electrochemical motive force
EVD	Electrochemical vapor deposition
G-P	Galvanostat-Potentiostat
NEMCA	Non-Faradaic electrochemical
PEVD	Polarized electrochemical vapor deposition
R&D	Research and development
SE	Secondary electron
SECV	Solid electrolyte cyclic voltammetry
SED	Solid electrochemical deposition
SEM	Scanning electron microscope
SOFC	Solid oxide fuel cell
SSI	Solid state ionics
TPB	Three-phase boundary
XRD	X-ray diffraction
YSZ	Yttria stabilized zirconia

Chapter 1. Introduction

There are two types of conductivity in nature: electronic and ionic. The first does not involve mass or material transport while the second does. Thus, ionic conduction is capable of converting chemical energy to electrical energy, or vice versa. Since Wagner's early works in the 1930s, defect solid state physics and chemistry has been an area of major scientific and technological interest, the resulting discoveries of solid state ionic materials and development of solid state ionic technology sustaining this interest. The stage has therefore gradually been set for a massive effort at developing applications.

The energy crisis in the early 1970's aroused a worldwide interest in energy converting applications based on ionic transport in solid state ionic materials. Since then this field has developed rapidly in order to serve ever-growing energy and environmental demands. Like solid state electronics, the device field of solid state ionics is quickly developing. The study of electronic-ionic processes in solid state ionic materials reflects the intimate relationship between science and technology; "pure scientific" results eventually find various practical applications. Present activity in this direction includes

the development of small batteries for pacemaker implants, high power batteries for energy storage systems, fuel cells for high-efficiency power generation, electrochromic windows for energy conservation, sensors for chemical pollutant detection, etc.

In spite of the great promise solid state ionic devices offer, few commercial successes have been reported to date. The major problems faced today in the field of solid state ionic devices are still material related. At present, the key technical challenge is development of reliable and cost-efficient techniques to synthesize solid state ionic materials to serve as solid electrodes and electrolytes (Takahashi, 1989). On the other hand, these materials are not used in isolation, but in an electrochemical system and must be in contact with each other. The response of solid state ionic materials in solid state ionic devices is highly related to the interface characteristics, which fix the external electrical conditions (electric potential and current density) and the external chemical conditions (chemical potential). The solid electrode/electrolyte interfaces must possess high ionic and electronic mobility. Thus, development of fabrication techniques to improve the interfaces assumes real significance. Under these circumstances, a new vapor deposition technique, polarized electrochemical vapor deposition (PEVD), was developed during the course of this study. Furthermore, PEVD has been applied to fabricate two types of solid state ionic devices, i.e., solid state potentiometric sensors and solid oxide fuel cells. Investigations show that PEVD is the most suitable technique to improve the solid electrolyte/electrode contact, and subsequently, the performance of these solid state ionic devices.

In order to present a critical, concise, systematic treatment of PEVD and its applications, the thesis is divided into five major chapters, i.e., Chapters 2 to 6. Chapter 2 is a brief overview of solid state ionic technology in the literature. Emphasis is placed on mass and charge transport in solid state ionic materials. This provides the background knowledge for the development of PEVD, and the foundation for PEVD's applications in the area of solid state ionic devices.

In Chapter 3, the fundamental aspects of PEVD are discussed and the general features of PEVD are illustrated. In order to keep the results general, discussion is based on a hypothetical PEVD system.

Chapters 4 and 5 are the major PEVD applications investigated during the course of the current study. In Chapter 4, PEVD is applied to deposit inorganic oxysalt auxiliary phases (Na_2CO_3 , NaNO_3 and Na_2SO_4) for solid state potentiometric gaseous oxide (CO_2 , NO_2 , SO_2) sensors. In Chapter 5, PEVD has been applied to deposit a thin layer of yttria stabilized zirconia at a pure metallic anode to form composite anodes for solid oxide fuel cells. The approach in both applications is a traditional materials engineering one, which links the properties to be realized with a theoretically ideal microstructure. Emphasis is placed on using the newly developed processing technique – PEVD to realize the desired microstructure.

In order to elucidate the kinetics of the PEVD reactions and subsequent product formation, in Chapter 6 a well-defined PEVD process is studied by both a steady-state potentiostatic method and a dynamic potential sweeping method.

In the final chapter, the results and the significance of this study are summarized and some general recommendations for future PEVD research and development are listed.

Chapter 2. Literature Review

2.1. Solid State Ionics

Solid state ionics (SSI) is a discipline that deals with combined ionic and electronic transport in condensed matter – solids. It is built upon various disciplines from the fields of thermodynamics, defect chemistry and solid state physics. It tries to determine why and how mass and charge can be transported through solids. This is feasible because the conductivity mechanism in solid state physics imposes some restrictions to an otherwise wide variety of possible combinations of defect chemical parameters. In this way a number of conclusions of general validity can be made (Sato, 1977). However, before application of such concepts from various disciplines, their basic origins must be considered carefully, and from these it must be checked as to whether the applications of solid state ionics in the current thesis are justified or not. This is the aim of the present section. Accordingly, some theoretical aspects to explain two basic features of solid state

ionics, i.e., the origin of the formation of the substantial disordering required for ionic conductivity in solids and the transport mechanism in such disordered structures, will be discussed in this section.

2.1.1. The Development of Solid State Ionics

Ionic conduction in solids is by no means a modern topic. Mass and charge transport associated with ionic conduction in solids have been observed since the 19th century. Early in 1834, Michael Faraday found that solid PbF_2 becomes an electrical conductor at about 500°C (Faraday, 1834). However, it took almost a century to explain this observation and establish that PbF_2 is an F^- ion conductor.

In 1910, systematic and detailed measurements of the ionic conductivities in solids were conducted by Tubandt and Lorenz (1914). They identified the high ionic conduction in Cu and Ag halides, and performed detailed measurements of electrical properties and their temperature dependence. In particular, the study of AgI reported in 1914 can be said to be the actual beginning of the study of solid state ionics. It was found in this study that the α -phase of AgI exhibits an anomalously high ionic conductivity above the phase transition temperature of 146°C , and that the amount of ionic conductivity increases with increasing temperature but decreases at the melting point 550°C . AgI has since been known as a prototype for solid state ionic materials.

The microscopic theory of ionic conductivity in solids has its origin in a paper by Joffe (1923) who introduced the concept of interstitial ions and vacancies. Shortly thereafter, the first tenable model for ionic conductivity was proposed by Frenkel (1926), who recognized that vacancies and interstitials could be formed internally in solids to account for ion movement and play a role in electrical conductivity.

Due to a general interest to study the dynamics of atomic motion and phase transitions in condensed matter, especially in random systems, the study of solid state ionics was extensively carried out using modern experimental methods beginning in the 1970s. Recently, methods such as light scattering with a laser source, X-ray scattering and absorption with synchrotron radiation, and neutron scattering with high flux reactors

have been developed to study condensed matter. Furthermore, computer simulations with the Monte Carlo method or molecular dynamics have been performed to study the diffusion mechanism associated with the dynamic nature of ion transport in solid state ionics.

2.1.2. Solid State Physics

The purpose of studying solid state ionics in solid state physics is to understand why ions with large radii can move easily, similar to the liquid state, among crystal lattices which are constructed of different kinds of ions, and what interactions among the mobile and the caged ions can cause such anomalous behavior.

Problems in solid state physics have been clarified based mainly on quantum mechanics. However, the phenomena associated with the motion of atoms or ions are caused by many-body effects of classical particle systems almost without quantum effect to date. This problem has to be solved in the statistical mechanics of the random system. The studies of the structure and the dynamic nature of ions carried out so far must be examined from such an aspect. For this purpose, we should first understand the structural characteristics and the anomalous behavior of the thermal motion of ions in various solids.

2.1.2.1. Defects in Solids

As illustrated in Figure 2-1, there are two common types of natural disorder in ionic solids. Schottky defects correspond to anion-cation vacancy pairs and occur typically in alkali halides and alkaline-earth oxides (Schottky, 1935). Frenkel defects correspond to ions promoted to interstitial sites from normal lattice positions and are found, for example, for cations in alkaline earth halides (Frenkel, 1926). Both Frenkel and Schottky defects can arise either from intrinsic or from extrinsic sources.

Intrinsic defects are a result of thermodynamic conditions. The driving force for their creation is the lattice disorder produced. In equilibrium at temperatures greater than 0°K,

even an exactly stoichiometric pure compound exhibits vacancies in the sublattices or interstitial ions. Concurrently, thermal activation of electrons from the valence band to the conduction band provides equilibrium concentrations of excess (free) electrons and electron holes.

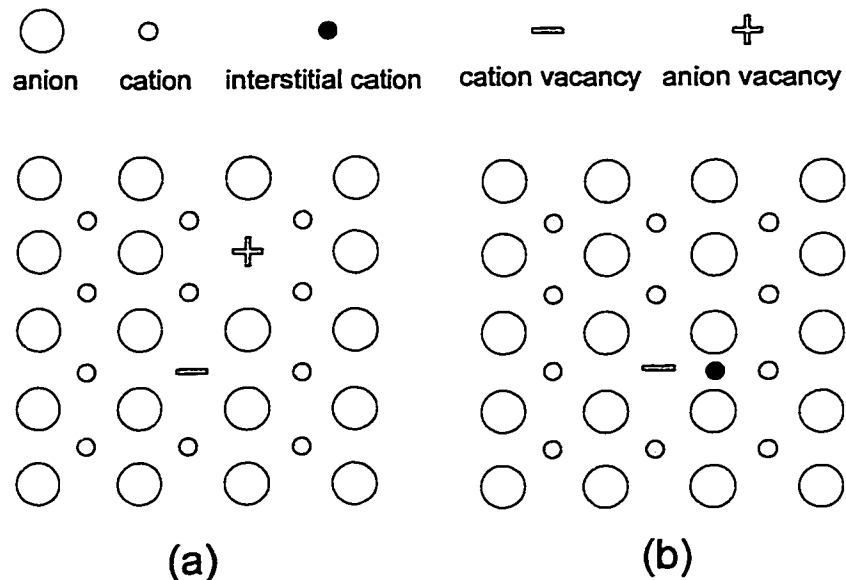


Figure 2-1. (a) A Schottky pair (a cationic and anionic vacancy) in a MX type of ionic compound; (b) A Frenkel pair (a cation interstitial and a cation vacancy) in a MX type of ionic compound.

Extrinsic defects are due to conservation of electroneutrality, i.e., they occur to compensate the charge of aliovalent impurities or dopants added. When foreign ions are present, they may take the places of normal lattice ions (substitutional incorporation) or, in theory, they may be in interstitial positions (interstitial incorporation). If substitutional foreign ions having a valency different from that of the host ions are incorporated, two mechanisms for the maintenance of electroneutrality are possible. Either free electrons or positive holes may result giving rise to n- or p-type electronic conductivity, or an equivalent amount of charged native lattice defects is formed or annihilated. The former one is related to the formation of extrinsic semiconductors. For the latter mechanism, impurities of different valency generate ionic defects; this is the mechanism that will be

mainly considered in this thesis. Currently, only experimental measurement can determine which mechanism is operable in a particular solid.

2.1.2.2. Ionic Transport in Solids

From a microscopic point of view, the reason for ionic transport in solids is the presence of Frenkel or Schottky defects in the crystalline lattice. In fluids, all species large and small are capable of substantial migration at all times. In solid crystals, however, only interstitial atoms and those next to vacant sites can enjoy any significant amount of motion. Thus, it was realized that the concentration of ionic defects is important, at least in connection with the ionic conductivity of solids.

The atomistic interpretation of ionic conduction in solids was largely established by the pioneering work of Joffe (1923), Frenkel (1926), Schottky (1935) and Wagner (1933) in the twenties and early thirties. These efforts established that ion conduction can take place either by hopping of ions through a series of interstitial sites (Frenkel disorder) or by hopping of vacancies among normal lattice positions (Schottky disorder). In solids with Schottky defects, the charge transfer is mainly due to the motion of vacancies through the lattice by successive ion hops in the direction opposite to vacancy motion. These materials exhibit rather low ionic conductivity. In solids with Frenkel defects, where the ionic conductivity is much higher, charge transfer is due to ion displacement through a series of interstitial sites. Thus, an ion in an interstitial site can either move to a neighboring interstitial site or replace a neighboring ion in a normal lattice site. The latter ion moves then to an interstitial site. In all cases, such diffusion is called jump diffusion. The self diffusion coefficient D , is expressed as

$$D = \frac{1}{3} \nu l^2 \exp(-E_a/kT) \quad (2-1)$$

where ν is the frequency of an ionic jump, l is the jump distance, E_a is the activation energy, k the Boltzmann constant and T is the temperature in Kelvin. The mobility of ions u is related to D by the famous Einstein relation:

$$u = \frac{zq}{kT} D \quad (2-2)$$

z is the valence of the ion and q is the electronic charge. If we use the diffusion coefficient D^* ($=fD$) measured by tracer methods, a correlation factor f should be introduced. Thus,

$$u = \frac{1}{f} \frac{zq}{kT} D^* \quad (2-3)$$

f is called the Haven ratio and its value depends on the structure as well as the type of defect. In general, f is less than 1. For example, in the case of diffusion through vacancies, $f = 0.78$ for the fcc lattice and $f = 0.72$ for the bcc lattice.

2.1.2.3. The Structure of Solid State Ionic Materials

One of the most important features of solid state ionic materials is their anomalously high ionic conductivity, with respect to other solid materials. Although ionic crystals show some ionic conduction, in particular, at temperatures near their melting points, the ionic conductivity of typical ionic crystals at temperatures removed from the melting point usually does not exceed a value of $10^{-9} (\Omega\text{cm})^{-1}$. On the other hand, "solid state ionic materials" is the term given to substances which exhibit large ionic conductivities far below their melting temperatures. For instance, the ionic conductivity of SSI materials under these conditions can reach $10^{-1} - 10^0 (\Omega\text{cm})^{-1}$. In general, a criterion for the level of ionic conductivity is a value somewhat greater than $10^{-4} (\Omega\text{cm})^{-1}$, but the conductivity varies strongly with temperature and, therefore, there is no rigid quantitative limit on the value of conductivity. For comparison, electronic conductivity of most metals is $10^4 - 10^6 (\Omega\text{cm})^{-1}$.

The physical mechanism providing ionic conduction in SSI materials is associated with a high concentration and high mobility of one ionic species in the rigid framework of another species. High ion mobility is attained if the following conditions are met:

Firstly, the number of vacant positions in the rigid framework should essentially exceed the number of ions able to occupy the vacant positions. Only the fulfillment of this condition can prevent “competition” between ions to occupy these positions.

Secondly, the activation energy for the transition between these positions should not be too high, or, more precisely, that the dimensionless E_a/kT ratio should not exceed a value of $2/3$ at a temperature below the melting point or the compound decomposition temperature.

Thirdly, there should exist a net of ion trajectories in a rigid framework that penetrates the entire structure; otherwise, no direct ionic current can flow. Particular arrangements of such trajectories may result in ionic conductivity of reduced dimensionality - one- or two-dimensional conductivity.

If the above-formulated conditions are met, ionic mobility in a solid is of the same order of magnitude as that observed in water at room temperature ($\sim 10^{-3} \text{ cm}^2/\text{Vs}$).

The concentration of defects in a solid state ionic material depends on a number of aspects, such as temperature, doping concentration and environment. The details will be discussed later. Usually, the concentration of defects in a solid state ionic material is on the order of 10^{20} cm^{-3} when they are caused by the two common types of disorder previously discussed. In addition, there is another type of solid, whose disorder is so great that one type of lattice ion assumes a random distribution between the lattice sites of the other type of ion. This structure may be pictorially represented as one consisting of a rigid anion sublattice “immersed” into a “cation liquid”. The concentration of defects in “structural disorder” is on the order of 10^{22} cm^{-3} . Furthermore, it should be recognized that disordered sublattice solids could be considered as compounds with an extremely high degree of Frenkel disorder. Therefore, the concepts “vacancy” and “interstitial” may be retained in this general consideration, although “interstitial lattice site” is arbitrary in such compounds. These solid state ionic materials, such as AgI and β -alumina, are usually called “superionic” conductors and exhibit some of the highest ionic

conductivities among the solid state ionic materials (Strock, 1936; Burley, 1967; Schulz, 1982).

2.1.2.4. Ionic Transport in Solid State Ionic Materials

Because of their unusually high defect mobility and concentration, the dynamics of ions in solid state ionic materials are considerably different from the usual ionic crystals. A characteristic of solid state ionic materials is that the activation energy is very low and the diffusion constant is very large. Furthermore, it has been found that the value of the Haven ratio is very small (Okazaki, 1967).

The conventional jump diffusion theory is based on the assumption that there are distinct sites for the mobile ions in the lattice and these ions can jump from one site to a neighboring site. Thus, it is also assumed that the mean residence time of mobile ions in the site is sufficiently long compared to the mean time of flight. However, if a disordered arrangement of mobile ions becomes prominent at elevated temperatures, the probability of finding ions in interstitial positions other than the equilibrium sites increases. This indicates that the simple hopping model without a correlation among the mobile ions is no longer applicable to the defects in SSI materials.

In order to explain his experimental results, Yokota (1966) proposed a diffusion process, which was called the caterpillar mechanism. According to this diffusion process, the mobile ion may jump to the neighboring site even if the site is occupied by the mobile ion. That is, jump diffusion takes place like a collision of billiard balls. Further investigations based on modern experimental methods indicate that the mechanism of diffusion in solid state ionic materials is different from substance to substance, depending on the structure as well as the temperature.

2.1.3. Defect Chemistry

As has already been discussed, ionic movement in solids can take place only when defects are present in the crystal lattice. Because of their unique crystallographic

structure, solid state ionic materials have high ionic mobility. Defect chemistry explains why and how defects in SSI materials respond to externally imposed conditions.

An important aspect of materials with high ionic mobility is the rapidity with which they can respond, at relatively low temperatures, to externally imposed conditions. Thermodynamic equilibrium, for example with an ambient atmosphere, is often established in practice. Equilibrium thermodynamics, therefore, is of great practical importance, and can be used to derive quantitative relations between carrier concentrations and chemical potentials of components in SSI materials. For instance, defects in SSI materials and adsorbed species at surfaces, which are generally in equilibrium with one another, are of great importance for the understanding of reactions inside and at the surface of SSI materials. It has been found that adsorbed atoms, molecules and ions, together with simple and complex vacancies in the adsorption layer at higher degrees of coverage, play a central role in recent investigations of processes involving interactions between SSI materials and gases (Wagner, 1970). The concentrations of ionic and electronic charge carriers in SSI materials are determined by the chemical composition of the substance, as is the case with electrolytic solutions and semiconductors. As the composition in SSI materials is subject to changes, significant values for electrical conductivity parameters can be determined or specified only if care is taken to control the SSI material's composition or environmental conditions in one way or another. In other words: physical properties of SSI materials are defined only if the chemical and thermodynamic conditions are well controlled. This is in contrast with, for instance, semiconductor materials in which, at the temperature of application, ions do not move under applied fields, and the chemical equilibria are effectively frozen in.

An elaborate analysis of thermodynamic equilibria of point defects was developed by Wagner and Schottky (1930), in which the laws relating defect concentrations to impurities, ambient partial pressures and temperature were worked out in detail (Wagner, 1935; Schottky, 1935). It was found that the nature of point defects and their concentrations in any SSI material could be determined by consideration of chemical equilibria among the various species. Kroger has reviewed the quantitative theory of such imperfections in great detail (Kroger, 1974). The different kinds of ionic and electronic defects, which may be presented in a solid, are conveniently presented using

Kroger-Vink notation (1956, 1958), which specifies the nature, location, and effective charge of a defect. Kroger-Vink notation will be used throughout this thesis and is summarized in Table 2-1.

For simplicity, the following discussion relating defect concentration in an SSI material to its environmental conditions is based on a binary compound MX with Frenkel disorder. It will be assumed that M and X are monovalent and a certain number of divalent foreign negative ions A^{2-} is present, i.e. extrinsic disorder exists in the compound. Replacement of a regular X^- ion by such a foreign one and capture of an electron results in an effectively negatively charged “acceptor center” A_X' . In pure compounds, the concentration of “acceptor centers” $[A_X']$ is zero.

When this arbitrary compound is brought into contact with the environment, we assume that the following three independent defect chemical equilibrium reactions can occur:



Eq. (2-4) shows the generation-annihilation reaction of metal interstitials and vacancies in the compound with assumed Frenkel disorder. Eq. (2-5) represents the electron-hole equilibrium. Eq. (2-6) indicates how interstitial ions can exchange with a neutral environment. In this case, charge balance is retained by combining with an electron.

The condition of thermodynamic equilibrium can further be expressed in the form of chemical potentials as follows (Guggenheim, 1967).

$$\mu_{M_i^\bullet} + \mu_{V_M'} = \text{constant} \quad (2-7)$$

$$\mu_e + \mu_h = 0 \quad (2-8)$$

$$\mu_{M_i^\bullet} + \mu_e = \mu_M^\bullet \quad (2-9)$$

Table 2-1. Principal equilibrium defects in solids and symbols used for their identification, according to Kroger and Vink.

Type	Description	Symbol	Meaning
Vacancy	A lattice position left empty by an ion	V_M	Singly ionized cationic vacancy (' means negatively charged)
		V_X^\bullet	Singly ionized anionic vacancy (\bullet means positively charged)
Electron	An electronic defect trapped at a lattice site or lying in the conduction band if sufficient thermal energy is available	e	
Electron hole	Positively charged electronic defect, sitting at the lattice sites or in the valence band	h	
Interstitial	Lattice or foreign impurity ion sitting in a interstitial position	M_i^\bullet	Cation in interstitial position
		X_i'	Anion in interstitial position
		A_i^\bullet	Foreign cationic impurity in interstitial position
Substitutional impurity	A foreign impurity sitting on a regular lattice position	A_M^\bullet or A_M'	A cationic type impurity on a cationic site
		A_X^\bullet or A_X'	An anionic type impurity on an anionic site

The “*” symbol represents the neutral species. According to the “ideal” law, the chemical potentials can be expressed in terms of concentrations c_j , if the defect concentration is low,

$$\mu_j = \mu_j^0 + kT \ln c_j \quad (2-10)$$

here the index j indicates the defect species and μ_j^0 is its standard chemical potential. With ideal behavior Eq.(2-7 to 2-9) can be replaced by the following “mass action” formulae:

$$[M_i^*][V_M^{\cdot}] = v_0^2 \quad (2-11)$$

$$np = n_0^2 \quad (2-12)$$

$$n[M_i^*] = a' \exp\left(-\frac{\mu_x^*}{kT}\right) = a'' P_x^{-1} \quad (2-13)$$

Here n and p are the concentrations of “free” electrons and holes, respectively. The quantities in brackets represent the concentration of the species included. v_0^2 , n_0^2 , a' and a'' are concentration-independent quantities. Both partial pressure P_x and chemical potential μ_x^* are the independent variables in these equations. In order to determine the concentrations of the four species involved, a fourth equation is required. Since the crystal as a whole is neutral, a fourth equation can be obtained from the requirement of electroneutrality. If a certain number of divalent foreign negative ions A^{2-} are also present, the fourth equation can be expressed as follows.

$$n + [A_X^{\cdot}] + [V_M^{\cdot}] = p + [M_i^*] \quad (2-14)$$

In practice, as only one term on either side of Eq. (2-14) dominates in a solid, the solution is relatively simple. Consequently, six limiting forms of the equation can be obtained if only one term on each side is retained. The six limiting forms characterize six possible types of solid as shown in the third column of Table 2-2.

Table 2-2 Classification of disorder and conductivity types for an MX compound with Frenkel disorder.

Type	Limiting neutrality equation	Transport species	Conductivity type	P_x range	Electron concentration n	Hole concentration p
A	$p = n$	Intrinsic electronic	Intrinsic semiconductor	All ranges	n_0	n_0
B	$p = [A_x']$	Acceptor dominated electronic	p-type semiconductor	High	$n_0^2 / [A_x'] = \text{constant}$	$[A_x'] = \text{constant}$
C	$n = [M_i^*]$	n-type mixed ionic electronic	n-type semiconductor	Low	$v_0 n_0 (aP_x)^{-1/2}$	$n_0 / v_0 (aP_x)^{1/2}$
D	$p = [V_M']$	p-type mixed ionic electronic	p-type semiconductor	High	$n_0^2 (aP_x)^{-1/2}$	$(aP_x)^{1/2}$
E	$[M_i^*] = [V_M']$	Intrinsic ionic	Ionic conductor or semiconductor	Medium	$v_0 n_0^2 (aP_x)^{-1}$	$1 / v_0 (aP_x)$
F	$[M_i^*] = [A_x']$	Acceptor dominated ionic	Ionic conductor or semiconductor	Medium	$v_0 n_0^2 (aP_x)^{-1} / [A_x']$	$1 / v_0^2 (aP_x) [A_x']$

Experimental values for the mobilities of electronic defects in ionic compounds are on the order of 100 - 1000 times greater than the mobilities of ionic defects. If the highly mobile species, either electrons or holes dominate in a solid (type A-D), the conductivity in the solid will be electronic. Consequently, the solid will be a semiconductor in the

usual sense. So only type E and F solids can be SSI materials with pure or mixed ionic conductivity. In both cases, the chemical potentials of the defects are constant with respect to variation of the independent environmental partial pressure as effectively shown in Table 2-2. Since in the model of the defect crystal lattice discussed previously, the defects represent the only mechanism by which energetic and statistical properties of the constituent ions in solids may vary, an important conclusion can be drawn. In ionic conductors, the chemical potentials of the ions must be independent of compositional variations induced by changes in the chemical potential of any component.

Theoretically, the P_X dependence for electron and hole concentrations can also be solved (Heyne, 1977) (Table 2-2). For instance, in the case of a pure MX compound with Frenkel disorder, the electron concentration is decreasing with increasing X partial pressure, so that there comes a point where the limiting electroneutrality equation for a type C solid is no longer satisfied. A type C solid becomes a type E solid. This means that a new type of disorder starts to dominate. In a similar way, a further increase in X partial pressure leads to new transition in disorder type to a type D solid.

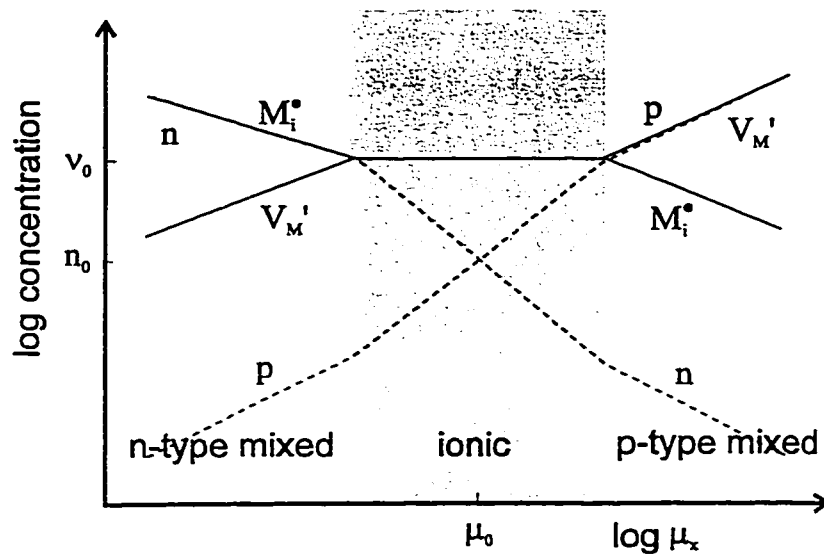


Figure 2-2. Defect (Brouwer) diagram of pure compound MX with Frenkel disorder. Dotted lines represent electronic defects; solid lines represent ionic defects.

Such transitions, together with the concentration dependence of the various defects, are clearly illustrated in the graphical representation of Figure 2-2; so-called Brouwer diagrams (Brouwer, 1954). The transitions are represented by kinks in the concentration curves. In reality such kinks should be replaced by smooth joints of the straight-line segments. However, since the logarithmic scales extend over many decades, the figure gives a fairly good representation of the real situation.

It should be pointed out that the above assumptions are made for the sake of a simple presentation only. Along completely analogous lines, similar results can be obtained if other assumptions about the type of disorder are used as a starting point.

2.1.4. Conductivities in Solid State Ionic Materials

2.1.4.1. Partial Conductivity

Since the point defects in solids are electrically charged species relative to the perfect lattice, at elevated temperatures the charged species will migrate through the lattice in response to a chemical and/or electric potential difference across the solid. The net drift represents the partial ionic conductivity of the charged species.

Referring again to a hypothetical compound MX with Frenkel defects, the partial ionic conductivity σ_j for charged ion species j is given by

$$\sigma_j = c_j q_j u_j \quad (2-15)$$

where c_j is the concentration of the charged ionic species. Similar equations stand for the partial electronic conductivities, σ_e and σ_h . The total electrical conductivity σ_t equals the sum of the partial ionic and electronic conductivities.

$$\sigma_t = \sigma_j + \sigma_e + \sigma_h \quad (2-16)$$

The ionic transference number for a charged ionic species j is defined by

$$t_j = \frac{\sigma_j}{\sigma_t} \quad (2-17)$$

The same is true for defining electronic transference numbers. The relative magnitudes of the ionic and electronic contributions establish the transference numbers for the compound, and in turn, determine whether the compound can function as an ionic conductor, a mixed conductor, or an electronic conductor.

2.1.4.2. Partial Pressure Dependence of Partial Conductivities

The partial conductivities plotted in Figure 2-3 are obtained by multiplication of the concentrations of Figure 2-2 with the respective charges and mobilities according to Eq.(2-15). A further necessary assumption is that the mobilities are independent of their own concentration and those of other defects. This condition has been found to be valid for sufficiently dilute defect concentrations at sufficiently high temperatures.

The various ranges of defect type as well as conductivity type indicated in Table 2-2 are clearly evident from Figure 2-3. The electrolytic conductivity domain in Figure 2-3 is appreciably narrower than the ionic disorder dominated range in Figure 2-2, and the partial ionic conductivity in the solid electrolyte region will also not change with partial pressure. The mixed conductor regions separate the electrolytic domain from pure semiconductor regions in Figure 2-3. If the ionic defect mobilities were very low, as is the case with most “normal” compounds, the separation of the electronic and ionic curves would be much wider and the mid-region of the diagram would correspond to “insulators”. Obviously, this is not the case for SSI materials.

Transport numbers of a solid, in logarithmic measure, can also be obtained from the conductivity diagrams as the distance between the ionic and electronic curves. The

electronic transport number t_e is minimum at the point of intrinsic electronic conductivity where the n- and p-type lines cross.

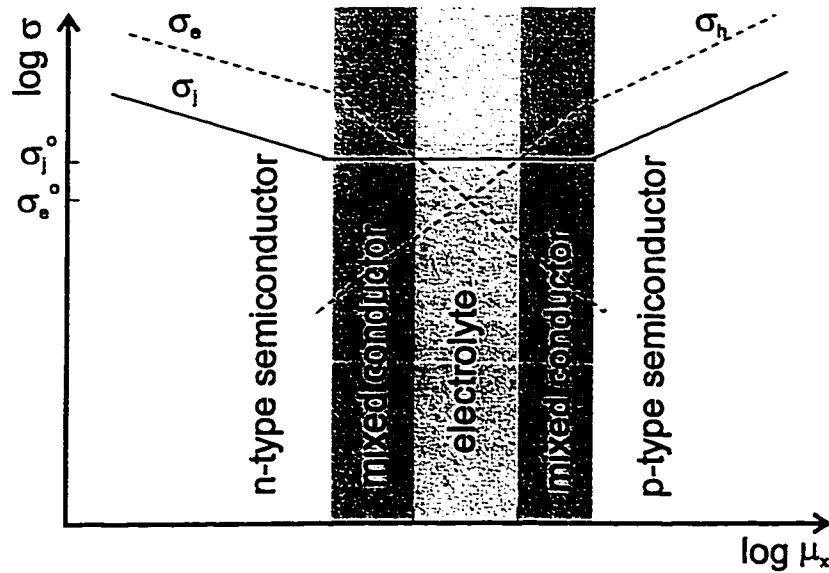


Figure 2-3. Conductivity diagram of pure compound MX with Frenkel disorder. Electrolytic domain boundaries are within the range of ionic disorder. σ_e^0 is the intrinsic electronic conductivity, σ_i^0 is the intrinsic ionic conductivity.

2.1.4.3. Temperature and Partial Pressure Dependence of Partial Conductivities

For various applications, it is highly desirable to learn the dependence of the various partial conductivities on temperature and partial pressure in SSI materials. If these could be determined reliably from direct experimental measurements, all the important predictions could be made. In this sense, defect theory and mass action laws which are used to rationalize the dependences would be of only secondary importance. However, it is not expedient to rely on measurements because too many would be required. Thus, the theory of defects provides a number of rather general laws concerning the dependencies

so that far fewer measurements are necessary to arrive at many meaningful predictions and useful extrapolations.

Briefly, the ionic conductivities of species in SSI materials can be written as

$$\sigma_j = c_j v_j l^2 q^2 / kT \quad (2-18)$$

where c_j is concentration, v_j is jump frequency, T is temperature and everything else is constant (jump distance l , Boltzmann's constant k and charge q). Thus, the temperature and partial pressure dependencies of the conductivities are due to those of c_j and v_j . In general, jump frequency v will always exhibit an Arrhenius dependence on temperature because hopping is a thermally activated process. No dependence of v on partial pressure is expected theoretically and none is found experimentally (Patterson, 1989). The concentration term has a bit more flexibility for different behaviors: two kinds of temperature dependencies (constant or exponential) and two kinds of partial pressure dependencies (constant or exponential). Beginning with the temperature dependence, c will either be independent of temperature or it will exhibit an Arrhenius dependence, albeit with a different activation energy than that exhibited by v . If the carrier concentration is fixed by extrinsic contaminations, deliberate or not, it will remain independent of partial pressure. In some cases, however, the concentration may be small enough that incorporation of X atoms from the ambient partial pressure will cause changes. On the basis of the law of mass-action, the concentrations generally vary as P_X^{2d} as effectively shown in Table 2-2. Here, d is a constant, usually a ratio of small integers, which is characteristic of the defect reaction whose equilibrium is involved.

In order to reveal the temperature and partial pressure dependence of partial conductivities more directly, a three-dimensional graph was introduced by Patterson (1971). This kind of graph is made by constructing the curves in Figure 2-3 for different temperatures, where the mass constants and the mobilities are modified.

2.1.4.4. Classification of Solids and Solid Electrolyte Domains

One possible classification of SSI materials, where ionic conductivity plays an important part, is given in Table 2-3 (Heyne, 1977) which shows two major kinds of SSI materials. A solid electrolyte is one with exclusively ionic conductivity; the mixed conductor is the one with appreciable electronic conductivity in addition to ionic conductivity.

Table 2-3. Classification of solid state ionic materials.

	Point defect type		Cation-disordered sublattice type	
	Dilute	Concentrated	Low temperature	High temperature
Solid electrolytes	NaCl, AgBr, LaF ₃	ZrO ₂ -Y ₂ O ₃ , CaF ₂	RbAg ₄ I ₅ , β-Al ₂ O ₃	Li ₂ SO ₄
Mixed conductors	β-Ag ₂ S	UO ₂	α-Ag ₂ S	SrO-LaCoO ₃

Roughly speaking, the reasons for ionic and for electronic conduction are independent (Heyne, 1977). The first is mainly related to crystal structure; the latter is determined by the electronic bandgap E_g , which depends more on the individual properties of the constituent ions.

The structure determines whether the electronic conductivity will be small or large, and is directly related to the band gap of the materials. Heyne (1973) has formulated a general semi-empirical rule for band gap values which give tolerable values of electronic conductivity. This can be stated as: "The electronic band gap of good solid electrolytes is always larger than $(T/300)$ eV." The basis of this rule is a direct calculation of the bandgap, which would give a maximum electronic conductivity less than $10^{-6} (\Omega\text{cm})^{-1}$ at any temperature. It may be noted that Heyne's condition is only a necessary condition but not in itself a sufficient condition for a material to be a good solid electrolyte. A rough guide for the selection of materials based on band gap (and hence color) is given in Figure 2-4 (Heyne, 1973).

If a crystal structure is favorable for fast ionic movement, its high ionic mobility may also be accompanied by a very low or very high electronic conductivity. A series of

compounds with comparable ionic conductivity, where the electronic conductivity varies from very low to quasi-metallic, was found. The first kind may find application as the electrolyte in solid electrochemical cells; the other might form a favorable class of materials for an electrode in such cells.

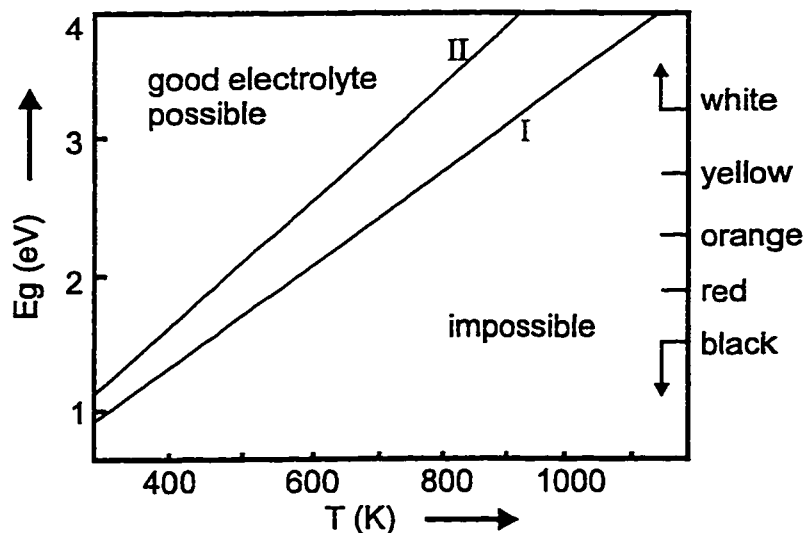


Figure 2-4. Minimum value of band gap for good electrolytes as a function of temperature (Curve I). A safety margin with a factor 100 is used for Curve II.

Both groups are subdivided further into two classes. In the first, the ionic movement is only by point defects in the crystal lattice. These lattice defects may, for example, be vacant lattice positions, or ions placed at normally unoccupied positions, so-called interstitial ions. They form only a small fraction of the normally placed ions and their concentration can be modified by doping with foreign ions. The defects can move by a jump mechanism often involving neighboring lattice ions as well. However, most of the ions at regular lattice positions cannot contribute to conduction or diffusion processes.

In the other class, there exists a large excess of available lattice positions for the mobile ion. The ions occupy the lattice in an unordered way, and moreover, they can change position very easily. A distinction between normal and interstitial positions in such a sublattice is meaningless from a defect physics point of view. All ions of the type concerned contribute to the electrical conduction and diffusion processes. The

magnitudes of the ionic conductivity and self-diffusion coefficient are comparable to those of liquid electrolytes. This is the case of “cation-disordered sublattice conductors”.

The two classes can be subdivided further as shown in Table 2-3, the cation-disordered sublattice compounds according to the temperature region where high conductivity exists, and the defect type compounds according to the concentration of lattice defects that can be introduced. A temperature is considered high if it is near the melting point of the SSI material.

2.2. Solid Electrolytes

Solid electrolytes, or as they are more popularly known, superionic conductors, are solid state ionic materials which possess an electric conductivity mainly due to ionic displacements (Hladik, 1972). The explosion of investigations of solid electrolytes dates from the sixties corresponding to the use of solid oxides (such as stabilized ZrO_2) for fuel cell research, as well as the discovery of new solid electrolytes (Bradley and Green, 1967) having conductivities, at or near room temperature comparable with conventional aqueous electrolyte solutions. In 1967, Na^+ - β/β' -alumina was found to be a good ionic conductor applicable to solid electrochemical sensors and solid state batteries (Yao and Kummer, 1967).

In this section, after briefly discussing the general features, various kinds of solid electrolytes will be introduced and classified. Because of the applications in the current thesis, emphasis is placed on two particular solid electrolytes, i.e., stabilized ZrO_2 and Na^+ - β/β' -alumina.

2.2.1. General Features of Solid Electrolytes

Solid electrolytes are ionic materials with high ionic conductivity. Ionic conductivity of solid electrolytes is comparable, in terms of order of magnitude, to values for melts and concentrated solutions of strong electrolytes. On the other hand, their mechanical

strength and elasticity are typical for solids. Thus, solid electrolytes could be considered as hybrids of liquid electrolytes and typical ceramic materials.

One of the most important features of solid electrolytes is their anomalously high ionic conductivity, with respect to other solid materials. Figure 2-5 (Rickert, 1978) shows the conductivity of some important solid electrolytes plotted as a function of reciprocal temperature along with the conductivity of a strong aqueous electrolyte, 37 wt.% H_2SO_4 , for comparison. Ionic conductivity of typical ionic crystals at temperatures not too close to the melting point does not exceed a value of $10^{-9} (\Omega\text{cm})^{-1}$, whereas the ionic conductivity of solid electrolytes (Gurevich, 1988) under the same conditions could be $10^{-1} - 10^0 (\Omega\text{cm})^{-1}$. This value is typically higher than the electrical conductivity of intrinsic semiconductors, but lower than that of metals.

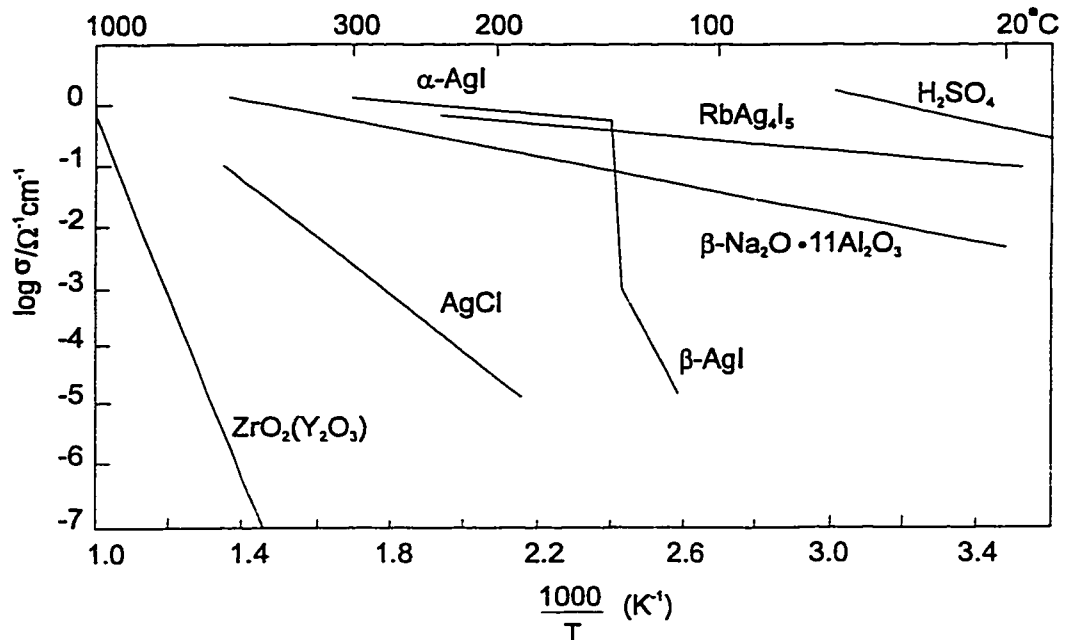


Figure 2-5. Temperature dependence of the conductivity of some solid electrolytes; comparison with the conductivity of concentrated H_2SO_4 (37 wt.%) is also shown.

In contrast to liquid electrolytes, where electrons contribute a negligible amount to the current flow in the solution, crystalline compounds exhibit partial electronic

conductivity, which is rarely negligible. By definition, solid electrolytes should exhibit exclusive ionic conduction with ionic transference numbers larger than 0.99. However, this condition is limited to a specific range of metal (or nonmetal) chemical potentials for solid electrolytes as shown in Figure 2-3 (Rapp and Shores, 1970).

The ionic conductivity σ in solid electrolytes can usually be described by the semiempirical equation (Vayenas et al., 1992):

$$\sigma = (\sigma_o / T) \exp\left(\frac{-E_a}{kT}\right) \quad (2-19)$$

where σ_o is a function of the ionic charge, the concentration of mobile ions, the frequency with which these ions attempt to move to a neighboring site (attempt frequency), and the distance of this movement (jump distance); E_a is the activation energy, on the order of 0.1 – 2 eV, for the mobile charged ionic species. The low energy of activation for ionic conductivity corresponds to the relative ease in which high mobility ions in good solid electrolytes can penetrate inter-site barriers in the crystal. Because of the higher activation energy of electronic conductivity compared with ionic conductivity, high temperature limits the solid electrolytic domain. The high activation energy of electronic conduction results from the high band gap required for the low electronic conductivity of a good electrolyte.

Several books and articles, which may be considered as comprehensive reviews or summaries of ionic conduction in solid electrolytes, have been published (Mott and Gurney, 1948; Wagner, 1957; Kroger, 1964; Alcock, 1968; Etsell and Flengas, 1970).

2.2.2. Classification of Solid Electrolytes

The number of synthesized and studied compounds with high ionic conductivity and low electronic conductivity under optimized conditions amounts to hundreds. Current carriers in these compounds are mono-, di-, and tri-valent cations, and halide and oxygen anions. Many kinds of solid state ionic materials are known and can be classified by

various criteria. A conventional way is to classify them by means of the kind of transport ions, such as Cu^+ , Ag^+ , Li^+ , Na^+ , K^+ and H^+ as cations and F^- , Cl^- and O^{2-} as anions. Some of the most common ones are collected in Table 2-4 (Rapp and Shores, 1970).

Table 2-4. List of selected solid electrolytes for each type of mobile ionic species.

Conducting species	Selected Compound	References
Fluorine (F^-)	CaF_2	Short and Roy (1963)
Chlorine (Cl^-)	BaCl_2	Tubandt (1932)
Bromine (Br^-)	BaBr_2	Tubandt (1932)
Iodine (I^-)	KI	Jost and Schweitzer (1933)
Oxygen (O^{2-})	$\text{Y}_2\text{O}_3(0.15) - \text{ZrO}_2(0.85)$	Steele and Alcock (1965)
Sulfur (S^{2-})	$\text{CaS}-\text{Y}_2\text{S}_3$	Worrell et al. (1969)
Carbon	$\text{BaF}_2-\text{BaC}_2$	Worrell (1974)
Nitrogen	AlN	Worrell (1974)
Hydrogen (H^+)	SrCeO_3	Iwahara et al. (1981)
Silver (Ag^+)	$\alpha\text{-AgI}$	Strock (1934)
Copper (Cu^+)	$\beta\text{-CuI}$	J.B.Wagner and C.Wagner (1957)
Lithium (Li^+)	LiH	Pretzel et al. (1960)
Sodium (Na^+)	$\beta\text{-Na}_2\text{O}\cdot 11\text{Al}_2\text{O}_3$	Yao and Kummer (1967)
Potassium (K^+)	KCl	Tubandt (1931)
Rubidium (Rb^+)	$\beta\text{-Rb}_2\text{O}\cdot 11\text{Al}_2\text{O}_3$	Yao and Kummer (1967)
Ammonium (NH_4^+)	$\beta\text{-(NH}_4)_2\text{O}\cdot 11\text{Al}_2\text{O}_3$	Yao and Kummer (1967)
Thallium (Tl^+)	$\beta\text{-Tl}_2\text{O}\cdot 11\text{Al}_2\text{O}_3$	Yao and Kummer (1967)
Magnesium (Mg^{2+})	MgO	Mitoff (1962)
Aluminum (Al^{3+})	Al_2O_3	Schmalzried (1963)

In order to understand the diffusion mechanism for the transport ions, it would be appropriate to classify them by structure according to Table 2-2, where solid electrolytes can be divided into two main types (Gurevich, 1988):

A type E solid electrolyte is a so-called intrinsic solid electrolyte. It is based on intrinsic structural disorder (Burley, 1967) with equal concentrations of corresponding defects. These are, in particular, β -alumina, α -AgI, a series of compounds with the α -AgI structure described by the general formula Ag_4MI_5 , (where $\text{M} = \text{Rb}, \text{K}, \text{NH}_4, \text{Cs}_{0.5}\text{K}_{0.5}$), and also fluorides of some di- and tri-valent metals ($\text{CaF}_2, \text{YF}_3, \text{LuF}_3$) where the high ionic conductivity is due to F^- anions. A distinctive feature of many superionic materials with intrinsic structural disorder is the existence of a certain critical temperature for each substance at which a jumpwise change in ionic conductivity due to crystal structure change is observed, as shown in Figure 2-5. Thus, they may have two qualitatively different states. At temperatures below the critical value, they behave as usual ionic crystals; above these temperatures, they acquire a superionic state as solid electrolytes.

A type F solid electrolyte is a so-called extrinsic solid electrolyte, and formed by compounds with dopant-induced structural disorder. The defect concentration is fixed by the amount of doping, and the high ionic conductivity is due to the high concentration of dopant ions, which promote structural disordering (Kroger and Vink, 1956). For instance, CaO can be introduced into the crystal lattice of ZrO_2 . Ca^{2+} ions are built into the Zr^{4+} lattice, whereas O^{2-} ions enter the oxygen sublattice. Since the charges of Zr and Ca ions are different, oxygen vacancies should necessarily appear in such a mixed crystal. If the number of such vacancies is sufficiently large, the mobility of oxygen ions markedly increases, and they start moving from one vacancy to another. Typical solid oxide electrolytes with dopant-induced disorder are compounds described by the general formulae $\text{MO}_2\text{-M}'\text{O}$ and $\text{MO}_2\text{-M}''_2\text{O}_3$, where M is a tetravalent metal (Zr, Hf, Ce), M' is a divalent metal (Ca, Sr, Ba), and M'' is a trivalent metal (Sc, Y). Unlike type E solid electrolytes possessing intrinsic structural disorder, compounds with dopant-induced disorder do not show a drastic temperature jump in ionic conductivity, although the ionic conductivity still increases with increasing temperature. Usually, the majority of solid electrolytes with dopant-induced disorder are the so-called high-temperature solid electrolytes.

In addition to the two major types of solid electrolytes, recently new types of solid electrolytes with noncrystalline structures have been studied (Liu et al., 1985; Minami,

1985). These include flexible mixed conductors (Aoustin et al., 1992; Tillement et al., 1992), ionic conductive mineral glasses (Ribes et al., 1979; Souquet, 1988), xerogels (Livage et al., 1988), composite ceramics and / or polymer electrolytes (Maier, 1988; Przulski and Wiczorek, 1989), and biological membranes (Stark, 1988). Because these materials lack the ideal characteristics required for classical utilization as electrodes or electrolytes, they are beyond the scope of the thesis.

2.2.3. β -alumina

The β -alumina type compounds, which are ternary oxides of the general formula $n\text{A}_2\text{O}_3 \cdot \text{B}_2\text{O}$ ($\text{A}^{3+} = \text{Al}^{3+}, \text{Ga}^{3+}, \text{Fe}^{3+}$; $\text{B}^+ = \text{Na}^+, \text{K}^+, \text{Rb}^+, \text{Ag}^+, \text{Tl}^+$, etc.), constitute an important group of solid electrolytes. The one utilized in the current thesis is the sodium aluminate in its two modifications (β - and β'' -aluminas), which is the most investigated β -alumina compound and has been known since 1916 (Rankin and Merwin, 1916).

The main characteristics of the Na^+ - β -alumina structure, with the ideal formula of $11\text{Al}_2\text{O}_3 \cdot \text{Na}_2\text{O}$ were determined in 1931 by Bragg et al. (1931). The symmetry is hexagonal (Steven et al., 1984), and the lattice constants are $a = 0.559$ nm, $c = 2.253$ nm. The space group is $\text{P}63/\text{mmc}$. The unit cell is composed of two spinel blocks separated by a mirror plane as shown in Figure 2-6(a). Na^+ - β'' -alumina with the ideal formula of $5.33 \text{Al}_2\text{O}_3 \cdot \text{Na}_2\text{O}$ has a rhombohedral symmetry (Bettman and Peters, 1969). The space group is $\text{R}3\text{m}$. In a system of hexagonal axes, the parameters of the unit cell are $a = 0.559$ nm, $c = 3.395$ nm. The structure as shown in Figure 2-6(b) is the result of the stacking of three spinel blocks, of the same type as those for Na^+ - β -alumina.

In 1967, Yao and Kummer (1967) found that Na^+ - β -alumina exhibited very high ionic conductivity, about 10^{-1} and $10^{-2} (\Omega\text{cm})^{-1}$ at 300°C and 25°C , respectively. This has led to an intense effort to use Na^+ - β/β'' -alumina as a solid electrolyte for a number of applications, such as solid electrochemical sensors and solid batteries. The properties described can be explained from the crystal structure. Both β - and β'' -aluminas are built of cubic blocks formed by the O^{2-} ions while the Al^{3+} ions take the same places in blocks as in spinel. These blocks are separated by loosely packed mirror planes containing only

O^{2-} and Na^+ . Thus, sodium ions are capable of moving two-dimensionally in the cleavage planes (Beevers and Ross, 1937) as schematically shown in Figure 2-7. Na^+ cations have a large mobility along these planes, and the fast diffusion of the Na^+ cations is responsible for the strong electric conductivity in $Na^+ - \beta/\beta''$ -alumina (Hoshino, 1991). The activation energy is extremely low at about 15.9 kJ/mol (0.17 eV). The bandgap is more than 6 eV. The high mobility of the sodium ions, which exists only in directions perpendicular to the c-axis, opens the possibility of replacing them by other monovalent ions like Ag^+ , K^+ and Rb^+ by means of an exchange reaction with a suitable salt melt. The conductivity along the c-axis is 100 to 1000 times weaker (Demott and Hancock, 1971).

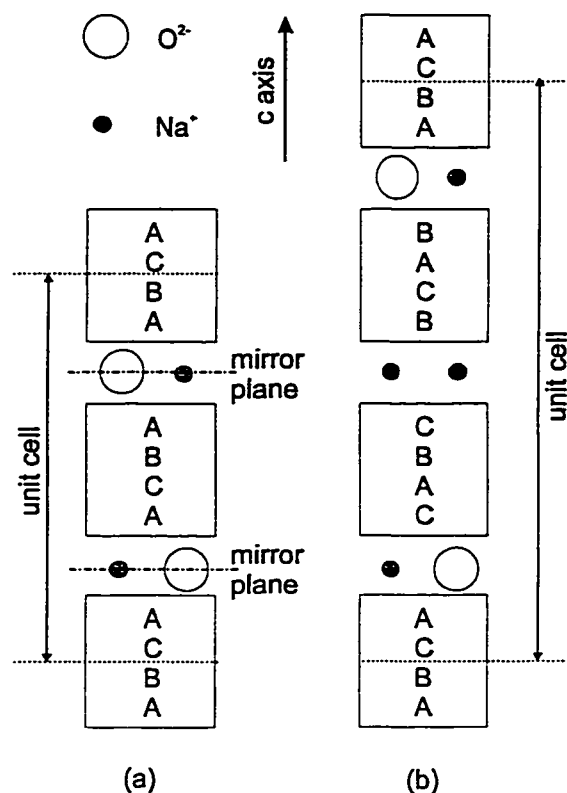


Figure 2-6. Oxide ion packing arrangement in β -alumina (a) and β'' -alumina (b). (Note: letters refer to stacking arrangement in spinel block, where ABC represents face-centered cubic packing while ABAB would represent hexagonal packing.)

Measurements have shown that the conductivity of Na⁺-β''-alumina is larger than that of Na⁺-β-alumina (Kummer, 1972). However, Na⁺-β''-alumina is a metastable phase. In order to stabilize the β''-phase and allow the preparation of compounds having good chemical stability and higher ionic conductivity for the applications as solid electrolytes, foreign ions (Mg²⁺, Li⁺) are usually added. Nevertheless, the β phase usually still exists in an almost inevitable small quantity. The Na⁺-β/β''-alumina samples used in the present study were supplied by Ceramatec, Inc., Salt Lake City, with a nominal composition of 8.85 wt.% Na₂O, 0.75 wt.% Li₂O and 90.40 wt.% Al₂O₃. The electric conductivity was given as 0.2 (Ωcm)⁻¹ at 300°C (Butchereit et al.).

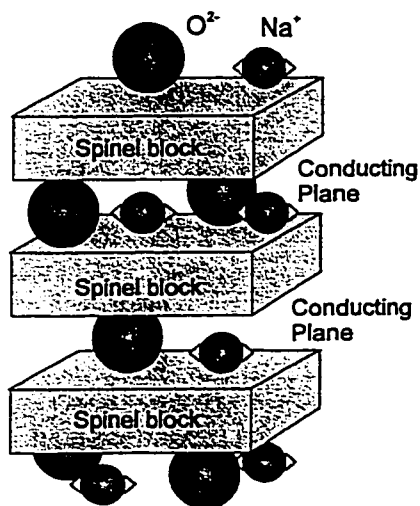


Figure 2-7. Two dimensional conduction in Na⁺- β/ β''-alumina.

2.2.4. Stabilized Zirconia

The ionic conductivity of stabilized zirconia was first observed by Nernst (1899) in 1899. However, it was the publication of two papers by Kiukkola and Wagner in 1957 (1957a; 1957b) which stimulated intense interest in stabilized zirconia. Currently, stabilized zirconia has been used not only in high-temperature research (Etsell and Flengas, 1970; Worrell, 1974) but also in electrochemical probes (Littlewood, 1966; Fitterer, 1966) and high-temperature fuel cells (Ruka and Weisbart, 1962; Sverdrup et al.,

1973). Several reviews on stabilized zirconia are available (Etsell and Flengas; Subbarao and Maiti, 1984; Stevens, 1986).

Pure ZrO_2 does not serve as a good electrolyte, primarily because its ionic transference number is too low. On the other hand, the low temperature monoclinic (m) form of ZrO_2 transforms to a tetragonal (t) form at 1170°C with a large contraction (3%-5%). The tetragonal form of ZrO_2 further changes at 2370°C to a cubic fluorite structure which exists up to the melting point of 2680°C. Doping ZrO_2 with certain aliovalent oxides stabilizes the cubic fluorite structure from room temperature to its melting point, and increases its oxygen vacancy concentration at the same time. Consequently, stabilized zirconia has high oxygen ionic conductivity.

The most commonly used stabilizing oxide or dopant is trivalent Y_2O_3 because of availability and cost. Other dopants are CaO , MgO , Sc_2O_3 , Yb_2O_3 , etc. These oxides exhibit a relatively high solubility in ZrO_2 and are able to form the fluorite structure, which is a face-centered cubic arrangement of cations with the oxygen ions occupying the tetrahedral sites as shown in Figure 2-8. This structure is stable over wide ranges of composition and temperature. Stabilization of ZrO_2 is accomplished by direct substitution of divalent or trivalent cations of appropriate size for the host lattice cation Zr^{4+} . The substitution not only stabilizes the cubic fluorite structure but also creates a large concentration of oxygen vacancies by charge compensation according to the following equation in Kroger-Vink notation for yttria stabilized zirconia (YSZ):



The high oxygen vacancy concentration gives rise to a high oxygen-ion mobility. Oxygen ion conduction takes place in stabilized ZrO_2 by movement of oxygen ions via vacancies in an analogous fashion to the conduction process in classical cation conductors such as $NaCl$ (Hagenmuller and van Gool, 1980; Rickert, 1982). Oxygen ion diffusion is many orders of magnitude larger than cationic migration. For example at 1000°C, the oxygen ion diffusion coefficient in 15 mol % calcia-stabilized zirconia is $3.5 \times 10^{-8} \text{ cm}^2/\text{s}$, while the diffusion coefficients of Zr^{4+} and Ca^{2+} are $1.2 \times 10^{-13} \text{ cm}^2/\text{s}$ and $4.4 \times 10^{-14} \text{ cm}^2/\text{s}$, respectively (Subbarao, 1980). Thus, the major ionic charge carrier in

stabilized zirconia is the oxygen ion. Over a wide range of temperature, the ionic conductivity of stabilized ZrO_2 is independent of oxygen partial pressure over many orders of magnitude. Under these conditions, electronic conduction is negligible and the ionic transference number is very close to unity.

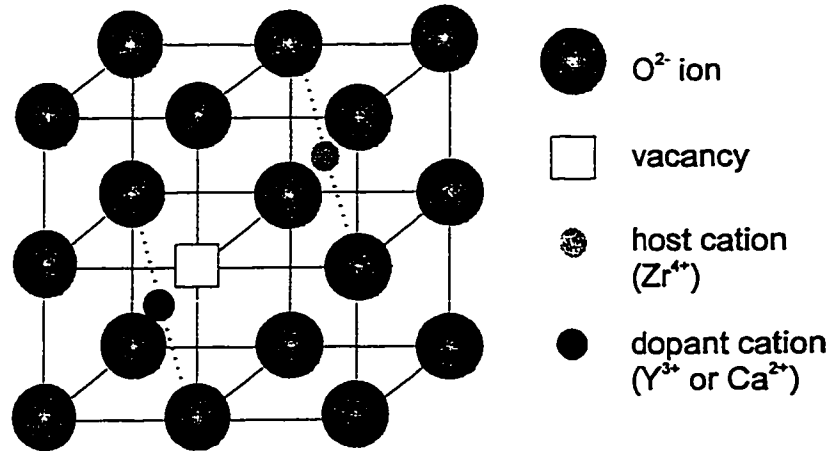


Figure 2-8. Schematic of one half of the unit cell of the fluorite structure of a ZrO_2 doped with a divalent (Ca^{2+}) or trivalent (Y^{3+}) cation.

The ionic conductivity of stabilized ZrO_2 depends on dopant concentration. Figure 2-9 (Baumard and Abelard, 1988) illustrates the variation of conductivity with dopant concentration for various doped ZrO_2 samples. Isothermal plots of conductivity exhibit a maximum conductivity, which corresponds to the minimum quantity of dopant required to fully stabilize the cubic fluorite phase. In this study, the stabilized zirconia was also supplied by Ceramtec, Inc. at a doping level of 6 mol % Y and 8 mol % Yb. The ionic conductivity at $1000^\circ C$ is expected to be $0.03 - 0.05 (\Omega cm)^{-1}$ with an activation energy of about 1 eV (Etsell and Flengas, 1970).

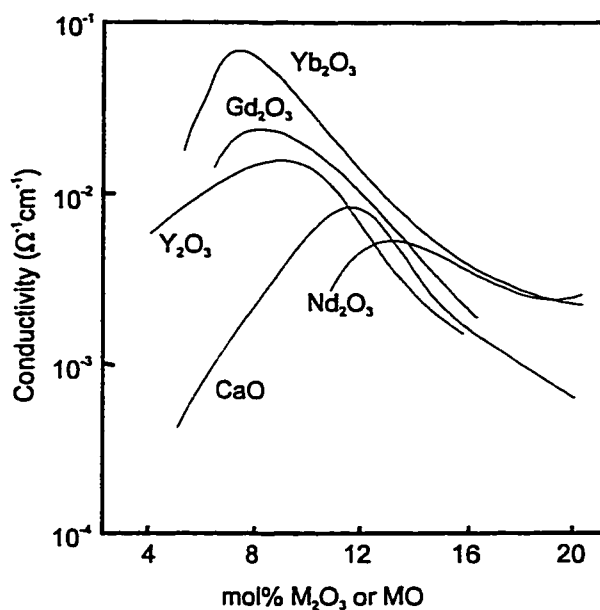


Figure 2-9. Variation of ionic conductivity of stabilized ZrO_2 with dopant concentration ($T = 1080 \text{ K}$).

2.3. Solid State Electrochemistry

2.3.1. *The Development of Solid State Electrochemistry – From Wagner’s Electrochemical Tarnishing Theory*

In 1933, C. Wagner (1933) combined the foregoing concepts of mass and charge transport in solids, and published a detailed analysis of the parabolic tarnishing of metals in aggressive environments. In that study, he assumed that:

- (a) transport of neutral species was negligible compared to that of ionic and electronic carriers in solids;
- (b) all the charged carriers in solids migrated with Einstein-type mobilities under the combined influences of chemical potential gradients and electric fields.

The assumptions made it possible to transform the problem of parabolic scale formation of metals to one of diffusional transport in an electrochemical medium – a solid scale product. The ions in the scaling product are due to dissociation of the host medium itself. However, because of the nature of solids as discussed previously, i.e.,

oppositely charged ions are usually not mobile, ionic movement is compensated by electronic movement in a solid electrochemical medium to maintain electroneutrality. The details of the phenomenological description of a scaling process are as follows:

For simplicity, the presentation here is still based on an arbitrary binary MX compound. Figure 2-10 facilitates the physical description by showing the compound MX attached as a scale layer to the substrate metal M on the left, and exposed to the non-metallic gas phase X on the right. Because the scale MX is an SSI material, X molecules, which are neutral in the gas phase, can be incorporated into the scale only as anions, which are negatively charged X^- anions. Conversely, each incorporated M atom must become a positively charged M^+ cation. This has important electrochemical consequences because the region at L is forced to become increasingly electron-deficient or positively charged as the negative anions are “formed” and then wander off toward the metal-rich left side under the electrochemical potential gradient of the X^- ions. Similarly, the metal at the left accrues a surplus of negative charge due to the electrons liberated when M atoms enter the scale as cations and move to the right under the electrochemical gradient of M^+ ions.

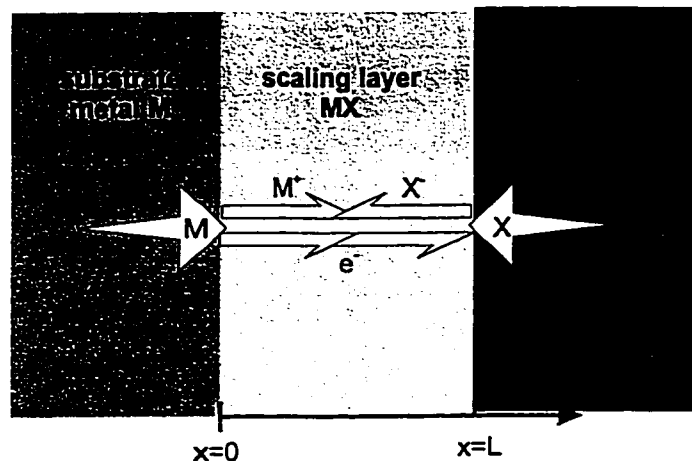


Figure 2-10. Physical arrangement of a metal (M) undergoing scaling at ambient atmosphere of X to form scaling product MX.

Eventually, the oppositely charged outside layers cause a very strong coulombic field to build up; it must be positive on the gas side and negative at the metal side. This polarity necessarily opposes the migration of both charged ionic species, and increases as

the charging continues to build. The incorporation of X atoms by the scale is self-defeating if electrochemical forces are at play. In fact, if there were no electronic leakage paths connecting the two surfaces, all cation and anion migration would soon grind to a halt. At this point, no further weight gain would be observed but an emf on the order of volts would be observed. Accordingly, the scaling products MX exhibit galvanic cell behavior.

Some degree of internal shorting within scales always occurs because scaling layers exhibit at least a trace of internal conduction by electronic carriers. For this reason, it is best to think of scales MX as mixed (ionic and electronic) conductors. The internal electronic leakage current weakens the oppositely charged coulombic field. Consequently, the migration of mobile ions resumes to the same extent as the electronic leakage current. This causes the continuous growth of the scale at the rate the electronic leakage current goes through the scale. This rate is parabolic in nature. If the scale exhibits a large conductivity for electrons (large compared to the ionic conductivity), massive internal shorting occurs and no coulombic retardation of ion movement is possible. In this situation, scaling proceeds as fast as the unhindered ions can diffuse through the scale. The scale product, MX, shows electrolysis effects. Although the growth kinetics will still be parabolic, no perceptible open circuit emf will be found over the scaling layer. This is the limiting case in which electronic conduction dominates in the scale.

This description of a scaling process shows that solids (scaling products) exhibit electrolytic behavior (Patterson, 1974), i.e., both electrolysis and galvanic cell effects. According to modern atomistic notions, an electrolytic medium is considered to be an assemblage of atoms and/or molecules of which at least a small fraction are mobile ions. They are electrically charged and they are also free to migrate about in the medium. Thus, solid scale products MX can serve as electrolytic media for a number of applications.

The prospect of controlling corrosion by controlling reactant transport through the scale products as suggested by the electrochemical tarnishing theory initially generated much excitement in corrosion engineering circles. However, because of various complicating factors (Choudhury and Patterson, 1971), this optimism was somewhat

misguided. Since material transport through scale products can hardly be controlled under actual corrosion conditions, only a limited number of metal scaling systems important to modern technology strictly conform to the conditions required by Wagner's tarnishing theory. Instead, modern interest in Wagner's theory is expected to derive from applications in solid state electrochemistry as well as in solid state ionic technology.

2.3.2. Solid Electrochemical Systems

A solid electrochemical system is a multiphase electrochemical cell in which the interphase potential differences result in net potential differences between the terminals. Historically, the foundations of electrochemical theory are derived from Faraday's study of aqueous systems. An electrochemical cell can either be a galvanic cell or an electrolytic cell. In a galvanic cell, the potential differences between phases result from the transfer of chemical species between phases. This converts chemical energy into electrical energy. In an electrolytic cell, a flow of current produces a chemical reaction; electrical energy from an external source is converted into chemical energy. By analogy to electrochemical cells with aqueous electrolytes, those with solid electrolytes consist of at least two solid electrodes separated by a solid electrolyte. Ideally, the solid electrolyte is an ionic conductor and an electronic insulator (Goodenough and Shukala, 1988).

Generally speaking, the ionic conductivity of solid electrolytes is much more selective than that of aqueous electrolytes. Because of the nature of defect energies involved, the imperfections of a crystalline lattice almost never contribute to the migration of more than one mobile ion species through a rigid lattice. The connective transport mechanisms that prevail in aqueous electrolytes are wholly absent in solids. Therefore, the competition of various ionic species in the electrode reactions is seldom a factor in the interpretation of solid electrochemical systems. This must be considered something of an advantage over aqueous electrochemical systems. However, anion and cation mobilities in an aqueous electrolyte are of the same order of magnitude and their simultaneous flow gives rise to three major problems:

- (a) corrosion of the electrodes;

- (b) consumption of the solvent (water) by electrolysis during recharging and by corrosion during storage, making necessary periodic refilling. If these two processes give off gases, totally sealed systems are prohibited.
- (c) containment problems which virtually preclude miniaturization of aqueous electrolyte energy cells.

On the other hand, the aqueous state offers very good contact with the electrodes and high ionic conductivities; transport in liquids permits ready access to the electrode reaction sites. In contrast to aqueous media, solid substances may exhibit substantial electronic conductivity. Accordingly, deviations from Faraday's laws or anomalously low open-circuit emf values for solid electrochemical systems are very often interpreted in terms of electronic conduction effects. Similar deviations in aqueous electrochemical systems are more often blamed on mixed electrode reactions, interaction of electrode reaction products, or electrode polarization effects. Thus the possibility of electronic conduction presents an additional complicating factor in the electrochemistry of solids.

The more or less mutually exclusive temperature ranges of application of aqueous and solid electrolytes give rise to another contrasting feature, especially for research applications of solid and aqueous electrochemistry. In some applications, the need for a heat source may constitute a disadvantage for the solid electrochemical systems. Of course, aqueous systems cannot survive at elevated temperatures. In low-temperature regimes, where aqueous electrolytes dominate, performance is often limited by electron and mass transfer at electrode / electrolyte interfaces. However, at the elevated temperatures at which solid electrolytes are used, electrode kinetics is so greatly accelerated that it frequently does not limit the performance of the solid electrolyte devices. Accordingly, solid electrochemical cells are commonly used to study chemical equilibria or kinetic processes in the bulk of the contacting electrode or in the electrode chamber as a whole. Studies in aqueous systems, on the other hand, very often pertain only to the interface region between the particular electrolyte and electrodes involved.

In contrast to pure electronic conduction, ionic conduction in an electrochemical system is always accompanied by chemical redox reactions, which occur at the interface of an electrochemical medium and its neighbor phases. Thus, it is a mixed physical and chemical phenomenon instead of a purely physical phenomenon. Consequently,

electrochemical cells are able to transfer electrical energy to chemical energy or vice versa.

In the following discussion, it will be accepted that, in the system considered, meaningful thermodynamic quantities such as chemical potentials μ and electrochemical potentials $\bar{\mu}$ can be defined, although flow of material is taking place in an electrochemical system, Figure 2-11. In an electrochemical system (one with electrical potential ϕ differences between phases), electrochemical potentials $\bar{\mu}$ replace chemical potentials μ in all thermodynamic equations. The gradient in the electrochemical potential $\bar{\mu}$ is the driving force for the flow of charged carriers in the solid electrochemical cell. Since the changes in chemical composition that accompany the development of interphase potential differences are extremely small, the chemical potential in an electrochemical system is the same as the chemical potential in the corresponding chemical system with no potential differences between phases.

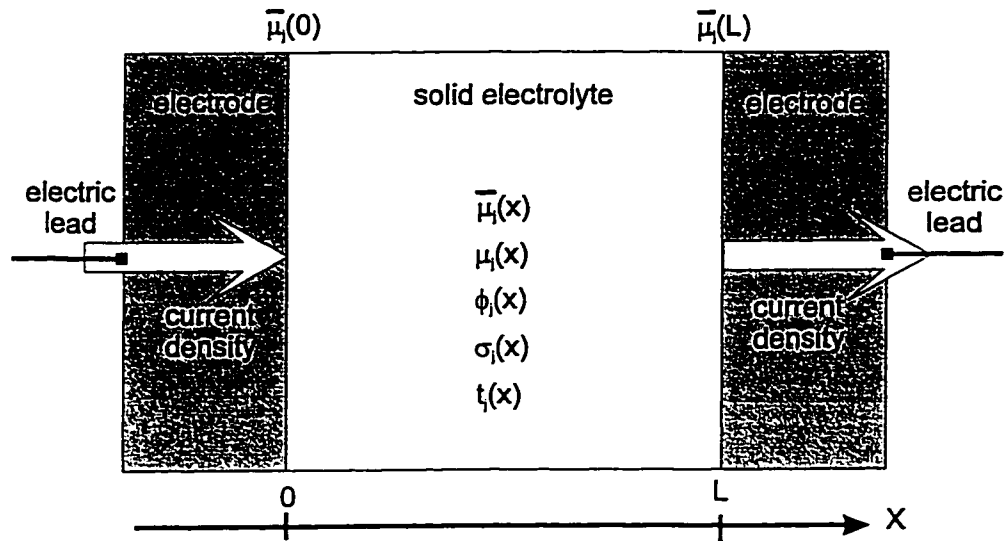


Figure 2-11. Illustration of the influencing parameters in a solid electrochemical cell.

Because ideas are presented in terms of single particles such as vacancies, interstitials, electrons and electron holes, the atomic unit is chosen instead of the gram-mol as the mass unit to define concentrations, chemical potentials, etc. In this way, equations are presented that conform to those used in semiconductor physics. This has

the further consequence that, in the formulae, the gas constant R is replaced by Boltzmann's constant k and the Faraday constant F by the absolute value of the electronic charge q . Onsager cross-coefficients (coupling between fluxes) are usually negligible in solid electrochemistry. Throughout this discussion, isothermal conditions will be assumed, and the equations will be kept simple by considering only one-dimensional geometry and isotropic solids (Wagner 1955; Heyne, 1977).

2.3.3. Energy Transfer in Solid Electrochemical Cells

Independent of any specific knowledge of the mechanism of ionic conduction in a solid electrolyte which exhibits exclusive ionic conduction, a simple consideration of energy conversion provides the relationship between the reversible cell potential E and the Gibbs free energy change ΔG for the virtual chemical reaction of the cell.

$$\Delta G = -nFE \quad (2-21)$$

n is the number of electrons involved in the electrode reactions passed through the external circuit for the reaction. In practice, however, the potential difference is not measured while the cell reaction is proceeding, since there is a finite current flow through the cell. Under these conditions, the current is almost always accompanied by polarization effects. The energy transfer under closed circuit conditions is discussed in the following.

If an electrical current is either forced or permitted to pass through any part of the components in a solid electrochemical cell, the partial current density i_j of any species j is, in general, proportional to the overall transport force acting upon that species. This force can be expressed as the gradient of the electrochemical potential $\bar{\mu}_j$ of the species in question. If transport involves no volume change (Wagner, 1975), the proportionality constant between the current and the electrochemical potential gradient $\bar{\mu}_j$ is given by the partial specific electrical conductivity σ_j of species j .

$$i_j(x) = -\frac{\sigma_j(x)}{z_j q} \left(\frac{\partial \bar{\mu}_j(x)}{\partial x} \right) \quad (2-22)$$

z_j is the effective valence, and q is the elementary charge. In order to obtain expressions for potential differences measurable between two positions in an electrochemical system, the electrochemical potential $\bar{\mu}_j$ is often split into a chemical and an electrical part.

$$\bar{\mu}_j(x) = \mu_j(x) + z_j q \phi(x) \quad (2-23)$$

$\phi(x)$ represents the electrostatic potential of charged carrier j at location x . Thus, the electric potential gradient is related to the current density and the chemical gradient of the charged carrier j :

$$\frac{\partial \phi_j}{\partial x} = -\frac{i_j(x)}{\sigma_j(x)} - \frac{1}{z_j q} \left(\frac{\partial \mu_j(x)}{\partial x} \right) \quad (2-24)$$

By integrating over the SSI material thickness, the electrical potential difference, E , between the two interfaces ($x = 0$ and $x = L$) of the material is obtained.

$$E = -\int_0^L \left(\frac{i_j}{\sigma_j} + \frac{1}{z_j q} \frac{\partial \mu_j}{\partial x} \right) dx \quad (2-25)$$

In a multi-component system, the total current density, i , due to all the carriers is the sum of the partial currents, i_j , of the j -carriers.

$$i = \sum_j i_j(x) \quad (2-26)$$

According to the definition of the transference number,

$$E = -\int_0^l \left(\frac{i}{\sigma_T} + \sum_j \frac{t_j}{z_j q} \frac{\partial \mu_j}{\partial x} \right) dx \quad (2-27)$$

The aforementioned expressions for the thermodynamic response of an SSI material during energy transfer show that the total conductivity σ_T and the transport numbers t_j of each of the charged particles are the only material properties which influence the energy transformation. The total conductivity is related to the total electrical resistance of the material by simple geometrical conditions. Furthermore, Eq.(2-27) shows that the energy transformation depends on two distinct parts: the intrinsic characteristic of the solid electrolyte (the first term in the equation) and the solid electrolyte/electrode interfaces characteristics (the second term in the equation).

Energy transfer does not occur under open circuit condition, when no current is passed through the external circuit after the initial charging process. The potential difference E of the cell, its electromotive force (EMF), could be multiplied by nF to give the maximum electrical work nFE . This quantity is equal to the negative of the Gibbs energy ΔG of the cell reaction. Furthermore, upon application of the Gibbs-Helmholtz relations to the temperature dependence of the cell voltage, reaction enthalpies ΔH and reaction entropies ΔS are also obtained for the virtual cell reaction. In the following, the origin of the EMF is discussed.

The requirement for charge neutrality has to be fulfilled under steady-state conditions:

$$\sum_j z_j i_j = 0 \quad (2-28)$$

So, the relationship between the chemical potential gradients and the electrostatic potential gradients become:

$$\text{grad}\phi = -\frac{1}{q} \sum_j \left(\frac{\sigma_j}{z_j \sum_j \sigma_j} \right) \text{grad}\mu_j = -\frac{1}{q} \sum_j \left(\frac{t_j}{z_j} \right) \text{grad}\mu_j \quad (2-29)$$

where t_j is the transference number. The generated electrical field gradient $\text{grad}\phi$ compensates the tendency for the ionized gaseous species to diffuse under the influence of the chemical potential gradient $\text{grad}\mu_j$. This compensating electrical field (EMF) is measured as an integral quantity between the left- and right-hand electrodes:

$$EMF = -\frac{1}{q} \int_l^r \sum_j \frac{t_j}{z_j} d\mu_j \quad (2-30)$$

Although no current passes through an electrochemical cell to transfer energy under the open circuit condition if the ionic transference number is unity, this equation shows that the chemical energy difference between the two sides of an electrochemical cell is transferred to an electric signal and can be read as the open circuit EMF value.

2.3.4. Material Transport in Solid Electrochemical Cells

For material transport in SSI materials, the conductivity mechanism imposes some restrictions on the otherwise wide variety of possible combinations of defect chemical parameters. Fundamental considerations of material transport in a solid electrochemical cell can be obtained by the local equilibrium approach. The electrochemical condition at each point in the solid state ionic material—i.e., the concentrations and mobilities of its constituent ions and electrons—is determined by the prevailing chemical potentials or activities of the constituent “atoms”, which are neutral. Accordingly, point-to-point variations in the medium are most meaningfully characterized either in terms of voltage profiles or in terms of chemical potential (activity) profiles of the appropriate neutral

species, or in terms of both. Only voltages and chemical potential differences for neutral species, (not those for the ions) are amenable to direct measurement and control (Guggenheim, 1929; 1930; Newman, 1967; Patterson, 1974).

To provide insight into the parameters that determine material transport in a solid electrochemical cell, the chemical potential in Eq (2-23) may be replaced by the activity by use of the defining equation

$$\mu_j = \mu_j^\circ + kT \ln a_j \quad (2-31)$$

where μ_j° is the chemical potential in the standard state ($a_j=1$).

The conductivity may be written in terms of the product of the concentration of the mobile species c_j and the diffusivity D_j :

$$\sigma_j = \frac{c_j D_j z_j^2 q^2}{kT} \quad (2-32)$$

From this equation it can be seen that D_j is also the quantity that contains the kinetic contribution to the conductivity of species j . This diffusivity is defined as the quantity that obeys the Nernst-Einstein relation (Nernst, 1888; Einstein, 1905) between the electrical mobility u_j (drift velocity per unit electric field) or the general mobility b_j (drift velocity per unit general force) (Wagner, 1930), and the diffusion coefficient, regardless of whether the material can be considered to be an ideal or a non-ideal solution.

$$D_j = u_j \frac{kT}{|z_j|q} = b_j kT \quad (2-33)$$

The diffusivity D_j is a measure of the random motion of the particles of species j in the absence of concentration gradients. It is related to the trace diffusion coefficient, which is determined by the use of radioactive isotopic tracers, D_j^* , by $D_j^* = f_j D_j$ (Bardeen and Herring, 1951), where f_j is the correlation factor, or more generally, the Haven ratio (Leclaire, 1970).

Combining all the above equations and Eq.(2-22) yields

$$i_j = -\sigma_j \frac{\partial \phi}{\partial x} - z_j q D_j \frac{\partial \ln a_j}{\partial \ln c_j} \frac{\partial c_j}{\partial x} \quad (2-34)$$

By assuming that there are no other forces involved in the transport of species j , such as correlation effects due to the simultaneous transport of other components, this equation is general for isothermal conditions and is valid at any point in a solid electrochemical cell. The first term on the right-hand side is identical to Ohm's law for the migration of species j under the influence of an internal electrostatic field. The second term is related to Fick's first law for diffusion under a concentration gradient. Thus, material transport in a solid electrochemical cell is a combination of conduction and diffusion.

2.3.4.1. Transport in a Solid Electrolyte

In most cases, one can assume that a solid electrolyte is characterized by a very large concentration of mobile ions or ionic defects. As a result, the chemical potential of the mobile ionic species, which is proportional to the logarithm of the activity, may be regarded as essentially independent of position within the material. Thus any ionic transference in such phases must be predominantly due to the influence of an internal electrostatic field:

$$i_j = -\sigma_j \frac{\partial \phi}{\partial x} \quad (2-35)$$

For electronic defects, excess electrons and holes, which can be considered to be relatively dilute in a solid electrolyte, the situation is different, and either an internal electrostatic field, a concentration gradient, or both may be important. This will depend upon the differences in chemical potentials of the electronic species at both sides of the solid electrolyte. When the concentration of the electronic species is high, the influence

of an internal electric field is more important than when the concentrations of such species are low.

If the ionic current is blocked in an application, which will be discussed later, so that only electrons and holes may pass through the electrolyte, the internal electrostatic field must become negligible under steady-state conditions. In that case, the transport of electronic species may occur only as the result of a concentration gradient.

2.3.4.2. Transport in a Mixed Conductor

A different situation holds in the case of a mixed conductor. Consider first a mixed conductor with an overwhelmingly high electronic conductivity such as the electrode in a solid electrochemical cell. It can be assumed that charge transport is predominantly due to the motion of electronic species. In that case the chemical potentials of the excess electrons or holes may be regarded as practically independent of location within the solid, due to their high concentrations and or mobilities. Thus, their transport is primarily due to the effect of an internal electric field in such materials. Because of the large concentrations of these electronic species, as well as their high mobilities, this field will, of course, be very small.

If ionic transport occurs across an electrode/solid electrolyte interface in connection with current flow by the motion of ionic species in the solid electrolyte, the ionic flux within the electronic conducting material must be predominantly determined by the presence of a local ionic concentration gradient in that phase (second term in Eq. 2-34).

$$i_j = -z_j q D_j \frac{\partial \ln a_j}{\partial \ln c_j} \frac{\partial c_j}{\partial x} \quad (2-36)$$

It should be noted that the thermodynamic factor ($\partial \ln a / \partial \ln c$) can sometimes be very large, and acts to enhance the ionic flux density above that which would be expected from the concentration gradient alone (Darken, 1948; Wagner, 1951; Heyne, 1968). In a predominantly electronic conductor in which the concentration of excess electrons or

holes is very large, so that the chemical potentials of the electronic species are essentially uniform throughout the body, the gradients of the chemical potentials of neutral atoms and their respective ions are identical. Thus the transport of ions may be considered to be the same as the net diffusion of neutral species.

If a mixed conductor is not predominantly an electron or hole conductor such that the sum of the transference numbers of the electronic species differs appreciably from unity, the internal electrostatic field may not be completely neglected with regard to the movements of ions. In such a case the transport of ionic species occurs under the combined influence of electrostatic and chemical potential gradients. This situation can be expressed as:

$$i_{j(\text{mixed conductor})} = -z_j q D_j W \frac{\partial c_j}{\partial x} \quad (2-37)$$

W is a more general “enhancement factor” (Weppner and Huggins, 1977). The values of this enhancement factor under various conditions were studied and summarized by Weppner and Huggins (1978).

In addition to being expressible in terms of thermodynamic quantities, the enhancement factor can be interpreted kinetically as the generation of an internal electric field by a displacement of the concentration profiles of two differently charged mobile species within the solid. If one of them, for example, electrons have a significantly greater mobility than the other ions. In a concentration gradient, the more mobile species will tend to move ahead of the other. The requirement for overall charge flux neutrality causes the more mobile species to be slowed down and provides an additional driving force for the less mobile one (Weppner and Huggins, 1977).

2.3.5. Interface Effects in Solid Electrochemical Cells

Material transport of a component in a solid electrochemical cell is also related to the solid electrolyte/electrode interface characteristics which fix the external electrical

conditions (electric potential and current density) and the external chemical condition (chemical potential). These interfaces in a solid electrochemical cell are located in a chain of electrical conductors where the conductivity changes in nature from electronic to ionic (Kleitz et al., 1975).

A criterion of thermodynamic equilibrium at an interface between the solid electrolyte and electrode is an equality of electrochemical potentials. If establishment and maintenance of the equilibria are rapid, then the response of the interface to a non-equilibrium field is to drive the equilibrium predominantly in one of the component directions resulting in rapid transfer across ideally reversible interfaces (Raleigh, 1975). In practice, if the current is not zero, it needs to be modulated by kinetic considerations (Gerisher, 1975). The treatment applies only to systems in which there is at most an infinitesimal flow of current, since equilibrium thermodynamics is inapplicable to irreversible processes.

2.3.5.1. Interface Polarization in Solid Electrochemical Cells

From an electrochemical point of view, the fundamental question is whether arriving charged particles can cross the interface regions or not. If they can, the interface is said to be non-polarized and, electrically, corresponds to a resistor. If charged particles cannot cross the interface, it is said to be polarized and it is electrically equivalent to a capacitor (Janata, 1978). The real situation usually corresponds to an intermediate case with a fraction of the transporting particles kept on one side of the interface. This leads to polarization effects in the interface region.

Without entering into details, if the interface material is infinitely conductive for a charge carrier j crossing the interface, then j is instantaneously distributed through the bulk of this material. The chemical potential of j at the interface is hardly different from the chemical potential of j in its bulk. This tends to be an ideal conducting interface for j with no polarization effect. A local equilibrium is attained at each interface point in a solid electrochemical cell.

On the other hand, if the interface material is a very poor conductor for j , then j is located in the perturbed layers near the interface. The material is a very poor homogeneous one. This leads to an increase in the chemical potential of j at the interface, which is very different from the chemical potential of j in its bulk. Thus, the driving force for j across the solid electrolyte decreases. This interface is a blocking interface for j with a high polarization effect.

Only in the first case, i.e., the interface is infinitely conductive, could the interface electrochemical potential of j in the aforementioned equations be replaced by the electrochemical potential of j in the bulk of the neighbor phase.

2.3.5.2. Current Conservation in Solid Electrochemical Cells

Due to the conservation of charges, the same value of total current I exists everywhere in a solid electrochemical cell. Nevertheless, the partial current of each charge carrier can change. The change in a partial current density may either occur in the same phase or be induced by an interface between two phases with different conductivity properties.

In the latter case, a non-stationary system must be considered and the flux given in Eq.(2-34) needs to be balanced. According to the equation of continuity or Fick's second law, for conservation of charged species j ,

$$\frac{\partial i_j}{\partial x} = -\frac{\partial n_j}{\partial t} \quad (2-38)$$

When charge transfer takes place in the interface region, this usually leads to an accumulation or depletion of charge carriers in perturbed layers located at both sides of the interface (Kleitz et al., 1975). The variation of concentration of a species directly influences the value of its chemical potential as well as the value of the electrical potential.

In the former case, the total charge transport within a solid may be composed of several partial currents whose magnitudes vary with position. Such a situation would not be measured by instruments in an external circuit, since they record only the total current passing through the overall electrochemical cell. However, an electrolyte in a solid electrochemical cell serves as an ion-pass filter. If the electronic conductivity is negligible and only ionic species can cross the electrolyte, the total externally measurable current must be equal to the partial ionic current within the electrolyte. The same is true for the electronic current in an electrode, if the ionic current is negligible.

As a last point, one needs to take into account the evolution of the cell with time. The current, I , passing through the external circuit between the connection leads induces a flow of ions through the electrolyte. The mole number, N_j , of the specie j which is transported between the two electrodes across the electrolyte during time Δt is given by Faraday's law:

$$N_j = \frac{t_j I \Delta t}{z_j F} \quad (2-39)$$

where t_j is the average transference number of the mobile species j in the solid electrolyte.

2.3.6. Solid State Electrochemistry for Theoretical Studies

Based on the knowledge of charge and material transport in solid electrochemical cells, cells with solid electrolytes could be built for thermodynamic as well as for kinetic measurements. Thermodynamically, the open circuit emf of solid electrochemical cells gives information about Gibbs reaction energies, reaction enthalpies and entropies, and also about activities, chemical potentials and partial pressures. From a kinetic point of view, the current through suitably built electrochemical cells with solid electrolytes can be a measure of reaction rates.

During the last 40 years, many types of reactions have been studied by high-temperature electrochemistry and applications of the technique are steadily increasing in number and becoming more ingenious. Among the features that make electrochemical methods very attractive is the fact that solid electrolytes may act as electrochemical transducers. Thermodynamic and transport quantities can be converted into easily and precisely measurable electrical quantities, e.g., voltages and currents. Compared to other techniques, the precision obtainable is very high. In short, applications in this area take advantage of electrical measurements to interrelate the thermodynamics and kinetics of a phase change or chemical reaction.

In the following, some general aspects of the applications will be discussed.

2.3.6.1. Solid State Ionics Technology for Thermodynamic Studies

In 1957 four independent publications by Kiukkola and Wagner (1957a, and b), Ure (1957) and Lidiard (1957) stimulated a general revival of interest in high-temperature galvanic cells incorporating solid electrolyte phases. They introduced the use of ZrO_2 -based and ThO_2 -based solid electrolytes for the determination of the standard free energy of formation of oxides. Since then, solid oxide and halide electrolytes have been extensively used in many thermodynamic investigations.

Wagner (1955) and Kroger (1964) have discussed broadly the types of electrodes and their possible combinations to form solid electrolyte galvanic cells. As in the electrochemistry of liquid electrolytes, galvanic cells with solid electrolytes may be treated from two different points of view:

- (a) that due to Helmholtz, in which the maximum available work done by the cell during the cell reaction is considered;
- (b) that due to Nernst, in which single electrode potentials are considered, and then summed to give the total emf of the galvanic cell.

The Helmholtz approach provides direct information about the emf of a cell, but little data on the factors causing the emf to assume a particular value and on the various physical processes taking place in the cell. More information of this type can be obtained

by using the Nernst approach whereby electrochemical and electrical potentials are considered.

During the last 40 years, the use of solid electrolytes for thermodynamic measurements received much of its impetus from the work of Kiukkola and Wagner (1957a and b) and Peters and Mobius (1958 and 1959). Thermodynamic investigations in solid state electrochemistry involving such galvanic cells with solid electrolytes permit the determination of quantities such as Gibbs reaction energies, chemical potentials, and activities or partial pressures. Reviews dealing with the use of solid state electrochemistry for thermodynamic studies have been published (Schmalzried, 1966; Raleigh, 1966; Alcock, 1968).

2.3.6.2. Solid State Ionics Technology for Kinetic Studies

Besides their use for thermodynamic measurements, solid electrochemical cells have become increasingly important for kinetic studies in solids and at surfaces and phase boundaries of solids. Kinetic measurements using solid electrolytes fall into two categories.

The first category includes the measurement of transport phenomena in solid electrolytes. The polarization technique devised by Hebb (1952) and Wagner (1955) may be used for this purpose. With the aid of polarization measurements on suitable galvanic cells, it is possible to obtain information about partial conductivities in solids.

The second category includes the use of a solid electrolyte to study transport phenomena in an electrode or the kinetics of a phase boundary reaction. Kinetic measurements with solid state galvanic cells involve diffusion processes or diffusion-controlled reactions, and reactions taking place at a solid/gas phase boundary or solid/solid phase boundary.

Each type of kinetic measurement is based on the combined use of Faraday's law and Wagner's equation. The combination of reaction rate measurements via electric current with determinations of thermodynamic quantities via the emf often permits the analysis of kinetic processes. These processes may be diffusion in solids and liquids, diffusion-

controlled solid-state reactions, and phase boundary reactions at solid/solid phase boundaries or at solid/gas phase boundaries, e.g., evaporation processes.

The dissolution and diffusion of interstitial and substitutional solutes into a single phase electrode have been investigated electrochemically. For instance, Raleigh et al. (Raleigh, 1967; Raleigh and Crowe, 1969) have studied the diffusion of silver in Ag-Au alloys. Wagner introduced a coulometric titration technique in 1953 to study the dependence on silver activity of the Ag/S ratio in Ag₂S (Wagner, 1953). Furthermore, the investigation of the interfacial reaction rate for various mobile ion activities was conducted by Rickert et al. (Rickert, 1960; 1968a and b; Mrowec and Rickert, 1961; Rickert and Wagner, 1962; Rickert and O'Briain, 1962; Donner and Rickert, 1968). Electrochemical investigations of the evaporation and condensation of species from compounds have also been made by Rickert et al. (Rickert, 1961; 1962; 1968a; Ratchford and Rickert, 1962; Detry et al., 1967; Mrowec and Rickert, 1962; Birks and Rickert, 1963). Solid state electrochemistry has also been applied to study heterogeneous catalytic reactions, and the non-Faradaic electrochemical NEMCA effect that was reported (Vayenas, 1990; Vayenas et al., 1992) in 1981.

A detailed review dealing with the use of galvanic cells for kinetic studies has also been published (Wagner, J.B., 1975).

2.4. Solid State Ionic Technology

In addition to theoretical studies in solid state electrochemistry, numerous energy conversion applications based on the energy transformation capability of SSI materials have boomed since the "energy crisis" in the 1970s (Tillement, 1994). Recently, principles from solid state electrochemistry have been combined with those from semiconductor physics and microelectronic technology to build a "solid state ionic technology" (Wagner, 1957c), which is a modern technology, based on applications of the presently available solid electrolytes.

Since solid electrolytes do conform to the conditions laid out in Wagner's electrochemical tarnishing theory, the fundamentals of solid state ionic technology are derived from two set of implications in Wagner's scale process investigation.

First of all, ionic and electronic transport within SSI materials permits material transport through solids in a controlled manner.

Secondly, since materials transport through SSI materials involves both ionic and electronic current flow, conversion between electrical and chemical energy in a solid electrochemical cell is possible.

The current technical applications of Wagner's theory in solid state ionic technology are largely focused on the second implication, i.e., energy transfer, in various kinds of solid state ionic devices. By comparison, applications utilizing the material transport capability of solid electrolytes to form useful products as presented in the first implication have been relatively insignificant to date. The likely reasons are:

- (a) The initial excessive enthusiasm for controlling corrosion in corrosion engineering circles by forming scale products did not materialize (Choudhury and Patterson, 1971).
- (b) The thermodynamic and kinetic conditions for controlling material transport in solid electrochemical cells to form useful product are difficult to control.
- (c) People tend to believe that utilization of condensed matter (solids) for material transport is not efficient.

2.4.1. Solid State Ionic Technology for Solid State Ionic Devices

The term solid state ionic device refers to all electrochemical devices which contain at least one solid electrolyte. These include solid potentiometric sensors, solid oxide fuel cells and solid state batteries. In all these devices, the solid electrolyte element can be expected to perform according to the second implication of Wagner's tarnishing theory (Patterson, 1974), i.e., combined ionic and electronic transport can take place to allow transformation from chemical energy to electrical energy (or vice versa). Currently, SSI devices represent a large field of interest and have been the subject of extensive research

for more than 30 years. Although the scale of their production is still limited, their economic importance and environmental impact are quickly growing.

2.4.1.1. Basic Devices

By choosing appropriate SSI materials as solid electrolytes and electrodes along with suitable interfaces in a solid electrochemical cell, a simple external electrical circuit can be used to study, monitor or convert the chemical characteristics of various neighbor compounds. This is the basis of solid state ionic devices.

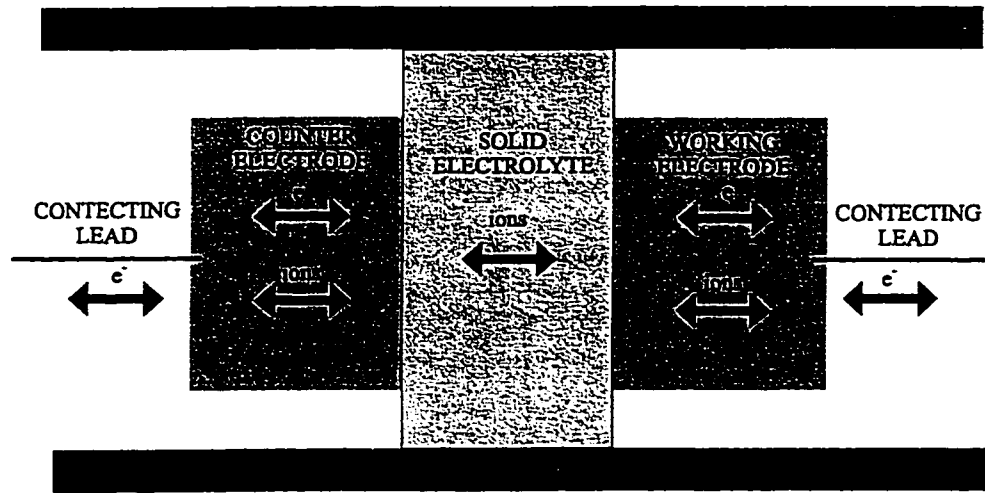


Figure 2-12. Schematic construction of basic SSI devices.

The central part of a basic SSI device, Figure 2-12, is a solid electrochemical cell. It corresponds to a three component device, two electrodes (counter and working) and one solid electrolyte, placed between two inert metallic conductors linked to the external circuit. When a current passes through the device, a chemical redox reaction takes place. The device can be viewed as a chemical reactor where the reactants are distributed over both the electrodes and separated by the solid electrolyte. The reaction occurs by the transfer of electrons through the external loads from one electrode to the other which is

simultaneously compensated by an ionic flow through the solid electrolyte. An SSI electrochemical device is designed to have an electronic current in the load of the external circuit and a predominantly ionic current in some part of the internal circuit.

The application of SSI electrochemical devices is guided by the properties of the “basic device”. In such a device, the ratio of the chemical potential of the electroactive component at both electrodes is directly transformed into an electrical signal in the external circuit. Accordingly, various kinds of SSI devices can be built. Two SSI devices closely related to the thesis will be discussed in detail in the subsequent sections. One of them is of the open circuit variety – solid potentiometric sensors for process control and environmental monitoring. The other is of the closed circuit variety -- solid oxide fuel cells for energy generation.

2.4.1.2. Solid Potentiometric Sensors - Open Circuit SSI Devices

Solid state potentiometric sensors are solid electrochemical devices that are used to determine the concentrations of particular chemical species, which are usually found in gases and liquids (Janata, 1989; Alcock, 1992; Azad et al., 1992). The general principle of potentiometric sensors is the direct conversion of chemical energy of the reaction of the mobile electroactive components with the detected species into electrical energy by an electrochemical concentration cell under open circuit condition. The chemical energy of the reaction is dependent on the chemical potential of the detected species, which therefore controls the emf value of the electrochemical cell according to Eq. (2-21).

As shown in Figure 2-13, a solid potentiometric sensor in the simplest form is a galvanic concentration cell consisting of a solid electrolyte, a reference electrode and a working electrode (Weppner 1987a). In order to determine the chemical potential of the detected species at the working electrode, the chemical potential of the detected species must be known and is usually fixed at the reference electrode. The measurement of the electrical potential difference between both electrodes is directly related to the difference in the chemical potential of the mobile species at both solid electrolyte/electrode interfaces. Thus, at equilibrium, the chemical potential of the detected species at the

working electrode can be determined directly from Nernst's equation (Eq. (2-30)) (Wagner, 1933).

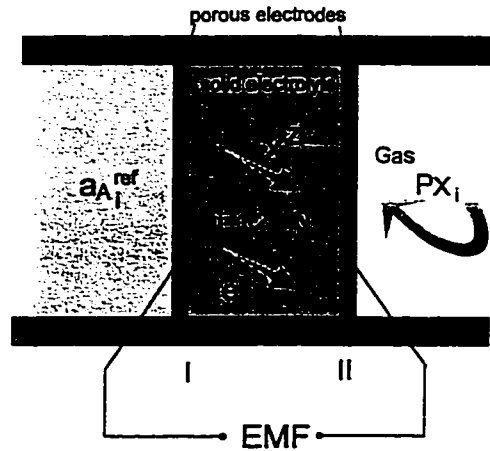


Figure 2-13. Solid potentiometric gas sensor.

Theoretically, the EMF of the galvanic cell is independent of the physical properties of the solid electrolyte. Consequently, the magnitude of the conductivity of the solid electrolyte is of secondary importance in solid potentiometric sensors. However, two limitations should be emphasized. First of all, the total resistance of the SSI sensor must be less than the impedance of the device used to measure the potential. Secondly, the electrolyte must possess high selectivity and very low electronic current. The effect of electronic conductivity is not only to lower the open circuit cell potential, but also to introduce an internal short-circuit which induces a diffusional process between the electrodes that changes the characteristics of the reference electrode. Thus, the performance of the solid potentiometric sensor is related to the selection of the solid electrolyte and other cell components.

The major advantages of solid state potentiometric sensors can be summarized in the following (Weppner, 1987a; Williams and McGeehin, 1984; Goto, 1983):

- Solid electrolytes provide the advantage that one type of ion is by far more mobile than the others, which makes the solid electrolytes selective to this component.

- Chemical potentials (or activities) of the detected species are directly transferred into easily and precisely measurable electrical quantities, which may be directly sent to feedback loops or processed further for display or process control.
- The EMF is independent of the size and geometry of the cell in a solid potentiometric sensor. This permits miniaturization and integration into microelectronic circuits.
- Performance is also generally more tolerant to processing parameters, such as the impurity level, the presence of grain boundaries and surface treatments, than other types (resistive and conductometric sensors).

To date a variety of SSI potentiometric sensors have been studied in detail, and several are commercially available. According to the electrode reactions at the working electrodes of sensors, Weppner (1986) has classified potentiometric sensors into three types.

Type I: The electrode reactions convert the detected species to mobile ions in the solid electrolyte.

Type II: The electrode reactions convert the detected species to immobile ions in the solid electrolyte

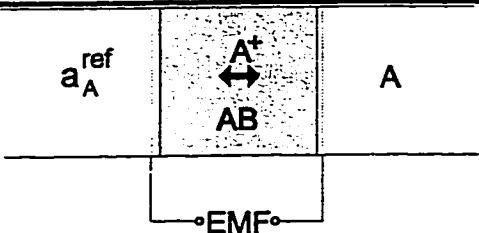
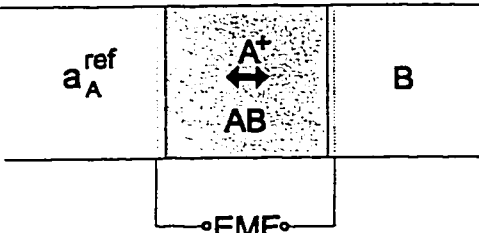
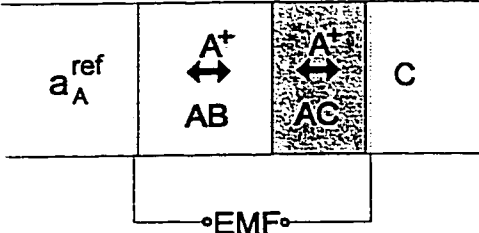
Type III: The electrode reactions convert the detected species to either mobile or immobile ions in the solid electrolyte through the mediation of auxiliary phases incorporated into the working electrodes.

The classification is illustrated in Table 2-5 (Yamazoe and Miura, 1995), together with some examples.

One of the older and simpler types of chemical sensors is the type I SSI sensors. These sensors are based on a direct measurement of the activity of the mobile species. The unknown species to be detected corresponds to the mobile ion species in the electrolyte. This can be done only when solid electrolytes are available to conduct the ionic state of the detected species. Applications have been found, such as analytical determinations in solution (Na^+ , K^+ , H^+ ...) (Morf, 1981) and measurements of di-atomic gas pressure (O_2 , H_2 ...) (Fouletier and Vitter, 1980; Schoonman, 1988). Among the developments, solid O^{2-} ion electrolytes, e.g., stabilized zirconia or thoria, have had the most commercial success. These sensors are able to cover a wide range of oxygen

activities and satisfy a large variety of applications. They are currently being used to determine the oxygen partial pressure in automobile exhaust systems, molten steel, food packaging, etc.

Table 2-5. Classification of solid potentiometric sensors.

Type	Cell structure	Solid electrolyte	Detected species
Type I		ZrO ₂ (+Y ₂ O ₃)	O ₂
		Sb ₂ O ₃ +4H ₂ O	H ₂
Type II		Li ₂ SO ₄ -Ag ₂ SO ₄	SO _x
		Ba(NO ₃) ₂ -AgCl ₂	NO ₂
		K ₂ CO ₃	CO ₂
		SrCl ₂ -KCl	Cl ₂
Type III		Na ⁺ -β-alumina (Na ₂ SO ₄ auxiliary phase)	SO _x
		NASICON (Ba(NO ₃) ₂ auxiliary phase)	NO _x
		NASICON (Na ₂ CO ₃ auxiliary phase)	CO ₂
		LaF ₃ (LaOF auxiliary phase)	O ₂

Type I sensors are restricted to the detection of the species where a convenient electrolyte exists. It is unlikely that such solid electrolytes will ever be found for the chemical detection of species that correspond to non-mobile ions (either very large, very charged or hetero-atomic ions). In order to overcome this problem, indirect sensors have been proposed (Gauthier and Chamberland, 1977; Weppner, 1990). These sensors can be built if there exists a known simple relation between the chemical potential of the non-mobile ionic species under study and the chemical potential of the mobile ionic species in the solid electrolyte. Usually, a chemical equilibrium is involved to meet this requirement.

In type II potentiometric sensors, chemical equilibrium is established between the species to be detected and an immobile component of the solid electrolyte. This requires a solid electrolyte which has a suitable immobile component. This restricts type II potentiometric sensors to a few of the presently known fast solid ionic conductors. For instance, due to the existence of good cation-conducting alkali metal sulfate electrolytes, many efforts have been conducted towards SO_x sensors (Worrel and Liu, 1977).

When the species to be detected are not present in the solid electrolyte, an auxiliary phase can be applied to link the chemical potential of the detected species to the mobile or immobile species in the solid electrolyte of the sensor. This is the so-called type III solid potentiometric sensor (Weppner, 1987b). Hotzel and Weppner (1985) have proposed different kinds of type III potentiometric sensors for Cl_2 , NO_2 and CO_2 detection by using either AgI or $\text{Na}^+ - \beta/\beta''$ -alumina with a corresponding auxiliary phase like AgCl, AgNO_3 or Na_2CO_3 . Indirect galvanic determination in type III potentiometric sensors is the most versatile method (Schoonman et al., 1986; Huang et al., 1992).

Both type II and type III sensors are especially important for detecting gaseous oxides such as CO_2 , NO_x and SO_x ; the details will be presented in Chapter 4.

2.4.1.3. Solid Oxide Fuel Cells - Closed Circuit SSI Devices

The principles of fuel cells were first proposed by Sir William Grove in 1839 (1839). A fuel cell is a primary electrochemical device in which the two electrodes are made with the two different chemical reactants. Fuels (H_2 , CO , CH_4 , CH_3OH ...) are fed to one

electrode (anode) and oxidized by oxygen supplied at the cathode (Jagannathan et al., 1980; Fickett, 1984; Goodenough and Shukla, 1988). Since the free energy of the reaction is negative, a spontaneous reaction takes place. Fuel cells are designed to use the chemical energy of a spontaneous redox reaction as a source of electrical energy. The electrochemical reactions taking place in fuel cells correspond to combustion reactions in conventional reactors. However, in an ordinary chemical reaction, oxidizers and reducing agents react directly with electrons to form the reaction products, and release or absorb energy usually as heat. In an electrochemical reaction, the energy transfer is manifested as a voltage and current flow in an electrochemical cell. A fuel cell is thus able to convert the free energy of a chemical reaction directly to electrical energy. Hence, it is not Carnot limited. From a thermodynamic point of view, fuel cells are more efficient compared to most conventional forms of power generation.

The feasibility of developing fuel cells with solid electrolytes was first demonstrated by Baur and Preis (1937) early in 1937. Since then, solid oxide fuel cell (SOFC) research has made excellent technical progress, particularly in recent years. The working principle of a solid oxide fuel cell is schematically shown in Figure 2-14 (Minh, 1993; van Herle and Thampi, 1994). Oxygen is reduced at the cathode to O^{2-} anions, which are transported through the ionic conducting solid electrolyte to the anode where they react electrochemically with fuel molecules, for instance H_2 , to give the combustion product H_2O . The electrons are released in this anodic reaction and transported back to the cathode through the external circuit, thereby delivering electrical power. The theoretical value of the open circuit voltage is about 1 V. In closed circuit working conditions, as for a battery, the voltage will drop as the current increases because of the internal resistance of the cell and electrode polarization.

Practical fuel cells are not operated as single units; rather they are connected in electrical series to increase voltage. A series of cells is referred to as a stack. An interconnect material is required to connect the anode of one cell to the cathode of the adjacent cell in a stack. Fuel cell stacks can be configured in series or parallel depending on the particular application.

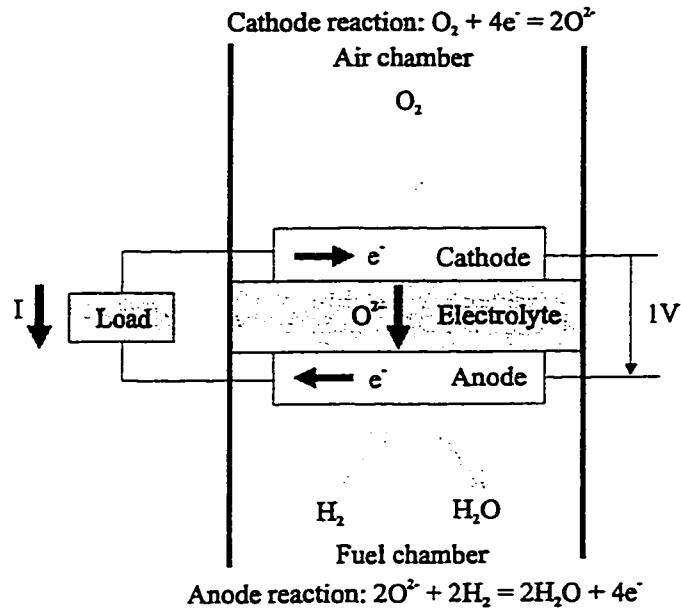


Figure 2-14. The working principle of a solid oxide fuel cell.

Research and development in the field of SOFCs has been in progress for the past 60 years. Multi-kilowatt SOFCs, based on stabilized zirconia electrolytes, have been operated for thousands of hours and have shown excellent performance. Currently, the SOFC is the most studied and advanced choice (van Herle and Thampi, 1994) for fuel cells. Compared to other types with aqueous, polymeric or molten electrolytes, the potential advantages of this energy conversion system are: 'clean' energy (low emissions), high efficiency, compact solid modules delivering high power densities, internal fuel reforming, recoverable heat as a byproduct and the possibility of cogeneration (Appleby and Faulkes, 1989).

In order to operate SOFCs with high energy conversion efficiency, the solid electrolyte must have good ionic conductivity and a very low electronic transference number to avoid ohmic losses and the short circuit effect in the electrolyte. It should also be impervious to gases. In order to operate with high efficiency at high intensities, the electrodes must exhibit very low polarization. They must possess sufficient porosity to permit adequate diffusion of the reacting and product gases; they must also present an optimal charge transfer reaction area where an electrochemical reaction is promoted. Finally, the electrolyte and electrode materials must have phase stability, matching

thermal expansion characteristics and chemical compatibility with contacting materials and reaction gases over a wide temperature range, i.e., from room temperature to the operating temperature (Steele, 1975; Hammou, 1988).

2.4.1.4. The Major Problems with Current SSI Devices

In spite of the great promise SSI devices offer, few of them have been commercialized today. At present, the key challenge is development of reliable and cost-efficient techniques to synthesize SSI materials to serve as solid electrodes and electrolytes in SSI devices (Takahashi, 1989). In addition, more sophisticated SSI devices have been developed. New components, such as chemical protection layers (Cogan et al., 1987; Jones et al., 1991), gas sensitive phases (Weppner, 1987b), regulatory layers (Miysmura et al., 1981) and electrocatalysts (White et al., 1992) with unique properties are added to the classical three-component electrochemical cell. Advanced fabrication techniques are required to put such a multi-phase device together.

The fabrication techniques for SSI devices are rather traditional. Some proven modern fabrication techniques for the microelectronics industry, such as chemical vapor deposition and physical vapor deposition, are not particularly applicable to SSI devices. The main reason is that components in SSI devices are not used in isolation, but form an electrochemical system and must be in contact with each other (Hagenmuller, 1988). The response of SSI materials in these devices is highly related to the interface characteristics, which fix the external electrical conditions (electric potential and current density) and the external chemical conditions (chemical potential). For instance, the solid electrode/electrolyte interfaces must possess high ionic and electronic mobility. Thus, developing fabrication techniques not only to synthesize each component, but also to improve the interfaces in SSI devices, assumes real significance (Kleitz et al., 1975).

2.4.2. Solid State Ionic Technology for SSI Device Fabrication – Solid Electrochemical Deposition (SED)

In order to meet the above-mentioned SSI device fabrication challenges, solid electrochemical deposition (SED) techniques have been developed and recognized recently. In general, SED takes advantage not only of energy transformation but also material transport itself during ionic and electronic transport in solids to form practical useful products. In contrast to the original unsuccessful applications to form passive layers for high temperature corrosion protection, material transport and product formation in SED occurs under well-controlled thermodynamic and kinetic conditions. This has renewed interest in Wagner's electrochemical tarnishing theory for controlling material transport for solid product formation.

Two kinds of SED techniques have been developed thus far. One is electrochemical vapor deposition (EVD); the other is polarized electrochemical vapor deposition (PEVD). The latter one is the central topic of the current thesis. Before discussing PEVD in the following chapters, it is necessary to briefly review EVD.

The desire of achieving thin and pore-free yttria stabilized zirconia (YSZ) films as an electrolyte over a porous electrode (cathode) to reduce the ohmic resistance of solid oxide fuel cells (SOFCs) led to the development of a new vapor deposition method. Electrochemical vapor deposition (EVD) was first introduced by Isenberg at the Westinghouse R&D center in Pittsburgh, Pennsylvania in the late 1970s (Isenberg, 1977 and 1981). Later, both university and industrial research laboratories in the US, Japan and the Netherlands continued to work to improve the EVD process. The work has led to numerous patents over the last ten years (Isenberg 1984, 1986a and 1988).

The principles of the EVD process, to deposit a thin layer of YSZ on a porous cathode for SOFCs, have been outlined extensively in the literature (Carolan and Michaels, 1987; de Haart et al., 1991; Dietrich and Schafer, 1984; Schoonman et al., 1991; Pal and Singhal, 1990a). The actual procedure is a CVD/EVD two-stage process as schematically shown in Figure 2-15. Briefly, the process consists of passing specific amounts of halides containing the required cations ($ZrCl_4$ and YCl_3) over one side of a porous substrate; the halides are chosen for their relatively high vapor pressures. Oxygen and/or steam at a given activity is passed on the other side of the substrate.

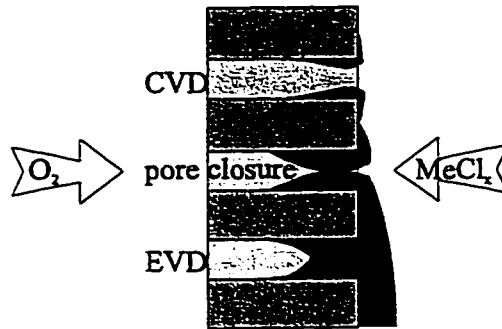


Figure 2-15. CVD/EVD process to deposit a YSZ thin film on a porous substrate.

The first stage is a counter-diffused chemical vapor deposition process. In this stage of the reaction, molecular diffusion of oxygen, steam and metal halides ($ZrCl_4$ and YCl_3) occurs through the pores in the substrate, and they react to fill the pores with the desired oxide according to the chemical reaction,



The processing pressure, temperature, type of halides and their respective flow rates are chosen so that the reaction is thermodynamically favored. After this counter-diffused CVD process, all the pores in the substrate are sealed by YSZ to form two separate compartments as source and sink sides of an EVD system (Lin et al., 1989a).

The actual EVD process occurs in the second stage (Isenberg, 1977). The gradient in oxygen potential that exists across the deposited YSZ (in the pores), between the halide (sink) side and the oxygen (source) side, causes solid-state electrochemical transport of the ionic species (O^{2-}) and an electronic species to maintain electroneutrality. At the sink side, both charged species electrochemically react with the reactants in the gas phase to form the desired product,



and the product continues to grow as a film over the substrate.

Thermodynamically, the driving force for the growth in EVD is the electrochemical reaction and formation of the product. This creates an oxygen chemical potential difference between the two sides of the substrate, which is sealed after the first stage of counter-diffusion chemical vapor deposition. Kinetically, the rate limiting step in an electrochemical reaction is the same as that in a chemical reaction, i.e., the slowest step controls the reaction as well as the deposition rate. Thus, all major kinetic effects should be considered such as pore diffusion, charge transfer reactions and bulk diffusion. In the past few years, several groups have investigated the kinetics of this EVD process. Both linear (Isenberg, 1977) and parabolic (Carolan and Michaels, 1990a; Pal and Singhal, 1990a) growth rates were observed. To explain this discrepancy, Lin et al. (1990) have developed a model which showed that there is always a transition behavior for any EVD process on porous substrates. At the beginning of EVD, diffusion of the oxygen source reactant through the substrate pores is the rate limiting step for layer growth. When the deposition layer thickness is larger than the so-called transition thickness, bulk diffusion through the film plays the dominant role in the film growth process (Heyne, 1977). This model further indicated (Lin et al., 1990) that transition thickness depends on deposition conditions such as substrate characteristics, experimental temperature and pressure.

Recently, a critical evaluation of the literature data was given by Dekker et al. (1992). In their study, all reported parabolic rate constants in EVD studies were gathered and presented in an Arrhenius plot, which strongly supported the argument that bulk diffusion of electrons in the product layer controls the product growth in an EVD process. This study also indicated that increasing the processing temperature will increase the growth rate, because electronic transport inside the product is a thermally activated process (Park and Blumenthal, 1989). Calculation shows that increasing the temperature from 1273 K to 1473 K causes the growth rate to increase more than six fold (Carolan and Michaels, 1990a). Based on the diffusion coefficients for electronic charged carriers in YSZ (Weppner, 1977a and b), a 6 $\mu\text{m}/\text{hour}$ growth rate can be obtained for 10 mol% YSZ at 1300 K (Dekker et al., 1989), which has been experimentally verified by Carolan and Michaels (1990a). However, in the case of pore diffusion limiting growth, a lower deposition rate of only 1 to 2 $\mu\text{m}/\text{hour}$ was reported (Lin et al., 1989b).

In order to eliminate other reaction limiting steps and to obtain the maximum deposition rates, parameters such as temperature and pressure in an EVD process are chosen so that the electronic transport inside the product thin film layer is the rate limiting step. Thus, the deposition is usually conducted at low pressure ($\leq 10^{-4}$ atm) and high temperatures (≥ 1273 K) to obtain fast surface reactions. Under these conditions, the solid-state electrochemical transport of minority carriers (electrons in this case) is the slowest step and controls the deposition rate (Pal, 1992).

Besides the high deposition rate, conducting the EVD process in the solid state transport limiting regime is critical to growing a uniform and gas-tight layer. Because the electrochemical reaction is limited by solid state transport, growth will be fastest in the shortest transport directions. Consequently, a fully dense and uniform layer of YSZ results.

Two types of surface morphology have been reported in the EVD growth of YSZ: a faceted type and a "cauliflower type" of surface (Dekker et al., 1989; Carolan and Michaels, 1990a). The difference in morphology can be explained by a change in relative rates of film growth and surface reconstruction, or possibly due to the thermodynamic instability of a surface species at high temperatures (Carolan and Michaels, 1990b).

In order to lower the operating temperature of SOFCs, EVD has received much attention over the past decade or so as a technique for the deposition of several other oxides, or for stabilizing ZrO_2 with dopants other than yttrium to provide lower resistance solid electrolytes for SOFCs.

Other than doping with yttrium to stabilize zirconia, EVD has also been utilized to deposit zirconia doped with ytterbium or codoped with yttrium and ytterbium (Schoonman et al., 1991).

Tanner et al. demonstrated an EVD process for depositing CeO_2 on dense Y_2O_3 -doped CeO_2 substrates for the fabrication of a two-layer composite electrolyte (Jue et al., 1992; Tanner et al., 1993; Tanner and Virkar, 1994a). In their studies, $CeCl_3$ vapor was used as the source of cerium. Unlike CVD/EVD processes for depositing YSZ on porous substrates, mass transport processes through different solid phases in the deposited thin film and the substrate should be taken into account in this case. The same group also showed the possibility of using a liquid $CeCl_3$ precursor to deposit CeO_2 on a Gd_2O_3 -

doped CeO_2 substrate (Tanner and Virkar, 1994b). The process was named electrochemical liquid deposition (ELD), and is similar to EVD in the same way that CVD is similar to chemical liquid deposition (CLD). This presents the possibility of expanding solid electrochemical deposition further to transport reactants through the solids and react with species in phases other than the vapor phase.

EVD has also been used to grow perovskite interconnection materials for fabricating tubular SOFCs at Westinghouse (Pal and Singhal, 1990b). Generally, the interconnection material used in SOFCs must have a high electronic conductivity, be gas tight and be stable in both oxidizing and reducing ambients. The current common choice is Mg doped lanthanum chromite (LaCrO_3), which is a p-type semiconductor with a small contribution from oxygen ion conductivity (Weber et al., 1987). Early studies by Isenberg (1978) on the EVD deposition of doped LaCrO_3 indicated a problem with the incorporation of dopants into the film. This problem is partially solved by adding an excess of the corresponding chloride (Singhal, 1985). However, high temperature is required for a reasonable deposition rate. Pal and Singhal (1989) have observed a growth rate constant of $1.8 \times 10^{-9} \text{ cm}^2 \text{ s}^{-1}$ at 1600K for 2 mol % Mg-doped LaCrO_3 . From their results, the activation energy for oxygen ion diffusion is estimated to be 0.8 eV, which is in the range of activation energies for oxygen ion diffusion in perovskite materials (Ishigaki et al., 1988). This again confirms Wagner's tarnishing theory that minority charge carriers control the growth of EVD products. In the case of electronic conducting LaCrO_3 , the growth is controlled by oxygen ion transport through the deposit by a vacancy mechanism (Pal and Singhal, 1990b).

Another application of EVD in SOFC fabrication was published in one of Isenberg's patents for fabricating Ni/YSZ cermet anodes using EVD methods (Isenberg, 1985). Isenberg reported that the resistance to sintering was improved in this kind of anode, but the details were not clear (Isenberg and Zymboly, 1986). EVD processes have also been applied to deposit YSZ on a Ru anode of an SOFC (Suzuki et al., 1993). It was reported that the YSZ grew along the surface of the Ru metal particles, and that Ru and YSZ were in good contact. The SOFC with this kind of cermet anode demonstrated good anode stability and very high power generation density. However, the mechanism was not discussed in the paper.

In addition to SOFC applications, the synthesis of thin dense films of solid state ionic materials on porous substrates is also of great interest for other SSI devices. More recent applications of EVD grown layers include oxygen sensors, electrocatalytic reactors and oxygen separation membranes. Particularly, in the last application, the thickness of the membrane layer is important, since the bulk electrochemical diffusion of oxygen ions through the layer is the rate limiting step in the separation process. Membrane layers should be as thin as possible to obtain a maximum oxygen permeation rate. By means of EVD, gas-tight layers of YSZ film (Lin et al., 1992) with thicknesses as small as 0.2-0.5 μm can be obtained on a coarse porous α -alumina substrate. EVD has become a key technology for depositing these kinds of layers. In another study by Brinkman and Burggraaf (1995), EVD was applied to deposit a thin dense layer of a zirconia/yttria/terbia solid solution (ZYT) on porous ceramic substrates as ceramic membranes for oxygen separation. Oxygen permeation values of the order of 10^{-8} mol/cm²s have been achieved in the temperature range 900 to 1000°C under a large oxygen partial pressure gradient.

In conclusion, the characteristic features of the EVD technique are as follows.

- Uniform and gas-tight compound layers with thicknesses as small as 0.2-0.5 μm can be obtained (Lin et al., 1992), and the deposited films adhere well to substrates.
- A single-step process can be used to grow films up to hundreds of microns thick, unlike sol-gel processes, which require multiple dip-coatings followed by several heating steps to synthesize films of a reasonable thickness (a few microns).
- Deposition temperatures are typically on the order of 1100 to 1200°C for many materials, while typical sintering temperatures are 1500 to 1600°C (Pal and Singhal, 1990b).

Several other techniques such as tape casting (Bentzen et al., 1989; Setohuchi et al., 1989), radio frequency sputtering (Green et al., 1976; Neglishi et al., 1981), plasma spraying (Hamatani et al., 1989) and low temperature CVD (Nguyen et al., 1989; Lessing, 1989) have been investigated in parallel. None of these have equalled the performance of electrochemical vapor deposition. Thus, EVD has become a key technology for SSI applications.

Chapter 3. Polarized Electrochemical Vapor Deposition Fundamentals

3.1. Introduction

The present availability of numerous types of solid electrolytes permits transport control of various kinds of mobile ionic species through those solid electrolytes in solid electrochemical cells, and permits electrochemical reactions to be carried out with the surrounding vapor phase to form products of interest. This interfacing of modern vapor deposition technology and solid state ionic technology has led to the recent development of polarized electrochemical vapor deposition (PEVD) in our laboratory.

Generally speaking, PEVD is a modified form of chemical vapor deposition (CVD). A comparison between PEVD and conventional CVD is schematically shown in Figure 3-1 for a product (D) formed from reactants (A) and (B). In a CVD process, both reactants (A) and (B) are supplied through a vapor phase at the same side of a solid substrate (E). They react chemically at the surface of the solid substrate (E), aided by some type of catalytic effect, to form a desired product (D). In a PEVD process, one

reactant (A) is transported from one side (source) of a solid substrate (E) to the other side (sink) under well-controlled thermodynamic and kinetic conditions. At the sink side, reaction with (B) occurs to form (D). Further growth of (D) into a continuous thin film with the desired thickness in a PEVD process also relies on (A) transported in the solid state through (D) to react with (B).

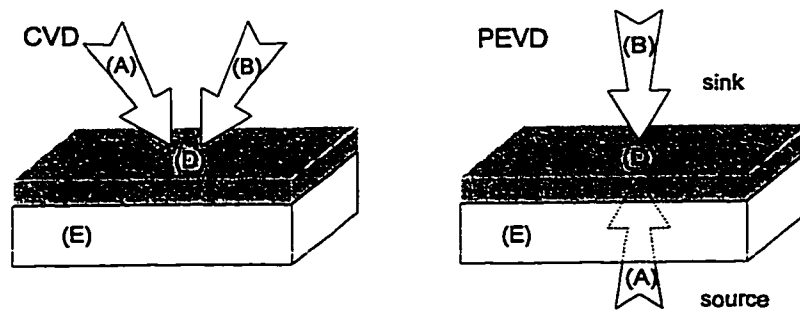


Figure 3-1. Comparison of PEVD and CVD processes.

The reason that reactant (A) can be transported through the solid substrate (E) and the solid deposited phase (D) is because both (E) and (D) are solid state ionic materials (Hladik, 1972), in which the ionic state of reactant (A) is mobile. As already discussed in Chapter 2, reactant (A) will be transported as a combination of corresponding ionic and electronic carriers under the mixed influences of chemical potential gradients and electric fields in the solids. Unlike the chemical reaction of vapor phase reactants (A) and (B) to form a deposit (D) in CVD, the reaction of the solid-state transported reactant (A) and the vapor phase reactant (B) to form a deposit (D) is electrochemical in nature in PEVD. The immediate advantage is that the deposition reaction in PEVD occurs at an electrochemically active area instead of a catalytically active area in the case of CVD. Consequently, reaction and deposition in PEVD take place only on the substrate, not on reactor walls, and there are no vapor phase reactions and powder deposition as might occur in CVD. The deposition products in PEVD are usually uniform and fully dense, due to the fact that the electrochemical potential gradient in (D) is the driving force for electrochemical reaction and deposition. Thus, where the film is the thinnest, the driving

force is the greatest. Through this self-leveling effect, uniform coverage of PEVD products is expected.

PEVD can be compared to another closely related vapor deposition technique, electrochemical vapor deposition (EVD), which has been introduced in Chapter 2. Both techniques utilize an electrochemical potential gradient as the driving force for solid-state transported reactant (A) diffusion through product (D) for further reaction and deposition. However, the way electronic carriers are transported within the substrate (E) distinguishes PEVD from EVD as schematically shown in Figure 3-2.

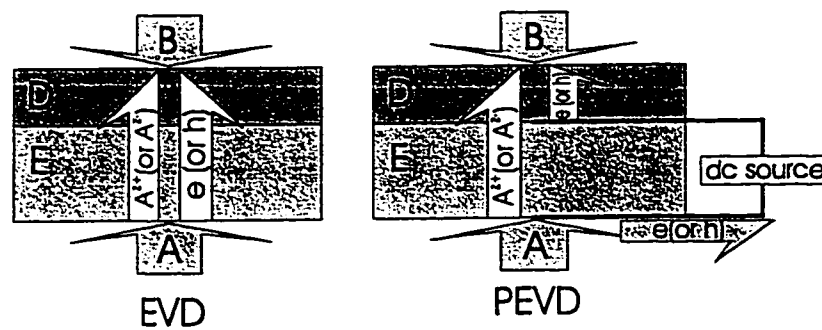


Figure 3-2. Comparison of EVD and PEVD processes.

In EVD, electronic carriers flow with ionic carriers through the solid substrate (E) to the deposited product (D). The substrate (E) can either be an ionic or a mixed conductor, as long as the major mobile ionic species is (A^{2+}) or (A^+). The driving force for reactant (A) transport through the solid substrate (E) and deposit (D) is (A)'s chemical potential difference between the two isolated compartments, i.e., the source and sink side of the substrate (E). At the source side, the chemical potential of reactant (A) is usually maintained constant. At the sink side, the chemical potential of reactant (A) is fixed by EVD reactions.

In PEVD, an applied voltage is used to transport (A) through the substrate (E). Usually, (E) is an exclusive ionic conductor for (A^{2+}) or (A^+). It serves as a solid electrolyte in a closed-circuit solid electrochemical cell, and is connected to an external electrical circuit with a dc electrical source by two electronic conducting electrodes at both the sink and source sides of (E). Consequently, only ionic carriers can be

transported through (E) to (D). The electronic carriers flow separately to (D) through the external electrical circuit. Instead of only relying on the chemical potential difference of the reactant (A) over the solid phase (E) as in EVD, the driving force for reactant (A) solid-state transported in PEVD is mainly controlled by the applied dc electric potential in PEVD. Thus, PEVD offers more control of the chemical potential gradient across the deposit (D) than EVD. Furthermore, isolation between the source and sink side in a PEVD system is not necessary for delivering the driving force.

The transport mechanism for reactant (A) through deposit (D) for further growth in PEVD is the same as in EVD. The characteristic feature of both EVD and PEVD is that deposit (D) growth is driven by the presence of a chemical potential gradient of reactant (A) across deposit (D). Deposit (D) growth follows Wagner's electrochemical tarnishing theory and is parabolic in nature. Unlike the initial applications of Wagner's theory in corrosion, solid-state transporting of the reactant in both EVD and PEVD is under well controlled thermodynamic and kinetic conditions, through solely sink and source vapor phases control in EVD, and mainly through dc electric potential control via a solid electrochemical cell in PEVD. Recently, a review of both EVD and PEVD was presented to illustrate the similarities and differences of both techniques (Tang et al., 1998).

3.2. PEVD System Basics

A fundamental PEVD system is schematically shown in Figure 3-3. From left to right, it consists of

- (1) a source (O) to supply the solid-state transported reactant (A);
- (2) a substrate (E) in a solid electrochemical cell with an external electric circuit connected from the source side by a counter electrode (C) and from the sink side by a working electrode (W);
- (3) a product (D) deposited at the sink side surface of the substrate; and
- (4) a sink (S) to supply reactant (B) in the vapor phase.

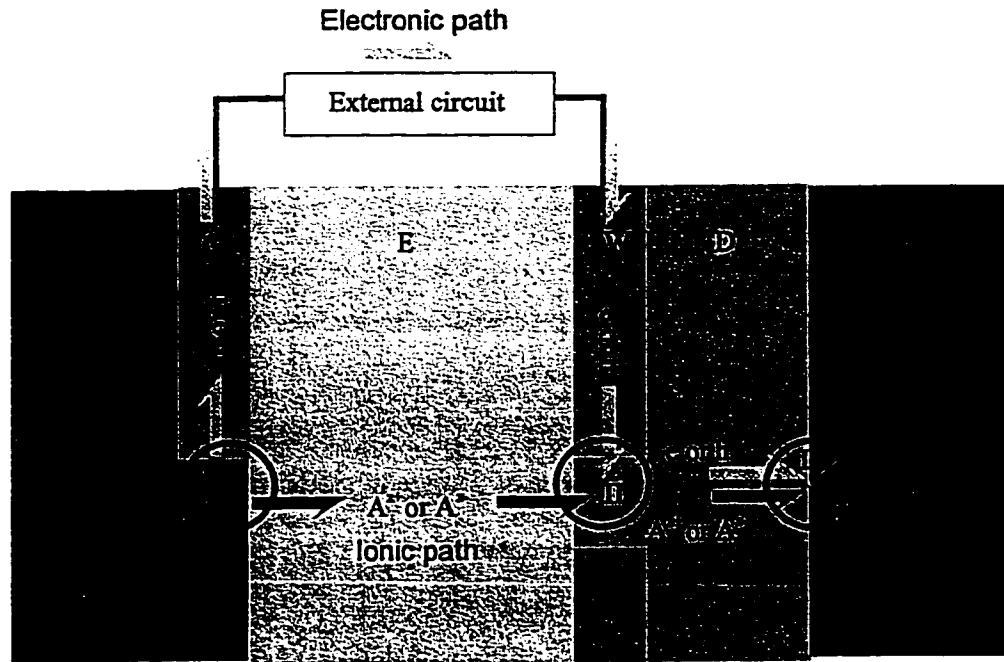


Figure 3-3. Schematic of a fundamental PEVD system.

As with CVD and EVD techniques, PEVD process design starts by considering the PEVD product (D). Either an anodic or cathodic half-cell electrochemical reaction at the sink side of the system can be applied for product (D) formation and subsequent deposition.



The equation of choice depends on whether the anion (A^{z-}) or cation (A^{z+}) of the deposit (D) is transported through the substrate as well as the product. If doping is also required for a PEVD product (D), additional electrochemical reactions for doping should be considered at the same time.

In order to carry out the electrochemical reaction for product (D) deposition in a PEVD process, the neutral reactant (B) and other possible reactants for doping are transported to the deposit (D) surface by diffusion in the sink vapor phase (S). Furthermore, if there are reaction products other than (D), they must also be driven away

from the reaction sites through the sink vapor phase. Extensive research in the field of vapor deposition technology has been conducted in the area of reactant supply and product (other than deposits) removal. The details will not be included here.

The charged reactants for the sink electrochemical reaction are supplied by the solid electrochemical cell of a PEVD system. The solid phase (E) is an exclusive ionic conductor for (A^{z+}) or (A^{z-}), and serves as the solid electrolyte. (C) and (W) are solid electronic conducting phases, and contact (E) from both sides as counter and working electrodes, respectively. They connect with the external electric circuit, which consists of a dc source and other possible measurement devices. Because the conductivity changes in nature from ionic to electronic at the electrode/electrolyte interfaces, the solid electrochemical cell in a PEVD system effectively separates the transport paths of ionic and electronic charged carriers from the source (O) to the sink (S) of a PEVD system. Thus, the solid electrochemical cell in a PEVD system has two basic functions. First of all, it provides the substrate onto which PEVD products are deposited at the sink side. Secondly, it controls ionic (A^{z+} or A^{z-}) and electronic (e or h) reactant movement from the source side (O) to the sink side (S) for participation in an electrochemical reaction and subsequent deposition through an external circuit. The requirements for a solid electrolyte in a PEVD system include:

- The only mobile ion in the solid electrolyte will be the ionic state of solid-state transported reactant (A^{z+}) or (A^{z-}).
- At the desired PEVD temperature, the solid electrolyte must have reasonable ionic conductivity when exposed to both sink and source side environments.
- Sufficiently high ionic current density must be obtained under the decomposition voltage.
- The solid electrolyte should be gas-impervious when the source and sink side are exposed to different gases or vapor phases.
- It should be stable in the PEVD environment (Worrell and Hladik, 1972).

During the last sixty years, hundreds of solid electrolytes have been found. Their ability to transport ionic species is indicated in Table 2-4.

Usually, the working electrode (W) is a porous metallic electrode. Thus, the reactant (B) in the vapor phase can reach the surface of the solid electrolyte for initial

electrochemical reaction at a three-phase boundary of solid electrolyte (E), working electrode (W) and sink vapor phase (S) as shown in Figure 3-3 (location II). All reactants for the sink side electrochemical reaction (3-1) or (3-2) are only available there. Subsequent reaction and deposition of the product (D) requires both electrons and ions to travel through the product (D) to the surface to react with vapor phase reactant(s) electrochemically at location III in Figure 3-3.

The role of the source (O) in a PEVD system is to provide a constant supply of the solid-state transported reactant (A) during a PEVD process. Theoretically, it can be either a solid, liquid or vapor phase, as long as it can supply the ionic reactant (A^{z+}) or (A^{z-}) to the solid electrolyte (E) and the electronic reactant (e) or (h) to the counter electrode (C) via a source side electrochemical reaction. Therefore, the source must be in intimate contact with both the solid electrolyte (E) and the counter electrode (C) for mass and charge transfer between the source and solid electrochemical cell at location I of Figure 3-3. Practically, it is preferable to fix the chemical potential at the source. Any gas or solid mixture which does not react with the cell components and which establishes a constant chemical potential of (A) is a suitable source. For instance, elemental (A) provides (A^{z+}) or (A^{z-}) according to the following reaction



The overall cell reaction in a PEVD process is the combination of both source and sink half cell reactions. It can be expressed as



This reaction does not have to be a thermodynamically favorable one, since an external dc electric potential is applied via the solid electrochemical cell in the PEVD system to drive the reaction in the right direction. Thus, the activity of (A) at the reaction site is controlled by the applied dc electric potential. Kinetically, this reaction can be monitored by an ammeter attached to the external electric circuit. Further discussion of mass and charge transport in a PEVD system will be given in the following.

3.3. Mass and Charge Transport in a PEVD System

According to the previous discussion, a PEVD process relies on mass and charge transport in two solid state ionic materials of a PEVD system, i.e., the solid electrolyte (E) and the product (D). Since mass and charge transport occur in solid state ionic materials, the conductivity mechanism imposes some restrictions, and fundamental considerations in a PEVD system can be obtained through the local equilibrium approach (Tillement, 1994). In the following, mass and charge transport in both phases will be discussed.

For convenience and simplicity, some assumptions are made. The solid electrolyte (E) is assumed to be an exclusive ionic conductor of mono-valent cation (A^+). Two porous electronic conducting electrodes (C) and (W) are attached to the solid electrolyte (E) from both the source and sink side, respectively. An external electric circuit with a dc source is connected to the solid electrochemical cell via both electrodes.

During mass and charge transport in a PEVD system, the solid electrolyte serves as an ion-pass filter and the external electric circuit as an electron-pass filter. Consequently, two kinds of conducting passes are separated in the system as shown in Figure 3-3. One is the ionic conduction path from location (I) through the bulk of the solid electrolyte (E) to location (II), then across the bulk of the PEVD deposit (D) to location (III). The other is the electronic conduction path from location (I) through the source electrode (C), the external electric circuit, and the sink electrode (W) to location (II), then across the bulk of the PEVD deposit (D) to location (III).

In this PEVD system, the source (O) will be a vapor phase, which contains elemental solid-state transported reactant (A), and an anode half-cell reaction



prevails at the three phase boundary (I) of the solid electrolyte (E), porous counter electrode (C) and source vapor phase (O). Assuming that the partial pressure of (A) in

the vapor phase (O) is constant during a PEVD process, the chemical potential of (A) at (I) is constant. The equilibrium equation for ionization of a neutral species (A) at (I) is:

$$\mu_{A(O)} = \bar{\mu}_{A^+(E)} + \bar{\mu}_{e^-(C)} \quad (3-6)$$

in which $\mu_{A(O)}$ is the chemical potential of (A) in the source (O), $\bar{\mu}_{A^+(E)}$ is the electrochemical potential of (A⁺) in the solid electrolyte at (I), and $\bar{\mu}_{e^-(C)}$ is the electrochemical potential of (e⁻) in the counter electrode at (I).

At the sink side, once initial formation of (D) has occurred, solid-state transported reactant (A), in the form of (A⁺) and (e⁻) from the bulk of (D), reacts electrochemically with reactant (B) from the sink vapor phase (S) to form PEVD deposit phase (D) at (III). Thus, a cathodic half-cell reaction at location (III) can be expressed as:



Accordingly, the following equilibrium equation holds,

$$\bar{\mu}_{A^+(D)} + \bar{\mu}_{e^-(D)} + \mu_{B(S)} = \mu_{D(D)} \quad (3-8)$$

It is assumed that the partial pressure of (B) in the sink vapor phase is also fixed during a PEVD process. Thus, the chemical potential of (B) is constant. The chemical potential of product phase (D) is equal to its Gibbs free energy of formation. The chemical potential of (A), which is the combination of the electrochemical potential of (A⁺) and (e⁻) according to Eq. (3-6), is fixed at location (III) at equilibrium. It is further assumed that the chemical potential of (A) at (I) is greater than its chemical potential at (III) in this PEVD system.

Because the cathodic reaction relies on the transport of both ionic and electronic species through the product (D), it should be considered as a mixed conductor, even in the case where one carrier has a much higher conductivity than the other. In this case the conductivity of other charged species in (D) is assumed to be negligible. The deposit (D)

is in contact with the solid electrolyte (E) and working electrode (W) at (II), which is a three-phase boundary in the general electrochemical sense. At location (II), the exchange of solid-state transported reactant (A^+) between solid electrolyte (E) and product (D) can be expressed as



and the exchange of electrons (e^-) between the sink working electrode (W) and the product (D) is



Thus, product (D) should be in intimate contact with both the solid electrolyte (E) and working electrode (W) at (II) for a PEVD reaction to occur. If interfacial polarization is negligible, equilibria exist for both mass and charge transport across the interfaces at (II). Consequently, from Eq. (3-9) and (3-10), the following electrochemical potential equilibrium equations at location (II) are valid:

$$\bar{\mu}_{A^+_{(E,II)}} = \bar{\mu}_{A^+_{(D,II)}} \quad (3-11)$$

$$\bar{\mu}_{e^-_{(W,II)}} = \bar{\mu}_{e^-_{(D,II)}} \quad (3-12)$$

3.3.1. Open Circuit Condition and Equilibrium Potentials of the PEVD System

Under open circuit conditions, the PEVD system is in equilibrium after an initial charging process. The equilibrium potential profiles inside the solid electrolyte (E) and product (D) are schematically shown in Figure 3-4. Because neither ionic nor electronic current flows in any part of the PEVD system, the electrochemical potential of the ionic species (A^+) must be constant across both the solid electrolyte (E) and deposit (D). It is equal in both solid phases, according to Eq. (3-11), at location (II). The chemical

potential of solid-state transported species (A) is fixed at (I) by the equilibrium of the anodic half cell reaction Eq. (3-6); and at (III) by the cathodic half cell reaction Eq. (3-8). Since (D) is a mixed conductor with non-negligible electronic conductivity, the electrochemical potential of an electron (which is related to the Fermi level, E_F) should be constant in (D) at the equilibrium condition. The transport of reactant (A) inside (D) is the combination of both ionic and electronic conduction. Thus, the chemical potential of (A) is constant across deposit (D) and the chemical potential of (A) at (II) equals that at (III). Accordingly, the electric potential ϕ across the deposit (D) must be constant.

The difference in chemical potential of (A) between the source and sink side of the PEVD system causes a gradient of the chemical potential of A across the solid electrolyte (E) between (I) and (II). In order to have a constant electrochemical potential of (A⁺) inside (E) to prevent ionic current under equilibrium, an internal electric field is built up inside the solid electrolyte (E). This is justified since electronic conductivity in (E) is negligible. The internal electric field causes an electric potential difference between (I) and (II). The value of the internal electric field is the EMF of the cell, and can be calculated from the chemical potential of (A) across the solid electrolyte (E) according to Nernst's equation given in Eq. (2-30). It can be measured by a high impedance electrometer in the external electric circuit. According to the Stockholm convention EMF is taken as positive if the right-hand electrode of the galvanic cell is positive (de Bethune, 1955). The flow of charge through the cell is called positive if a positive electric current flows from left to right through the cell. In this case, the value of the EMF is positive. It can be expressed as

$$EMF = \phi_{II} - \phi_I \quad (3-13)$$

In summary, the relation between the chemical potential of (A) at (I), (II) and (III) under open circuit conditions is:

$$\mu_A^{III} = \mu_A^{II} = \mu_A^I - qEMF \quad (3-14)$$

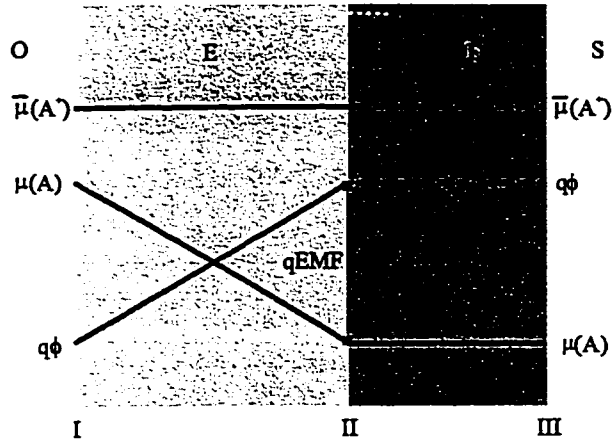


Figure 3-4. The potential profiles in the PEVD system under open circuit conditions.

3.3.2. Closed Circuit Condition and Steady-State Potentials in a PEVD System

Under closed circuit conditions, the electric potential between the two electrodes (C) and (W) is set by an applied dc electric potential V_a .

$$V_a = \phi_{II} - \phi_I \quad (3-15)$$

Consequently, a gradient in the electrochemical potential of (A^+) exists inside the solid electrolyte (E), and electrons are able to conduct through the external circuit except when the applied dc electric potential is equal to the open circuit EMF value. Under this condition, the applied dc potential prevents both ionic and electronic current flow through the PEVD system. The potential profiles in the PEVD system are now the same as for the open circuit condition except the electric potential difference at locations (I) and (II) is caused by the applied dc electric field instead of the internal electric field. The value of this applied electric potential corresponds to the stop electric potential E_{stop} commonly referred to for electrolytic cells. In theory, the value of the closed circuit stop potential is equal to the open circuit equilibrium EMF value at the steady-state condition.

$$V_{stop} = EMF \quad (3-16)$$

When $V_a < V_{stop}$, the electric potential difference between (II) and (I) is reduced, and this immediately causes a electrochemical potential gradient of (A^+) . This gradient is initially equal to the difference between V_a and V_{stop} . An ionic current of (A^+) will flow from (I) to (II) under the electrochemical potential gradient. If the ionic transport of (A^+) is blocked at (II) or solid-state transport of (A) is blocked in the deposit (D), (A^+) will accumulate at (II), as do electrons (e^-) from the external circuit. This is equivalent to accumulation of the neutral species (A), and will increase the chemical potential of (A) at (II) until the electrochemical potential of (A^+) reaches the same level as at (I).

Thus, ionic current inside the solid electrolyte (E) and electronic current through the external electric circuit will cease after a short transition time. The chemical potential of (A) at (I) and (II) will then have the following relationship.

$$\mu_A'' = \mu_A' - qV_a \quad (3-16)$$

Because ionic current cannot cross the interface at (II), the equilibria (Eq. (3-11) and (3-12)) at the interfaces at location (II) are not fulfilled. The chemical potential of (A) inside deposit (D) won't change and it will remain the same at (III).

Deposition in a PEVD system is accomplished by transporting both (e^-) and (A^+) across the interfaces at (II), and from (II) to (III) to react with (B) from the sink vapor phase. This is equivalent to the transport of neutral species (A) from (II) to (III) under a chemical potential gradient of (A). Consequently, the chemical potential of (A) at (II) is reduced. In order to restore it, transport of (A^+) inside the solid electrolyte (E) and (e^-) inside the external electric circuit resume. Thus, under closed circuit conditions, the chemical potential of (A) is floating at (II), and electrochemical potential gradients of the charged species exist across both the solid electrolyte (E) and deposit (D). This causes mass and charge transport of reactant (A) from the source (O) to the sink (S) in the PEVD system. The entire PEVD system can be viewed as a reactor. The overall reaction is the combination of the anodic and cathodic reactions to form the desired PEVD product (D) and can be expressed as



When both reactions in Eq. (3-5) and (3-7) proceed to the right, the equilibria at both sides of the cell no longer exist. This will decrease the chemical potential of (A) at (I) and increase it at (III). If the current in the PEVD system is assumed to be very small, the change in chemical potential of (A) at both the source and sink side will not be significant. The steady state potential profiles of the PEVD system are illustrated in Figure 3-5.

When the current is limited by the solid transport of (A) in both the solid electrolyte (E) and product (D), the chemical potential of (A) at (II) for the PEVD system is related to the current in both phases. Thus, the chemical potential of (A) at (II) is critical to reveal the current and potential behavior in the PEVD system.

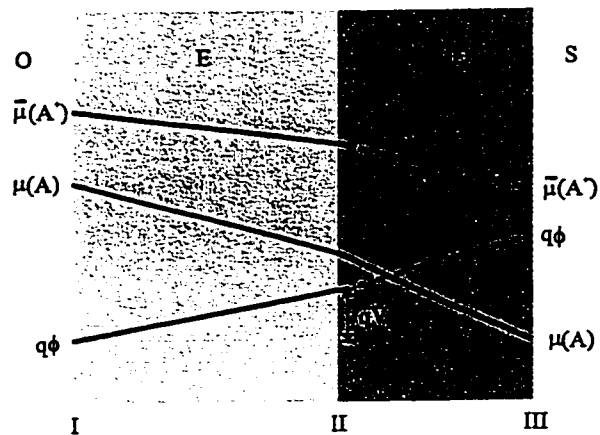


Figure 3-5. Potential profiles inside the solid electrolyte (E) and product (D) under closed-circuit conditions.

In the following, the floating chemical potential of (A) at (II) is solved under the assumption that the equilibria of mass and charge transport across the interfaces at (II) are rapidly reached during the mass and charge transfer in a PEVD process. In addition, some further assumptions are needed for steady-state conditions during a PEVD process:

- Despite the flow of current at (I) and (III), the change in chemical potentials of (A) at (I) and (III) are negligible.
- Only resistive overpotential in the bulk of (E) and (D) of the PEVD system is considered.
- Surface leakage current from the source (O) to the sink (S) in the PEVD system is negligible.

Due to conservation of charges as discussed in Chapter 2, the total current I_t in any part of the solid electrochemical cell of the PEVD system is the same.

$$I_{e,(W)} + I_{i,(W)} = I_{e,(E)} + I_{i,(E)} = I_t \quad (3-18)$$

Since the electronic current $I_{e,(E)}$ and the ionic current $I_{i,(W)}$ inside the solid electrolyte (E) and the external electric circuit, respectively, are negligible, the electronic current $I_{e,(W)}$ flowing through the external electric circuit equals the ionic current $I_{i,(E)}$ flowing through the solid electrolyte (E).

$$I_{e,(W)} = I_{i,(E)} = I_t \quad (3-19)$$

Because all ionic and electronic current arriving at (II) will be drained away via the deposit (D), the ionic current $I_{i,(E)}$ flowing through the solid electrolyte equals the ionic current $I_{i,(D)}$ flowing through deposit (D) under steady-state conditions. The same is true for the electronic current through the external electric circuit and deposit (D). Thus, we have the following relation involving currents:

$$I_{e,(W)} = I_{i,(E)} = I_{e,(D)} = I_{i,(D)} \quad (3-20)$$

Consequently, the electronic current measured in the external electric circuit reveals the ionic current in the solid electrolyte (E) and the deposit (D), as well as the electronic current in the deposit (D).

The current relation in Eq. (3-20) is achieved by adjusting the chemical potential of (A) at (II) under closed circuit conditions. According to Eq. (2-22), the gradient in electrochemical potential is the driving force for the flow of charged particles in the multiphase PEVD system. The current density carried by (A⁺) in either the solid electrolyte (E) or deposit (D) can be written as:

$$i_{A^+}(x) = -\frac{\sigma_{A^+}(x)}{z_{A^+}q} \left(\frac{\partial \bar{\mu}_{A^+}(x)}{\partial x} \right) \quad (3-21)$$

Accordingly, the current density of (A⁺) inside the solid electrolyte (E) is

$$i_{A^+,E} = -\frac{\sigma_{A^+,E}}{z_{A^+}q} \left(\frac{\bar{\mu}_{A^+,II} - \bar{\mu}_{A^+,I}}{L_E} \right) \quad (3-22)$$

assuming the solid electrolyte (E) is homogeneous. L_E is the thickness of the solid electrolyte (E). Splitting the electrochemical potential into both its chemical and electric potential components, and considering Eq. (3-15), yields

$$i_{A^+,E} = -\frac{\sigma_{A^+,E}}{z_{A^+}q} \left(\frac{\mu_{A,II} - \mu_{A,I} + qz_{A^+}V_a}{L_E} \right) \quad (3-23)$$

In this equation, two variables exist. One is the applied potential, the other is the chemical potential of (A) at (II). The same equations apply to the current density of (A⁺) inside deposit (D) when (D) is homogeneous and the thickness of (D) is L_D .

$$i_{A^+,D} = -\frac{\sigma_{A^+,D}}{z_{A^+}q} \left(\frac{\bar{\mu}_{A^+,III} - \bar{\mu}_{A^+,II}}{L_D} \right) \quad (3-24)$$

or

$$i_{A^+,D} = -\frac{\sigma_{A^+,D}}{z_{A^+}q} \left(\frac{\mu_{A,III} - \mu_{A,II} + qz_{A^+}(\phi_{III} - \phi_{II})}{L_D} \right) \quad (3-25)$$

Since the chemical potential of (A) is fixed by the cathodic reaction at (III), a chemical potential gradient of (A) exists inside product (D). This causes an open circuit internal electric field to build up to oppose the tendency of (A⁺) to move across product (D). However, product (D) is a mixed conducting product. As in a scale product, the electronic leakage current weakens the internal electric field in (D). Thus, the electrochemical potential gradient exists to move (A⁺) from location (II) to location (III) to react with vapor phase.

The electric potential difference between interfaces (III) and (II) depends on the electronic conductivity of deposit (D). If the deposit is an exclusive electronic conductor, the difference is close to zero and the current is limited by ionic conduction in the deposit; on the other hand, if it is an exclusive ionic conductor, an internal potential close to the open circuit emf value is built up. Ionic conduction relies on the leakage electronic current. In either case, the electric potential difference across (D) can be expressed as

$$\phi_{III} - \phi_{II} = EMF_D = -\frac{t_A}{qz_{A^+}} (\mu_{A,III} - \mu_{A,II}) \quad (3-26)$$

Combining Eq. (3-26) and (3-25), yields

$$i_{A^+,D} = -\frac{\sigma_{A^+,D} t_{e^-}}{z_{A^+}q} \left(\frac{\mu_{A,III} - \mu_{A,II}}{L_D} \right) \quad (3-27)$$

Both current densities are assumed to be uniform in the solid electrolyte (E) with effective area A_E and in the deposit (D) with effective area A_D . The ionic currents should be equal according to the charge conservation in Eq. (3-20), and we have

$$A_E i_{A^+,E} = A_D i_{A^+,D} \quad (3-28)$$

If Eq. (3-23) and (3-27) are substituted into Eq. (3-28), then

$$-\frac{A_E \sigma_{A^+,E}}{z_{A^+} q} \left(\frac{\mu_{A,II} - \mu_{A,I} + qz_{A^+} V_a}{L_E} \right) = -\frac{A_D \sigma_{A^+,D} t_{e^-}}{z_{A^+} q} \left(\frac{\mu_{A,III} - \mu_{A,II}}{L_D} \right) \quad (3-29)$$

For simplicity, two conductances, G_E and G_D , can be defined as follows:

$$G_E = \frac{A_E \sigma_{A^+,E}}{L_E} \quad (3-30)$$

$$G_D = \frac{A_D \sigma_{A^+,D} t_{e^-}}{L_D} \quad (3-31)$$

Both G_E and G_D depend on the physical and geometrical properties of the solid electrolyte (E) and the deposit (D), respectively. Eq. (3-29) then becomes

$$G_E (\mu_{A,II} - \mu_{A,I} + qz_{A^+} V_a) = G_D (\mu_{A,III} - \mu_{A,II}) \quad (3-32)$$

From Eq. (3-32), the chemical potential at (II) can be expressed as

$$\mu_{A,II} = \frac{G_E \mu_{A,I} + G_D \mu_{A,III} - qz_{A^+} G_E V_a}{G_E + G_D} \quad (3-33)$$

According to the above equation, the chemical potential of the solid-state transported reactant at (II) depends on a number of factors. These are the physical and geometrical properties of the phases in the PEVD system, except the applied dc potential V_a . Although varying physical and geometrical parameters affect a PEVD process, adjusting the applied dc electrical potential is the most effective way to control the driving force for ionic transport.

3.4. Electrochemical Control and Monitoring of a PEVD Process Through the Solid Electrochemical Cell of a PEVD System

The most distinguishing feature of PEVD process control is made possible because of the solid electrochemical cell involved in a PEVD system. Compared with other vapor deposition techniques, utilization of solid electrochemical cells is one of the most significant advantages of the PEVD technique, since deposition process control and monitoring are easy to realize. By connecting several measurement devices to the external electrical circuit of a PEVD system, the reaction in a PEVD process is easily monitored and possibly controlled by the electrical current and applied potential, respectively (Tang et al., 1996).

3.4.1. PEVD Process Monitoring

The current, I , in a PEVD process can be recorded simultaneously by an ammeter in the external circuit to reveal the kinetics of the PEVD reactions. As discussed in the last section, solid-state reactant (A) needs to be transported as a combination of ionic and electronic species from the source to the sink side through the solid electrochemical cell to participate in a PEVD reaction with vapor phase reactant (B). The PEVD reaction rate, and subsequent product (D) formation rate, $v(t)$, can be expressed as

$$v(t) = \frac{1}{V} \frac{dn}{dt} \quad (3-34)$$

where V is the molar volume of the PEVD product (D), and n is the mole number of ionic species travelling through the PEVD system. From Faraday's law and Fick's second law discussed in the previous section, the current passing through the external circuit of a PEVD system is

$$I = \frac{dQ}{dt} = \frac{zFdn}{dt} \quad (3-35)$$

Combining Eq.(3-34) and (3-35) yields

$$I = v(t)V_zF \quad (3-36)$$

Thus, the rate of PEVD product formation is proportional to the current flowing through the external electric circuit. Furthermore, taking into account the evolution of the cell with time, the amount of reaction product formed, M , at time t is easily monitored during PEVD by integrating the current from 0 to t .

$$M = \int_0^t I dt = \int_0^t v(t)V_zF dt \quad (3-37)$$

Although it is not as severe in PEVD systems as in aqueous electrochemical systems in which various kinds of mobile ions are present in the electrolytes, it should be pointed out that in the presence of reactants at the sink electrode surface, other electrochemical reactions might also take place in parallel with the desired one at the sink side. If side reactions exist, usually such parallel reactions' contributions to the measured current are not very easy to quantify. If it is desired to use current to monitor the reaction and product formation in PEVD, side reactions should be eliminated or at least controlled. Fortunately, only one ionic species is usually mobile in a solid electrochemical cell because of the nature of the solid electrolyte, as already discussed in Chapter 2. As long as the vapor phase is properly controlled, usually one electrode reaction is predominant over a wide range of PEVD applied potentials. Virtually 100% current efficiency for product formation can be expected.

3.4.2. Process Control Via the Applied dc Electric Potential

Based on Eq. (3-33), possible process control during PEVD includes many aspects, such as process temperature, the vapor phase at the sink side, the activity of the solid-state transported reactant (A) at both sink and source sides, etc. Further discussion of

these factors is subject to the individual process and will be presented later. In this section, PEVD process control is discussed under the assumption that all other parameters are constant. The current-potential behavior reveals that the thermodynamic driving forces for the overall reaction and ionic transport are controllable by the applied external dc electrical potential in PEVD.

According to Eq. (3-33), adjusting the applied dc electrical potential controls the chemical potential of (A) at (II) and, subsequently, the chemical potential difference of the solid-state transported reactant (A) across the deposited product (D). Consequently, the applied potential controls the reaction rate in a PEVD system when solid transport of (A) through the product is the rate-limiting step for the process. Because the thermodynamic driving force for PEVD is not solely based on the chemical potential difference of solid-state transported reactant between the sink and source side, isolation of both sides is not necessary. This provides a great practical advantage of PEVD over EVD.

In order to reveal the kinetics of the PEVD reaction, the chemical potential of (A) at (II) from Eq. (3-33) is substituted into Eq. (3-27),

$$I = I_{A^+,E} = I_{A^+,D} = -\frac{G_D}{qz_{A^+}} \left(\mu_{A,III} - \frac{G_E \mu_{A,I} + G_C \mu_{A,III} - qz_{A^+} G_E V_a}{G_E + G_D} \right) \quad (3-38)$$

and therefore,

$$I = \frac{1}{qz_{A^+}} \frac{G_D G_E}{G_E + G_D} (\mu_{A,I} - \mu_{A,III}) - \frac{G_D G_E}{G_E + G_D} V_a \quad (3-39)$$

G_t can be defined as the total conductance of the PEVD system,

$$G_t = \frac{G_D G_E}{G_E + G_D} = \frac{A_E \sigma_{A^+,E} A_D \sigma_{A^+,D} t_{e^-}}{A_E L_D \sigma_{A^+,E} + A_D L_E \sigma_{A^+,D} t_{e^-}} \quad (3-40)$$

According to this definition, G_r depends on the physical and geometric properties of both the solid electrolyte (E) and product (D). G_r is fixed if the PEVD system is fixed. By substituting G_r into Eq. (3-39), the current and applied potential have the following simple relation:

$$I = G_r \frac{\mu_{A,I} - \mu_{A,IV}}{qz_{A^+}} - G_r V_a \quad (3-41)$$

In this ideal condition, the current vs. applied potential curve in a PEVD process is schematically shown in Figure 4-6. The applied dc potential V_a is linearly related to the current I , and the slope is $-G_r$. The stop potential at zero current is

$$V_{stop} = V_a = \frac{\mu_{A,I} - \mu_{A,III}}{qz_{A^+}} \quad (3-42)$$

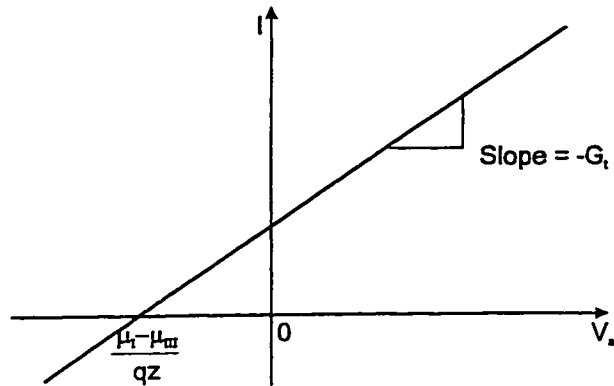


Figure 3-6. Ideal current-applied potential behavior of a PEVD system.

Before discussing general conclusions regarding the current and applied dc potential in a PEVD system, the initial assumptions made in this discussion have to be examined carefully. The above discussion is based on the assumption that all interfaces at (I), (II) and (III) are ideal non-polarizable interfaces, and equilibrium electrochemical potentials of (A^+) and (e^-) prevail across these interfaces during mass and charge transport in the PEVD system. Thus, the aforementioned expressions for mass and charge transport in a

PEVD system indicate that the transport rate (current) only depends on bulk material properties and simple geometric aspects. The thermodynamic equilibrium criterion at one interface between two phases is an equality of electrochemical potential of the charged particles. If establishment and maintenance of the equilibria are rapid, then the response of the interface to a non-equilibrium field is to drive the equilibrium predominantly in one of its component directions, which results in a basically non-resistive transfer of ideally reversible interfaces (Raleigh, 1975). Only in this case, can the bulk value of the electrochemical potential be substituted for the interface electrochemical potential in the aforementioned equations.

In practice, when current flows in the system, thermodynamic equilibrium conditions no longer exist at the interfaces. The response of the PEVD system is also related to the interface characteristics, which are fixed by the external chemical and electrical conditions for each phase. Polarization usually exists in the interface region. The interfaces need to be treated by kinetic considerations (Gerisher, 1975). Nevertheless, mass and charge transport in a PEVD process at elevated temperatures is frequently determined by the rate of diffusion in the solid reaction product rather than by the rate of phase boundary charge transfer. On the other hand, overpotential in a PEVD reaction and product formation can be caused by other factors, such as gas phase diffusion and crystallization. The resultant current-applied potential curve could be more complicated than the ideal one in Figure 4-6. The details of those kinetic considerations on a well-defined PEVD system will be presented in Chapter 6.

3.5. General Product Deposition Behavior in PEVD

The advantages of PEVD are not only based on the close electrochemical control, but also arise from the unique electrocrystallization behavior during growth of PEVD products. In order to give the prerequisites for understanding the mechanism of PEVD product growth, it is necessary to consider the transport processes of the charged reacting species in the PEVD product phase.

3.5.1. Selective Deposition

As schematically shown in Figure 3-7, initial PEVD reaction and product nucleation occurs at the three-phase boundary of solid electrolyte (E), working electrode (W) and the sink vapor phase (S). Only here are all reactants available for the half-cell electrochemical reaction at the sink side of a PEVD system. Although the ionic and electronic species can sometimes surface diffuse at elevated temperature to other sites to react with (B) in the vapor phase, the supply of the reactants continuously along the diffusion route is less feasible and the nuclei are too small to be stabilized under normal PEVD conditions. Only along the three phase boundary line are all the reactants available for further growth to stabilize the nuclei. Consequently, deposition in a PEVD process is restricted to certain areas on a substrate where all reactants for the sink electrochemical reaction are available.

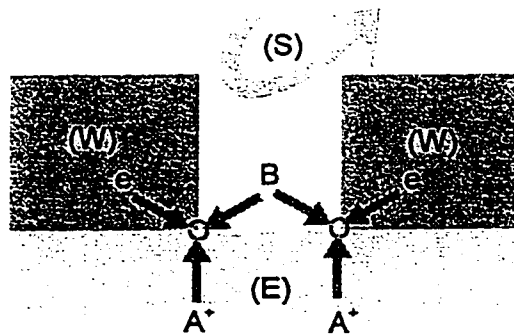


Figure 3-7. The initial PEVD reaction and product nucleation occurs at the three-phase boundary of solid electrolyte (E), working electrode (W) and the sink vapor phase (S).

3.5.2. Growth on Electrically Shorted Surfaces

During the crystal growth stage, the availability of reacting species for the electrochemical reaction also controls the growth of the PEVD products. The further

growth of product nuclei can be divided into two stages. During the first stage, the solid electrolyte (E) and working electrode (W) are still exposed to the sink vapor phase (S). Since the ionic conductivity in the solid electrolyte (E) is generally much higher than that in the PEVD product, and the electronic conductivity in the working electrode (W) than in the product, two kinds of electrically shorted surfaces exist as shown in the Figure 3-8. One is an ionically shorted surface (X) along the solid electrolyte (E) and the other is an electronically shorted surface (Y) along the working electrode (W). Although the growth kinetics along these surface directions will still be parabolic, no ionic and electronic electrochemical potential gradient will be expected in the two directions, and charged species transport is driven by the concentration gradient of electrons and ions (Ilschner-Gensch and Wagner, 1958). This is a unique case compared with common gas-solid reactions. The second stage starts when at least one of the electrically shorted surfaces is covered by PEVD product (D). The growth behavior in both stages is quite different if the PEVD reaction limiting step is solid-state transport of reactant through PEVD product (D).

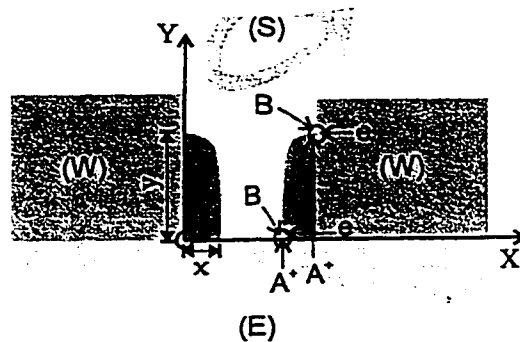


Figure 3-8. PEVD product growth on both ionically and electronically shorted surfaces.

Along the X direction, i.e., the surface of the ionic conducting material, the reaction limiting step is electron transport in the product phase (D). The growth distance, x , can be expressed as:

$$x = (V_D \sigma_e \Delta G t / F^2)^{1/2} \quad (3-43)$$

σ_e is the average electronic conductivity in the product phase (D), V_D is the molar volume of the deposit (D), t is time, and ΔG is the Gibbs free energy change for reaction (3-4) for product formation. Specifically,

$$\Delta G = \mu_{D,III} - \mu_{B,III} - \mu_{A,II} \quad (3-44)$$

Along the Y direction, i.e., the surface of the electronic conducting material, the reaction limiting step is mobile ionic reactant (A^+) transport in the product phase (D). No perceptible open circuit emf will be expected over the growth distance, and charged species are driven by the concentration gradient. The growth distance, y , can be expressed as:

$$y = (4/\pi) (V_D \sigma_{A^+} \Delta G t / F^2)^{1/2} \quad (3-45)$$

where σ_{A^+} is the average ionic conductivity in the product phase (D).

The ability of PEVD to deposit thin SSI materials can be expressed by the ratio of the Y to X direction growth length, y/x , which can be written as

$$\frac{y}{x} = \frac{1.265 \sqrt{\sigma_{A^+}}}{\sqrt{\sigma_e}} \quad (3-46)$$

This ratio is only related to the ionic and electronic conductivity of the PEVD product (Rapp and Shores, 1970). Thus, overgrowth along the electronic conducting surface indicates ionic conductivity is significantly higher than electronic conductivity in the PEVD product phase. For overgrowth along the ionic conducting surface, electronic conductivity must be significantly higher than ionic conductivity in the PEVD product phase.

Based on Eq. (3-46), the ability to grow a thin ionic conducting layer along the electronic conducting surface is illustrated in Figure 3-9. Accordingly, the minimum product thickness attainable depends on the electronic transference number of the product (D), as well as the growth distance along the electronic conducting surface. For instance, in order to cover an electronic conducting working electrode (W) surface 100 μm long with an ionic conducting product less than 1 μm thick, the electronic transference number of the ionic conducting product should be less than 0.0016.

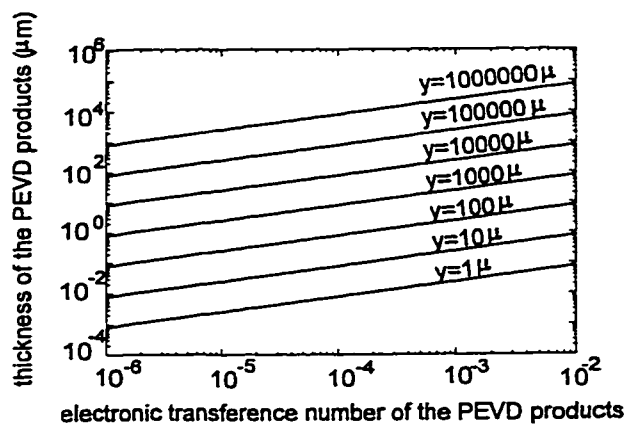


Figure 3-9. Plot of PEVD product thickness vs. electronic transference number for varying lengths (y) of the product.

3.5.3. Self-Leveling Effect

Once the working electrode (W) is covered by the ionic conducting product or the entire solid electrolyte (E) is covered by the electronic conducting product, no electrically shorted surface exists. Thus, further growth in thickness has to involve diffusion of both the ionic species and electrons to the surface to react with the gas phase. Practically, diffusion of one species is much faster than the other. However, electroneutrality must be maintained under this open circuit condition. The growth rate is determined by either migration of electrons or mobile ionic reactants in the deposit (D). In both cases, the increase in thickness should follow the parabolic law (Pilling and Bedworth, 1923)

$$\delta = (2kt)^{\frac{1}{2}} - (2kt_s)^{\frac{1}{2}} \quad (3-47)$$

where δ is the thickness of the product (D) at time t , k is the rate constant of Tammann's rate law (Tammann, 1920) and t_s is the initial growth time along the x direction. This corresponds to the differential equation

$$\frac{\partial \delta}{\partial t} = \frac{k}{\delta} \quad (3-48)$$

and the boundary condition

$$\delta = 0 \quad \text{at} \quad t = t_s \quad (3-49)$$

Because the increase in thickness is expected to follow parabolic behavior, the thicker the product, the slower the grow rate. Thus, a dense and uniform coverage is expected decreasing the aspect ratio of the surface in a step-wise fashion, as indicated by the numbered dotted lines in Figure 3-10.

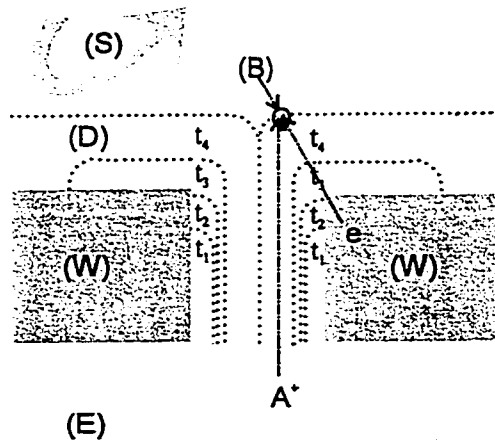


Figure 3-10. The step by step increase of PEVD product (D) thickness which reduces the aspect ratio at the working electrode. From t_1 to t_4 , the deposition time increases.

Chapter 4. Applying Polarized Electrochemical Vapor Deposition (PEVD) for Auxiliary Phase Deposition at Working Electrodes of Gaseous Oxide Sensors

PEVD was developed initially in the course of fabricating type III potentiometric sensors for gaseous oxide (CO_x , SO_x and NO_x) detection in our lab. Three kinds of PEVD products (NaNO_3 , Na_2CO_3 and Na_2SO_4) were deposited as the auxiliary phases at the working electrode of NO_2 , CO_2 and SO_2 sensors, respectively. Because of the underlying similarities, all discussion in this chapter will focus on CO_2 gas sensors. The similar cases of depositing NaNO_3 and Na_2SO_4 auxiliary phases for type III NO_2 and SO_2 potentiometric sensors, respectively, can be treated analogously.

4.1. Gaseous Oxide Sensors and Corresponding Kinetics

It is well known that gaseous oxides (CO_x , SO_x and NO_x) are responsible for global environmental problems such as acid rain and the greenhouse effect. The concentrations of typical air pollutants in the atmosphere and in combustion or other exhausts are listed

in Table 4-1. To date, these gaseous oxides have been analyzed mostly with analytical instruments based on IR absorption, UV absorption and chemiluminescence. Although these instruments provide precise analytical data, they are expensive with time-consuming procedures and hence do not fit well with a feedback control system. In order to treat combustion exhausts in chemical processes and to monitor the environment, there has been an ever-increasing need for compact, low-priced solid-state gas sensors (Gopel, 1994; Forlani, 1991) that are capable of detecting gaseous oxides in-situ. Various types of sensor prototypes have been studied (Madou and Morrison, 1989; Gopel, 1989). Among them, solid electrolyte potentiometric gas sensors have attracted widespread attention in recent years, not only for process control due to their high stability, but also for the detection of air pollutants due to their high sensitivity and selectivity.

Table 4-1. Gaseous oxides in environment and current detection methods.

Type of gaseous oxides	Environmental problems	Concentration range (ppm)		Current detection methods
		Air	Exhaust	
SO _x	Acid rain	10 ⁻³ – 10	10 – 2000	Flame photometer UV fluorescence IR absorption UV absorption PS electrolysis
NO _x	Acid rain	10 ⁻³ – 10	1 – 2000	Chemical luminescence IR absorption PS electrolysis
CO ₂	Greenhouse effect	300 – 1000	10 ⁴ – 2 × 10 ⁵	IR absorption ISE (pH) Thermal conductivity

4.1.1. The Development of Solid-State Potentiometric Gaseous Oxide Sensors

As was discussed in Chapter 2, Weppner (1987a) has classified potentiometric sensors into three types, depending on the gas electrode reactions at the working electrodes of the sensors.

Because of the unavailability of the requisite solid electrolytes to form a concentration cell of gaseous oxides, it is impossible to fabricate type I potentiometric sensors for detecting gaseous oxides.

In 1977, Gauthier and Chamberland (1977) first demonstrated the possibility for type II potentiometric detection of gaseous oxides using solid electrolytes of inorganic radicals, such as K_2CO_3 , $Ba(NO_3)_2$, and K_2SO_4 . Since then, much effort has been devoted to the development of type II potentiometric sensors (Gauthier and Chamberland, 1977; Gauthier et al., 1977; Worrell and Liu, 1982; Jacob and Rao, 1979). For instance, the simple cell shown in Figure 4-1 was employed to measure the equilibrium partial pressure of CO_2 in a gaseous mixture (Adachi and Imanaka, 1991; Cote et al., 1984). The galvanic cell expression is

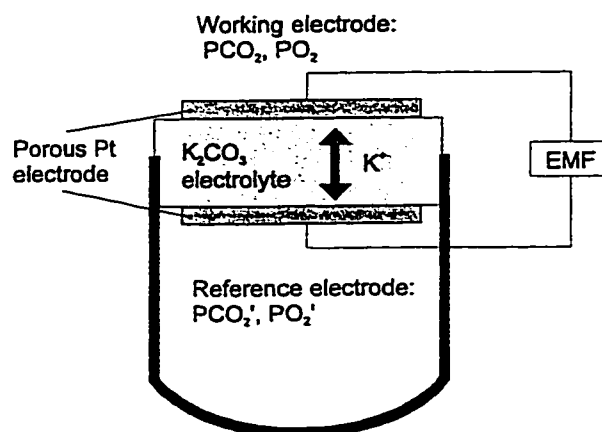
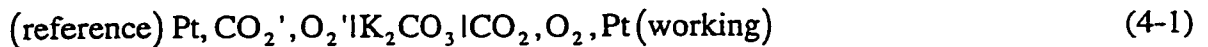
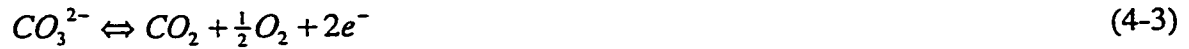


Figure 4-1. A type II potentiometric sensor for CO_2 detection.

Under open circuit conditions, the half cell equilibrium electrochemical reaction



prevails at the reference electrode, while the half cell equilibrium electrochemical reaction



prevails at the working electrode. According to the Gibbs-Duhem relation at constant temperature and total pressure, the chemical potentials of CO_3^{2-} and K^+ in the solid electrolyte K_2CO_3 are related, although CO_3^{2-} is immobile and K^+ is mobile in K_2CO_3 . Thus, the sensor galvanic cell can be viewed as an indirect CO_3^{2-} concentration cell with the overall cell reaction



The theoretical electromotive force (EMF) of the sensor is given by a Nernst equation:

$$EMF = \frac{RT}{2F} \ln \frac{P_{CO_2} P_{O_2}^{\frac{1}{2}}}{P_{CO_2}' P_{O_2}'^{\frac{1}{2}}} \quad (4-5)$$

where P_{CO_2} and P_{O_2} are the partial pressures of CO_2 and O_2 , respectively. If the oxygen partial pressure is same at both electrodes, then the EMF of the cell can be simplified to

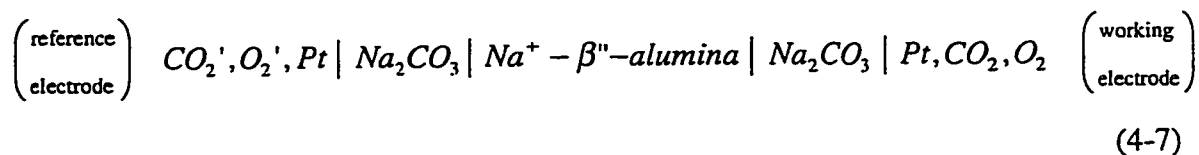
$$EMF = \frac{RT}{2F} \ln \frac{P_{CO_2}}{P_{CO_2}'} \quad (4-6)$$

The partial pressure of CO_2 at the working electrode can be directly compared with the partial pressure of CO_2 at the reference electrode. A galvanic cell like in Eq. (4-1) can

also be applied to SO₂ and NO₂ gas sensors by using sulfate and nitrate inorganic radicals in solid electrolytes, respectively.

Although employing inorganic radicals in solid electrolytes opens the possibility to detect gaseous oxides by a potentiometric method, it is a chemical choice rather than a material choice for solid electrolytes. Since salts involving inorganic radicals are usually not good solid electrolytes due to limited chemical stability, poor sinterability, phase transitions and low ionic conductivity, sensors made from those cells are unsuitable in practical applications (Saito et al., 1981; 1984a; 1984b).

Instead of a chemical approach to solid electrolyte selection in type II potentiometric sensors, type III potentiometric sensors for gaseous oxide detection have been considered from a material approach by first selecting good solid electrolytes (Weppner, 1979). According to classic electrochemical theory, an indirect (exchange) electrode can be used in cells for the determination of thermodynamic data for reactions involving an element for which a solid electrolyte is not available. The indirect electrode then serves as an auxiliary phase where the activity of the component of interest can be related to the activity of another component in a solid electrolyte. Of particular importance is the applicability of this electrochemical technique to those gaseous species for which a solid electrolyte is not available. As a result, a large selection of solid electrolytes can be used for gaseous oxide sensors, especially several fast sodium ionic conductors, such as β -alumina (Shimizu et al., 1991; Akila and Jacob, 1989) and Nasicon (Na₃Zr₂Si₂PO₁₂) (Miura et al., 1993; Yao et al., 1992 and 1991; Maruyama et al., 1987b). For instance, a type III CO₂ potentiometric gas sensor, shown in Figure 4-2, which obeys the following cell expression has been widely recognized as the best potentiometric sensor prototype for CO₂ gas detection (Weppner, 1979 and 1987a; Maruyama et al., 1987b; Yamazoe and Miura, 1995).



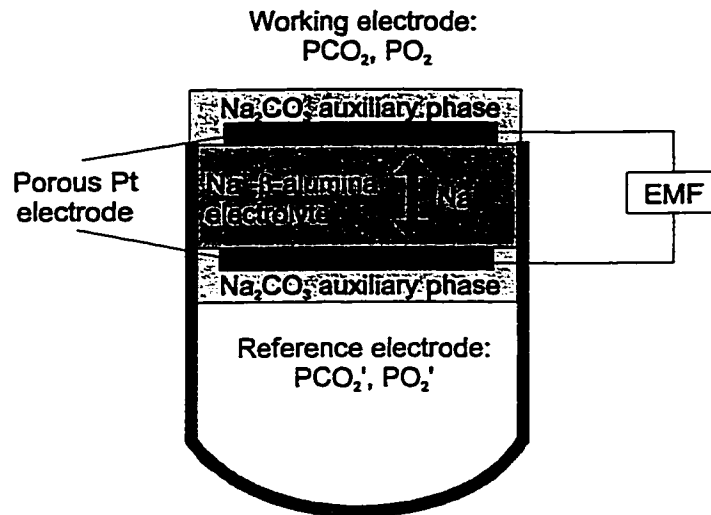


Figure 4-2. A type III potentiometric sensor for CO₂ gas detection.

The sensing mechanism of the sensor was studied in detail by Hotzel and Weppner (1985) from a thermodynamic point of view. Under open circuit conditions, the equilibrium half cell electrochemical reaction at the reference electrode is



and the equilibrium half cell electrochemical reaction at the working electrode is



The overall electrochemical reaction is



which is the same as for a type II potentiometric sensor. The EMF expression is also identical to a type II potentiometric sensor. However, an important feature of this kind of sensor is the Na₂CO₃ auxiliary phase. It provides a unique relationship between the partial pressure of the gaseous components (CO₂ and O₂) and the chemical potential of

the mobile sodium ions in the solid electrolyte Na^+ - β -alumina. Thus, the auxiliary phases are of vital importance for type III potentiometric sensors. Generally, an auxiliary phase should be a fast, mixed ionic and electronic conductor, be located at the area of change from ionic to electronic conductivity in the galvanic cell, and be involved in the cell reaction.

The results obtained to date with type III potentiometric sensors have shown them to be successful and promising for detecting gaseous oxides. Recently, this topic was reviewed by Yamazoe and Miura (1995 and 1994).

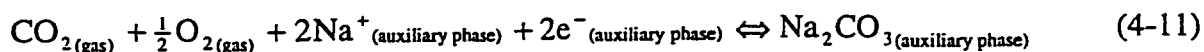
Although the basic principles of type III potentiometric sensors are applicable for gaseous oxide detection, this should not obscure the fact that these sensors still require further development. This is especially true in view of the kinetics of equilibria and charged species transport across the solid electrolyte/electrode interfaces where auxiliary phases exist. Real life situations have shown that, in practice, gas sensors rarely work under ideal equilibrium conditions. The transient response of a sensor, after a change in the measured gas partial pressure, is in essence a non-equilibrium process at the working electrode. Consequently, although this kind of sensor has been studied for almost 20 years, practical problems still exist and prevent its commercialization. These problems include slow response, lack of sensitivity at low concentrations, and lack of long-term stability (Miura et al., 1992a; Chu et al., 1992; Veonhard et al., 1993). It has been reported (Miura et al., 1992a; Chu et al., 1992) that the auxiliary phases were the main cause for sensor drift, and that preparation techniques for electrodes with auxiliary phases were very important to sensor performance (Leonhard et al., 1993). In order to improve the performance of this kind of sensor, most recent investigations (Miura et al., 1994; Yan et al., 1992) have focused on the chemical and electrochemical aspects of the auxiliary phases to improve their chemical and thermal stability. However, few researchers have considered the effects of geometric structure of the auxiliary phases at the working electrodes.

4.1.2. Gas Electrode Reactions in Type III Potentiometric CO₂ Sensors

4.1.2.1 A Kinetic Gas Sensing Model for Type III Potentiometric CO₂ Sensors

Previous kinetic studies of sensing mechanisms for potentiometric sensors were mostly based on type I and type II sensors that do not include an auxiliary phase. Therefore, the search for a detailed mechanism of gas electrode reactions in type III potentiometric sensors, with auxiliary phases, is essential.

Thermodynamically, the equilibrium EMF of a type III potentiometric CO₂ sensor represented by cell Eq. (4-7) can be obtained only when full equilibria are reached in the Na₂CO₃ auxiliary phase. At the working electrode of cell Eq. (4-7), the overall gas electrode reaction equilibrium with the Na₂CO₃ auxiliary phase can be expressed as:



Usually, the inorganic radical auxiliary phases are treated as mixed ionic and electronic conductors (Weppner, 1981). For example, cationic Frenkel defects (Ramastry and Murti, 1968; Cleaver, 1965), a cation vacancy + an interstitial cation ($V_{\text{Na}}\text{Na}_i^\bullet$), are the most likely lattice defects in inorganic radical phases, such as Na₂CO₃, NaNO₃ and Na₂SO₄. In these phases, the sodium ion is the majority carrier. Excess electrons as minority carriers co-exist in these solid phases at elevated temperature. According to the basic ideas within the framework of Wagner's description of solid ionic conductors (Kiukkola and Wagner, 1957a and b), the subsurface of the Na₂CO₃ auxiliary phase is assumed to be continually in equilibrium with the contacting gas under open circuit conditions, when no current flows through the galvanic cell. However, during the transition period, after changing the measured gas partial pressure, defects in solids and adsorbed particles at the surfaces are generally not in equilibrium with one another. The transition approach to equilibrium inside the auxiliary phase under open circuit conditions is of great importance for the understanding of the kinetics of type III potentiometric sensors. Specifically, the interaction of adsorbed gas phase molecules with subsurface electronic donor states, and local equilibrium of subsurface electronic

donor states with the mobile ionic species in the auxiliary phase, play a central role in kinetics (Wagner, 1970). Accordingly, the overall electrode reaction may be divided into several possible rate-limiting steps as follows:

(a) Gas phase adsorption and desorption at the auxiliary phase surface. In the case of gas ($\text{CO}_2 + \frac{1}{2} \text{O}_2$) adsorption on the Na_2CO_3 auxiliary phase surface, the following mechanism may, for example, be proposed for surface adsorption and desorption equilibrium:

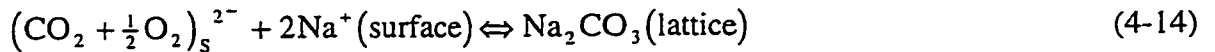


where S represents surface adsorption sites. This step also includes gas phase diffusion to the surface.

(b) Incorporation of the surface adsorbed species $(\text{CO}_2 + \frac{1}{2} \text{O}_2)_\text{S}$ in the Na_2CO_3 auxiliary phase lattice. This involves the capture of electrons by the adsorbed species in the subsurface of the Na_2CO_3 auxiliary phase to form donor electronic surface states, or vice versa, according to the following equation:



(c) Local equilibrium of the donor electronic surface states and the mobile ionic species in the Na_2CO_3 auxiliary phase lattice. This can be expressed by the following process in the sub-surface region of the auxiliary phase:



The model for this approach can be sketched as shown in Figure 4-3. Accordingly, slow response in a type III potentiometric sensor can arise from any one of the above steps. Step (a) is related to the gas phase diffusivity and the surface properties of the auxiliary phase. This step is not electrochemical in nature; thus, it is excluded from this model.

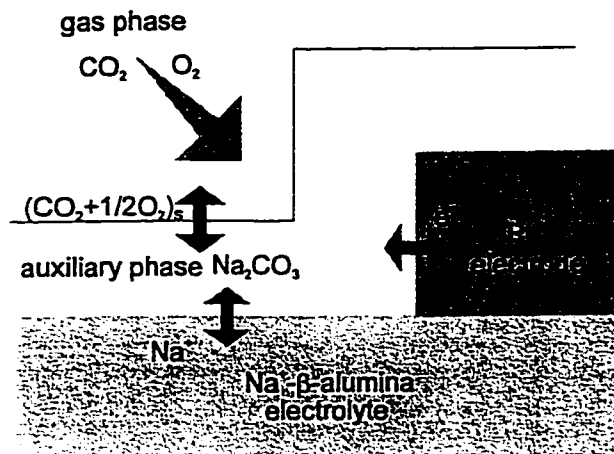


Figure 4-3. Gas electrode reaction model for type III CO₂ potentiometric sensors.

Generally, the equilibrium processes in the bulk of the auxiliary phase are governed by diffusion controlled adjustments to the electrochemical potential profiles for both ionic and electronic carriers in Na₂CO₃. According to the overall electrode reaction in Eq.(4-11), the relevant equation relating the corresponding chemical (μ) and electrochemical potentials ($\bar{\mu}$) is easily deduced, giving the relation

$$\bar{\mu}_{e^-} = \frac{1}{2}\mu_{Na_2CO_3} - \frac{1}{2}\mu_{CO_2} - \frac{1}{4}\mu_{O_2} - \bar{\mu}_{Na^+} \quad (4-15)$$

Since the chemical potential of pure Na₂CO₃, $\mu_{Na_2CO_3}^\circ$, equals its standard molar Gibbs free energy, $G_{Na_2CO_3}^\circ$, Eq.(4-15) can be written as

$$\bar{\mu}_{e^-} = \frac{1}{2}G_{Na_2CO_3}^\circ - \frac{1}{2}\mu_{CO_2}^\circ - \frac{RT}{2}\ln P_{CO_2} - \frac{1}{4}\mu_{O_2}^\circ - \frac{RT}{4}\ln P_{O_2} - \bar{\mu}_{Na^+} \quad (4-16)$$

The electroneutrality condition in Na₂CO₃ requires (in Kröger-Vink notation) that

$$[Na_i^\bullet] = [V_{Na}^\bullet] + [e^\cdot] \quad (4-17)$$

Because of the large bandgap in Na_2CO_3 , the electron concentration remains very small with respect to the other concentrations in Eq.(4-17); also we can reasonably assume that the concentration of Na^+ is constant for reaction (4-11). Actually, under steady-state potentiometric conditions, the electrochemical potential of sodium ions $\bar{\mu}_{\text{Na}^+}$ in cell (4-7) is constant throughout the auxiliary Na_2CO_3 phase and the Na^+ - β -alumina electrolyte, and fixed at the reference electrode. Any variation would induce current and mass fluxes, which are inconsistent with steady-state conditions. Thus, any change in the measured gas phase partial pressure induces only a change in electron concentration. As a result, the electrochemical potential of electrons (Fermi level) in Na_2CO_3 is governed by the analyzed gas, which adsorbs on the surface and exchanges electrons with the Na_2CO_3 subsurface.

As schematically shown in Figure 4-3, at the contact between the platinum coating and the auxiliary Na_2CO_3 phase, an equilibrated electron exchange is assumed to prevail at the interface.

$$\bar{\mu}_{e^-(\text{Pt})} = \bar{\mu}_{e^-(\text{Na}_2\text{CO}_3)} \quad (4-18)$$

Thus, a change in $(\text{CO}_2 + \frac{1}{2} \text{O}_2)$ at the auxiliary phase surface results in an electron electrochemical potential difference $\Delta\bar{\mu}_{e^-}$ between the surface of Na_2CO_3 and its interface with the Pt coating. A shift in the electronic Fermi level within the Na_2CO_3 auxiliary phase is induced (Kleitz and Siebert, 1989).

Theoretical EMF values for galvanic cell (4-7) can only be obtained after readjustment of the electron electrochemical potential profile inside the auxiliary phase is completed. Therefore, Eq.(4-18) can extend to the gas electrode reaction zone at the Na_2CO_3 auxiliary phase surface. The usual thermodynamic split can be applied to Eq. (4-16).

$$\begin{aligned} \bar{\mu}_{e^-} &= \mu_{e^-} - F\phi_{\text{Pt}} \\ \bar{\mu}_{\text{Na}^+} &= \mu_{\text{Na}^+} + F\phi_{\text{Na}_2\text{CO}_3} \end{aligned} \quad (4-19)$$

where ϕ_{Pt} and $\phi_{Na_2CO_3}$ are the average internal electric (Galvani) potentials in Pt and Na_2CO_3 , respectively. One now obtains

$$\phi_{Pt} - \phi_{Na_2CO_3} = \frac{1}{F}(\mu_{e^-} + \mu_{Na^+} - \frac{1}{2}G_{Na_2CO_3}^{\circ} + \frac{1}{4}\mu_{O_2}^{\circ} + \frac{RT}{4}\ln P_{O_2} + \frac{1}{2}\mu_{CO_2}^{\circ}) + \frac{RT}{2F}\ln P_{CO_2} \quad (4-20)$$

In this expression, the term μ_{e^-} , representing the chemical potential of electrons in Pt, is constant. Similarly, the chemical potential of Na^+ ions in the Na_2CO_3 phase is also constant. Therefore, the electric potential of Pt versus that of Na_2CO_3 can be predicted from the Nernst law. The sensing electrode potential, E_{Pt} , is given by

$$E_{Pt} = \phi_{Pt} - \phi_{Na_2CO_3} = E^{\circ} + \frac{RT}{2F}\ln P_{CO_2} \quad (4-21)$$

where E° is a constant, provided the partial pressure of oxygen is fixed.

According to this electrode reaction model, since Na_2CO_3 is predominantly an ionic conductor, step (b) is more likely than step (c) to be the electrode reaction (4-11) limiting step. Therefore, a thin auxiliary phase layer, which intimately contacts the metallic coating, is critical to the performance of this kind of sensor. Since electron transfer is two dimensional across the interface, maximum contact area is desired. Furthermore, such a readjustment of electron electrochemical potential generally implies local variations in electron concentration and, therefore, variations in the concentration of sodium ions according to Eq.(4-17). The latter variations are relatively small but can, during the transient period, be sufficiently slow to induce significant effects (Heyne and den Engelsen, 1977), especially when the contact between Na^+ - β -alumina and Na_2CO_3 is poor. As a result, step (c) may limit the overall electrode equilibrium reaction (4-11) under certain conditions.

4.1.2.2. Geometric Criteria for the Best Auxiliary Phases for CO₂ Sensors

Based on the preceding sensor electrode reaction model, the gas electrode reactions for type III potentiometric CO₂ sensors in cell (4-7) are essentially charge transfer reactions between the Na₂CO₃ auxiliary phase and the gaseous species. This certainly depends on the gas phase and the auxiliary phase, as well as the interface between them. For instance, high operating temperatures will increase the surface adsorption and desorption rates in step (a), the electronic conductivity in step (b) and ionic conductivity in step (c). Thus, the kinetic response of the sensor will be improved at higher operating temperature. On the other hand, the operating temperature of a sensor has to be considered as a balance against other sensing properties, such as accuracy, sensitivity, selectivity and stability. There are a number of limitations to increasing the operating temperature. For instance, electronic conductivity and hence electronic transference number in the solid electrolyte will increase to shift the equilibrium EMF value, and the resulting electronic leakage current will eventually damage the reference electrode. An alternative method to improve kinetics was proposed (Gopel, 1985), which involves an electronic conducting phase, such as platinum, dispersed within the auxiliary phase to increase its electronic conductivity. However, this method is limited by fabrication problems. Adjustment of the physical properties (conductivity) of the auxiliary phase to improve the kinetic performance of a type III potentiometric gaseous oxide sensor is very limited.

The sensing model developed here also implies that the geometric properties, instead of solely the physical properties of the auxiliary phase at the working electrode, are critical for kinetic performance. Accordingly, the four most important geometric criteria for an auxiliary phase are as follows:

- (1) For step (a), the aspect ratio of the auxiliary phase at the working electrode should be as low as possible to improve gas phase diffusion.
- (2) For step (b), the auxiliary phase should intimately contact the metallic electrode, and the interface should be as large as possible since transport of electrons is two-dimensional across the interface.

- (3) Also for step (b), the auxiliary phase should be as thin as possible to allow readjustment of the Fermi level within the auxiliary phase.
- (4) For step (c), the auxiliary phase should intimately contact the solid electrolyte to ensure transport of mobile ionic species. This will benefit the performance of sensors under certain conditions.

Besides the geometric requirements suggested by the above mentioned gas-sensing model, two more criteria can be deduced from other considerations. First of all, as a general requirement of applying an indirect electrode (Rapp and Shores, 1970), the auxiliary phase should separate the reactants in the gas phase from the electrolyte. Otherwise, displacement reactions can damage the contact between the solid electrolyte and auxiliary phase layer and affect stability. These reactions can also generate a mixed sensor EMF response leading to selectivity and sensitivity problems. Thus:

- (5) The auxiliary phase should cover the entire solid electrolyte surface.

Secondly, from Wagner's theory, the metallic coatings forming the electrodes are viewed as mere electronic probes for the local electronic distribution in the auxiliary phase. They should be chemically inert. For operation in the lean regime, it is highly desirable that their chemical catalytic activities be as low as possible (Haaland, 1980). Hence:

- (6) The auxiliary phase should cover the entire metallic electrode. This also provides maximum interface contact as required in criterion (2).

4.1.2.3. Previous Auxiliary Phase Preparation Techniques and Their Problems

Previously, several methods (Maruyama et al., 1987a and 1991; Miura et al., 1992b) have been reported for applying auxiliary phases to the porous metallic working electrodes of gaseous oxide sensors. Figure 4-4 compares the geometric structure of the ideal auxiliary phase arrangement (Fig. 4-4a) according to the above six criteria to various reported techniques such as in-situ formation (Figure 4-4b), mechanically pressed discs (Figure 4-4c), physical vapor deposition (Figure 4-4d), and melting and quenching (Figure 4-4e). It is clear that none of these previously reported techniques meet all the

geometric requirements for an ideal auxiliary phase. This will lead to sensor sensitivity, selectivity, stability and response time problems.

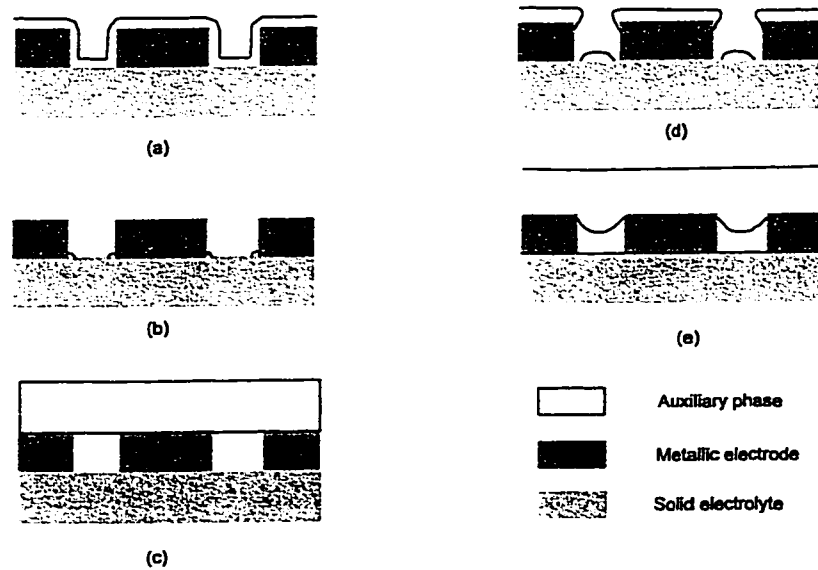


Figure 4-4. Comparison of geometric structure of an ideal auxiliary phase (a) with those prepared by current techniques, such as in-situ formation (b), mechanically pressed discs (c), physical vapor deposition (d), and melting and quenching (e).

In what is the essence of materials engineering, structure and preparation will undoubtedly be of vital important to final properties. In order to deposit better auxiliary phases with close control to meet all six geometric criteria, polarized electrochemical vapor deposition (PEVD) has recently been applied in our lab to deposit auxiliary phases at the working electrodes of gaseous oxide sensors (Tang et al., 1996).

4.2. Polarized Electrochemical Vapor Deposition to Deposit Auxiliary Phases at the Working Electrode of Type III Potentiometric CO₂ Sensors

4.2.1. PEVD Process Design

The basic principles governing PEVD process design have been discussed in Chapter 3. In the case of depositing a Na_2CO_3 auxiliary phase at the working electrode of a CO_2 potentiometric sensor, the substrate or solid electrochemical cell for this PEVD process is well defined. Although other solid electrolyte and metallic electrode combinations were reported in previous investigations, the use of Na^+ - β -alumina as the solid electrolyte and a porous Pt thick film as the metallic working electrode is the most common choice for type III potentiometric CO_2 sensors. A cross-section view of the substrate is schematically shown in Figure 4-5. Because of the nature of screen printing technology, the thickness and porosity of the Pt thick films may vary from one study to another. Usually, the Pt thick films are highly porous (larger than 50 vol % pore phase) and irregularly shaped, and they have very high aspect ratios (larger than 3). Depositing a compound thin film of Na_2CO_3 on such a substrate to meet all above-mentioned geometric criteria by conventional deposition techniques is almost impossible.

Sodium is selected as the solid state transported reactant in PEVD. This is because not only is Na^+ a component in the PEVD product phase Na_2CO_3 , but also the mobile ionic species in the solid electrolyte (Na^+ - β -alumina) and in the auxiliary phase of the sensor. Thus, PEVD can take advantage of the solid electrochemical cell (substrate) of the sensor to transport one reactant (sodium) across the substrate under an electrochemical potential gradient. This gradient is mainly provided by a dc electric potential under closed circuit conditions. The vapor (or gas) phase at the sink side of the PEVD system should be made up of the other components of the PEVD product Na_2CO_3 , i.e., carbon and oxygen. This can be realized by using CO_2 and O_2 as the vapor phase reactants at the sink side of the PEVD system. Thus, the electrochemical reaction for PEVD Na_2CO_3 product formation will involve the solid state transport of sodium ions through the solid electrolyte to obtain electrons from the metallic electrode and react with CO_2 and O_2 from the sink side vapor phase. The cathodic half-cell electrochemical reaction at the sink side can be expressed as



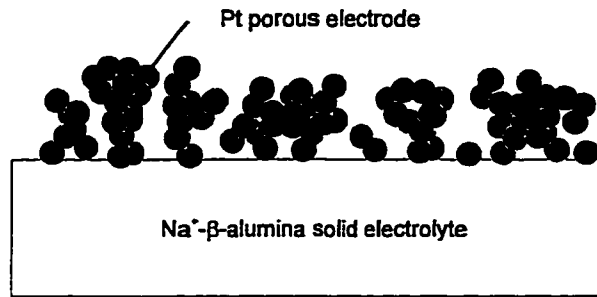


Figure 4-5. Schematic cross-section of a Pt thick film electrode on a Na⁺-β-alumina solid electrolyte of a type III potentiometric CO₂ sensor.

In order to sustain this reaction at the sink side of the PEVD system, a source is required at the other side of the substrate (anode) to supply sodium. Otherwise, depletion of sodium in the Na⁺-β-alumina solid electrolyte will lead to an α-alumina phase buildup at the anode that will block the ionic transport path of the PEVD system. The electrolytic properties of the solid electrolyte in this PEVD system will then be lost. Elemental sodium, for instance, could be the source giving the following anodic reaction:



This kind of source has the advantages of the fixed chemical potential of sodium, good contact between liquid sodium and the solid electrolyte, and no additional electronic conducting electrode is needed as the counter electrode (C) to connect with the external electric circuit. In practice, elemental sodium is too active, and a very tight seal is required to prevent sodium vapor from migrating and reacting chemically with CO₂ and O₂ in the sink vapor phase. Consequently, the system setup becomes more complex. The choice of the source in the current study is a combination of Na₂CO₃, CO₂ and O₂ gas phase, and an inert Pt counter electrode. The anodic reaction will be a decomposition reaction of the Na₂CO₃ solid phase,



This anodic reaction provides sodium ions and electrons to the solid electrolyte and the inert Pt counter electrode, respectively, at the source side. Both the sodium ions and electrons will then travel through the solid electrochemical cell along previously-mentioned ionic and electronic paths to sustain the PEVD cathodic reaction for Na_2CO_3 product formation at the sink side. Furthermore, based on anodic reaction (4-24), the chemical potential of sodium is fixed by the vapor phase at the source side. Under open circuit conditions, this type of source can also serve as the reference electrode for a CO_2 potentiometric sensor.

The PEVD system for Na_2CO_3 auxiliary phase formation, at the working electrode of a type III potentiometric CO_2 sensor, is schematically shown in Figure 4-6. The electrochemical cell for this PEVD process can be expressed as:

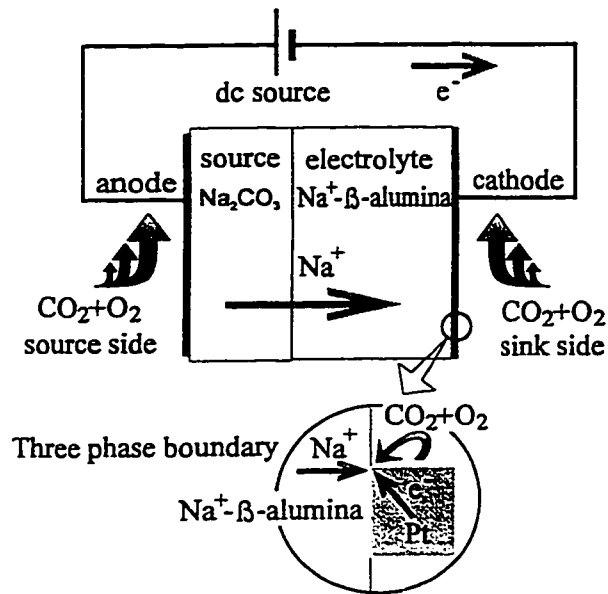
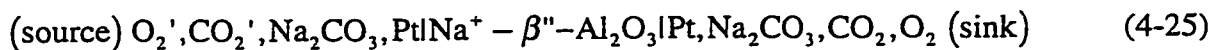


Figure 4-6. PEVD process design for applying an auxiliary phase (Na_2CO_3) at the working electrode of a type III potentiometric CO_2 gas sensor.



The overall cell reaction is:



This overall electrochemical cell reaction is equivalent to transporting the Na_2CO_3 phase physically from one side of the substrate to the other.

During the PEVD process, a chemical redox reaction takes place and the whole PEVD system can be viewed as a chemical reactor where the reactants are distributed over both the source and sink side. According to the discussion in Chapter 3, the driving force for this PEVD process can be solely provided by a dc electric potential, so that isolation of the source and sink vapor phases is not necessary. Consequently, the PEVD process is equivalent to physically moving a solid phase Na_2CO_3 through another solid phase (Na^+ - β -alumina) by electric energy. Furthermore, it should be pointed out that the overall cell reaction in this PEVD system is reversible.

NaNO_3 and Na_2SO_4 auxiliary phases can be deposited by a similar PEVD method for type III NO_2 and SO_2 potentiometric sensors, respectively.

4.2.2. Experimental Procedure

4.2.2.1. PEVD System Setup

A sample of a PEVD system used in this investigation in a sample holder is schematically shown in Figure 4-7. A commercially available fully dense Na^+ - β/β'' -alumina disc (Ceramatec, Inc.), with a nominal composition of 8.85 wt.% Na_2O , 0.75 wt.% Li_2O and 90.40 wt.% Al_2O_3 was used as the solid electrolyte. The disc is 16 mm in diameter and 5 mm in thickness. The sodium ionic conductivity is given as $0.2 (\Omega\text{cm})^{-1}$ at 300°C .

The working electrode (sink) of the system is a screen-printed platinum thick film. Screen printing is a simple and effective method for metallic electrode fabrication (Yentekakis and Vayenas, 1988). In this study, a Pt paste (No. 5544, Electro-Science Laboratories, Inc.) was first applied to the surface of the Na^+ - β/β'' -alumina disc by

forcing the paste to pass a nylon screen with a squeegee. Then the printed paste was subjected to a drying, burn out and sintering procedure to eliminate the organic vehicles in the paste, and to improve adhesion of the sintered porous Pt to the substrate.

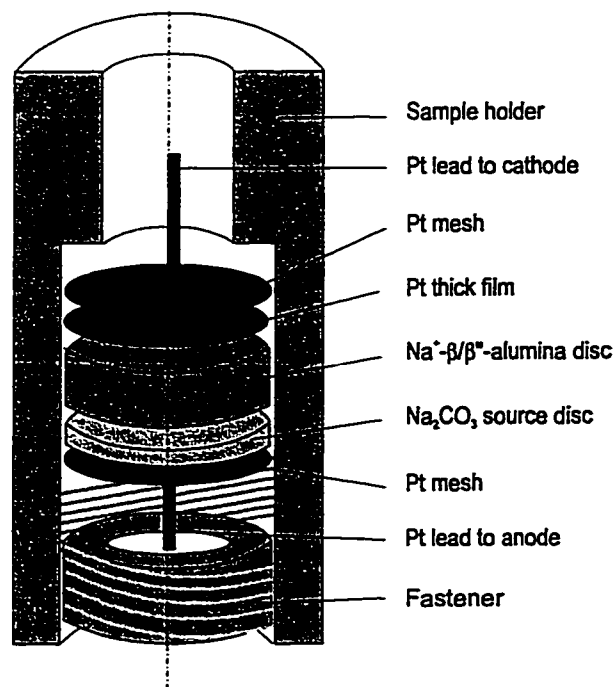


Figure 4-7. The PEVD system and sample holder.

The calcination procedure plays a key role in obtaining well-adhered Pt thick films with desired porosity and surface area on the $\text{Na}^+\text{-}\beta/\beta''\text{-alumina}$ substrates. The calcination of the Pt pastes in this study was conducted in a lab-made tube furnace. The temperature cycle is recorded in Figure 4-8. The Pt paste was first dried at room temperature for about 20 min, and then heated up to 140°C at a ramp rate of $2^\circ\text{C}/\text{min}$. Heating was continued to 300°C at a ramp rate of $5^\circ\text{C}/\text{min}$ to burn out the organics in the paste. Finally, the sample was heated to 980°C at a ramp rate of $10^\circ\text{C}/\text{min}$ and left for 15 min for sintering. During the entire calcination process, a high flow rate of air (greater than 300 sccm) was maintained. The thickness of the film depends on a number of process parameters, such as viscosity of the paste, pore size of the screen, the force applied on the squeegee, and the numbers of passes used. Since all the parameters were controlled manually in this study, consistent results depend on operator experience. Pt

thick films of 7 μm in thickness were selected for the working electrode in this investigation. At this thickness, the discontinuous part of the Pt thick films is less than 1%. The porosity of the Pt thick film is in the range of 65 to 75% according to weight assessments, in which the weight of the Pt porous films is compared with the weight of a fully dense Pt layer. The average pore size is about 2 μm and ranges from 0.5 - 5 μm according to microstructure studies. The area of the thick film is the same as the substrate at about 200 mm^2 . The thick film surface area was estimated at 300-3000 times the paste surface area for 7 μm in thickness (Vayenas and Neophytides, 1991). Increasing the calcination temperature even by 20-30 $^{\circ}\text{C}$ leads to increased sintering and, consequently, an increase in average pore size and lost surface area.

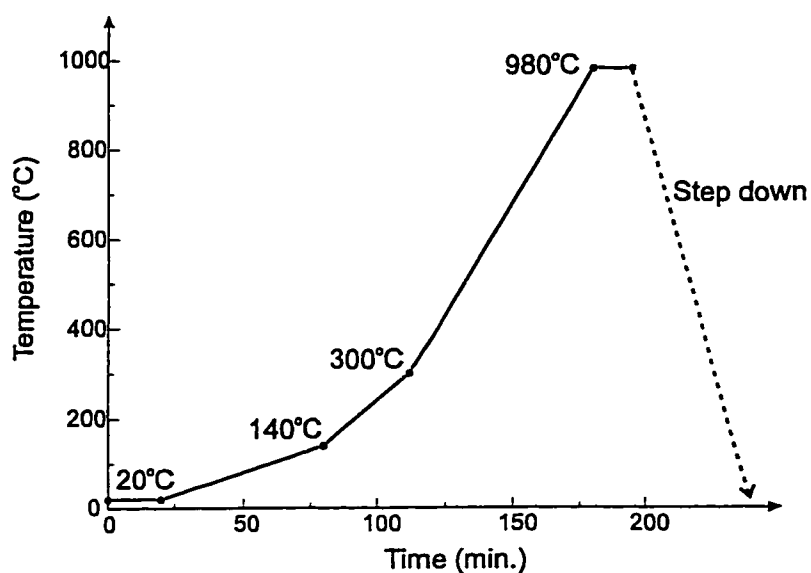


Figure 4-8. Sintering procedure for the Pt thick film working electrode.

In order to connect the Pt paste of the working electrode with the external electric circuit, a Pt mesh with a spot-welded Pt lead was used as the current collector. Good mechanical and electric connections were ensured by pressing the mesh onto the surface of the Pt thick film, heating to 960 $^{\circ}\text{C}$ at a rate of 20 $^{\circ}\text{C}/\text{min}$, and co-sintering for 20 min. The thickness and porosity of the Pt thick film did not change much after this procedure.

A source Na_2CO_3 disc was made by pressing Na_2CO_3 powder (99.99%, Aldrich) in a 19-mm die at 207 MPa. The green body was then pressed on to a Pt mesh with a spot-

welded Pt lead, heated at a ramp rate of 10°C/min and sintered at 800°C for 60 min. The final dimensions of the disc were 2 mm in thickness and 16 mm in diameter. In order to provide reasonable contact between the source Na₂CO₃ disc and the solid electrolyte, both discs were pressed together mechanically in a sample holder as shown in Figure 4-7, and co-sintered at 810°C for another 60 min.

4.2.2.2. PEVD Process

A PEVD sample was placed into a lab-made PEVD apparatus, which is schematically shown in Figure 4-9. The apparatus has three basic functions, i.e., to set the processing temperature, to control the gas phases at both the source and the sink of the PEVD system, and to control and monitor the PEVD process through an external electric circuit.

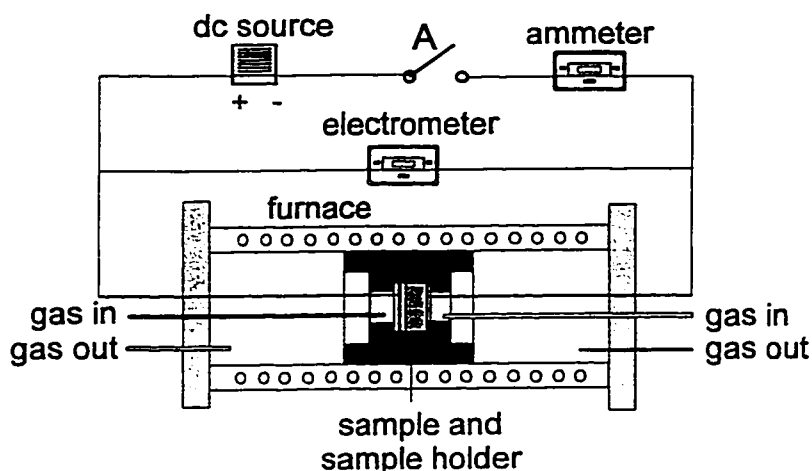


Figure 4-9. PEVD apparatus for Na₂CO₃ formation at the working electrode.

According to mass and charge transport behavior in a PEVD system discussed in Chapter 3, process control depends on three parameters.

a. Temperature

Operating temperature affects the ionic conductivity in both the solid electrolyte and the PEVD product phase Na₂CO₃. The higher the operating temperature, the higher the

ionic conductivity and, consequently, the PEVD current and reaction rate. Temperature also increases the electronic conductivity inside both solid phases. Although a higher electronic conductivity will increase the sodium solid-state transport rate inside the product Na_2CO_3 phase, it also increases the leakage current through the solid electrolyte. 500°C was selected for the current experiment. The samples were placed in a uniform temperature zone of a tube furnace (Lindberg). During the PEVD process, the temperature was monitored by two K-type thermocouples placed close (less than 5 mm) to the samples on both the source and sink sides. The temperature difference between both sides was less than 1°C . Thus, the chemical potential difference due to a thermal gradient was negligible.

b. Vapor phase

In order to eliminate the driving force generated by a chemical potential difference between the sink and source side, the same vapor phase was used at both sides. The vapor phase consisted of air (Praxair, ultra zero grade with 293 ppm CO_2 and 21% O_2) at atmosphere pressure. It was passed through a set of drying units (Drierite and P_2O_5 , Fisher Scientific) before entering the PEVD apparatus. The inlet gas tubes on both sides were placed close (less than 10 mm) to the source and sink surfaces of the PEVD system to minimize gas phase diffusion effects. The flow rate of both inlet gases was in the range of 100 - 400 sccm and regulated by two flowmeters with needle valves (Matheson).

c. Applied potential and current monitoring

An external electric circuit as shown in Figure 4-9 was connected to a PEVD sample through the Pt leads from both the source and the sink sides. The driving force for the PEVD was supplied by a stable dc electric source (model 1090, Brunelle Instruments, Inc.). The sink and source side were set as the cathode and anode, respectively. A PEVD process started when gate A (Figure 4-9) was closed. Both potentiostatic (constant dc potential) and galvanostatic (constant PEVD current) methods could be applied in PEVD processes. An electrometer (Keithley 616) was used to measure the close circuit applied potential during the PEVD process. An ammeter (Keithley 713) was used to monitor the current and, subsequently, the PEVD reaction rate according to Faraday's law. Both the

ammeter and electrometer were connected to a dual channel analog recorder (Brinkmann 2742-3).

4.2.2.3. PEVD Product Microstructure Studies

The phases, microstructure and chemical composition at the sink side of the PEVD system were studied before and after the PEVD process by x-ray diffraction (XRD), scanning electron microscopy (SEM) and energy dispersive x-ray (EDX) spectroscopy, respectively. The SEM used was a Hitachi H-2700 equipped with a Link eXL X-ray detector operated in windowless mode for EDX studies. The XRD used was a Rigaku unit with Jade software system.

Both plan-view and cross-section samples were made for microstructural studies. Plan-view samples require minimal preparation, and reveal the microstructure of the working electrode surface without damage to the PEVD substrates. Thus, a PEVD system can even be studied at intervals during PEVD by simply stopping the process, analyzing it, and then returning it to the PEVD apparatus. Furthermore, plan-view samples can also be used for XRD to reveal crystallographic information.

Cross-section samples reveal the interfacial microstructure of the PEVD systems. However, cross-section sample preparation is destructive. Samples can only be made after an entire PEVD process is completed. Two kinds of cross-section samples were prepared in this investigation. One type was simply made by cleaving the PEVD substrate prior to analysis, producing a fresh break. Imaging of this type of sample takes advantage of the large depth of field of SEM secondary electron (SE) images. Thus, 3-D geometrical information could be revealed regarding product coverage at the working electrode after a PEVD process. Local chemical information for each phase could also be obtained through EDX spot analysis.

The other type of cross-section samples was made by sectioning the PEVD substrates into small pieces. The pieces were then mounted for grinding and polishing to produce flat surfaces for subsequent EDX x-ray mapping. Since both Na_2CO_3 and $\text{Na}^+ \text{-}\beta/\beta''$ -alumina are not stable in water, it was essential to keep the sample dry. In practice, both

cutting oil and CCl_4 were used for as lubricants for cutting, grinding and polishing the samples. All samples were stored in desiccators to minimize degradation from moisture in the atmosphere.

4.2.3. Results

4.2.3.1. Microanalysis of the PEVD Deposit

Figures 4-10(a) and (b) show SEM secondary electron (SE) plan-view micrographs comparing the sink side of a PEVD sample before and after a PEVD process, respectively. Before PEVD, a porous Pt thick film with ~60% porosity covered the entire $\text{Na}^+/\beta/\beta''$ -alumina substrate at the working electrode of the CO_2 potentiometric sensor. The pore size was in the range of 0.5 to 5 μm , with an average estimated at 2 μm .

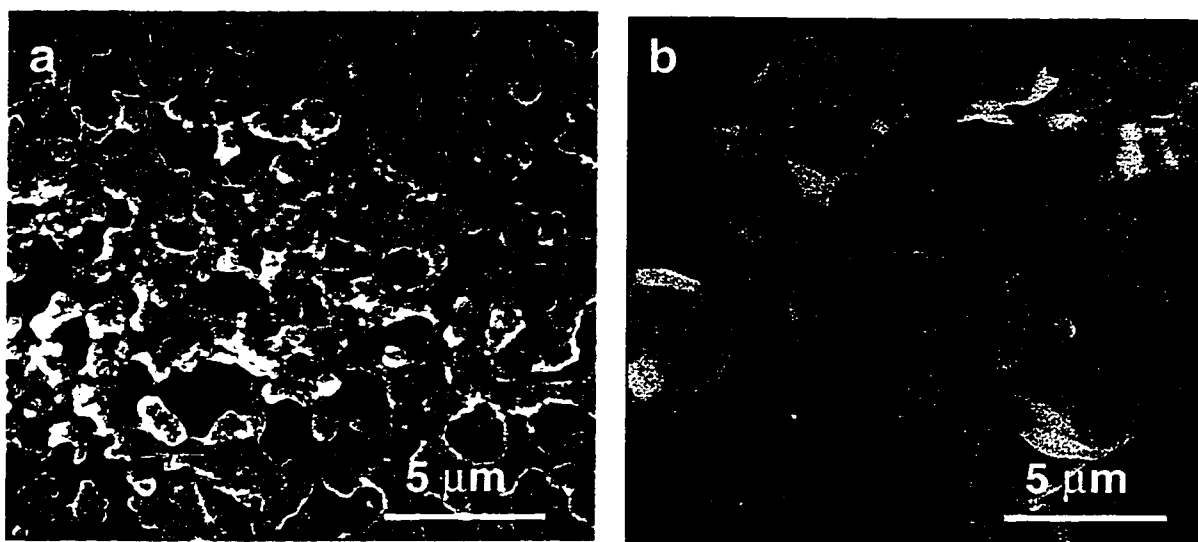


Figure 4-10. SEM SE plan-view images of the working electrode (a) before and (b) after a PEVD process.

The corresponding XRD spectrum is plotted as curve (a) in Figure 4-11. The Pt phase is dominant with a trace amount of $\text{Na}^+/\beta/\beta''$ -alumina. After PEVD, the porous Pt thick film was covered by a dense PEVD product. The corresponding XRD spectrum is plotted as curve (b) in Figure 4-11. The spectrum indicates that the PEVD product is a

Na_2CO_3 crystal phase. Because of the penetration depth of the x-rays, the underlying Pt phase was still detectable by XRD as shown in spectrum (b) in Figure 4-11. The x-ray intensities do not exactly match those from standards, as the samples were not in powder form and, therefore, were not completely randomly oriented.

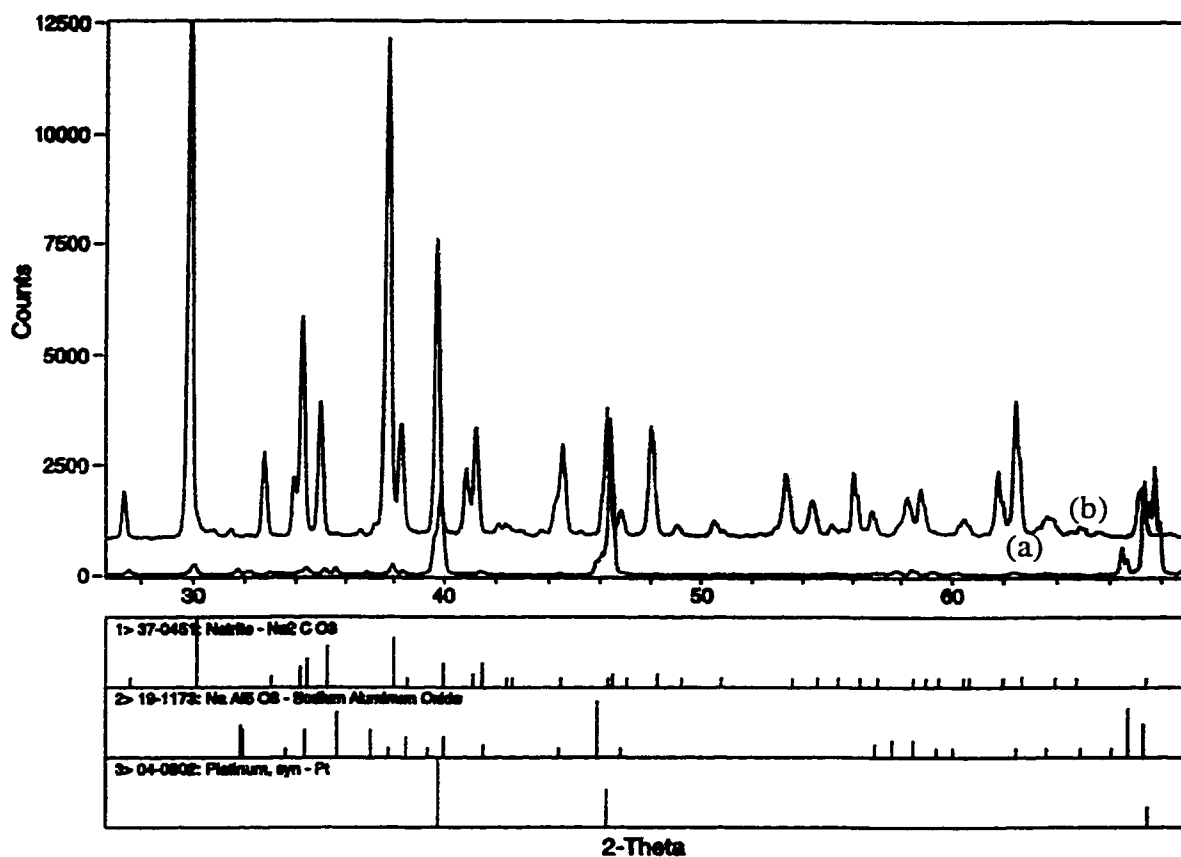


Figure 4-11. XRD spectra at the working electrode of the PEVD system; Spectrum (a) before PEVD; and spectrum (b) after PEVD.

Figure 4-12 is an SEM SE plan-view image of another PEVD sample, where the Pt thick film coverage at the sink side of the sample is not entirely continuous. After PEVD, the product (Na_2CO_3) only formed in area (A), where the Pt thick film of the working electrode is continuous and connected to the external circuit. No PEVD product formed in area (B), where the Pt thick film is discontinuous appearing as individual islands (white spots in the figure) on the $\text{Na}^+\text{-}\beta/\beta''\text{-alumina}$ substrate.

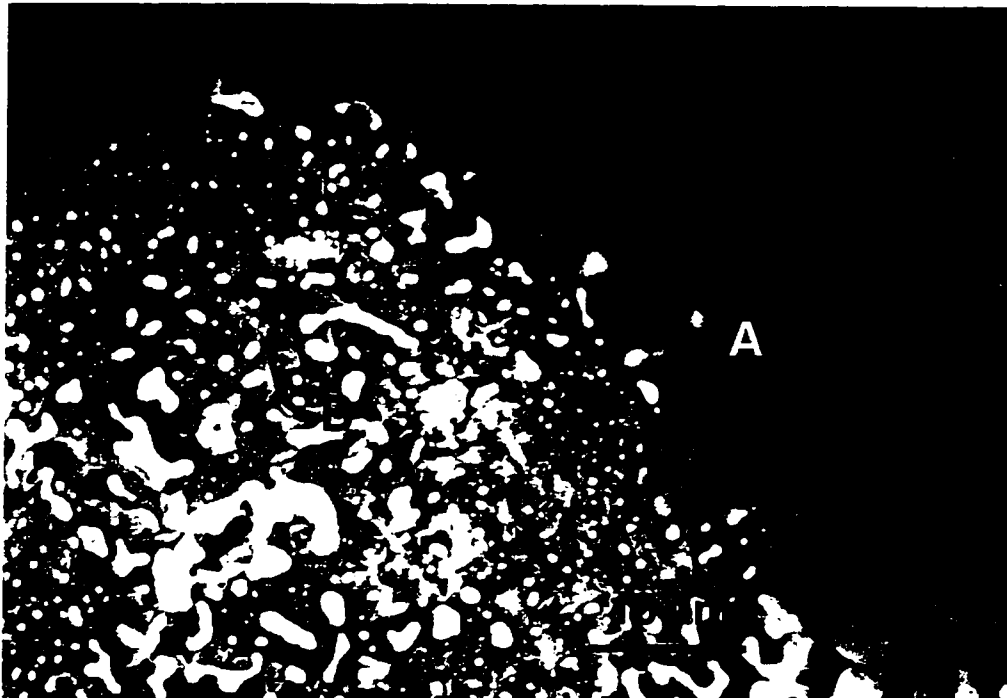


Figure 4-12. Selective deposition: (A) continuous Pt thick film area; (B) discontinuous Pt thick film area.

Figure 4-13 is an SEM SE image of the sink side of a cleaved cross section sample after PEVD. EDX analysis was done on areas (A), (B) and (C), and the resultant spectra are shown in Figure 4-14(a), (b) and (c), respectively. Area (A) is the Na^+ - β/β'' -alumina substrate; area (B) is the Pt thick film; and area (C) is the PEVD product Na_2CO_3 . Figure 4-13 indicates that Na_2CO_3 can reach the bottom of deep holes of the very irregularly shaped, porous and high aspect ratio Pt thick film substrate. The Na_2CO_3 coverage on the Pt thick film is uniform and fully dense. Since the sample was prepared by cleavage, the ductile Pt thick film structure is well preserved. Although the image gives a good three-dimensional indication of how the PEVD product deposited on the sink side of the PEVD system, the Na_2CO_3 coverage close to the cleavage plane was damaged because of the brittle nature of solid Na_2CO_3 .



Figure 4-13. Cross section SE image from a cleaved sample. Area (A) is the Na^+ - β -alumina solid electrolyte; area (B) is the Pt thick film electrode; and area (C) is the PEVD product Na_2CO_3 .

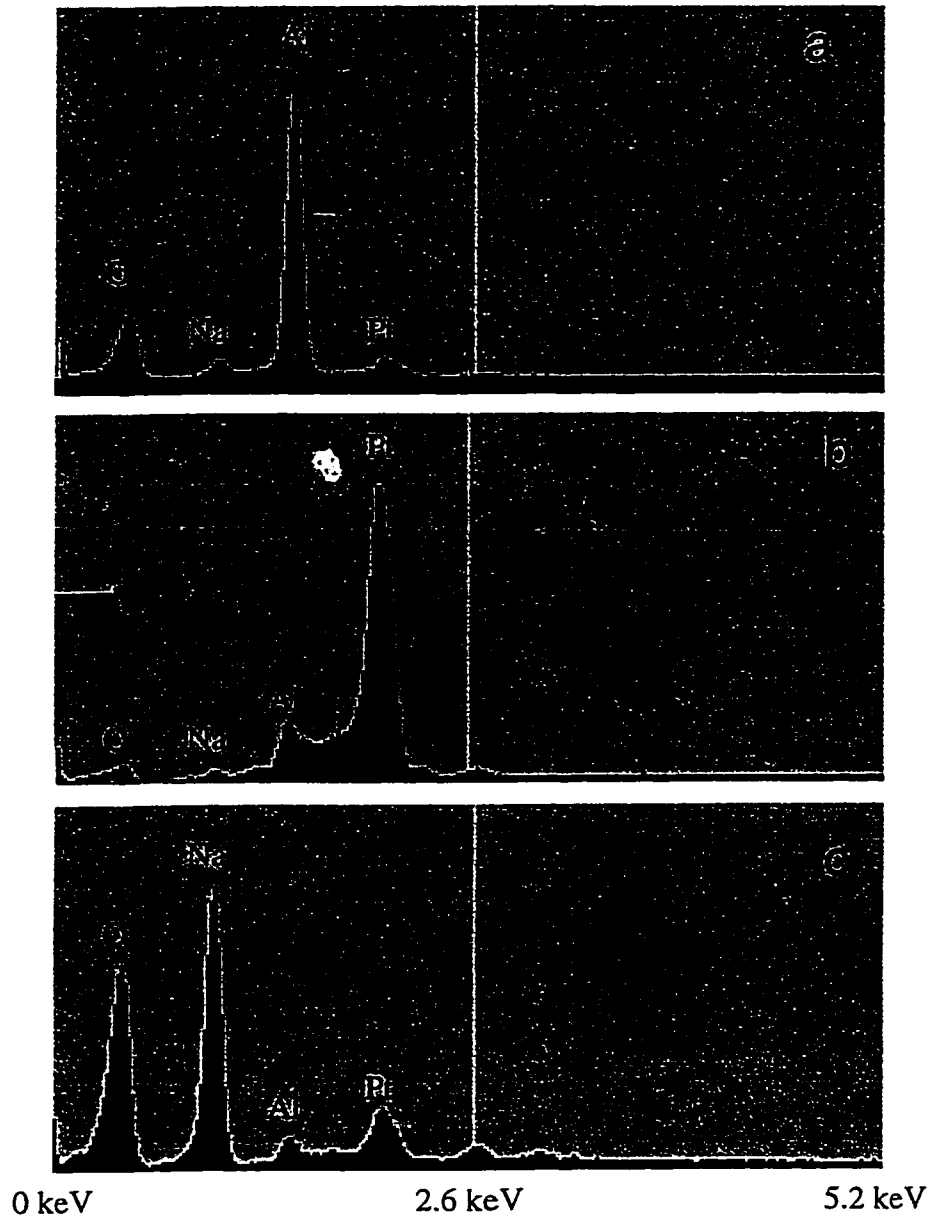


Figure 4-14. EDX spectra (a), (b) and (c) of areas (A), (B) and (C) in Figure 4-13. (Full scale intensity: 5000 cts.)

In order to reveal Na_2CO_3 coverage more precisely, polished cross-section samples were also examined in this study. A cross-section SEM SE image in Figure 4-15, as well as corresponding x-ray maps of the same area in Figure 4-16, reveal the geometric structure of the product at the sink side of the PEVD system. The high dot density

regions in the sodium element x-ray map correspond to PEVD Na_2CO_3 . The high dot density areas in the aluminum and platinum element x-ray maps show the microstructures of the Na^+ - β -alumina and the Pt coating at the cathode, respectively. It appears that the PEVD product not only intimately contacts the Na^+ - β -alumina and the Pt porous thick film, but also uniformly covers the Pt porous thick film. This is clearly revealed by a notch directly above a hole in the Pt thick film. The notch is indicated by an arrow in Fig. 4-15. More careful examination of the SEM picture in Fig. 4-15 shows that a boundary exists in the middle of the channel. It should be pointed out that the Pt area is not well preserved because of the ductile nature of the Pt thick film. Thus, small pores of the Pt thick film were destroyed during sample preparation. On the other hand, the PEVD product phase was well preserved.

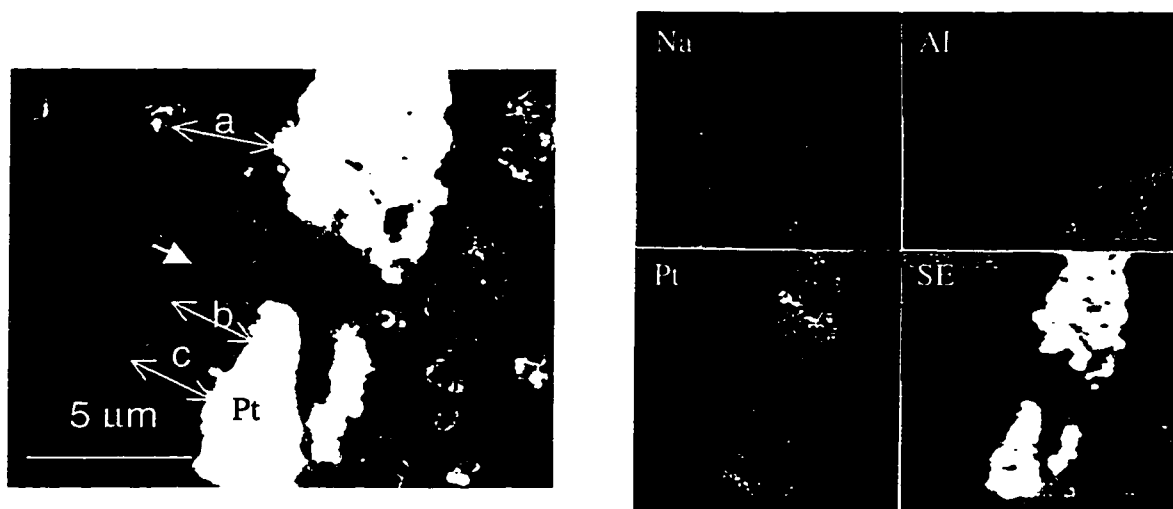


Figure 4-15. Cross section picture from a polished sample, the average thickness of Na_2CO_3 layer is about $2.5 \mu\text{m}$ according to the measurements along arrows a, b and c.

Figure 4-16. X-ray maps of the same area as shown in Figure 4-15.

4.2.3.2. Current and Flux During PEVD

For initial PEVD process studies in this section, the potentiostatic method was predominantly used in order to better control the electrochemical driving force.

According to the theoretical discussion in Chapter 3, the applied potential and current in PEVD processes should be linearly related. However, the results from this study were not consistent even for the same sample. Current varied throughout a process when the applied potential was fixed. A detailed study of PEVD current and applied potential will be presented in Chapter 6 with the help of an additional reference electrode on the source side.

In a potentiometric PEVD process, a dc potential of 2 V was applied. The resulting current, monitored over 50 hr and ranging from 52 to 205 μA (Table 4-2), is plotted as a function of time in Figure 4-17. The current was relatively stable for the first 93 min, varying from 187 to 205 μA . Then, it suddenly dropped to 56 μA within 12 min. After that, the current was again relatively stable for the remaining time.

Table 4-2. The current during a 50-hour potentiostatic PEVD process.

PEVD processing time ($\times 1000$ s)	PEVD current (μA)	PEVD processing time ($\times 1000$ s)	PEVD current (μA)
0	(194)*	6.18	69
0.6	205	6.3	56
1.2	199	7.3	54
1.8	201	10.8	54
2.4	187	14.4	52
3.0	191	18.0	53
3.6	188	36.0	51
4.2	190	54.0	52
4.8	191	72.0	56
5.4	194	90.0	55
5.58	194	108.0	55
5.7	171	126.0	52
5.82	143	144.0	54
5.94	112	162.0	53
6.06	84	180.0	52

* Estimated value.

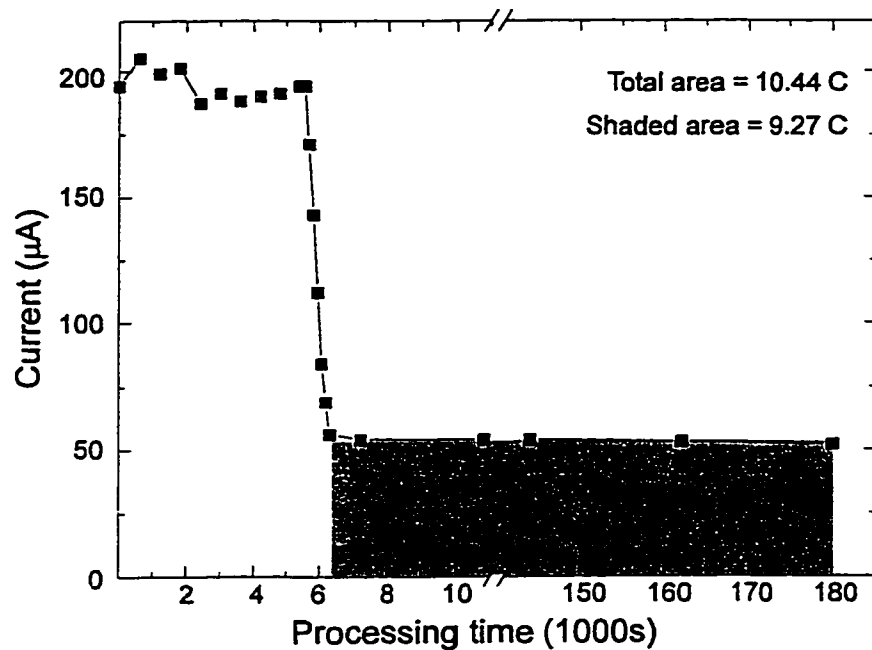


Figure 4-17. Current – time plot for a 50-hour PEVD process.

4.2.4. Discussion

4.2.4.1. Formation of Na_2CO_3 by PEVD

According to the discussion in Chapter 3, the mass and charge transport in the current PEVD process can be described as follows:

Under a negative dc applied potential, reaction (4-24) goes to the right resulting in Na_2CO_3 decomposition at the source side. Both sodium ions and electrons are given up by the source Na_2CO_3 disc at the anode of the electrochemical cell. Sodium ions travel through the solid electrolyte (Na^+ - β/β' -alumina) to the sink reaction sites at the cathode. Electrons are conducted through the external electric circuit and the porous Pt thick film to the sink reaction sites. The sink side gas components, CO_2 and O_2 , move through the pores in the porous Pt thick film to the same sink reaction sites. The PEVD reaction (4-22) proceeds to the right at the cathode. As a result, Na_2CO_3 is formed.

The potential profiles in this PEVD system are illustrated in Figure 4-18. Although there is no driving force due to a difference in the chemical potential of sodium in the

current PEVD system, the applied dc potential provides the thermodynamic driving force for the overall cell reaction (4-26). Consequently, electrical energy is transferred in this particular PEVD system to move Na_2CO_3 from the anode to the cathode of the solid electrochemical cell by two half-cell electrochemical reactions. In short, this PEVD process can be used to deposit Na_2CO_3 at the working electrode of a potentiometric CO_2 sensor.

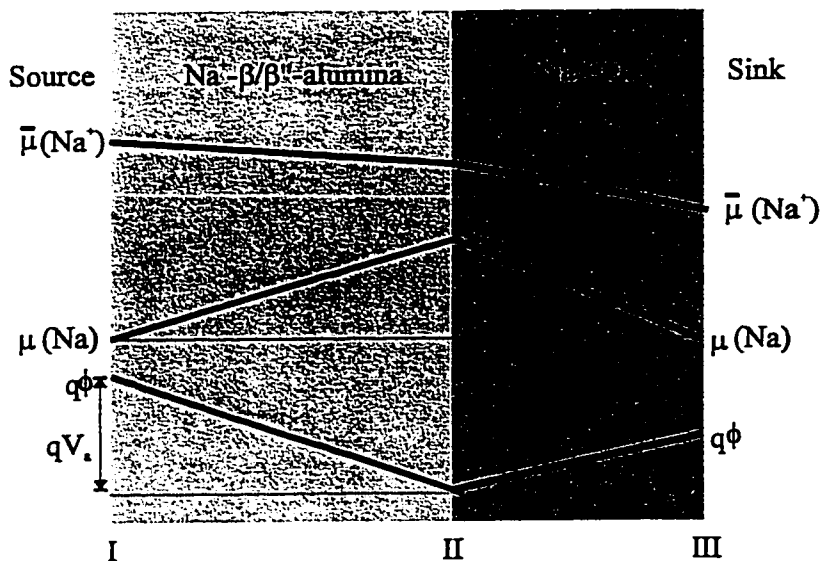


Figure 4-18. Potential profiles in the PEVD system.

4.2.4.2. Selective Deposition in PEVD

Selective deposition in PEVD is clearly indicated in Figure 4-13. As discussed previously in Chapter 3, this is because of the unique feature of the electrochemical reaction for deposition. As schematically shown in Figure 4-19, the only area to meet the requirement for nucleation is the three phase boundary (point O) of Na^+ - β/β'' -alumina, Pt and gaseous phase, where Na^+ , e^- and gaseous phase reactants ($\text{CO}_2 + \text{O}_2$) are all available. Thus, any PEVD product Na_2CO_3 formed at the sink must be in intimate contact with both the solid electrolyte and electrode in the PEVD system to have both the ionic and electronic paths connected, respectively. In other words, the Na_2CO_3 auxiliary phase formed by PEVD must contact both the solid electrolyte and the Pt working electrode of

a potentiometric CO₂ sensor. This feature makes the PEVD auxiliary phase fit geometric criteria (2) and (4) discussed in Section 4.1. Furthermore, the selective deposition in PEVD indicates that the reaction for product deposition is surface dependent. On the other hand, in order to obtain uniform deposit coverage on the working electrode, the porous metallic electrode must be uniform and continuous.

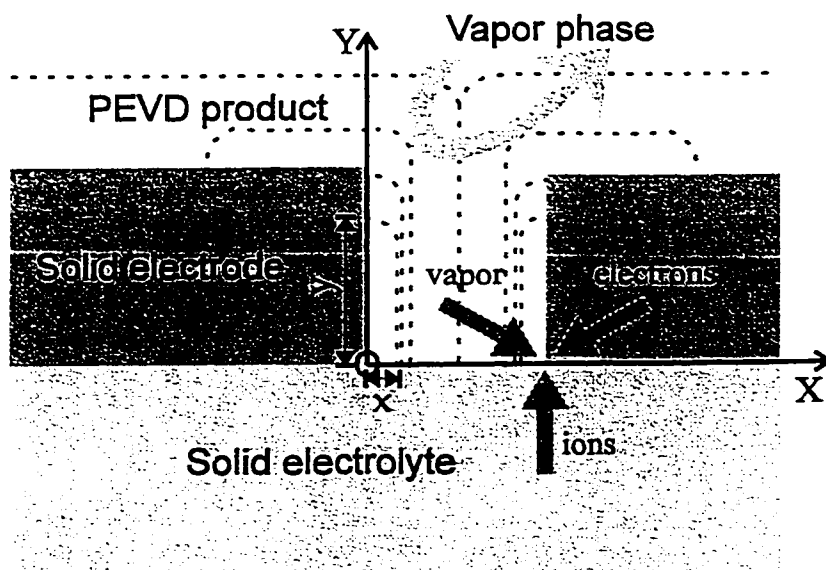


Figure 4-19. The nucleation and growth of Na₂CO₃ at the working electrode of a type III potentiometric sensor.

4.2.4.3. PEVD Product Phase Growth Behavior

After nucleation, PEVD product crystals can grow along two directions, X and Y , from point O . (In order to simplify the discussion, two dimensions instead of three will be used to discuss PEVD product phase growth at a cathode.)

The X direction is along the surface of the solid electrolyte Na⁺-β/β"-alumina, where Na⁺ and the gaseous phase have easy access, but e⁻ have to diffuse through the PEVD product phase Na₂CO₃ to the reaction zone front.

The Y direction is along the surface of the Pt metallic electrode, where e^- and gaseous phase have easy access, but Na^+ has to diffuse through the PEVD product phase Na_2CO_3 to the reaction zone front.

According to Chapter 3, if the cathodic reaction along the X direction is limited by electron migration through the product Na_2CO_3 , the growth distance x at time t along the ionically shorted surface would be expressed by

$$x = (V_{Na_2CO_3} \sigma_e \Delta G t / F^2)^{1/2} \quad (4-28)$$

where σ_e is the average electronic conductivity of the Na_2CO_3 phase, ΔG is the Gibbs free energy of reaction (4-22), and $V_{Na_2CO_3}$ is the molar volume of Na_2CO_3 .

If the cathode reaction in direction Y is limited by sodium ion migration through the product Na_2CO_3 , the growth distance y at time t along the electronically shorted surface would be expressed by

$$y = (4/\pi) (V_{NaNO_3} \sigma_{Na^+} \Delta G t / F^2)^{1/2} \quad (4-29)$$

The ratio of y to x is related to the conductivities of the sodium ions and electrons in the Na_2CO_3 phase (Ilshner-Gensch and Wagner, 1958).

$$\frac{y}{x} = \frac{1.265 \sqrt{\sigma_{Na^+}}}{\sqrt{\sigma_e}} \approx \frac{1.265}{\sqrt{t_e}} \quad (4-30)$$

Since Na_2CO_3 is a predominantly ionic conductor with a much higher ionic conductivity than electronic conductivity, the PEVD product Na_2CO_3 prefers to grow a thin layer along the Y direction, and wrap the entire Pt working electrode surface first. After the whole working electrode is covered, the Na_2CO_3 phase can only grow along the X direction to increase the thickness of the Na_2CO_3 auxiliary phase. According to the discussion in Chapter 3, the coverage should be uniform because of a self-leveling effect

during the solid-state transport of sodium across the PEVD product for further growth. This is clearly indicated by both cross-section images in Figures 4-13 and 4-15.

Inside a pore of a Pt thick film, the thickness of the PEVD product will increase and eventually fill the pore as schematically illustrated by Figure 4-19, where the dotted lines indicate several consecutive PEVD processing steps. Accordingly, Na_2CO_3 grains from both side walls of a pore should meet at the middle of the pore, and leave a grain boundary in the middle of a pore and a notch on the top of a pore. Microstructural evidence of this growth model was captured in Figure 4-15, where a grain boundary exists in the middle of a pore and a notch exists on top of the pore (indicated by an arrow). A uniform increase in thickness will eventually reduce the high aspect ratio of the porous working electrode surface as schematically shown in Figure 4-19.

4.2.4.4. PEVD Current

The current in a PEVD process reveals the kinetics of the PEVD cathode reactions, which in turn indicates the PEVD product growth behavior. Since the electronic transference number in Na^+ - β/β'' -alumina is less than 10^{-6} and can be ignored under the current experimental conditions, it is reasonable to assume that the only current passing through the internal circuit of the PEVD system is the sodium ionic current. On the other hand, ionic current cannot flow in the external electrical circuit. All the Na^+ ionic current must be drained away by the gas electrode reactions, and the reaction rate, $v(t)$, can be expressed as

$$v(t) = \frac{1}{2V_{\text{Na}_2\text{CO}_3}} \frac{dn_{\text{Na}^+}}{dt} \quad (4-31)$$

where n_{Na^+} is the number of mols of sodium ions at the cathode. Also, from Faraday's law,

$$I = \frac{dQ}{dt} = \frac{z_{Na^+} F dn_{Na^+}}{dt} \quad (4-32)$$

Combining Eq.(4-31) and (4-32) yields

$$v(t) = \frac{I}{2V_{Na_2CO_3} z_{Na^+} F} \quad (4-33)$$

Thus, the cathode reaction rate is proportional to the ionic current. Kinetic information about the gas electrode reactions can then be obtained by monitoring the current during a PEVD process.

For instance, the PEVD current-processing time curve in Figure 4-17 offers an easy way to control the thickness of the product layer. According to the mechanism for PEVD product growth, the reaction rate will decrease dramatically after the PEVD product covers the entire Pt surface. This corresponds to a sudden drop in the current as shown in Figure 4-17. In order to deposit the thinnest possible film, this dramatic current decrease denotes the end point of a PEVD process. According to Eq.(3-37), the mass of Na_2CO_3 formed during the PEVD process can be obtained by integrating the current over the processing time. From the total area below the I-t curve in Figure 4-17, a total of 10.44 C of Na^+ ions was transported through the PEVD system. Thus, about 5.7 mg of the Na_2CO_3 auxiliary phase formed in this PEVD process. The second stage of growth started after 105 min of deposition. If the coverage on the top of the Pt thick film is assumed to be zero, the amount of the product deposited on the top of the working electrode can be estimated by integrating the shaded area of Figure 4-17. Accordingly, the PEVD flux during this period of deposition was 9.27 C, which is equivalent to 5.1 mg of Na_2CO_3 . The PEVD product is uniform and fully dense on the top of working electrode. Since the density of Na_2CO_3 is 2.5 g/cm^3 and the surface area is 200 mm^2 , the thickness of the PEVD auxiliary phase on the top of the Pt thick film can be calculated at $10.2 \text{ }\mu\text{m}$. As shown in Figure 4-15, three measurements of the thickness of the Na_2CO_3 coverage on the top of Pt thick film were taken as indicated by line (a), (b) and (c). The average thickness is $2.5 \text{ }\mu\text{m}$. Thus, most of the second stage growth involves filling the

pores of Pt thick film. The effective growth area is about four times larger than the Pt thick film screen-printing area.

4.2.4.5. PEVD Auxiliary Phases

The geometric structure of an auxiliary phase deposited by the PEVD technique is very similar to the previously discussed ideal auxiliary phase illustrated in Figure 4-4 (a). Table 4-3 compares the geometric properties of PEVD auxiliary phases with other reported techniques using the six proposed criteria.

Table 4-3. Geometric properties of auxiliary phases deposited by various techniques.

Geometric criteria	PEVD	melting -quenching	in-situ	disc
contact to electrode	good	good	good	poor
contact to electrolyte	good	poor	good	poor
thickness control	good	poor	poor	poor
aspect ratio	low	low	high	high
coverage on electrode	good	fair	poor	poor
coverage on electrolyte	good	poor	poor	poor

The advantages of applying the PEVD process to deposit auxiliary phases are not only based on the mechanism of PEVD product crystal growth, but also arise from close control over the entire process achieved by adjusting the applied dc electric potential and monitoring current. Thus, the superiority of PEVD is obvious since the Na_2CO_3 auxiliary phase can be deposited in a well-controlled manner at the working electrode to meet all six geometric criteria. Furthermore, the success in realizing the geometric requirement of Na_2CO_3 auxiliary phases for potentiometric CO_2 sensors in our lab encouraged us to further apply PEVD to deposit the auxiliary phases NaNO_3 and Na_2SO_4 for NO_2 and SO_2 potentiometric sensors, respectively. The results are similar to those reported in this chapter. Thus, PEVD is the best technique to form auxiliary phases for gaseous oxide sensors.

Improvement of the geometric structures of the auxiliary phases using the PEVD technique will benefit the performance of gaseous oxide sensors in many ways, e.g., increasing selectivity and stability, shortening response time, and decreasing the influence of gas flow rate (Tang et al, 1996b).

4.3. Sensor Response Behavior Testing

Early in this chapter, the geometric requirements of the auxiliary phase at the working electrode of type III potentiometric sensors were studied and six geometric criteria were proposed (Tang et al., 1998). In the last section, study has shown that PEVD is the best technique to realize these criteria. Improvement of the geometric structure of the working electrode by a well-controlled PEVD process benefits the performance of a CO₂ sensor in many ways. However, in the kinetic model and criteria proposed in Section 4.1, two conflicting requirements exist when attempts are made to improve the kinetic response of type III potentiometric sensors. One of these is that the auxiliary phase thickness should be minimized; the other is that the aspect ratio of the porous working electrode should be minimized.

To optimize kinetic behavior, the response and recovery times of CO₂ potentiometric sensors were studied at various auxiliary phase coverages. This was realized by a unique experimental arrangement to deposit the Na₂CO₃ auxiliary phase in-situ at the working electrode of type III potentiometric CO₂ sensors by PEVD in a step-wise fashion. Since the current and flux of solid state transport material in a series of PEVD processes can be easily monitored to control the amount of deposit formed after each step of PEVD according to Eq. (3-37), the response behavior of the sensors after each PEVD auxiliary phase step increase can be characterized.

4.3.1. Experimental Procedure

As illustrated in Figure 4-20, the experiments in this study included three aspects:

- (a) Na_2CO_3 auxiliary phase deposition at the working electrodes of type III potentiometric CO_2 sensors by PEVD;
- (b) sensor response behavior testing;
- (c) microanalysis of the working electrode of the sensor.

According to previous discussion, the amount of the Na_2CO_3 auxiliary phase deposited at the working electrode of a CO_2 potentiometric sensor can be recorded precisely during well-controlled PEVD processes. In this study, the amount of auxiliary phase at the working electrode of the sensors was increased in a step-wise fashion. After each step of the auxiliary phase deposition process, the sensor's response behavior was studied under open circuit conditions. Before moving forward to the next PEVD processing step, microstructural analysis of the covered working electrodes was performed with the SEM. Finally, results from 14 steps revealed the relationship between the response behavior of the sensor and the corresponding geometric structure of the auxiliary phases at the working electrodes of type III potentiometric CO_2 sensors.

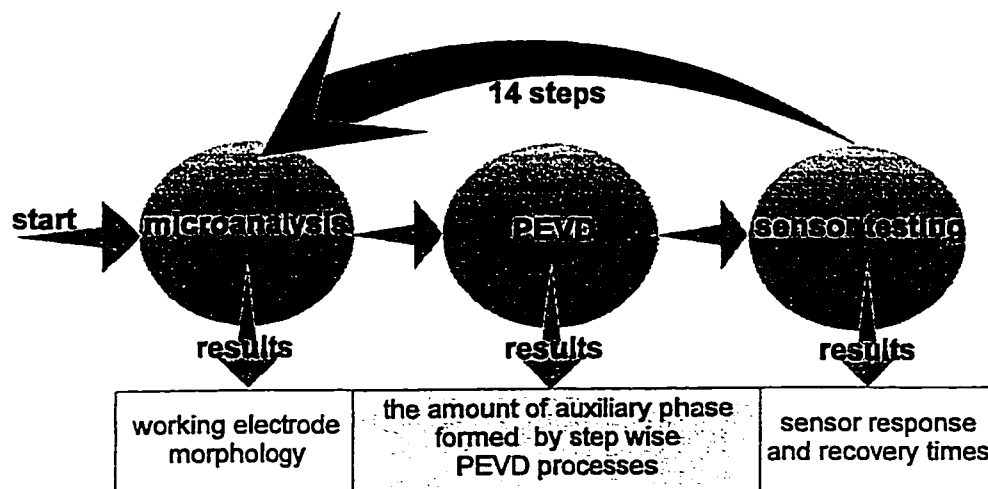


Figure 4-20. PEVD auxiliary phase deposition and sensor testing procedure.

The sample system used in this investigation is similar to the one described previously. It consists of a solid electrochemical cell which has two functions, i.e., a closed circuit electrolytic cell (4-25) for the PEVD process and an open circuit galvanic cell (4-7) for sensor testing. Thus, the sink and source side of a PEVD system also act as

the working and reference electrodes of a sensor. Figure 4-21(a) schematically shows the sample system in a gas-tight sample holder. The components in this sample system were almost the same as the ones in Figure 4-7. However, gas seals were required to separate the reference electrode from the working electrode of the sensors in this investigation. Therefore, two Pt or Au rings were inserted at the source and sink side of the sample holder (Figure 4-7) to ensure a gas-tight metallic seal between both sides of the solid electrochemical cell.

The sample holder was then put into a joint PEVD/sensor testing facility, as shown schematically in Figure 4-21(b). The temperature during both PEVD processing and sensor testing was set at 500°C. Atmospheric pressure was maintained throughout the experiment at both chambers. In order to check the consistency of the results, the study was repeated on two sample systems.

During PEVD, a high gas flow rate ($\gg 100$ sccm) of type 1 gas, dry air with 293 ppm CO₂ (Praxair), was used at both the source and sink sides. In order to control the PEVD reaction rate, a galvanostatic method was used during the PEVD processes. The external electric circuit during PEVD processing is schematically shown in Figure 4-21(b). A constant dc current of 100 μ A was supplied by a steady dc source (Brunelle Instrument, Inc.) The resulting potential was monitored by an electrometer (Keithley 616).

After each step of auxiliary phase deposition, the PEVD process was stopped for sensor response behavior testing by opening Gate A (Figure 4-21(b)). Under the open circuit condition, the EMF of the sensor was indicated by the electrometer. A high flow rate at both sides remained until the equilibrium EMF value of the sensor, zero in this case, was reached.

During sensor response testing, the flow rate was initially reduced on both sides by mass flowmeters with needle valves (Matheson). Then, the gas at the working electrode was changed to a gas mixture of type 1 and type 2 (CO₂-free dry air, (Praxair)), mixed at a ratio of 1:9 by a gas mixer (Matheson 7371, with rotometer 600 and 601). Thus, the virtual CO₂ partial pressure decreased by an order of magnitude at the working electrode while the oxygen partial pressure remained the same at both sides. After the equilibrium EMF value of the sensor was reached, the gas at the working electrode was then changed back to type 1 gas. The EMF response of the sensors during CO₂ partial pressure change

at the working electrodes was monitored and recorded by the electrometer connected to an analog recorder (Brinkmann 2742-3).

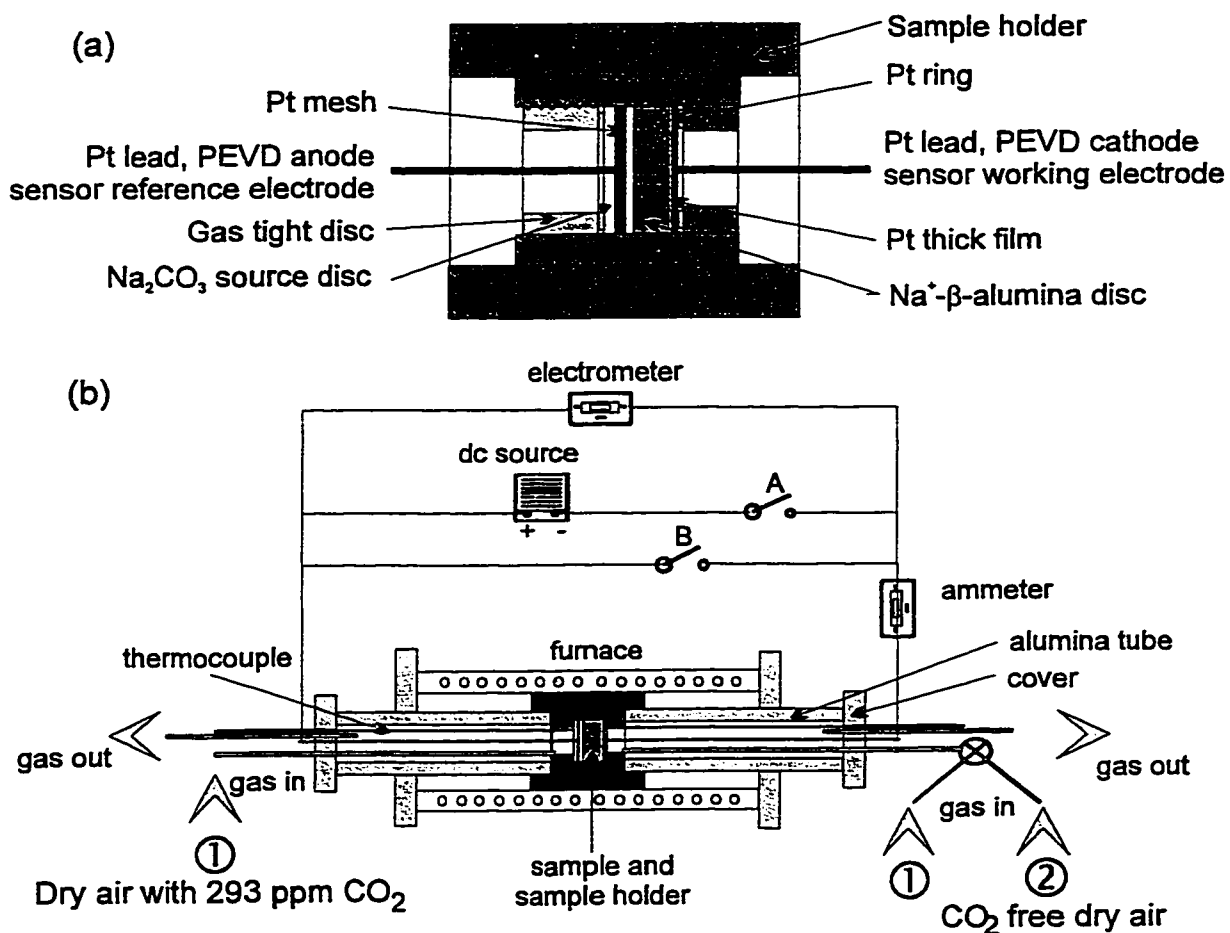


Figure 4-21. Schematic of (a) sample holder; (b) a joint PEVD and sensor testing facility.

In order to reveal the influence of gas flow rate to the response behavior of the sensors, the response behavior has also been tested at two gas flow rates (40 or 80 sccm) at the working electrode side.

Before moving forward to the next round of auxiliary phase deposition and subsequent sensor response testing, the sample was taken out of the experimental apparatus for microanalysis to check auxiliary phase coverage. At the end of the experiment, cross-section samples were prepared by cleaving the sample to evaluate the thickness of the Na₂CO₃ product phase covering the working electrode of the sensors.

4.3.2. Results

4.3.2.1. PEVD Auxiliary Phase Step Coverage at the Working Electrode

Two identical samples (#1 and #2) were tested in this investigation. At a constant current of 100 μA , the resulting dc potential for both samples fell in the range of 0.5 to 5 V during the entire PEVD process. According to Eq. (4-33), the flux of Na^+ , in coulombs, through the PEVD system can be calculated. Consequently, the amount of product formed at the sink side (working electrode) could be obtained. The processing time and flux for both samples are reported in Table 4-4.

Table 4-4. PEVD processing time at each step for both samples at the same gas flow rate.

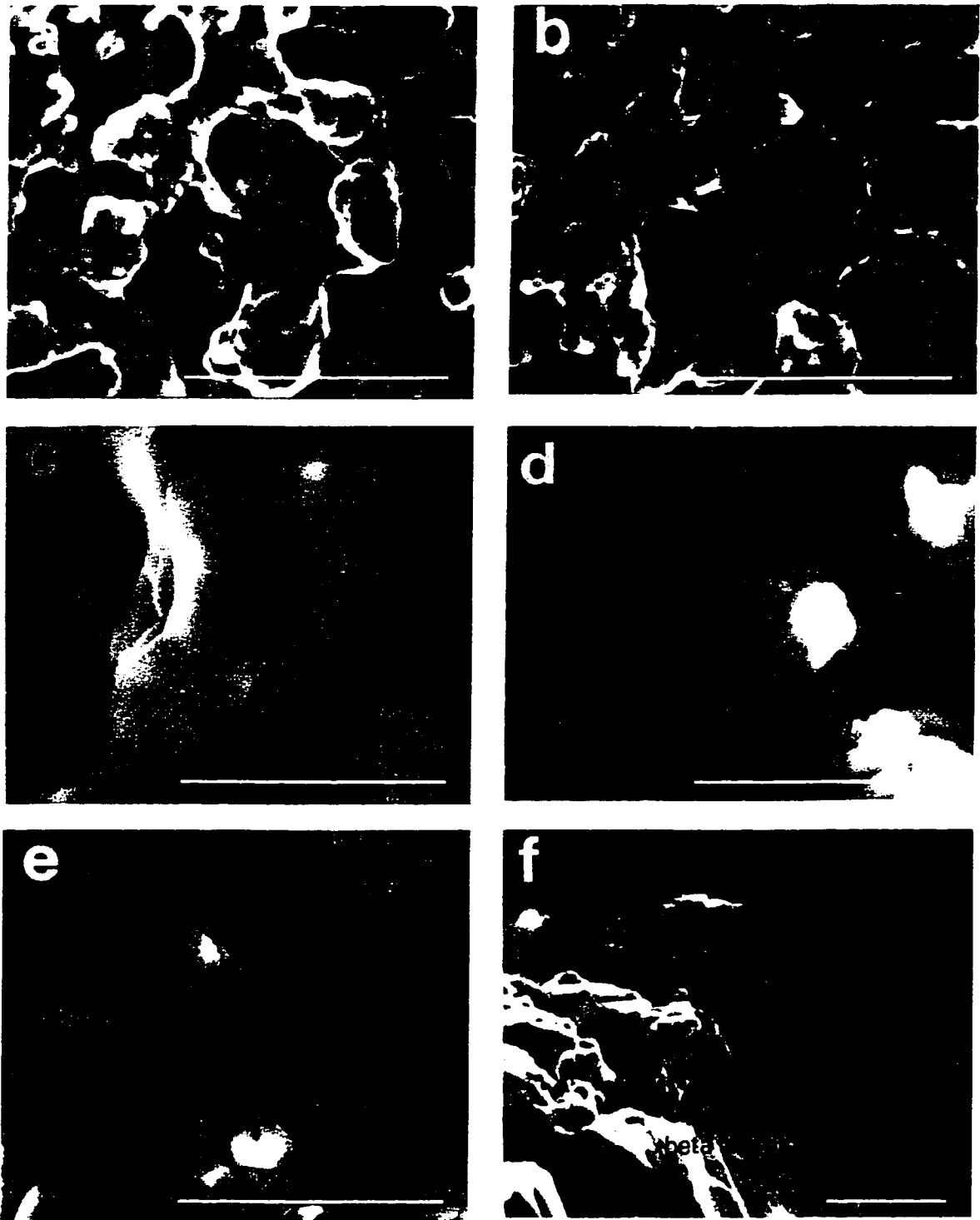
Step	Sample #1			Sample #2	
	Processing time (min)	PEVD flux (C)	Micro-analysis	Processing time (min)	PEVD flux (C)
0	0	0	a	0	0
1	78	0.468	b	66	0.396
2	91	0.546		76	0.456
3	127	0.762		106	0.636
4	157	0.942	c	142	0.852
5	193	1.158		180	1.080
6	235	1.410		213	1.278
7	274	1.644		254	1.524
8	310	1.860	d	296	1.776
9	346	2.076		329	1.974
10	383	2.298		365	2.190
11	428	2.568		408	2.448
12	467	2.802		452	2.712
13	512	3.072		485	2.910
14	540	3.240	e, f	530	3.180

Figures 4-22(a)-(e) show SEM SE plan-view images of the first sample at five selected PEVD steps, indicated by (a) - (e) in Table 4-4. The auxiliary phase coverage at the working electrode of the sensor increased with PEVD processing time and PEVD flux from (a) to (e). After 14 steps of auxiliary phase deposition and sensor response testing, the final thickness of the product was about 3 μm , which was estimated from an SEM SE image of a cleaved cross-section sample (Figure 4-22(f)).

4.3.2.2. Sensor Response

According to the Nernst equation (Eq. (4-6)), the theoretical equilibrium EMF value of the sensor should be 76.7 mV at 500°C after the CO_2 partial pressure decreased by an order of magnitude at the working electrode. In this experiment, the emf value was slightly lower than the theoretical calculated value at about 76 mV.

The general response of the sensor after changing the CO_2 partial pressure at the working electrode is shown in Figure 4-23, which is the response curve obtained after 7 steps of auxiliary phase deposition for the first sample. When the CO_2 partial pressure decreases at the working electrode, the emf of the cell increases dramatically at first and then slowly reaches an equilibrium value of 76 mV. The time to reach the equilibrium value is the recovery time of the sensor. The same is true when the partial pressure increases at the working electrode of the sensor, and the time to reach the equilibrium value is the response time of the sensor. In practice, researchers commonly use the time for 90% attainment of the theoretical emf value change as the response and recovery time (Fouletier et al., 1974). This convention will be used in the current investigation.



Figures 4-22 (a-f). SEM SE images of the working electrode: (a) before PEVD; (b) first stable EMF response; (c) when the response time of the sensor just passed the minimum point; (d) when the recovery time of the sensor just passed the minimum point; (e) final auxiliary phase coverage (plan view); (f) final auxiliary phase coverage (cross-section). (Bars = 5 μm)

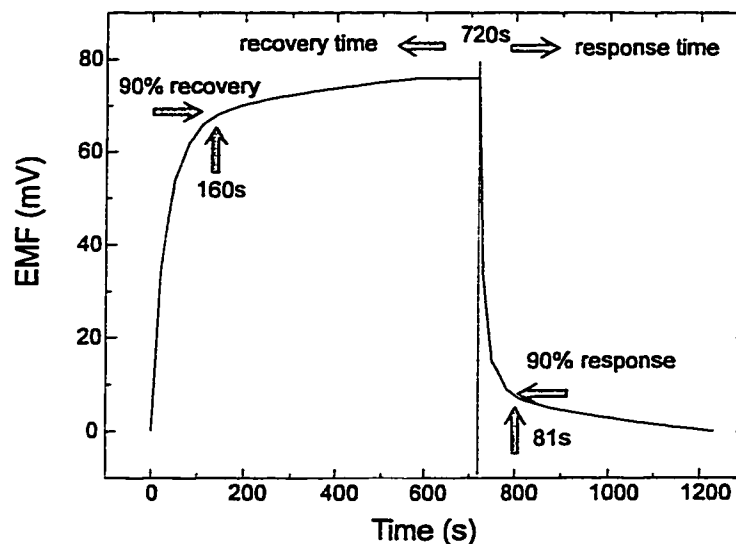


Figure 4-23. A typical EMF response curve for a type III CO₂ potentiometric sensor.

For sample #1, a stable EMF response from the sensor was obtained after passing about 0.468 C of Na ions. According to the previous discussion, this corresponds to the point where the PEVD auxiliary phase just covers the entire Pt thick film surface. The response times and recovery times of the sensor after each PEVD process step are recorded in Table 4-5. Accordingly, both response and recovery times are plotted against the Na ion flux through the solid electrolyte during the PEVD process in Figure 4-24. Curve (1) is the response time and curve (2) is the recovery time.

Table 4-5. The response and recovery times for sample #1 with increasing PEVD auxiliary phase coverage at the working electrode.

Step	Flux (C)	Response time (s)	Recovery time (s)
1	0.468	1240	4970
2	0.546	370	4630
3	0.762	35	3410
4	0.942	37	2180

5	1.158	51	740
6	1.410	69	310
7	1.644	81	160
8	1.860	104	180
9	2.076	152	330
10	2.298	220	420
11	2.568	270	560
12	2.802	360	790
13	3.072	420	1210
14	3.240	630	1810

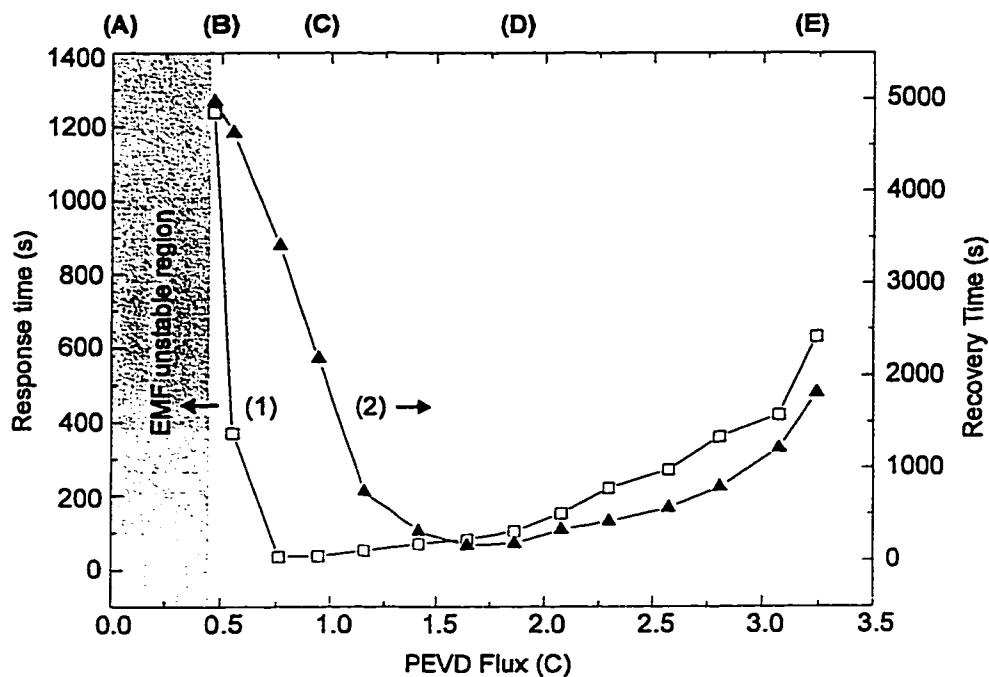


Figure 4-24. The response (curve 1) and recovery (curve 2) behavior of the type III potentiometric CO₂ sensor (sample #1) with increasing PEVD auxiliary phase at the working electrode.

In sample #2, the sensor response was also tested at various flow rates at the working electrode. The results are presented in Table 4-6. The response time and recovery time

of the sensor at both flow rates are plotted in Figures 4-25 (a) and (b), respectively. Accordingly, the effects of flow rate on response and recovery times at the working electrode were evaluated in Figures 4-25 (a) and (b). After doubling the flow rate to 80 sccm, the data in curve (B) show a dramatic decrease (improvement) in response time for a small auxiliary phase thickness, and the response time does not change very much after reaching the minimum response time. The same is true for the recovery times.

Table 4-6. The response and recovery times for sample #2 with increasing PEVD auxiliary phase coverage at the working electrode.

Step	PEVD flux (C)	Flow rate 40 sccm		Flow rate 80 sccm	
		Response time (s)	Recovery time (s)	Response time (s)	Recovery time (s)
1	0.396	970	5010	340	1170
2	0.456	290	3910	112	1020
3	0.636	98	2840	53	970
4	0.852	19	1530	11	630
5	1.080	26	620	19	310
6	1.278	44	350	42	170
7	1.524	68	190	37	172
8	1.776	90	240	59	139
9	1.974	112	380	107	165
10	2.190	190	520	142	330
11	2.448	270	660	230	460
12	2.712	380	860	310	710
13	2.910	450	1400	390	1320
14	3.180	610	1840	510	1810

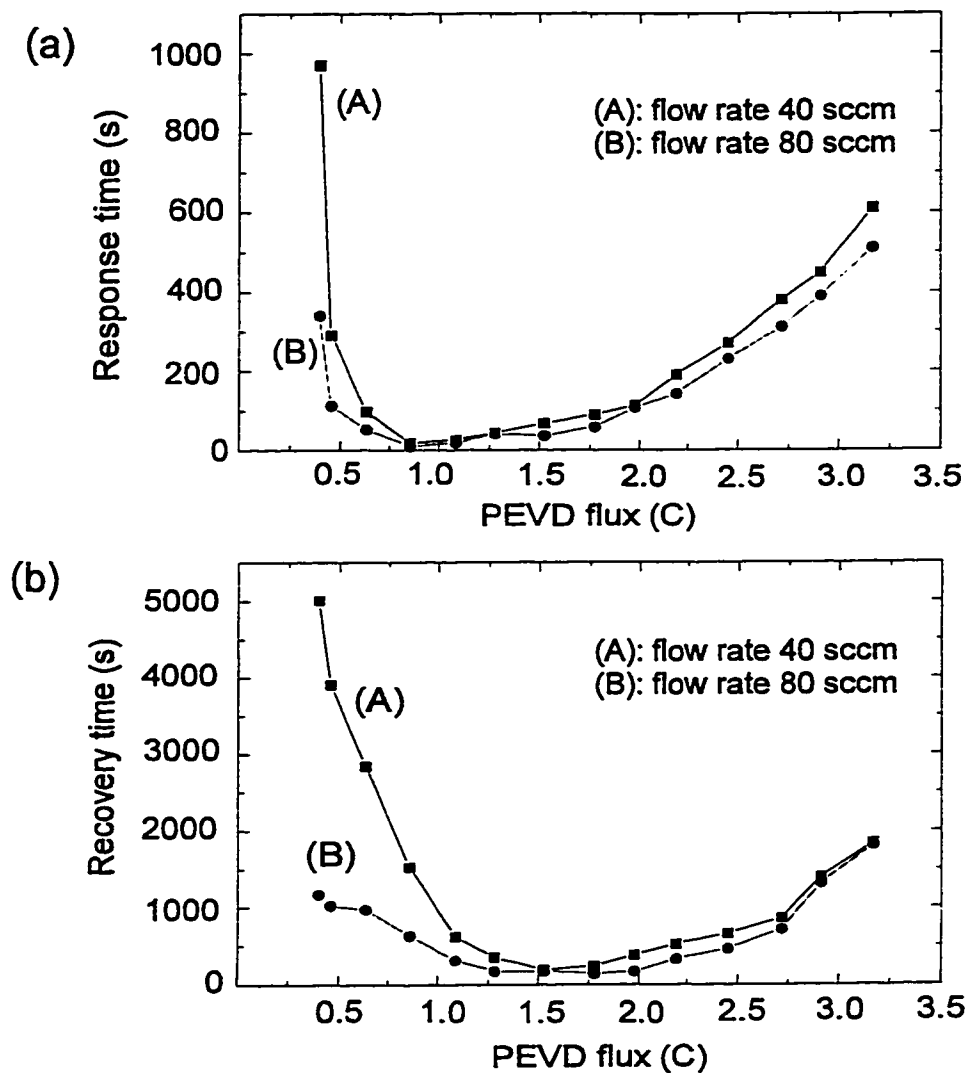


Figure 4-25. The response time (a) and recovery time (b) of sample #2 at various gas flow rates (curve (A) at 40 sccm and curve (B) at 80 sccm).

4.3.3. Discussion

The response and recovery times of both samples at each PEVD step are compared at a working electrode flow rate of 40 sccm in Figure 4-26 (a) and (b), respectively. Because of the inability to fabricate a consistent Pt thick film at the working electrode of both sensors, the response and recovery curves do not exactly match. However, the curves from both samples follow the same trends. Taking into account the geometric

factor for both samples, the results from this study can be considered to be fairly consistent.

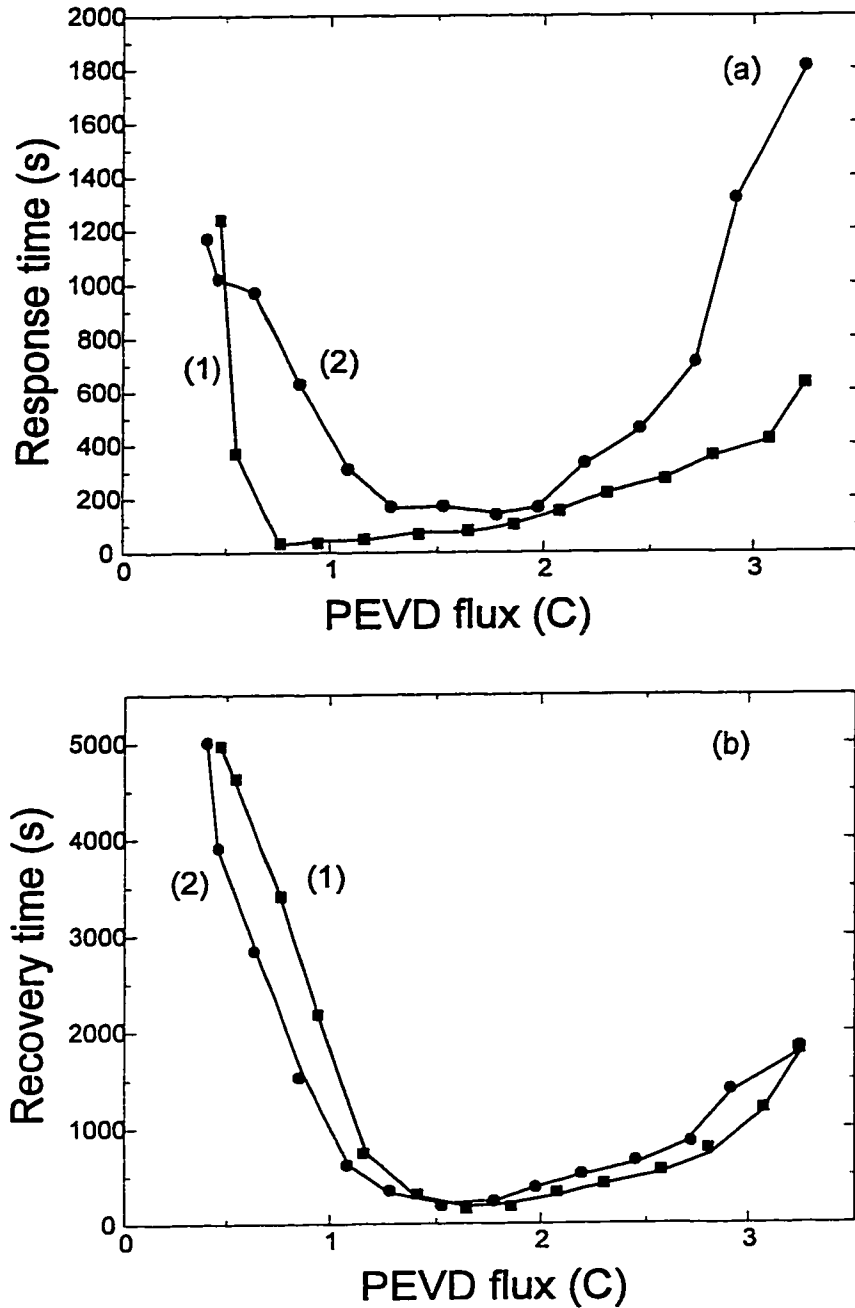


Figure 4-26. Comparison of the response time (a) and recovery time (b) for the two sensors at the same working electrode flow rate of 40 sccm.

The sensor response and recovery behavior for various auxiliary phase coverages at the working electrode of a type III potentiometric sensor are revealed for the first time through a combination of Figure 4-24 and Figures 4-22(a)-(e). Furthermore, according to the discussion in a previous section, the increase in PEVD auxiliary phase thickness is uniform, and linearly related to the PEVD flux throughout the process. With the help of the cross-section SEM image in Figure 4-22(f), the horizontal scale in Figure 4-24 can be converted to the thickness of the auxiliary phase on top of the Pt porous thick film at the working electrode. By taking the final thickness as 3 μm when the PEVD flux reaches 3.24 C after step 14, and an initial thickness of zero when the PEVD flux is 0.468 C at step 1, the sensor response behavior at various auxiliary phase thicknesses is plotted in Figure 4-27.

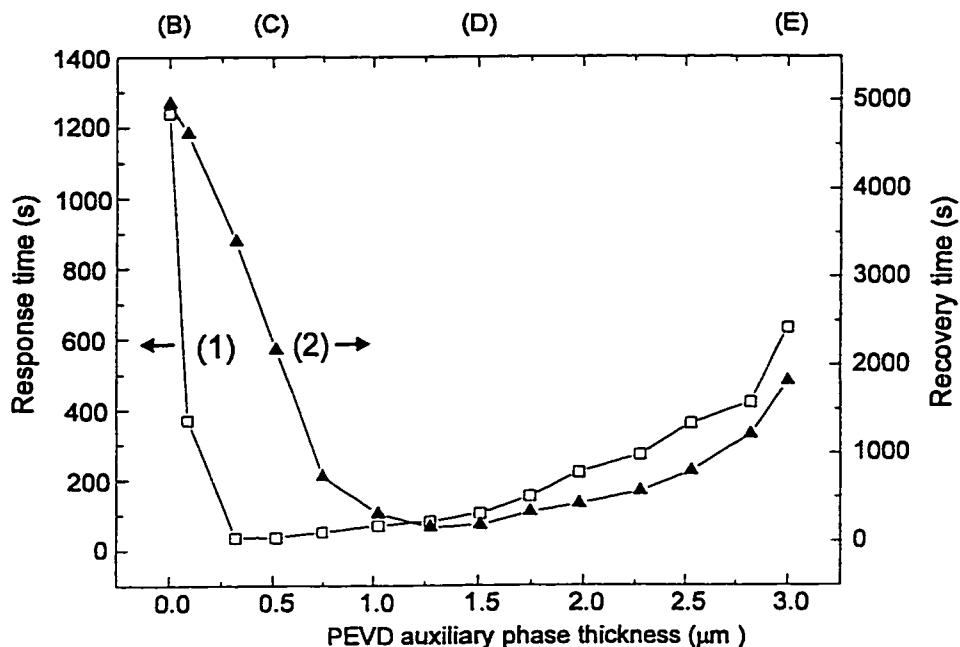


Figure 4-27. Response and recovery times vs. the thickness of the auxiliary phase.

Both the response and recovery times first drop dramatically with increasing auxiliary phase thickness, reach a minimum point, and then increase steadily with increasing auxiliary phase thickness. The minimum response time is 35 s when the auxiliary phase thickness is about 0.3 to 0.5 μm . The minimum recovery time is 160 s corresponding to

an auxiliary phase thickness of about 1.2 to 1.5 μm . Since most of the pores in the Pt thick film are under 3 μm in size and are filled with the auxiliary phase at this time, the aspect ratio of the working electrode of the sensor is very low [Figure 4-22(d)] when the recovery time of the sensor reaches its minimum value.

The results indicate that sensor response behavior is not only related to the thickness of the auxiliary phase, but is also controlled by other working electrode geometric factors - most likely the aspect ratio of the working electrode surface. Because of the high aspect ratio, the response and recovery times of the sensor are limited by surface adsorption, desorption and gas phase diffusion at small PEVD auxiliary phase thicknesses (Akila and Jacob, 1989). Recovery time, which corresponds to a desorption process, at the working electrode, is affected more by the aspect ratio than the response time, which corresponds to an adsorption process. Accordingly, in order to make a potentiometric sensor with a fast response, the best geometric structure for the working electrode is one which has a low aspect ratio and is covered with as thin a layer of auxiliary phase as possible. For Pt thick film metallic electrodes, this thickness is about 1 to 1.5 μm depending on the average pore size and thickness of the Pt electrode itself.

In conclusion, because of PEVD's ability to control the deposition process and its unique product phase growth behavior, it is possible to prepare, by means of PEVD, a working electrode with the best geometric structure. The response behavior of a potentiometric sensor depends on the thickness of the auxiliary phase and the aspect ratio of the working electrode surface. In an optimized condition, a potentiometric CO_2 sensor can be obtained with a response time of less than 1 min and a recovery time of less than 3 min, for a CO_2 partial pressure at the working electrode varying from 30 to 300 ppm at 500°C. This is about 10 times lower than the previously reported value under the same sensing conditions (Miura et al., 1992a, 1993; Chu et al., 1992; Veonhard et al.1993).

This investigation not only confirms the reaction mechanism proposed in Section 4.1, but also demonstrates the ability of PEVD to control auxiliary phase thickness and the aspect ratio of the working electrode of a sensor.

4.4. Conclusions

In this chapter, the development of type III potentiometric gaseous oxide sensors was reviewed, and a gas electrode reaction model was proposed. It was found that the geometric structure of auxiliary phases at working electrodes is very important to the practical performance of gaseous oxide sensors. In order to deposit an auxiliary phase at a porous working electrode to meet all six geometric criteria, the newly developed PEVD technique was applied. The results of this study show that the advantages of applying the PEVD process for auxiliary phase deposition are not only based on the unique PEVD product growth behavior to meet all six geometric criteria, but also arise from close electrochemical control over the process. Furthermore, the superiority of a type III potentiometric CO₂ sensor with a PEVD auxiliary phase during the transition when the CO₂ partial pressure changes at the working electrode, has been demonstrated in this chapter.

Chapter 5. Applying Polarized Electrochemical Vapor Deposition to Composite Anode Fabrication for Solid Oxide Fuel Cells

5.1. Introduction

As introduced in Chapter 2, solid oxide fuel cells (SOFCs) are solid-state energy conversion devices with the potential advantages of high efficiency, silent operation and low emissions. However, the high operating temperature (1000°C) of SOFCs places stringent requirements on components, and the practical application of SOFCs is limited by a number of problems (Negichi et al., 1981; Inoue et al., 1990; Kawada et al., 1990a; Suzuki et al., 1993). Among them, the performance of the anode is a significant one. Investigations have shown that approximately one-third of the total potential loss in a state-of-the-art SOFC is caused by anode polarization (Suzuki et al., 1993; Kawada et al., 1990a). In addition, the compatibility of anodes with solid electrolytes and the long-term stability of anodes in an SOFC operating environment are not satisfied from a commercialization point of view.

Investigations in this field have indicated that it is imperative to fabricate efficient and compatible anodes for SOFCs to minimize polarization loss and concurrently achieve long term stability. In this chapter, a critical review of previous studies is given and several criteria for a theoretically ideal anode are summarized. In searching for the best fabrication techniques for anodes in our laboratory, polarized electrochemical vapor deposition (PEVD) (Tang et al., 1996) was used to fabricate efficient and compatible composite anodes in the hope of lowering polarization loss and simultaneously achieving long term stability in SOFCs.

5.2. SOFC anodes

5.2.1. Previous Investigations of SOFC Anodes

According to the principle of SOFCs, at an SOFC anode, fuel gas is oxidized in the electrochemically active region, that is, close to a three phase boundary of an ionic conducting phase, an electronic conducting phase and a vapor phase where all reacting species are available. The basic requirement of the anode materials is to possess both high electric conductivity and high anodic reaction rate (Inoue et al., 1990).

Since anodes work in a reducing fuel gas environment, theoretically, pure porous metallic electrodes can be used. For instance, Ni (Dees et al., 1987; Kawada et al., 1990a; Murakami et al., 1991a), Ru (Suzuki et al., 1993) and Pt (Setogichi et al., 1992) have been studied as anode materials. Pure metallic anodes have high electric conductivity. However, as schematically shown in Figure 5-1, contact between the pure metallic electrode and the solid electrolyte is two-dimensional in a solid state electrochemical system. Unlike an aqueous electrochemical system, the electrochemically active area is limited to the region close to the three phase boundary along this contact surface. Thus, the number of electrochemical reaction sites is insufficient, particularly when SOFCs operate at low temperature and high current density. High overpotential loss is to be expected. In addition, because of the thermal expansion coefficient mismatch between the metallic electrode and solid electrolyte, induced stresses can be a problem. Since there is no “wetting” at a solid-solid contact,

the thermal stresses can easily create cracks which deteriorate the contact further after several heating and cooling cycles. Furthermore, vapor loss, sintering and poisoning of metallic electrodes over a long period of exposure to harsh SOFC operating conditions also cause serious stability problems.

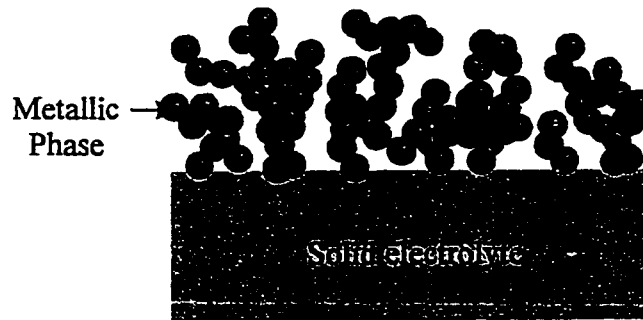


Figure 5-1. Two-dimensional schematic of the microstructure of a pure metallic SOFC anode.

In order to overcome the problems with pure metallic anodes, ceramic-metal (cermet) composite anode concepts have been overwhelmingly accepted. Many methods of producing composite anodes have been investigated during the past 10 years. These include slurry coating (Dees et al., 1987; Kawada et al., 1990a; Murakami et al., 1991a), wet powder spraying (Sammes et al., 1994) and vapor deposition (Isenberg, 1986a and b; Ogumi et al., 1995; Pal and Singhal, 1990a; Carolan and Michaels, 1990a and b; Singhal, 1991). Each of these methods offers advantages; however, each presents its own difficulties such as higher sheet resistances, high costs and performance degradation.

Among these techniques, a slurry coated cermet anode provides a compromise because it is an inexpensive method that has been shown to give reproducible results in terms of porosity and layer thickness (Sridhar and Pal, 1996; Jensen, 1990). The process consists of coating the electrolyte substrate with a slurry of mixed metallic and ceramic particles and, after drying, subjecting it to a number of sintering cycles. The microstructure of a slurry coated cermet is schematically shown in Figure 5-2. The role of the cermet structure is to provide both ionic and electronic conducting paths through connected ceramic and metallic particles, respectively. In addition, there have to be

sufficient contact points between the ceramic and metallic particles. Thus, a slurry-coated cermet anode expands the electrochemically active area from the region close to the three-phase boundary on a two-dimensional solid electrolyte/anode interface to the entire three-dimensional anode volume. This reduces overpotential loss and improves the performance of SOFCs significantly. For instance, Singh (1991) reported that a decrease in polarization was observed in a power generation test using a slurry-coated Ni/YSZ cermet anode. However, in order to match the thermal expansion of the solid electrolyte of an SOFC, the metallic phase content in this kind of cermet anode must be as low as possible (Easler et al., 1986). According to percolation theory (Dees et al., 1987), no continuous metallic phase will exist to provide an electronic conducting path when the metallic phase content is lower than 30%. Even within this limitation, the mixed ceramic and metallic particles reduce the electronic conducting path dramatically, resulting in a high sheet resistance. Consequently, slurry-coated cermet anodes have their limitations; the reduction in overpotential loss is offset by increasing sheet resistance and thermal compatibility problems with the solid electrolyte.

Furthermore, slurry-coated cermet anodes have various long-term stability problems, particularly due to the fine particle size of the metallic component (Murakami et al., 1991b; Kawada et al., 1990a). It has also been reported that the tolerance for impurities in fuels is very limited (Weissbart and Ruka, 1963; Dees et al., 1989). High levels (100 ppm) of H_2S may cause significant irreversible performance loss due to anode poisoning.

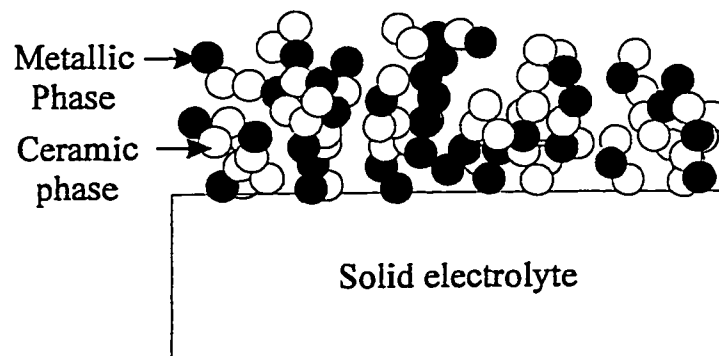


Figure 5-2. Two-dimensional schematic of the microstructure of a slurry-coated cermet anode.

5.2.2. The Criteria for a Theoretically Ideal SOFC Anode

Although the current performance of SOFC anodes is still far from satisfactory, they are mainly being studied solely in terms of the electrochemically active area, the electric conductivity, thermal expansion, stability and reactivity with the solid electrolyte. It is commonly believed, however, that anode performance is not only attributable to the materials, but also to the interfacial structure. Consequently, previous investigations in this area have indicated the importance of a number of microstructural criteria for the best SOFC anodes. These criteria can be summarized as follows:

(1) Overpotential loss is inversely proportional to the electrochemically active area. Thus, a composite anode with three phases is preferred, i.e., ceramic (ionic conduction), metallic (electronic conduction) and pore (gas diffusion) phases mixed together to expand the electrochemically active area to a three-dimensional anode volume (Ogumi et al., 1995; Sridhar and Pal, 1996; Dees et al., 1987; Isenberg, 1982).

(2) Ionic path impedance through the ceramic phase and electronic path impedance through the metallic phase have been found to be dominant factors in determining the electrode characteristics (Kawada et al., 1990b). In order to provide a low sheet resistance anode, it is imperative that the metallic and ceramic phases have maximized continuous paths that allow ionic and electronic migration from the electrolyte/anode interface through out the entire anode.

(3) Due to thermal expansion incompatibility, a metallic phase will not by itself adhere very well to the solid electrolyte of an SOFC (Easler et al., 1986). Thus, it is desirable to have a thermal expansion compatible ceramic phase in intimate contact with both the solid electrolyte and the metallic electrode at the anode/solid electrolyte interface of an SOFC for “wetting” purposes.

(4) The metallic phase is vulnerable in SOFC operating environments. It suffers from vapor loss, sintering, and poisoning over time. Consequently, it is recommended that the ceramic phase both support and protect the metallic phase to achieve long-term stability (Isenberg, 1986; Suzuki et al., 1993).

According to the above, the ideal anode microstructure is shown in Figure 5-3. However, finding a cost-efficient way to fabricate an SOFC anode with this kind of microstructure assumes real difficulties. The challenge of improving anode performance is not only based on having suitable materials to serve as anodes, but also having proper fabrication techniques to incorporate the materials into practical SOFC stack configurations. A good example is the development of electrochemical vapor deposition (EVD) (Isenberg, 1981; Carolan and Michaels, 1990a and b). This technique has made it possible to fabricate fully dense thin ionic conducting films on a porous substrate as the solid electrolytes of SOFCs and, consequently, to minimize the internal resistance loss of the solid electrolytes (Doklya et al., 1989; Balachandran et al., 1989; Eguchi et al., 1989).

In searching for the best fabrication techniques for anodes in our laboratory, PEVD (Tang et al., 1996) was applied to fabricate efficient and compatible composite anodes to lower polarization loss and simultaneously achieve long term stability in SOFCs.

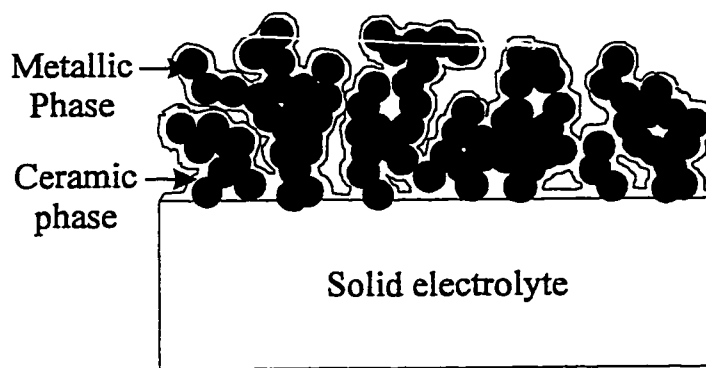


Figure 5-3. Two dimensional schematic of the microstructure of the theoretically ideal composite anode.

5.2.3. PEVD Composite Anode Design

In the last section, a critical review of previous investigations of SOFC anodes was presented, and several criteria regarding anode materials and microstructure were summarized. According to previous applications to solid state potentiometric sensors, PEVD seems to be a possible technique to deposit in-situ a layer of an oxygen ion

conducting phase on a metallic anode of an SOFC. Thus, a composite anode with both a PEVD product and a metallic anode could be realized to overcome the aforementioned anodic limitations.

According to the principles of PEVD process design in Chapter 3, consideration of PEVD processing starts with the PEVD product. Ytria doped zirconia was chosen to be the product in the current investigation due to its high stability and high oxygen ionic conductivity in the anode environment. The details of the PEVD process design for anodic PEVD reactions to form yttria doped zirconia at a Pt thick film metallic anode of an SOFC are schematically shown in Figure 5-4.

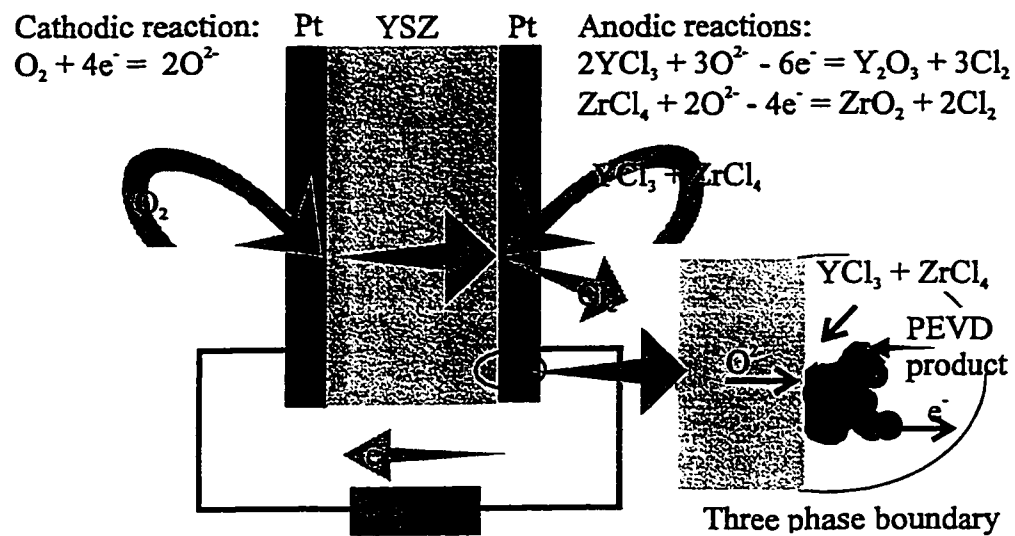


Figure 5-4. PEVD process for fabricating a composite SOFC anode.

The PEVD process takes advantage of the solid electrochemical cell of an SOFC. Oxygen is chosen to be the solid state transported reactant. At the source side (the cathode of the SOFC), oxygen in the source gas phase is reduced to oxygen anions (O^{2-}) through a cathodic reaction



to supply the solid state transported reactant during the PEVD process.

Oxygen anions travel from the source side through the solid electrolyte to the sink side (anode) under the combination of the influence of an applied dc electric field and an oxygen chemical potential gradient. At the sink side (the anode of the SOFC), the oxygen anions react electrochemically with both zirconium and yttrium reactants from the sink vapor phase to form the desired product, yttria doped zirconia, and release electrons to the metallic anode. Electrons travel through the external electrical circuit back to the source side for further cathodic reaction.

ZrCl₄ and YCl₃ were chosen as sink vapor reactants due to their relatively high vapor pressures. The equilibrium vapor pressures of ZrCl₄ and YCl₃ are indicated in Figures 5-5. As with conventional CVD, the Y doping level or concentration of Y₂O₃ in the PEVD product (Y₂O₃-ZrO₂) can be controlled by the partial pressures of YCl₃ and ZrCl₄ in the sink vapor phase.

The main anode reaction for the PEVD process is:



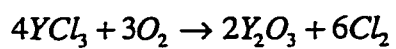
The anode doping reaction is:



Since the chlorine released from both anodic reactions is in vapor form, it can be driven away easily through the sink vapor phase. The overall reaction for ZrO₂ formation in this PEVD process is:



and the overall doping reaction for Y₂O₃ formation is:



(5-5)

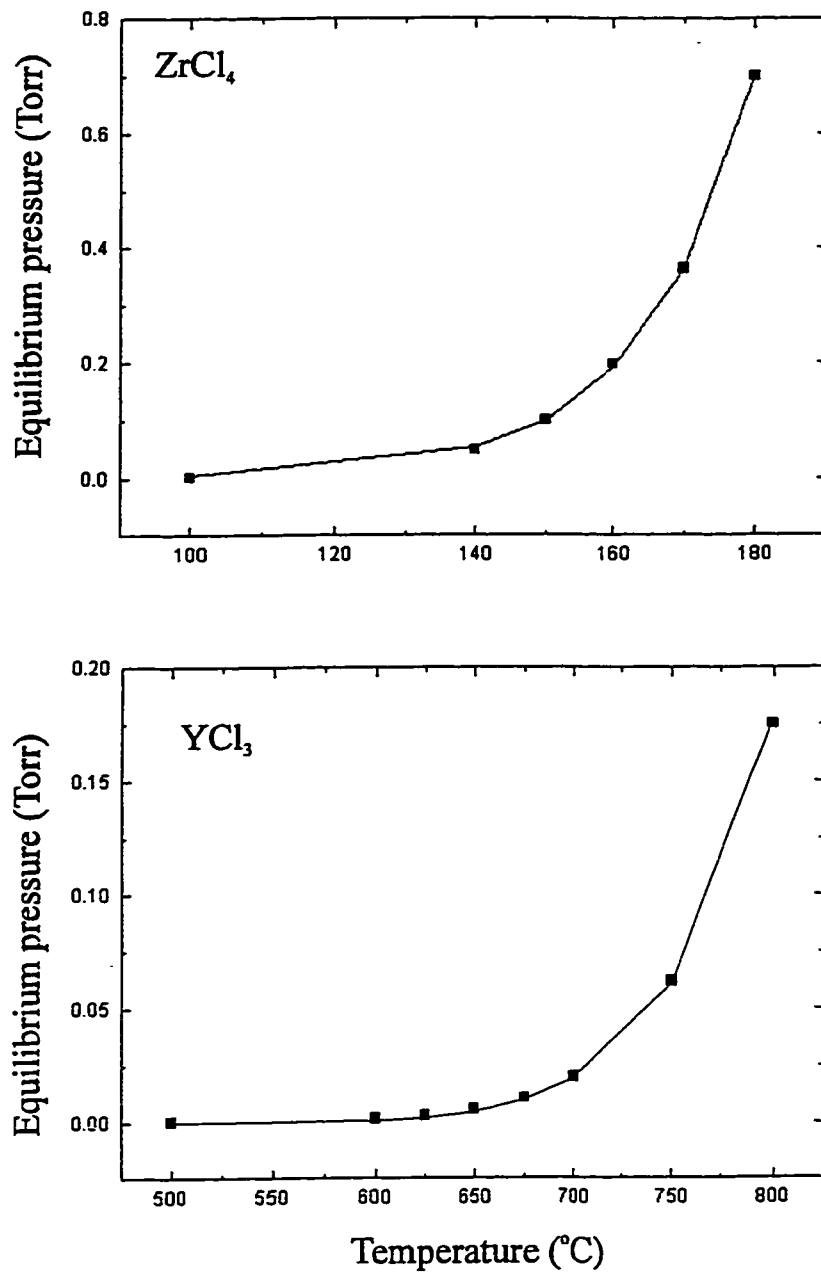


Figure 5-5. The calculated equilibrium vapor pressures of ZrCl₄ and YCl₃.

The PEVD process is closely related to electrochemical vapor deposition (EVD), which was developed to form gas-tight YSZ thin films as solid electrolytes at Westinghouse by Isenberg in the 1970s (Isenberg, 1977; de Haart et al., 1991; Dekker et al., 1992). Recently, both PEVD and EVD techniques and their applications were reviewed by Tang et al. (1997). It was shown that both processes have fundamental similarities in terms of mass and charge transport through the products required for further deposition. The differences between EVD and PEVD for depositing yttria doped zirconia are schematically shown in Figure 5-6. The major difference is that a solid electrochemical cell is used in PEVD to set the driving force for oxygen ion transport inside the solid electrolyte and the deposition product.

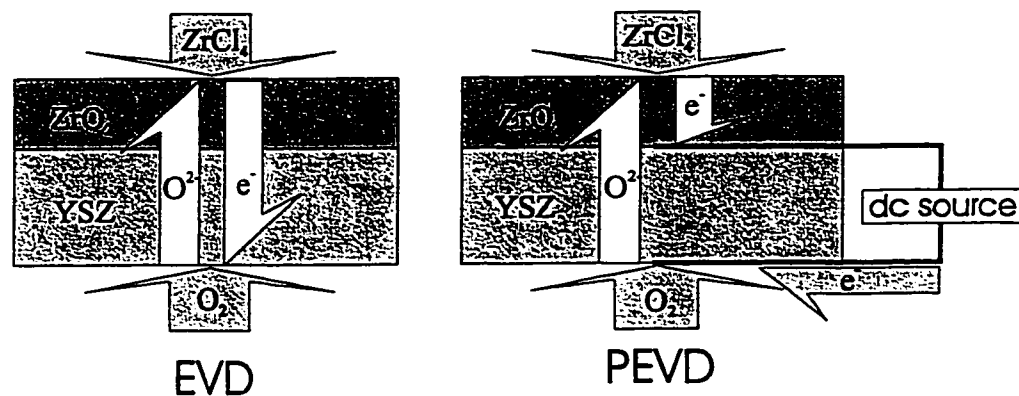


Figure 5-6. Comparison of EVD and PEVD processes.

Utilization of solid electrochemical cells is one of the most significant advantages of the PEVD technique, since deposition process control and monitoring are easy to realize. According to previous investigations in Chapter 4, by connecting a simple external electrical circuit to a PEVD system, the chemical redox reaction in PEVD is easily monitored and controlled through the electrical current and applied potential, respectively.

5.3. Experimental Aspects

5.3.1 PEVD Sample Preparation

Figure 5-7 schematically shows the PEVD sample utilized in this investigation. It is a solid electrochemical cell with an ytterbia and yttria stabilized zirconia pellet ($8\%Yb_2O_3$ - $6\%Y_2O_3$ - ZrO_2 , from Ceramatec Inc., Salt Lake City), 15 mm square and 1.5 mm in thickness, as the solid electrolyte to conduct oxygen anions from the source to sink side.

A commercially available Pt thick film paste (Electro-Science Laboratories, Inc., 5544) was screen printed on the center of both surfaces of the solid electrolyte disk. The screen printed paste was first heated at $120^\circ C$ to burn out organic components and then sintered at a peak temperature of $980^\circ C$ for 15 min to ensure a continuous, but porous structure. The thickness of the porous Pt electrodes was about $15\ \mu m$, and the geometric area of the thick films was $100\ mm^2$. Two Pt meshes, with spot welded Pt leads, were then pressed on the top of the porous Pt thick films, and co-sintered at $1050^\circ C$ for 15 min to ensure good electrical contact (van Herle et al., 1994). The porosity of the thick film was about 60% based on weight measurement. The sample was then mounted on the end of a small fully dense alumina tube (McDanel) and secured with high-temperature cement (Ceramabond 503, Aremco Products).

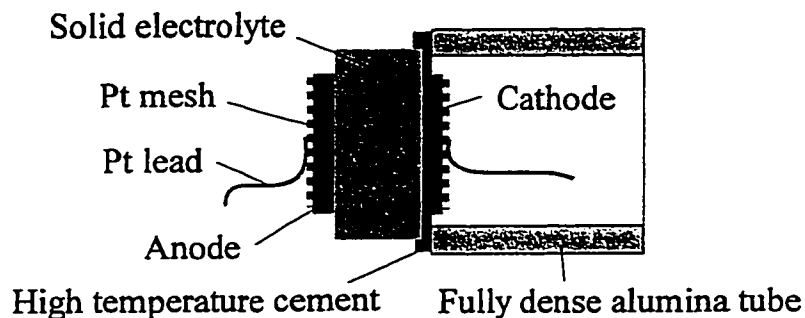


Figure 5-7. PEVD sample system.

5.3.2. PEVD System Setup

Figure 5-8 shows a schematic diagram of a lab-made PEVD reactor for depositing yttria doped zirconia. The sample tube was placed at the center of a large fully dense alumina reactor tube (McDanel) in an electric furnace (Lindberg). Thus, the sample tube separated the reactor tube into two chambers; the air chamber inside the sample tube and the chloride chamber between the sample and reactor tubes. The ends of both tubes were sealed by rubber stoppers. Both chambers were evacuated separately by two mechanical pumps (Welch 1400, Franklin Electric), and the vacuums inside the chambers were monitored with a mercury vacuum gauge.

Both sample electric leads were connected to a dc power supply (Brunelle Instruments Inc., 1090) as shown in Figure 5-8. The external electric circuit can be operated either under closed circuit or open circuit conditions via Gate A. The open circuit emf and the closed circuit applied dc potential were monitored by a digital electrometer (Keithley 616). The closed circuit current was measured by an ammeter (Keithley 713). Both current and applied dc potential were followed with a dual channel analog recorder (Brinkmann 2742-3).

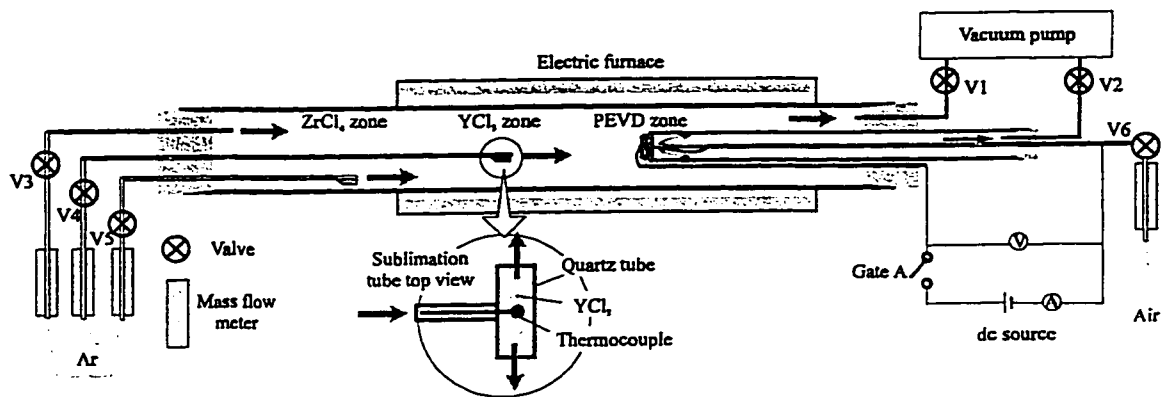


Figure 5-8. PEVD reactor setup.

The sublimation tubes for both chloride sources were made of quartz glass as shown in Figure 5-8. The working end of the tube was "T" shaped to store the chloride powders, and K type thermocouples were embedded in the tubes close to the powders. The positions of the sublimation tubes were adjusted manually during the deposition process to ensure that both $ZrCl_4$ (>99.9% purity, Aldrich Chemical, Milwaukee, WI) and

YCl_3 (>99% purity, Aldrich Chemical, Milwaukee, WI) were heated at the proper sublimation temperatures for the desired vapor pressures. Each vaporized chloride was supplied to the reaction zone using Ar (Praxair) as a carrier gas, which passed through a series of driers and oxygen removal units before entering the chloride chamber. The flow rates through the chamber, and ZrCl_4 and YCl_3 sublimation tubes, were controlled by needle valves V3, V4 and V5, respectively. At the source side, air (Praxair) was bled into the sample tube. The flow rate was controlled by needle valve V6.

5.3.3 PEVD Procedure

The details of the PEVD process for this study are summarized as follows:

(1) Valves V1 and V2 were opened to evacuate both the chloride and air chambers to a pressure of less than 1 torr.

(2) Needle valves V3, V4 and V5 were opened and adjusted to bleed carrier gas into the chloride chamber at a rate of 5, 10 and 2.5 sccm, respectively. Needle valve V6 was opened and adjusted to bleed air into the air chamber at a rate of 5 sccm.

(3) After purging both chambers for about 5 min, V1 and V2 were adjusted to maintain both chambers at 1 torr. The oxygen partial pressure in the air chamber was 0.21 torr.

(4) The electric furnace then heated the reactor to 1000°C in the PEVD zone. During this initial system heating, both chloride sublimation tubes were placed on the extreme left side of the chloride chamber and remained at low temperature (less than 50°C).

(5) Before heating up the chloride sublimation tubes, the oxygen impurity in the chloride chambers was determined by the open circuit emf value of the PEVD electrochemical cell. This gives the oxygen partial pressure difference between the air and chloride chambers. A gas mixture (Ar - 5% H_2) was sometimes used at the beginning of the purge to reduce the oxygen partial pressure in the chloride chamber to about 10^{-15} torr, which corresponds an emf value of -900 mV. This minimized the chloride vapors that reacted chemically with residual oxygen in the vapor phase.

(6) Gate A was closed and a reverse dc potential (stop potential) of -900 mV was applied to prevent oxygen leakage from the air chamber to the chloride chamber

electrochemically in the closed circuit condition. Consequently, the closed circuit current was initially zero.

(7) The $ZrCl_4$ sublimation tube was placed in a position corresponding to a temperature of $160^\circ C$. This gave an equilibrium vapor pressure of about 0.2 torr. The YCl_3 sublimation tube was placed at a position corresponding to a temperature of $700^\circ C$ giving an equilibrium vapor pressure of about 0.025 torr. Thus, the partial pressure ratio of $ZrCl_4$ vs. YCl_3 was 8:1.

(8) The reverse dc potential was decreased to a less negative value; an oxygen ionic current flowed from the air to the chloride chamber. The dc potential and current were simultaneously recorded with a dual channel analog recorder. Thus, current vs. applied dc potential curves could be drawn.

(9) For this PEVD process, a dc applied potential of -450 mV was selected, and current in the range of 500 to $100 \mu A$ was recorded for 300 min. To ensure that oxygen evolution at the anode was negligible, the oxygen partial pressure was checked several times during and after the process through the open circuit emf reading from the electrometer.

5.3.4. Microstructure Studies

In order to examine the PEVD product at the anode of the samples, both plan-view and cleavage cross-section specimens were prepared. The phases, microstructure and chemical composition of the anode were studied using XRD (Rigaku) with Jade analysis software (Materials Data, Inc.), SEM (Hitachi H-2700) and EDX (Link eXL x-ray detector in Be window mode), respectively.

5.4. Results

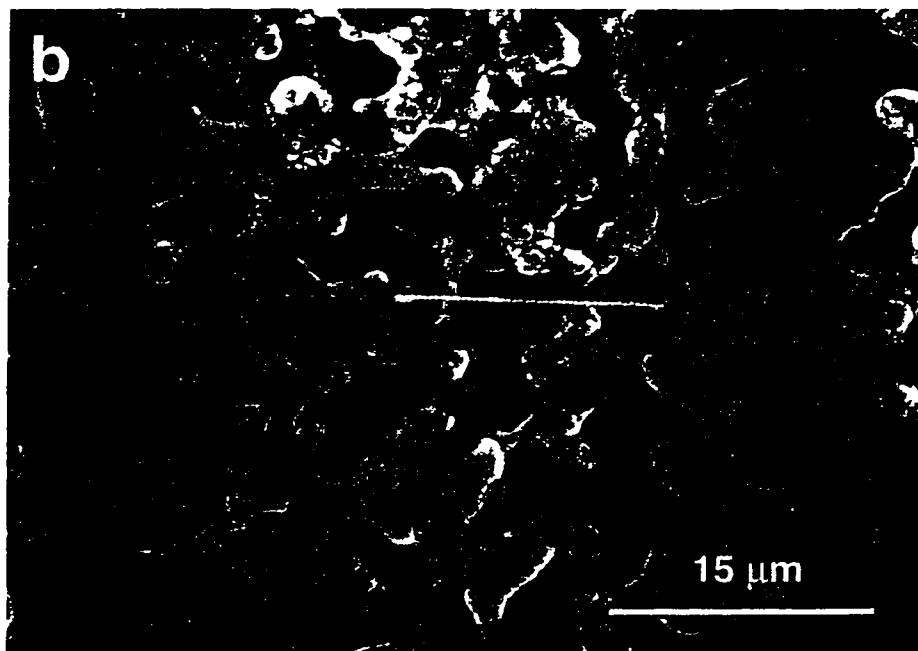
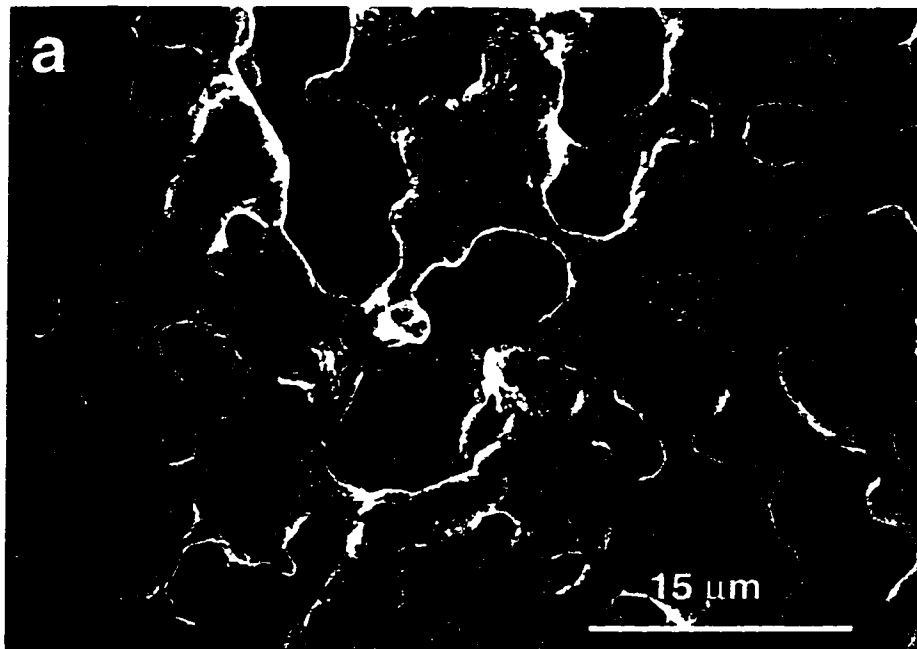
In order to compare the original microstructure of the Pt porous metallic anode with the PEVD composite anode, the anodic surface of the sample was examined by SEM before and after PEVD. Figure 5-9a is an SEM secondary electron (SE) image of the

anode of a sample before PEVD. The anode is a Pt thick film. Because of higher sintering temperature, the microstructure of the Pt thick film used here was different than the ones used in Chapter 4. The pore size in the thick film is increased and ranges in size from 1 to 10 μm . The porosity of the thick film is decreased to about 60%. For this calcination treatment, the boundaries of the Pt grains are still visible. The Pt grain size increase was not significant; the grain size was maintained at 1-2 μm . However, some small step-like features developed on the surface of the Pt grains.

Figure 5-9b is an SEM SE image of the anode after PEVD. PEVD products had formed at the edges of the pores, and the small step-like features that used to be on the surface of the Pt grains before PEVD had disappeared. This indicates that a layer of PEVD product had formed at the anode to wrap the Pt thick film. Since the porosity of the anode did not decrease much after PEVD and the grain boundaries of the Pt thick film are still visible in Figure 5-9b through the PEVD product at a 20 keV operating voltage in the SEM, the product layer covering the Pt metallic electrode must be quite thin (less than 1 μm).

In addition, anode crystallographic information after PEVD was obtained with XRD. The XRD spectrum of the PEVD composite anode is presented in Figure 5-10. Three phases exist in the XRD spectrum; i.e., an yttria stabilized zirconia phase (cubic), a pure zirconia phase (monoclinic) and a metallic Pt phase. The x-ray intensities do not match exactly with those from standards, as the samples were not in powder form and, therefore, were not completely randomly oriented.

The Pt phase shows up in the spectrum because the PEVD product on top of the Pt is thin enough to allow x-rays to penetrate the product phase to reach the underlying Pt phase. Based on the relative peak intensity, yttria stabilized zirconia is the major phase in the PEVD product. However, a certain amount of pure zirconia is evident. Thus, the zirconia in the PEVD product is partially stabilized. According to the discussion in Chapter 2, the Y doping level in the PEVD product is lower than 8%. It is worth pointing out that the equilibrium partial pressure ratio of YCl_3 to ZrCl_4 was set at about 1:8 during PEVD. The reason for this yttrium deficiency in the PEVD deposited phase requires further investigation.



Figures 5-9(a) and (b). SEM SE plan-view images of the anode of the sample before (a) and after (b) PEVD.

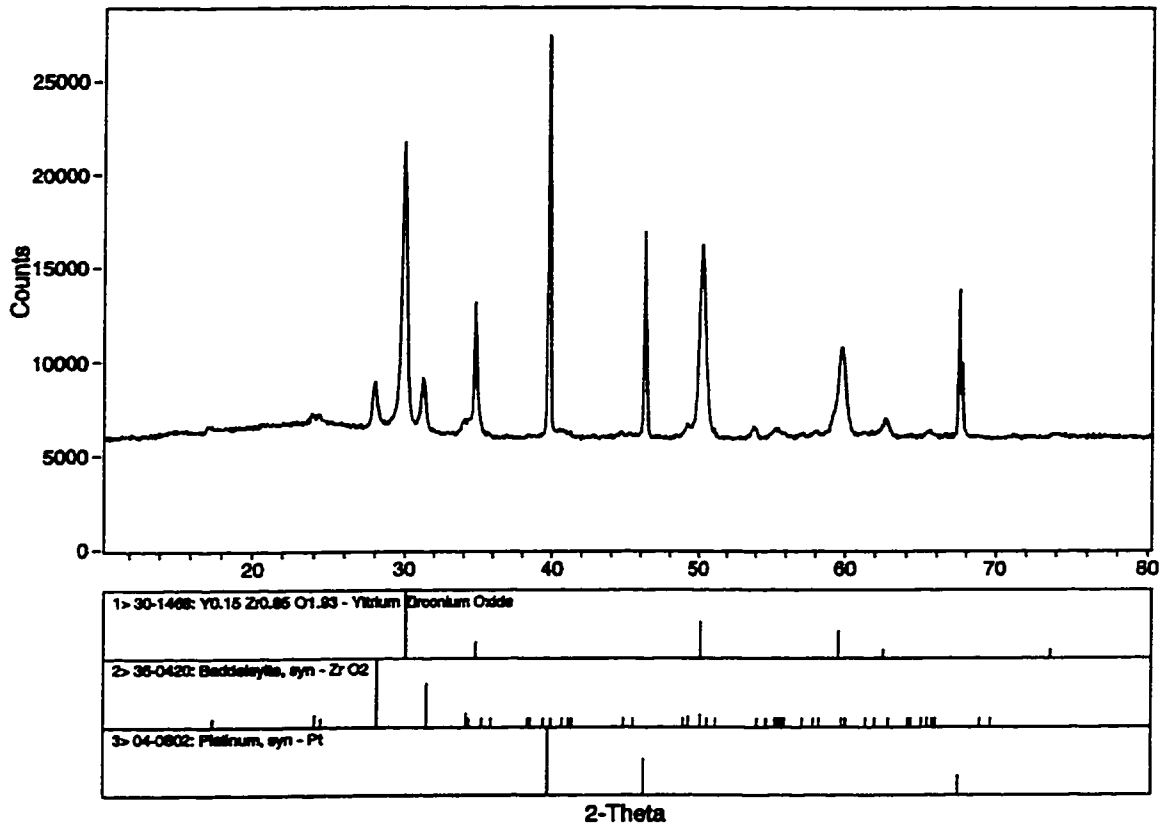


Figure 5-10. XRD spectrum of the anode of the sample after PEVD. Also shown are representative spectra from standard Y_2O_3 - ZrO_2 , ZrO_2 and Pt specimens.

The solid electrolyte/anode interfacial region was examined using cleavage cross-section samples. Figure 5-11 shows an SEM back scattered electron (BSE) image of a cross-section sample at a tilt angle of about 15 degrees. The phase differences are distinguishable through different gray scale levels. The whitest area is Pt due to its high atom number ($Z=78$). Although both the solid electrolyte substrate and the product of the PEVD system are mainly zirconia, the substrate is a little bit lighter than the product due to the higher atomic number of Yb ($Z=70$) in the substrate.

The microstructure of the PEVD composite anode is further displayed by an SEM SE image at higher magnification in Figure 5-12. Figures 5-13 shows the EDX spectra for areas A, B and C in Figure 5-12. Since the energy difference between the major zirconium and yttrium $L\alpha$ peaks in EDX spectra is only 120 eV, these peaks are unresolvable by EDX. Higher energy $K\alpha$ peaks (820 eV apart) need to be used to distinguish Zr and Y. As accelerating potential of 30 keV was therefore used to perform EDX analysis. Accordingly, point A is the solid electrolyte substrate with three elements, i.e., Yb, Zr and Y, in the spectrum. Point B is the Pt thick film of the PEVD composite anode with mainly Pt in the spectrum. Since the area is small, and the sample was prepared by cleavage, it is not perfectly flat. A certain amount of Zr from the surrounding area was picked up in the EDX spectrum. Point C is the PEVD product with Zr and Y in the spectrum. The results match well with those from the BSE image in Figure 5-11.

Figure 5-12 also shows that the deposited PEVD product phase is in intimate contact with both the solid electrolyte and the Pt electrode. In the anode/solid electrolyte interface region, the deposited zirconia phase formed a dense layer encompassing the Pt electrode. This provides extra "wetting" for the metallic electrode and solid electrolyte contact. Conventional vapor deposition techniques are unable to deposit products at the bottom of this kind of high aspect ratio and irregularly shaped substrate. The deposited zirconia phase continuously covers the entire metallic electrode surface from its contact with the solid electrolyte to the top of the composite anode. Thus, there is little Pt phase shown in this cleavage sample, since the break is mainly through the pores in the anode region of the specimen.

In order to show the phase boundary between the solid electrolyte and PEVD product, an EDX line scan for Yb was performed along a 6 μm long dotted line between point A and C. The electronic signal (gray level) and Yb $L\alpha$ intensity are recorded in Figures 5-14a and b, respectively. The Yb x-ray intensity curve in Figure 5-14b dropped smoothly across the microscopic boundary. This kind of smooth transfer in Figure 5-14b is due to the limited spatial resolution of x-rays. The valley in the gray level curve in Figure 5-14a indicates the position of the interface in the SEM SE image in Figure 5-12.

Figure 5-15 is an SEM SE plan-view image at the anode of another sample after completing an 18 hr PEVD. The PEVD product thickness further increases at the anode. Consequently, the Pt electrode was invisible in the 20 keV SE image, and most of the pores in the anode were filled with PEVD product.

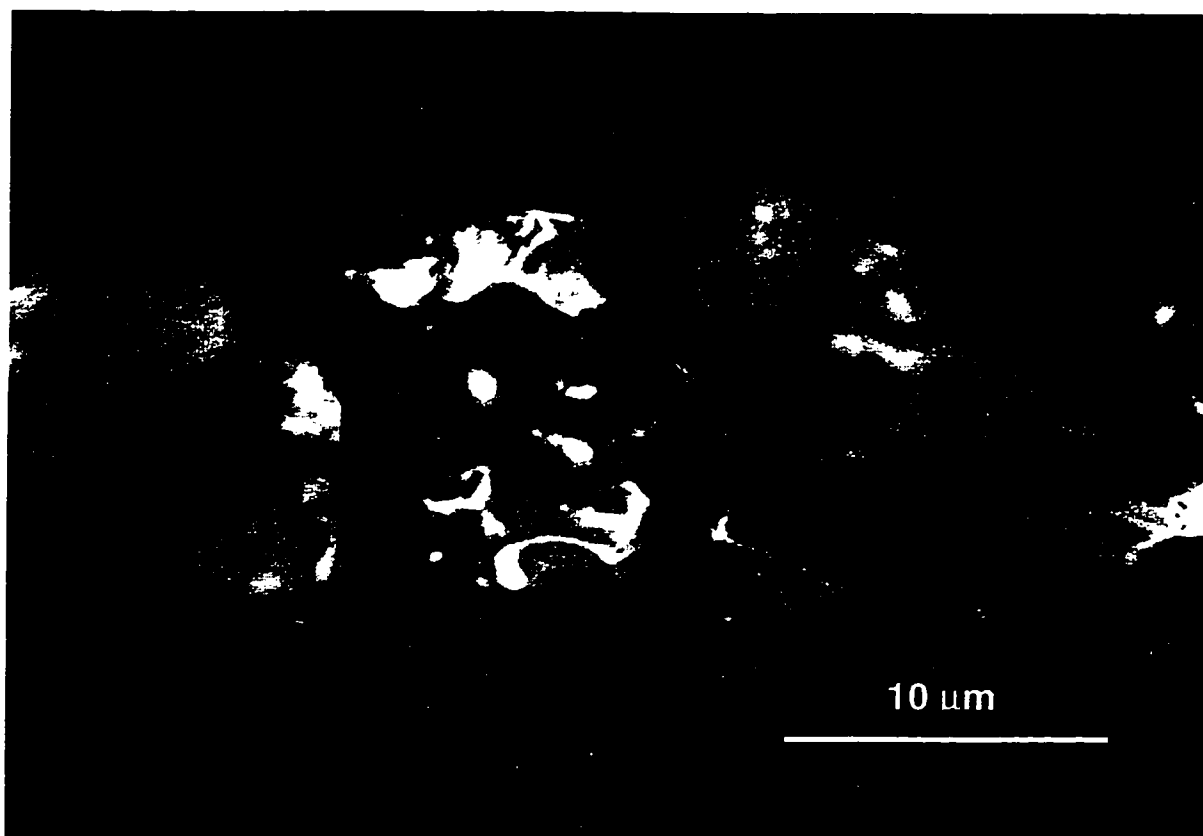


Figure 5-11. SEM BSE image of the anode/solid electrolyte interfacial region.

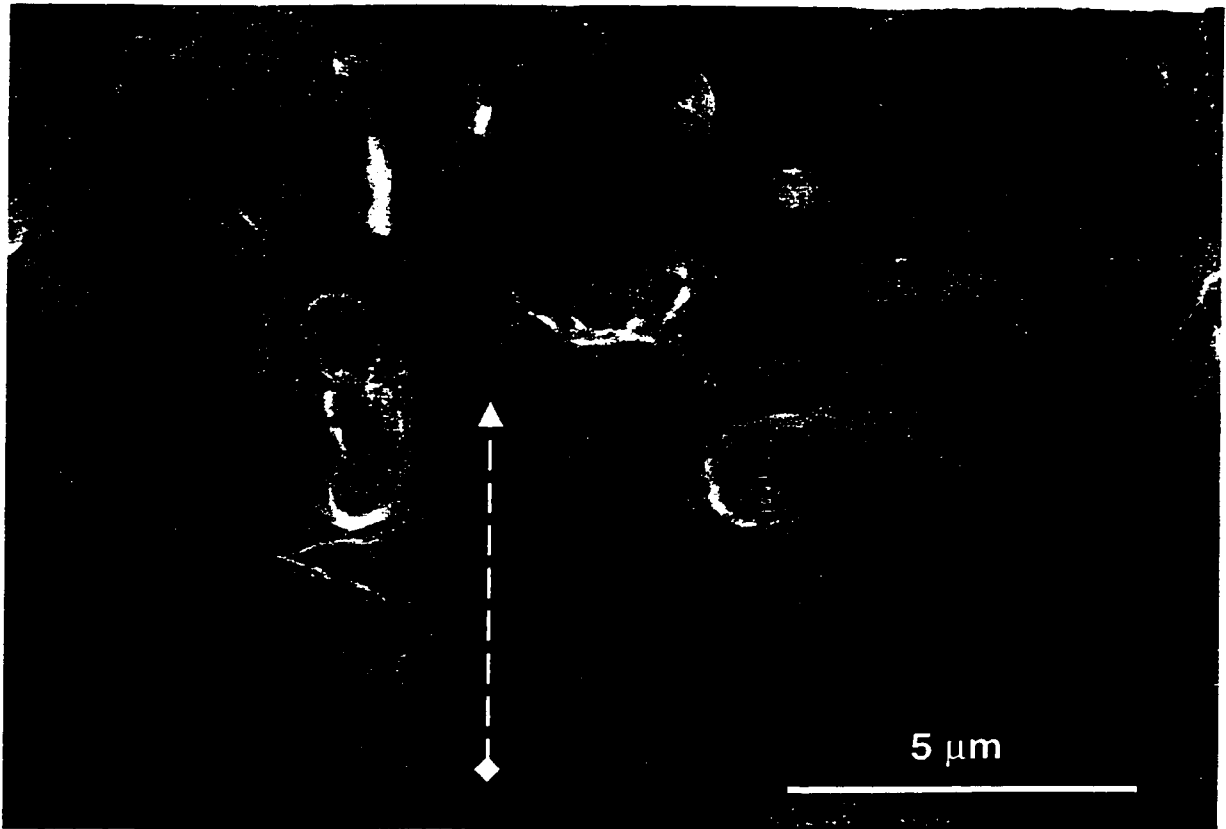


Figure 5-12. SEM SE image of the anode/solid electrolyte interfacial region.

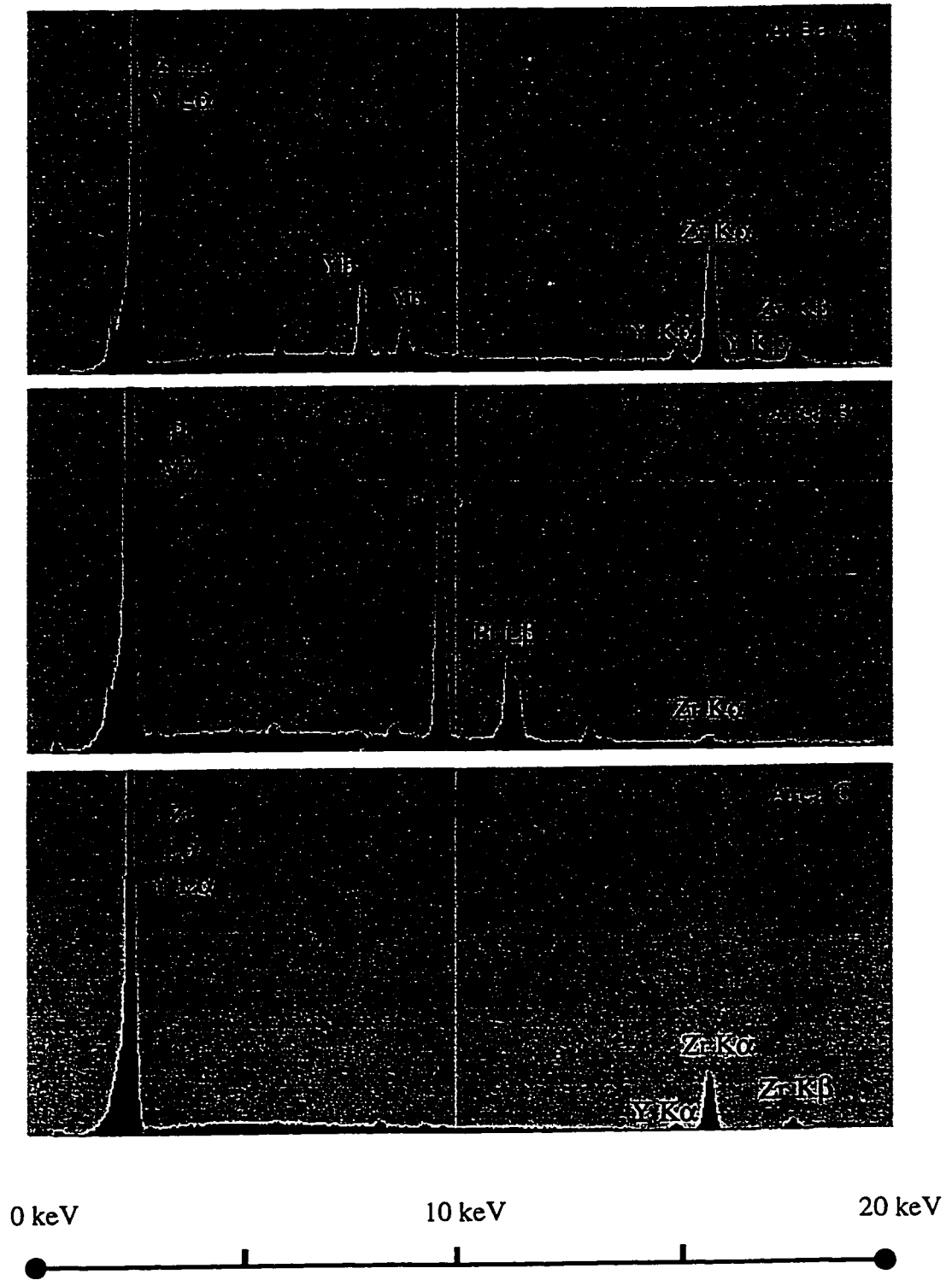
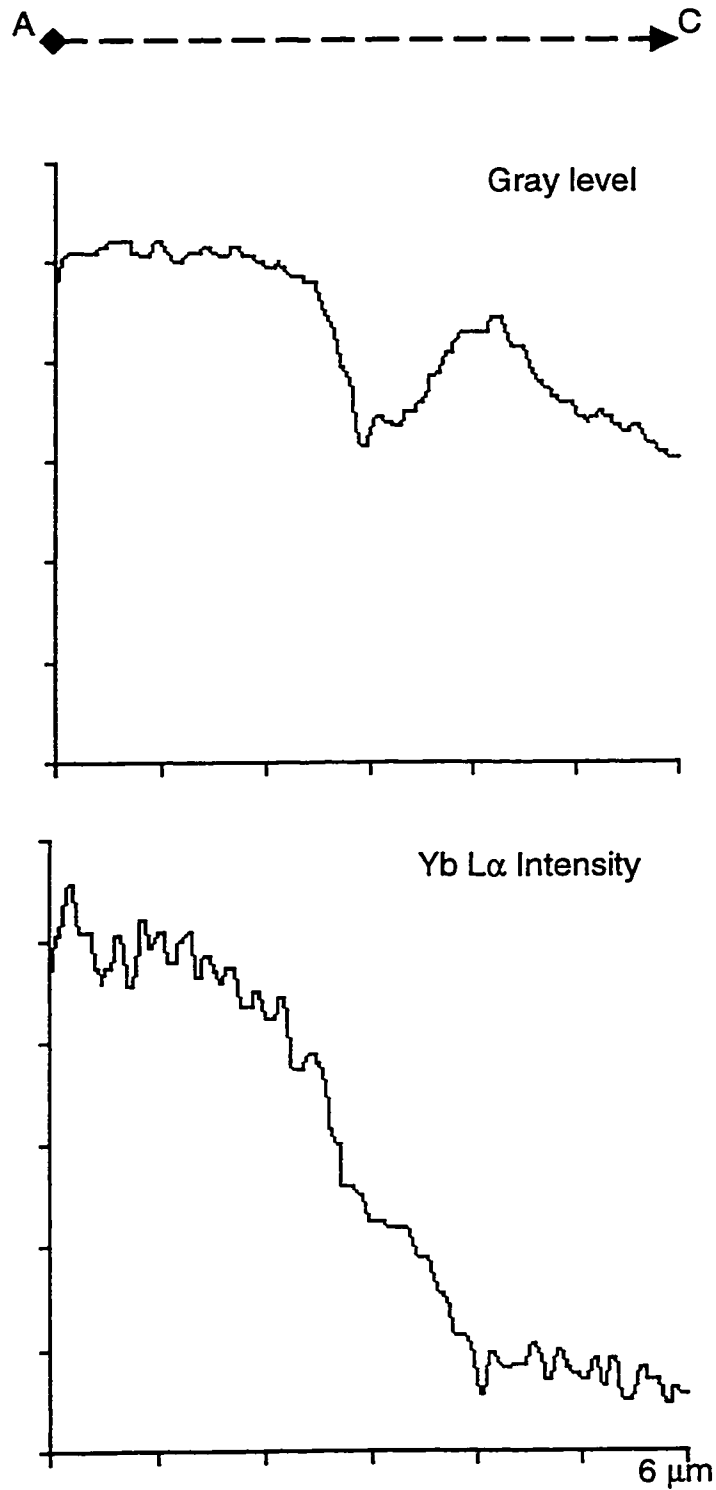


Figure 5-13. EDX spectra from areas A, B and C in Figure 5-12.



Figures 5-14 (a) and (b). EDX line scan from point A to point C. (a) gray level; (b) Yb L α intensity.

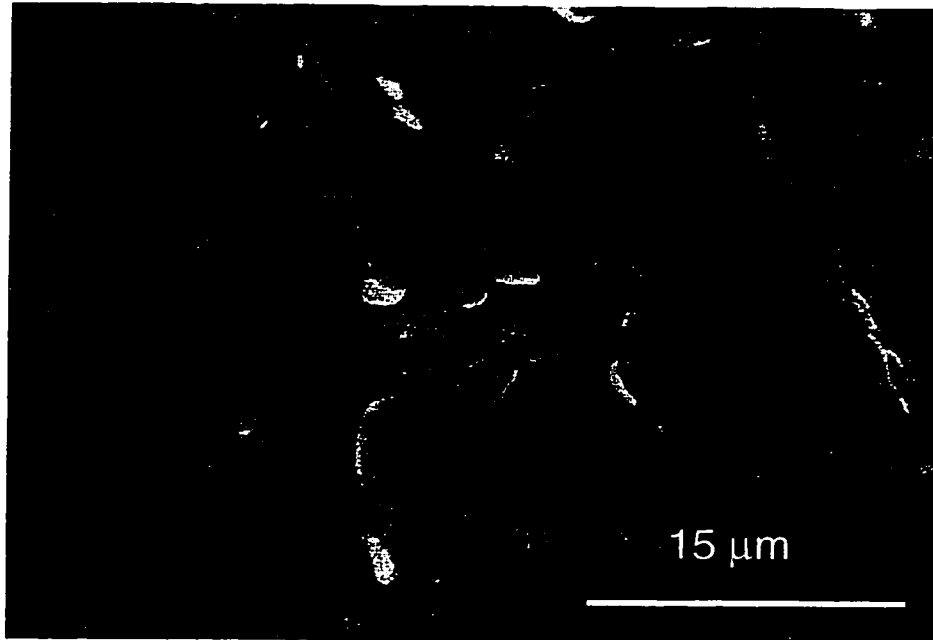


Figure 5-15. SEM SE plan-view image of an anode after a longer PEVD time.

5.5. Discussion

Based on the proceeding microstructural analysis results, it is clear that PEVD is capable of depositing a thin layer of yttria-doped zirconia to form a composite anode. This phase is not only in intimate contact with both the solid electrolyte and metallic electrode, but also covers the entire porous metallic (Pt) electrode surface. This coverage by the ceramic phase protects the metallic electrode from vapor loss, sintering and poisoning in the harsh SOFC operating environment. The intimate contact of the deposited ceramic phase in the interface region also improves the contact between the solid electrolyte and metallic electrode. Furthermore, at the interface between the solid electrolyte and composite anode, the ceramic phase is dominant. This increases the thermal shock resistance of the interface. PEVD yttria-doped zirconia also has continuous oxygen ionic conducting paths in the anode. Since the deposited ceramic phase is thinner at the other area than the solid electrolyte/electrode interface, the porosity of the anode does not decrease significantly. This ensures that all three phases for the SOFC anode reaction coexist in the PEVD composite anode. This is the optimum way to expand the electrochemically active area to a three-dimensional anode volume. Unlike slurry coating of cermet anodes, formation of ionic conducting paths in PEVD composite anodes reduces the overpotential loss but does not sacrifice the electronic conducting path. Thus, the sheet resistance of the PEVD composite anode remains virtually the same as the pure metallic anode.

According to the discussions in Chapters 3 and 4, the above mentioned PEVD composite anode microstructure is largely based on PEVD's unique electro-crystallization behavior (Tang et al., 1996 and 1997).

First of all, because of the availability of reactants for PEVD electrochemical reactions (5-2) and (5-3) at the anode, initial product phase nucleation can only occur at the three-phase boundary of solid electrolyte, metallic electrode and vapor phase indicated as point O in Figure 5-16. Further growth of the PEVD product phase can only proceed from such nuclei. PEVD can reach the bottom of high aspect ratio substrates with very irregular shape, as in the case of a 15 μm thick Pt porous metallic electrode screen printed on a solid electrolyte.

Secondly, further PEVD electrochemical reaction and subsequent growth of the product phase needs a continuous oxygen ionic path and electronic path from the solid electrolyte and metallic electrode, respectively. Therefore, PEVD deposits are bound to be in intimate contact with both the solid electrolyte and metallic electrode.

Finally, according to electrocrystallization and growth behavior at electrically shorted surfaces (Ilschner-Gensch and Wagner, 1958), different growth rates of PEVD product occur along ionically and electronically shorted surfaces. The growth of an ionic conducting phase is schematically shown in Figure 5-16. Along the electronically shorted surface of the metallic electrode in the X direction, growth will be limited by transport of ions through the product. Along the ionically shorted surface of the solid electrolyte in the Y direction, growth will be limited by transport of electrons through the product. Thus, ionically conducting yttria-doped zirconia will exhibit preferred growth along the electronically shorted surface to cover the entire metallic electrode with a thin layer regardless of the aspect ratio and irregularity of the substrate.

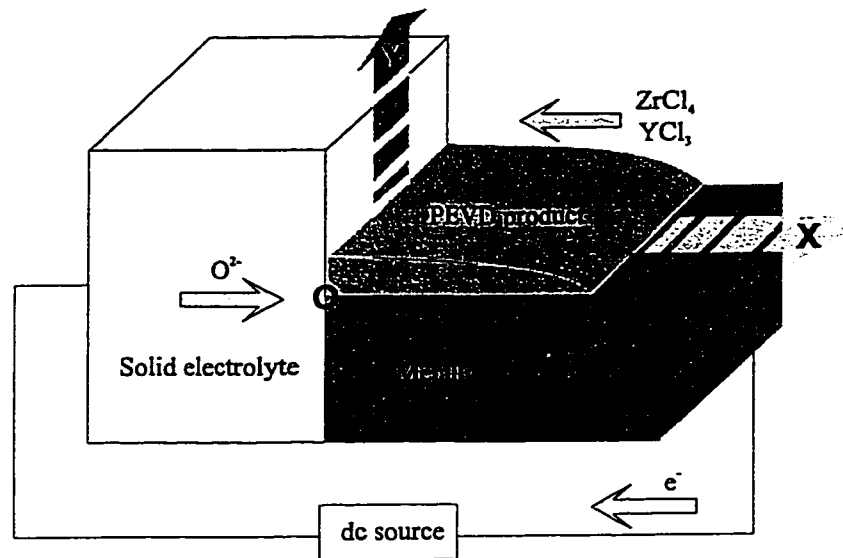


Figure 5-16. PEVD preferred growth of an ionic conducting layer on an electronically shorted surface (metallic electrode surface).

Based on the above discussion, PEVD has the capability of fabricating composite anodes to meet all the criteria for theoretically ideal anodes as illustrated in Figure 5-3. Furthermore, with regard to cost efficiency, PEVD is a single step process for composite anode formation. It can be conducted in situ to coat the pure metallic anodes, or even to repair damaged composite anodes for SOFCs.

5.6. Conclusions

In this chapter, a critical review of previous investigations of SOFC anodes was presented, and several criteria regarding anode materials and microstructure were summarized. Accordingly, a theoretically ideal SOFC composite anode was proposed. It appears that the emergence of the PEVD technique for ceramic phase deposition on high aspect ratio and very irregularly shaped metallic electrodes has made possible the successful fabrication of composite anodes similar to the theoretically ideal one. Consequently, SOFCs with PEVD composite anodes should have higher electrical conductivity, lower overpotential loss, and exhibit better long-term stability. Further investigations are needed to test their performance in actual SOFC operation.

Chapter 6. PEVD Process Electrochemical Studies

6.1. Introduction

In the previous chapters, PEVD thermodynamic equilibrium relationships were discussed in connection with electrocrystallization phenomena occurring in PEVD processes for applications in sensors and fuel cells. However, the migration of charged ionic and electronic carriers in an electric field during PEVD is a kinetic process. Overpotential exists both in the bulk of the solid phases and within the diffuse double layer formed at the phase boundaries. Consequently, the applied potential and current in a PEVD process do not follow exactly the linear relations predicted from the thermodynamic equilibrium approach taken in Chapter 3. Furthermore, it is necessary to discuss the changes at the working electrode during a PEVD process. Because such changes are accompanied by electrochemical reactions for PEVD product formation, the thermodynamic approach must, therefore, be complemented by kinetic considerations to evaluate electrocrystallization behavior during a PEVD process.

The task related to studying PEVD working electrode kinetics in this chapter is to explain the sequence of partial reactions constituting the overall PEVD electrochemical reaction for product formation at the working electrode. The dependence of current density, or of reaction rate, upon working electrode overpotential and temperature was studied by both a steady-state potentiostatic method and a dynamic potential sweeping method (solid electrolyte cyclic voltammetry), in the hope of resolving PEVD reaction rate-limiting steps. The results from this investigation will help in understanding the kinetics of the PEVD reaction and subsequent product formation at the working electrode of a PEVD system, improve knowledge of PEVD kinetics, and elucidate the possibility of further process control in PEVD.

6.2. Theoretical Considerations

6.2.1. Overpotential in a PEVD System

When a current flows through an electrochemical cell in the hypothetical PEVD system proposed in Chapter 3, the applied d.c. potential V_a defines the potential difference V_{WC} between the working and counter electrode. This value deviates from its open-circuit value V_{WC}° , which is generally computable via a Nernst equation

$$V_{WC}^\circ = \frac{kT}{nz_A q} \ln \frac{a_{A^+(W)}}{a_{A^+(C)}} = \frac{\mu_{A,I} - \mu_{A,III}}{qz_A} \quad (6-1)$$

where all terms have been defined in Chapter 3.

According to the fundamental theory of overpotential for aqueous electrochemical systems (Vetter, 1967; Vayenas et al., 1992), the electrochemical cell overpotential is defined as the potential difference deviation from the open-circuit value. The electrochemical cell overpotential η_{WC} is then defined as:

$$\eta_{WC} = V_{WC} - V_{WC}^{\circ} = V_a - \frac{\mu_{A,I} - \mu_{A,III}}{qz_A} \quad (6-2)$$

Thus, the applied electric field and the chemical potential difference of solid-state transported reactant (A) between the sink and source determine the total overpotential η_{WC} of the PEVD system. Accordingly, Eq. (3-41) can be expressed as

$$I = -G_i \eta_{WC} \quad (6-3)$$

where the PEVD current I and the total overpotential of the PEVD system η_{WC} are linearly related to each other. The slope is the conductance $-G_i$, which has been defined in Chapter 3. However, this equation was obtained under the assumption that equilibria are attainable at all interfaces in the PEVD system. In practice, this assumption is valid only in a limited number of cases. Generally, when a current passes through the PEVD system, various kinds of overpotentials might exist at any part of the system, such as the counter electrode, solid electrolyte and working electrode. The overpotential η_{WC} of the electrochemical cell in the PEVD system is the sum of three terms:

$$\eta_{WC} = \eta_W + \eta_C + \eta_{E,WC} \quad (6-4)$$

where η_W , η_C are the overpotentials of the working (W) and counter (C) electrodes, respectively, and $\eta_{E,WC}$ is the ohmic overpotential due to the resistance of the solid electrolyte (E) between the working and counter electrodes. Thus, the current – applied potential curve in a PEVD process is usually not linear as expected from Eq. (6-3). In order to further understand mass and charge transport during PEVD, the kinetics of a PEVD process and, consequently, various kinds of overpotential should be considered as well.

Since only the working electrode overpotential and current reveal, respectively, the thermodynamic and kinetic information of a PEVD reaction for product formation, it is imperative to distinguish the working electrode overpotential η_W from the total

overpotential η_{WC} . This is possible with the help of a reference electrode (R). The overpotential between the working and reference electrodes can also be expressed as

$$\eta_{WR} = \eta_W + \eta_R + \eta_{E,WR} \quad (6-5)$$

where η_R is the overpotential of the reference electrode, and $\eta_{E,WR}$ is the ohmic overpotential due to the resistance of the solid electrolyte between the working and reference electrodes. During a PEVD process, no current flows through the open circuit between the reference and working electrode; therefore, both η_R and $\eta_{E,WR}$ are zero (Bebelis and Vayenas, 1989; Neophytides and Vayenas, 1989; Vayenas and Neophytides, 1991). Thus, it is reasonable to assume that the potential difference V_{WR} between the working and reference electrode reveals the overpotential at the working electrode η_W only.

$$V_{WR} = \eta_W \quad (6-6)$$

The working electrode overpotential η_W can be measured by an electrometer between the working and reference electrodes.

6.2.2. Working Electrode Overpotential in a PEVD System

When a PEVD system is at equilibrium under open circuit conditions, a thermodynamically defined reversible inner (or Galvani) potential ϕ_W° is set up at the working electrode. The equilibrium involved is a dynamic one, in which the rates at which charge carriers pass through the interface at the working electrode in both directions are equal. This rate is the exchange current density i_0 .

$$i_+ = |i_-| = i_0 \quad (6-7)$$

When current flows through an electrode, its inner potential ϕ_w assumes a value different from the equilibrium inner potential ϕ_w° . This deviation of the electrode potential is the overpotential at the working electrode (Caspari, 1989).

$$\eta_w = \phi_w - \phi_w^\circ \quad (6-8)$$

An anodic (positive) and cathodic (negative) current always generates a positive and negative overpotential, respectively. Although working electrode overpotential is usually associated with working electrode/electrolyte interfaces in electrochemistry, in reality it refers to, and is measured as, deviations in the inner potential of the working electrode. The formation of the current-controlled overpotential in the working electrode originates in the hindrance of the overall electrochemical reaction for PEVD product formation. The total working electrode overpotential can be divided into activation η_a , resistance η_Ω , concentration η_c and crystallization η_y overpotential according to the four possible types of rate-control in PEVD electrochemical reactions. The total overpotential of the working electrode is given by the algebraic sum of the various components, since several of them usually operate simultaneously.

$$\eta = \eta_a + \eta_\Omega + \eta_c + \eta_y \quad (6-9)$$

Resistance overpotential η_Ω and activation overpotential η_a are characteristic of irreversible reactions and are therefore termed “irreversible overpotentials”. Since deviations from the equilibrium potential due to changes in the concentrations of the reactants are largely reversible, concentration overpotential η_c is known as a “reversible polarization”. The crystallization overpotential η_y is more complicated. It can be caused either by “reversible polarization” or “irreversible polarization”. The details will be discussed later.

In electrode kinetics, as in chemical reaction kinetics, the slowest partial reaction is rate determining for the total reaction. The magnitude and type of working electrode overpotential is therefore governed by the slowest partial reaction, which might have

been included in the measurement. Thus, distinguishing various overpotentials during PEVD is critical to understand the kinetics of a PEVD process. However, the various components of the total working electrode overpotential can only be resolved under suitable conditions. If several of the reactions have slow reaction rates of similar orders of magnitude, the corresponding overpotentials are superimposed to form the total overpotential. Separation of the various components becomes very difficult. Before moving on to distinguish the overpotentials at the working electrode during a PEVD reaction, their causes will first be discussed.

6.2.2.1. Activation Overpotential

An overall electrode reaction differs from an overall chemical reaction in that at least one partial reaction of the overall electrode reaction must be a charge-transfer reaction. Activation overpotential at the working electrode of the PEVD system is due to slow charge transfer reactions at the working electrode/solid electrolyte interface (location (II) of Figure 3-3). During the charge-transfer reaction, charge carriers (A^+ and e^-) are transported against the potential controlled activation energy from solid electrolyte (E) and working electrode (W) into PEVD product (D) across the electrical double layer. The rate of the charge-transfer reaction is determined by the potential difference across the double layer. Thus, it is a measure of how easily charged particles (A^+ and e^-) cross the interfaces at location (II).

If only the charge-transfer reaction is hindered and not any of the other preceding or following partial reactions, the experimentally measurable total overpotential at the working electrode η_w of the PEVD system equals the activation overpotential η_a and is related to the PEVD current via the Butler-Volmer equation (Hotzel and Weppner, 1980):

$$I = I_o \left[\exp\left(\frac{\alpha_a F \eta}{RT}\right) - \exp\left(-\frac{\alpha_c F \eta}{RT}\right) \right] \quad (6-10)$$

where I_0 is the exchange current at the interface. It measures the polarizability of a solid electrolyte/electrode interface. It is worth noting that I_0 is, in general, strongly dependent both on temperature and on gas composition. α_a and α_c are the anodic and cathodic transfer coefficients, respectively, and were introduced by Erdey-Gruz and Volmer (Erdey-Gruz and Volmer, 1930). Generally, transfer coefficients have values ranging from zero to unity ($0 < \alpha < 1$). It has been experimentally shown that, within a certain potential range, this coefficient is independent of potential.

When $|\eta| > 100$ mV then the Butler-Volmer equation reduces to its “high field approximation” form:

$$\ln\left(\frac{I}{I_0}\right) = \frac{\alpha_a F \eta}{RT} \quad (6-11)$$

for anodic ($I > 0$, $\eta > 0$) operation and

$$\ln\left(-\frac{I}{I_0}\right) = \frac{\alpha_c F \eta}{RT} \quad (6-12)$$

for cathodic ($I < 0$, $\eta < 0$) operation. Thus, in a conventional Tafel plot of $\ln |I|$ vs. η , a linear region (Tafel region) is obtained at $\eta > 100$ mV. The exchange current I_0 can be obtained by extrapolating the linear part of the $\ln |I|$ vs. η plot to $\eta_a = 0$. The slopes of the linear parts of the plot give the transfer coefficients α_a and α_c .

6.2.2.2. Resistance Overpotential

Resistance overpotential η_Ω , which corresponds to an ohmic potential drop at the working electrode, is usually negligible in a common electrochemical system, provided the electrode is sufficiently conductive. However, resistance overpotential can be created by a number of causes, such as the presence of surface films. In the PEVD system, the

“surface film” is the product of the PEVD process. Thus, resistance overpotential could be a major contributor to the overall overpotential at the working electrode of a PEVD system. The solid-transported reactant (A) must migrate from location (II) through the deposit (D) to react with the sink vapor phase at location (III) of Figure 3-3. As discussed in Chapter 3, this transport process in a solid phase is the combination of both ionic (A^+) and electronic (e^-) carriers migrating under an electrochemical potential gradient. If the other overpotentials at the working electrode of the PEVD system are negligible, the transport rate is related to the total overpotential at the working electrode η_w and can be expressed as:

$$I = -G_D \eta_w \quad (6-13)$$

where G_D is the conductivity of (A) in deposit (D) as defined in Chapter 3. Accordingly, if G_D is constant during a PEVD process, the transport rate or PEVD current is linearly related to the overpotential η_w at the working electrode.

6.2.2.3. Concentration Overpotential

Concentration overpotential η_c in a PEVD process is due to slow mass transfer of gaseous reactants and/or products involved in the overall working electrode reaction. During the passage of a current, the activities (or concentrations) of the gaseous reactants near the working electrode surface undergo a concentration change from the bulk sink gas phase, resulting in a corresponding shift in the equilibrium electrode potential. Concentration overpotential can be further subdivided into diffusion overpotential η_d and reaction overpotential η_r .

Diffusion overpotential η_d is caused by depletion or enrichment of the reactants at the surface of the working electrode. A transport process is involved in the overall electrode reaction by which the substances formed or consumed during the reaction are transported to or from the working electrode surface. This mass transport is necessary for the overall electrode reaction and takes place by diffusion to or from the surface, since the

substances which are to be converted according to Faraday's law are present in sufficient quantities only in the bulk of the sink gas phase. Therefore, a concentration gradient or, more accurately, an activity gradient is established at the electrode surface. Pure diffusion overpotential η_d is encountered if mass transport by diffusion to and from the surface is the slowest process among the partial reactions involved.

Reaction overpotential η_r is caused by chemical reactions whose rates are lower than the preceding or following charge transfer reactions. The equilibrium concentrations required to produce the reversible EMF of the cell are not established quickly enough.

The diffusion and chemical reaction rates depend only on the concentration of gaseous reactants at the working electrode surface, and by definition, are independent of electrode potential. When concentration overpotential dominates the total overpotential at the working electrode, a limiting current I_L exists. This limiting current is the maximum current obtained when the electrochemical reaction is completely mass-transfer controlled (Bockris and Reddy, 1970).

In aqueous electrochemistry, concentration overpotential is frequently important due to low reactant and/or product diffusivities in the aqueous phase and a low operating temperature. In the solid electrolyte cell of the PEVD system, mass transfer in the gas phase and chemical reaction at higher temperatures are usually rapid and, consequently, concentration overpotential is not that significant, especially at low PEVD currents and high PEVD operating temperatures.

6.2.2.4. Crystallization Overpotential

Crystallization overpotential is treated as a special type of overpotential. In the PEVD system, any barrier to the process by which atoms are incorporated into or removed from the crystal lattice of the PEVD product (D) leads to crystallization overpotential η_y .

According to Stranski's theory of crystal growth, each component of the deposited product (D) must first find its way to a suitable site at the edge of a lattice plane before it

can be accepted into the lattice (Stranski, 1928). The additional overpotential observed when this reaction is inhibited is known as crystallization overpotential.

Electrocrystallization in PEVD may be split into the following three stages:

- (a) transition;
- (b) surface diffusion to the growth center;
- (c) inclusion in the lattice.

The characteristics of the observed crystallization overpotential are again determined by the stages which proceed at the lowest rate. Usually, step (c), inclusion into the lattice, is not a rate limiting step.

If step (a), the transition of charged components, is a limiting step, an inhomogeneous electric field is set up at the surface of the deposit (D) to guide the charged components into the active positions, and a linear relationship should, therefore, exist between the process rate and overpotential. This overpotential, which is due to distortion of the electric field, is usually small and is part of the resistance overpotential.

If step (b), surface diffusion to the growth center, is a rate limiting step, component concentration gradients are formed at the surface of the deposit (D). The observed overpotential could then be interpreted as a form of concentration overpotential, and is independent of the working electrode potential of the PEVD system.

On the basis of previous experimental evidence in this field, it has not as yet been possible to decide in favor of one or the other of the two theoretical transport mechanisms, as no unequivocal conclusions may be drawn from the measured steady-state current-potential curves. On the other hand, impurities will have a strong influence on crystallization overpotential.

6.3. PEVD System for Electrochemical Studies

6.3.1. PEVD System Setup

The PEVD process for Na_2CO_3 auxiliary phase deposition at the working electrode of a potentiometric CO_2 sensor was selected for the current electrochemical studies. Various kinds of overpotentials at the working electrode during the PEVD process were evaluated by both steady-state potentiostatic and dynamic potential sweeping methods in the hope of understanding the process kinetics.

The PEVD system used in this investigation is schematically shown in Figure 6-1. A $\text{Na}^+\text{-}\beta/\beta''\text{-alumina}$ disc from Ceramatec, Inc., Salt Lake City, 16 mm in diameter and 5 mm in thickness, was used as the solid electrolyte with a working electrode on one side and both counter and reference electrodes on the other. To simplify data interpretation, the same electrode material, a Pt thick film, was used for all three electrodes, so the measured potential difference V_{WR} could be directly related to the average inner potential difference between the working and reference electrode (Vayenas et al., 1990; Ladas et al., 1991). The preparation of Pt thick films for electrodes by screen printing has been presented in Chapter 4. In order to make good electrical and mechanical contact, Pt meshes, with spot-welded Pt wires, were sintered on the Pt thick films as electron collectors and suppliers.

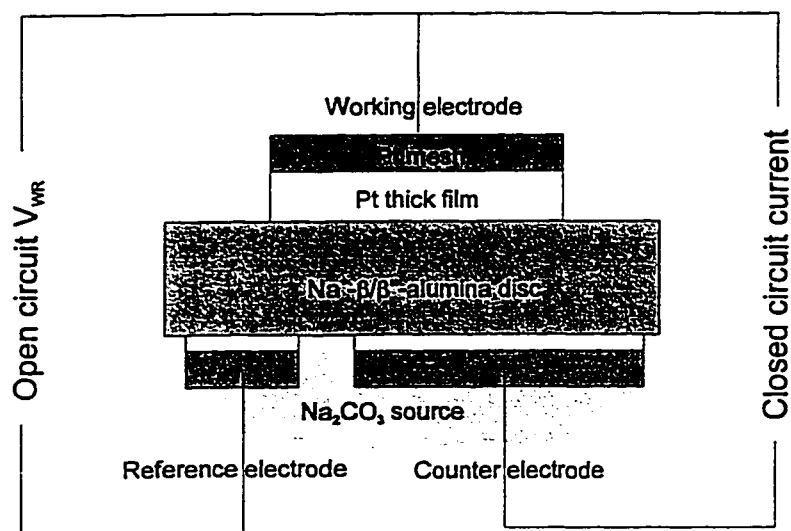


Figure 6-1. The PEVD system setup.

At the source side of the PEVD system, a counter electrode and a reference electrode were deposited on substrate areas of 1 cm^2 and 0.1 cm^2 , respectively. The thickness of both electrodes was about $3 \text{ }\mu\text{m}$. Because rapid equilibration must be established for the electrochemical reaction at the source side during the electrochemical studies, it is important to minimize polarization at the counter and reference electrodes. Thus, the source Na_2CO_3 in this PEVD system wrapped both the counter and reference electrodes due to a melting and quenching technique. The Na_2CO_3 powder was first heated in an alumina crucible above its melting point at 852°C . Then the source side of the PEVD system was quickly dipped into the melt. After cooling to room temperature, a layer of Na_2CO_3 covered both the counter and reference electrodes. Generally, the higher the temperature of the melt, the thinner the wrapped Na_2CO_3 layer. This type of source had a lower overpotential loss. However, the thickness consistency was not very good. In general, the thickness was less than 1 mm when the Na_2CO_3 melt was at 900°C .

At the sink side of the PEVD system, a porous Pt thick film about $7 \text{ }\mu\text{m}$ in thickness was applied to a substrate area of 1 cm^2 . As discussed in Chapter 4, the PEVD process can be divided into two stages. In stage I the PEVD product does not cover the entire Pt thick film; while in stage II, it does. According to previous experiments, the kinetics of the PEVD process are different in both stages. In order to reveal the kinetics of PEVD working electrode reactions at stage I and stage II separately, two kinds of PEVD samples with working electrode Na_2CO_3 coverage corresponding to stage I and stage II were prepared by PEVD. The Na_2CO_3 depositions were similar to those discussed in Chapter 4. Na_2CO_3 coverage at the working electrode was controlled during a potentiometric PEVD process by controlling processing current, and subsequently confirmed by SEM microstructure studies.

During electrochemical studies, either a stage I or stage II PEVD sample system was placed in the constant temperature zone of a tube furnace to maintain a uniform temperature at both the sink and source sides. The same gas phases (ultrazero, Praxair) were fed into both sides of the system at a high flow rate (larger than 100 sccm). The three electrodes of the PEVD system were connected to the external circuit to give two solid electrochemical cells. One was a closed circuit cell from the counter electrode to the working electrode:

(counter) $\text{CO}_2, \text{O}_2, \text{Na}_2\text{CO}_3, \text{Pt}|\text{Na}^+ - \beta / \beta''$ –aluminalPt, $\text{Na}_2\text{CO}_3, \text{CO}_2, \text{O}_2$ (working) (6-14)

The other was an open circuit cell from the reference electrode to the working electrode:

(reference) $\text{CO}_2, \text{O}_2, \text{Na}_2\text{CO}_3, \text{Pt}|\text{Na}^+ - \beta / \beta''$ –aluminalPt, $\text{Na}_2\text{CO}_3, \text{CO}_2, \text{O}_2$ (working) (6-15)

Because the atmosphere at both the source and sink sides was the same, the chemical potential of sodium was equal and fixed by the Na_2CO_3 phase in equilibrium with the same atmosphere at all three Pt electrodes, when no electric field was present. At this point, the equilibrium electrochemical reaction



prevailed at all three electrodes. Accordingly, the equilibrium potential was zero under both open and closed circuit conditions if there was no applied electric potential. By adjusting V_{WR} in the open circuit electrochemical cell, the working electrode overpotential η_w varied according to Eq.(6-6). Correspondingly, the current through the closed circuit between the working and counter electrodes changed to reveal the kinetics of PEVD working electrode reactions as well as the mass and charge transport rate through the PEVD system. A negative V_{WR} or η_w increased the chemical potential of Na at the working electrode, and reaction (6-16) moved to the right forming Na_2CO_3 at the working electrode. A positive V_{WR} decreased the chemical potential of Na at the working electrode, and reaction (6-16) moved to the left resulting in Na_2CO_3 decomposition at the working electrode.

6.3.2. PEVD Reaction Rate Limiting Steps at the Working Electrode

For Na_2CO_3 formation at the working electrode of a PEVD sample, the overall electrochemical reaction can be divided into six rate-limiting steps as schematically shown in Figure 6-2. These steps are

Step 1: Charge transfer reaction at location (II).



If this step is the rate limiting step for the PEVD reaction at the working electrode, the working electrode overpotential is dominated by an activation overpotential η_a .

Step 2: Solid-state transported reactant Na diffusion from location (II) to (III).

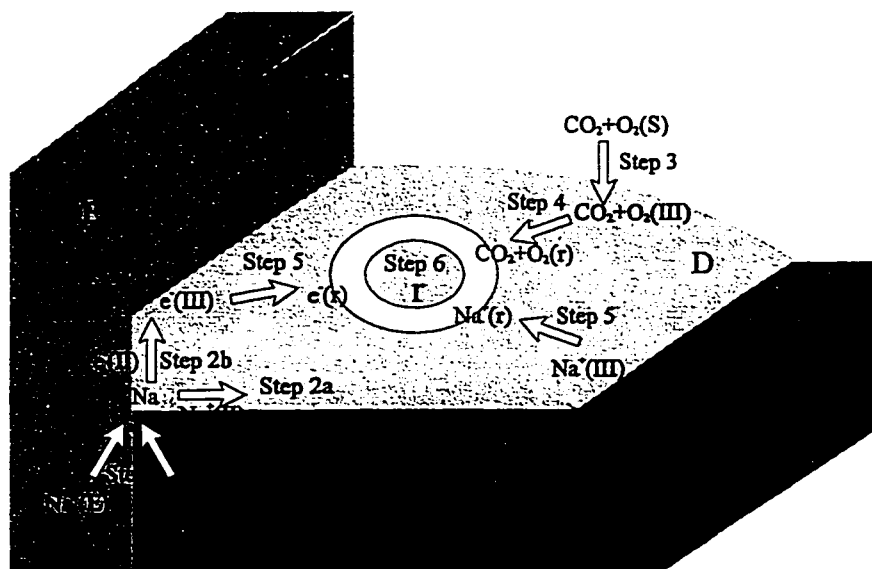


Figure 6-2. The kinetic steps for PEVD reaction at the working electrode.

If this step is the rate limiting step for the PEVD reaction at the working electrode, the working electrode overpotential is dominated by a resistance overpotential η_r . This can be considered separately for both stage I and stage II PEVD samples. For Na_2CO_3 formation at the working electrode of a stage I PEVD sample, the working electrode of the PEVD system has not been covered by the product. Thus, an electronically shorted surface exists to transport electrons from the location (II) to (III). Growth is preferred along the Y direction (Figure 3-8). The process is limited by the diffusion of Na^+ from location (II) to (III).



For Na_2CO_3 formation at the working electrode of the PEVD system during stage II growth, the Pt electrode in the PEVD system has already been covered with a layer of Na_2CO_3 . Further growth is in the X direction to increase the thickness of the product. According to the discussion in Chapter 3 and 4, this step is limited by electron diffusion.



Step 3: Gas phase diffusion and surface adsorption of CO_2 and O_2 from the bulk of sink gas phase (S) to the working electrode surface at location (III).



If this step is the rate limiting step for the PEVD reaction at the working electrode, the working electrode overpotential is dominated by a concentration overpotential η_c (diffusion overpotential η_d).

Step 4: Surface transport of neutral reactants at the working electrode surface to the reaction sites (r).



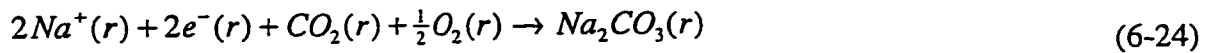
If this step is the rate limiting step for the PEVD reaction at the working electrode, the working electrode overpotential is dominated by a crystallization overpotential η_y . This crystallization overpotential behavior is similar to a concentration overpotential.

Step 5: Surface transport of charged reactants at location (III), the product surface, to the reaction sites (r).



If this step is the rate limiting step for the PEVD reaction at the working electrode, the working electrode overpotential is dominated by a crystallization overpotential η_y . This crystallization overpotential behavior is like a resistance overpotential.

Step 6: Chemical reaction at the reaction sites (r) to form the product Na_2CO_3 .



If this step is the rate limiting step for the PEVD reaction at the working electrode, the working electrode overpotential is dominated by a concentration overpotential η_c (reaction overpotential η_r).

6.4. Steady-State Potentiostatic Studies

The purpose of steady-state potentiostatic studies is to obtain a series of PEVD working electrode overpotentials and corresponding steady-state current values at various

processing temperatures. According to the previous discussion, each possible kinetic limiting step for the overall PEVD reaction causes different effects in steady-state I - η curves. Furthermore, from the temperature dependence of the PEVD current, the activation energy for various PEVD processing conditions can be obtained to determine the possible reaction limiting step.

6.4.1. Experimental Methods

During the steady-state potentiometric study, a potentiostat-galvanostat (Princeton Applied Research 371) was connected to the three electrodes of the PEVD sample. A constant dc electrical potential V_{WR} across the open circuit electrochemical cell between the working electrode and reference electrode was set up manually with the potentiostat-galvanostat. According to Eq.(6-6), V_{WR} is equivalent to the working electrode overpotential η_w of a PEVD system. At each η_w , a current I , that flows through the closed-circuit electrochemical cell between the working and counter electrode, was then measured by the potentiostat-galvanostat. However, it is current density, instead of current, that is directly related to the kinetics of a PEVD reaction at the working electrode. In order to relate the potentiostat-galvanostat measured current directly to the kinetics of a PEVD reaction at the working electrode, it is imperative to maintain the reaction area at the working electrode relatively unchanged during the time of testing. As discussed previously, the PEVD working electrode undergoes constant change due to the formation of PEVD products. This is especially true for a stage I PEVD sample. No steady-state current can be obtained at a constant V_{WR} . Thus, a steady-state potentiostatic study is unsuitable to study the kinetics of stage I PEVD reactions.

For a stage II PEVD sample, on the other hand, a steady-state current can be obtained at a constant V_{WR} after a period of charging time. This is because the working electrode surface reaction area is constant during stage II PEVD growth. For instance, the current response of a stage II PEVD sample after V_{WR} is increased from 20 to 40 mV at 530°C is recorded in Figure 6-3. The current increases sharply upon increasing V_{WR} , and then

decays exponentially to approach a stationary value. This kind of current response is common for an electrochemical system with a non-negligible capacitance. In order to reach a steady-state current, a period of time is necessary to allow the charging current to die out. However, because the PEVD product thickness continues to increase at the working electrode during the delay time, the solid-state transport distance in the PEVD product will increase. Thus, it is advantageous to shorten the waiting time for the current reading at each step. According to Figure 6-3, a 60 s waiting time is a compromise solution, since the charging current component at 60 s is less than 20% of the final steady-state current. In this way, the I - η behavior for a stage II PEVD reaction was also experimentally repeatable.

Experiments on a stage II PEVD sample were conducted at six temperatures from 500 to 550°C at 10°C intervals. At each temperature, V_{WR} was increased step-wise from 0 to 450 mV with 60 s for each step. The resultant current flow through the working and counter electrode was measured simultaneously. Both V_{WR} and I were recorded by a dual channel analog recorder (Brinkmann 2742-3).

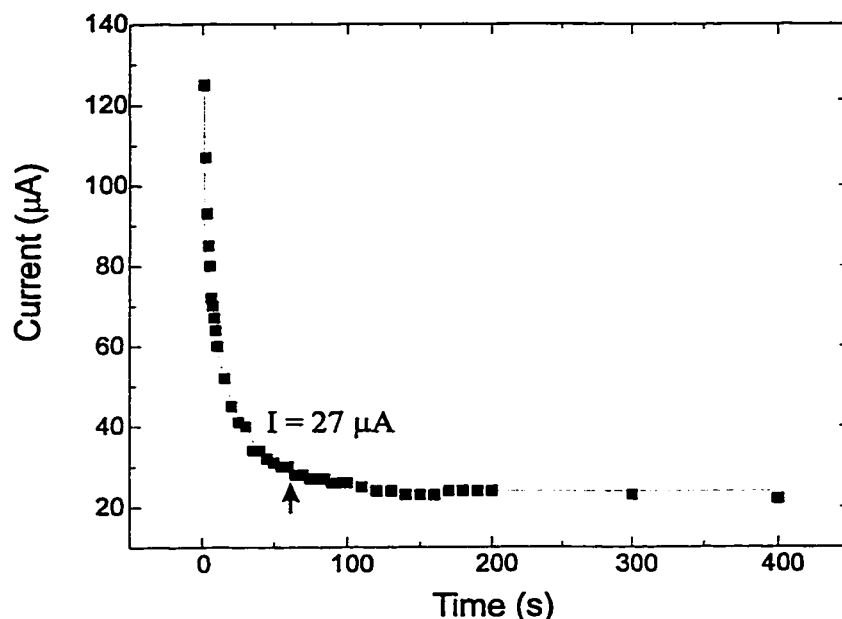


Figure 6-3. Current decay during the charging process.

6.4.2. Results

6.4.2.1. Current – Overpotential Behavior

The PEVD reaction current, 60 s after changing the working electrode overpotential at each step, from a stage II PEVD sample is listed in Table 6-1. The results were repeatable.

Table 6-1. The overpotential and corresponding current during the second stage of growth.

Overpotential (mV)	PEVD current (μ A)					
	550°C	540°C	530°C	520°C	510°C	500°C
0	0	0	0	0	0	0
10	10	7.2	5.3	2.9	0.9	0.3
20	19	14	11	5.9	1.9	1.1
40	48	37	27	13	4	1.7
60	70	51	35	18	6.7	2.3
80	88	64	44	25	8.9	3.2
100	102	75	52	31	12	4.1
120	122	90	62	38	14	5
140	145	106	74	42	17	6
160	172	123	88	49	19	7.1
180	204	147	104	57	22	8.2
200	235	174	124	63	24	9
220	278	206	147	70	27	10
240	329	248	175	76	30	11
260	382	291	195	83	32	13
280	390	342	210	88	35	14
300	387	344	225	93	37	15
320	391	344	240	105	40	16
340	398	347	256	111	42	17
360	390	350	271	116	45	18
380	388	348	285	121	47	19
400	388	348	286	127	50	20
450	391	347	285	143	56	22

Two kinds of plots are commonly used to show the dependence of the current on overpotentials at various temperatures. One is a current vs. overpotential plot as shown in Figure 6-4; the other is a $\ln(\text{current})$ vs. overpotential plot (Tafel plot) in Figure 6-5.

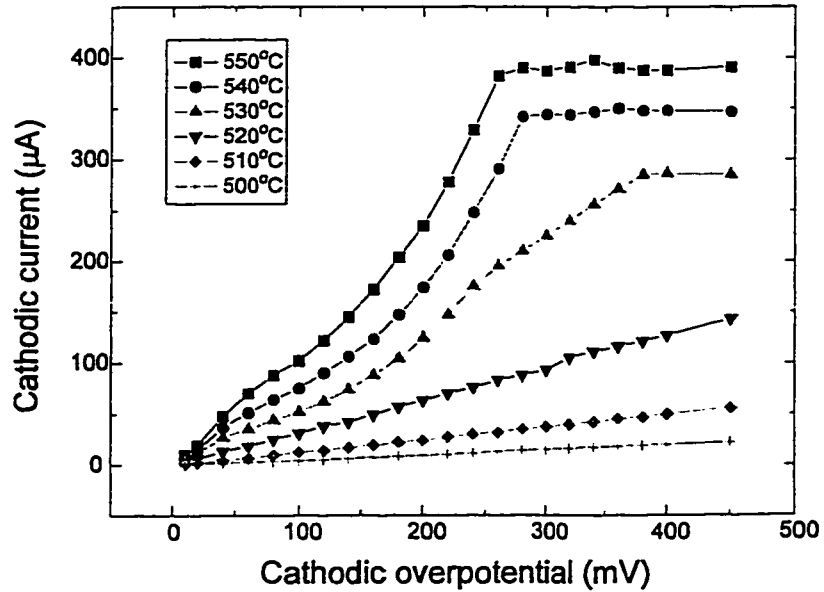


Figure 6-4. Current-overpotential behavior (I - η curves) of a stage II PEVD process at various temperatures.

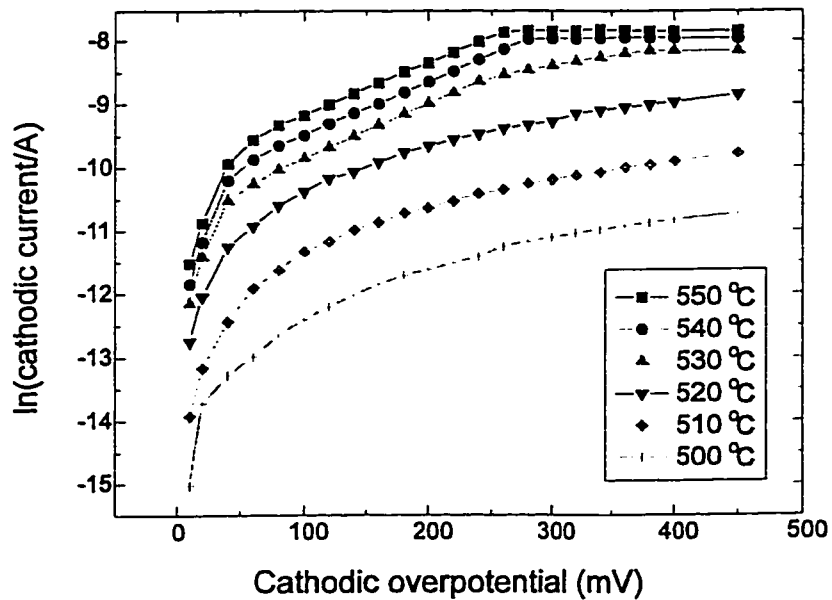


Figure 6-5. Tafel plot ($\ln(I)$ vs. η) of the current-overpotential behavior in Figure 6-4.

At lower temperatures, e.g. 500°C, the I - η curve is almost linear from the abscissa up to a cathodic overpotential of 450 mV. This kind of linear I - η behavior occurs since resistance or crystallization overpotential dominates the total working electrode overpotential. According to the previous discussion, the PEVD reaction rate-limiting step at the working electrode is either Step 2b (electron diffusion) or Step 5 (surface transport of charged reactants).

At higher temperatures, e.g. 550°C, the current-overpotential behavior is similar to that for common electrochemical systems. There are two regions separated at about 260 mV. In the lower overpotential region, a linear curve from 100 to 260 mV is obtained on the Tafel plot (Figure 6-5). This I - η logarithmic relation indicates that activation overpotential dominates the total working electrode overpotential, and the PEVD reaction rate-limiting step is Step 1 (charge transfer reaction). In the higher overpotential region, the current does not respond to further increase in overpotential. This limiting current can be caused by concentration overpotential η_c due to either Step 3 (diffusion overpotential η_d) or Step 6 (reaction overpotential η_r). This can also be caused by crystallization overpotential η_y due to slow surface transport of neutral reactants (Step 4).

The I - η behavior at four intermediate temperatures (540, 530, 520 and 510°C) was also studied to show the transition from lower temperature to higher temperature kinetic behavior. It was found that the 510 and 520°C curves are similar to the lower temperature one at 500°C, in which the current response to the overpotential is linear through the entire testing range. The 540°C curve resembles the 550°C curve, in which a linear logarithmic response is followed by a limiting current at higher overpotential. At 530°C, all three kinds of kinetic response, i.e., logarithmic, linear and constant with increasing overpotential, exist in the I - η curve. Thus, the kinetic transition from low temperature to high temperature behavior in the current PEVD system occurs around 530°C.

6.4.2.2. Activation Energy of PEVD Reaction

In order to further distinguish the PEVD reaction rate limiting steps, activation energies of the PEVD reaction were studied at two overpotentials. Figure 6-6 is the Arrhenius plot of $\ln(I)$ vs. $1/T$ at an overpotential $\eta_w = 100$ mV. Two regions are resolved. In the higher temperature region above 530°C , an activation energy of 185 kJ/mol or 1.9 eV is obtained. This is close to the previously reported activation energy for a charge transfer reaction (Wang and Nowick, 1979a and 1981). In the low temperature region below 530°C , an activation energy of 516 kJ/mol or 5.4 eV is obtained. This value is much higher than would be expected for Step 5, surface diffusion of charged particles. Thus, the possible kinetic limiting step is Step 2b, the diffusion of electrons in the product Na_2CO_3 . However, the value of 5.4 eV is a little less than the activation energy for electronic conduction, which should be close to the bandgap E_g of the product. For inorganic oxysalts, the E_g is expected to be ~ 6.0 eV. One possible explanation is impurity levels may exist between the conduction and valence band (Couturier et al., 1983).

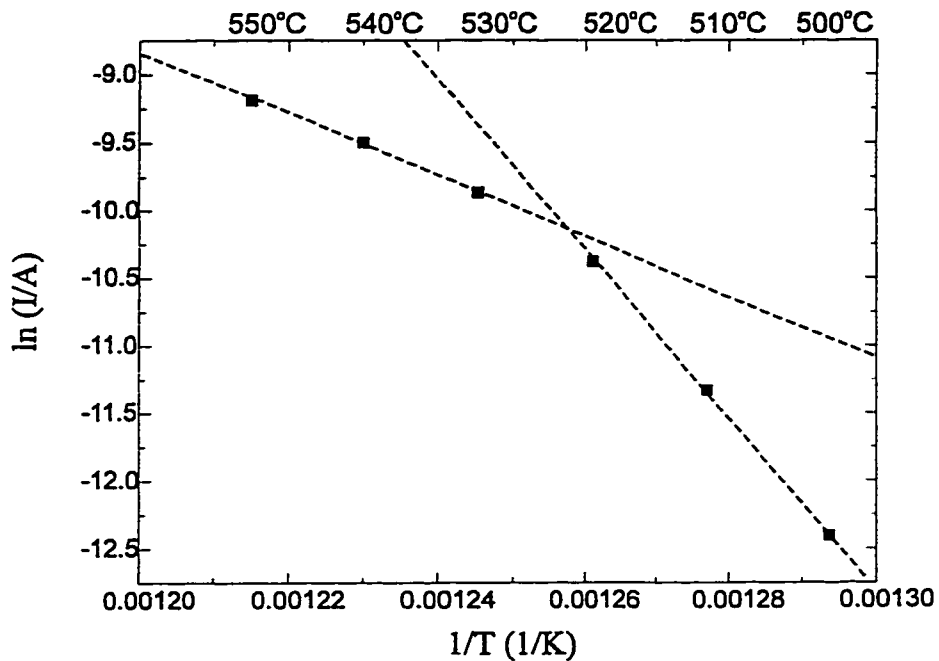


Figure 6-6. Arrhenius plot at $\eta = 100$ mV.

Figure 6-7 is an Arrhenius plot of $\ln(I)$ vs. $1/T$ at an overpotential $\eta_w = 400$ mV. Again there are two regions. The slope of a linear regression curve at the low temperature region is similar to that at the lower overpotential, $\eta = 100$ mV. Thus, the kinetic limiting step is still Step 2b, the diffusion of electrons. The calculated activation energy $E_a = 4.9$ eV in this plot is actually a little lower than the previous one (5.4 eV). This difference could be due to the changes in the working electrode during product formation. Thus, the most reliable activation energy for Step 2b could be extracted from the slopes of the I - η curves at the lower temperatures as shown in Figure 6-8. Accordingly, the activation energy is 464 kJ/mol, or 4.8 eV.

At higher temperatures in Figure 6-7, an activation energy of 84 kJ/mol or 0.8 eV is obtained. Although increasing temperature will increase gas phase diffusion through an increase in molecular diffusion velocity, the mean free path will decrease. The result is only a weak thermal activation of gas phase diffusion for step 3. The activation energy value is more likely to be due to Step 4 (surface diffusion of neutral reactants) or Step 6 (chemical reaction).

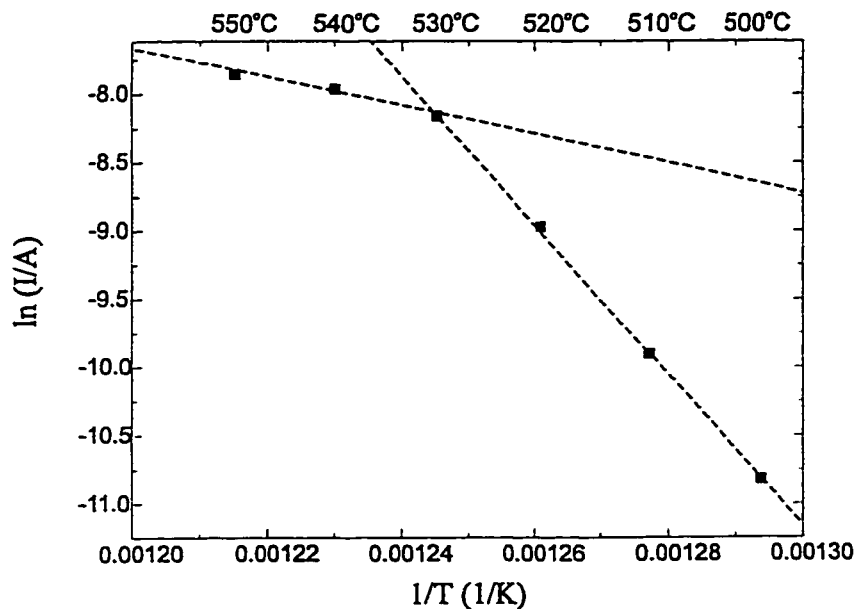


Figure 6-7. Arrhenius plot at $\eta = 400$ mV.

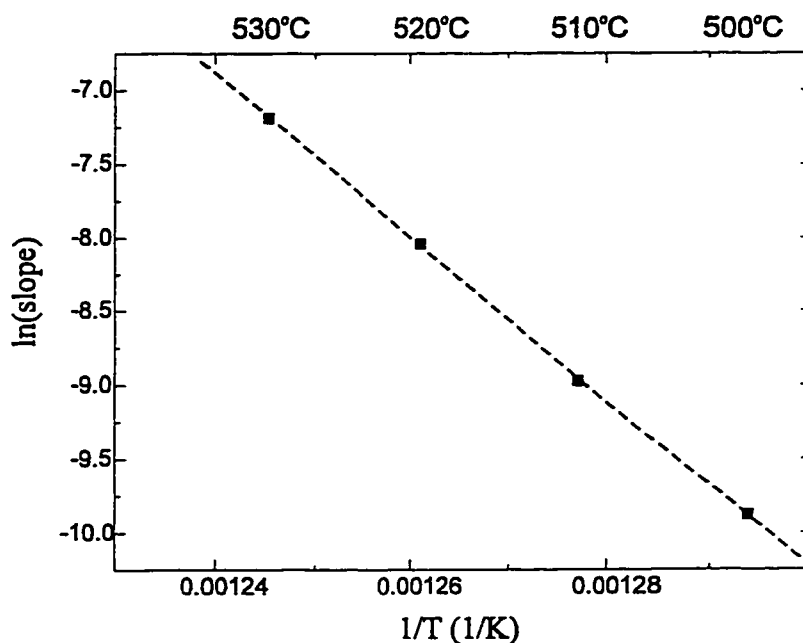


Figure 6-8. Arrhenius plot of the slope of the I - η curves at lower temperatures.

6.4.2.3. Exchange Current for the PEVD System

The exchange current I_0 and cathodic transfer coefficient α_c for the PEVD system can be extracted from standard Tafel plots (Figure 6-5) as described in detail previously, and provide a measure of the nonpolarizability of the solid electrolyte/electrode interface (Wayenas et al., 1988; Robertson and Michaels, 1990). The values of I_0 and α_c at various temperatures are shown in Table 6-2. The activation energy of the exchange current can then be obtained from an Arrhenius plot in Figure 6-9 as 200 kJ/mole (2.1 eV), which is fit to those in the literature in the range of 1.2 to 2.7 eV (Wang and Nowick, 1979b).

The cathodic transfer coefficient α_c is generally invariant with temperature (Bard and Faulkner, 1980). A constant value from this experiment further indicates the reliability of using the steady-state potentiostatic method to study stage II PEVD reactions.

Table 6-2. Temperature dependence of exchange current and cathodic transfer coefficient.

Temperature (°C)	Exchange current I_0 (μA)	Cathodic coefficient α_c
550	45.5	0.58
540	32.2	0.59
530	22	0.60

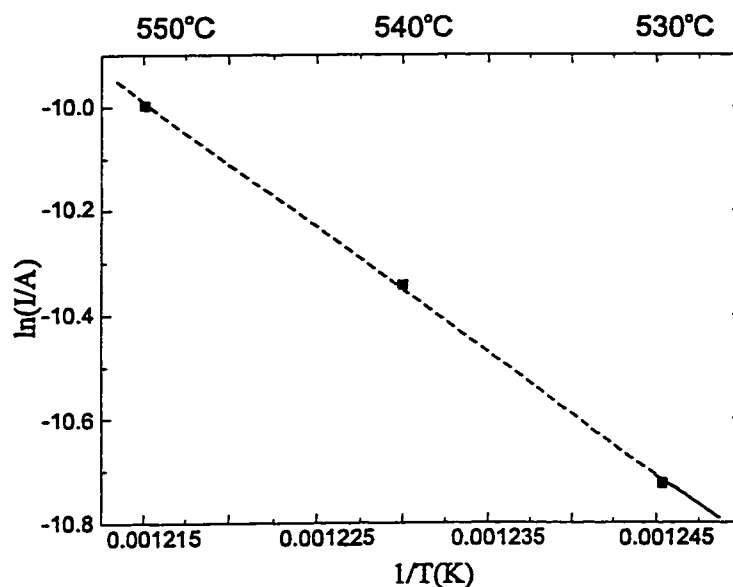


Figure 6-9. Activation energy of the exchange current.

6.4.3. Summary

The current-overpotential behavior of the cathodic PEVD product formation at the working electrode during stage II of PEVD has been studied at various temperatures. The repeatability of the I - η curves in stage II of a PEVD process is fairly good. Thus, the change in geometric factor of the working electrode during the period of potentiostatic study is negligible. Accordingly, the PEVD reaction rate-limiting steps at the working electrode for a stage II PEVD process are collected in Table 6-3.

Table 6-3. Stage II PEVD steady-state potentiostatic study results.

PEVD parameters		I - η relation	Dominant η	Rate limiting steps	Activation energy (eV)
Temp. (°C)	η_w (mV)				
500, 510, 520	0 - 450	Linear	η_Ω	Step 2b, diffusion of electrons	4.8
530	0 - 220	Logarithmic	η_a	Step 1, charge transfer reaction	1.9
	230 - 380	Linear	η_Ω	Step 2b, diffusion of electrons	4.8
	390 - 450	Limiting	η_y	Step 4, surface diffusion of neutral reactants	0.87
			η_c	Step 6, chemical reaction	
540, 550°C	0 - 260	Logarithmic	η_a	Step 1, charge transfer reaction	1.9
	270 - 450	Limiting	η_y	Step 4, surface diffusion of neutral reactants	0.87
			η_c	Step 6, chemical reaction	

6.5. Cyclic Voltammetry Studies

The technique of cyclic voltammetry or, more precisely, linear potential sweep chronoamperometry, is used routinely in aqueous electrochemistry to study the mechanisms of electrochemical reactions (Bard and Faulkner, 1980; Beden et al., 1982; Papoutsis et al., 1987; Lamy-Pitara et al., 1989; Vayenas et al., 1991). Currently, cyclic voltammetry has become a very popular technique for initial electrochemical studies of new systems and has proven very useful in obtaining information about fairly complicated electrochemical reactions (Bard and Faulkner, 1980). There have been some reported applications of cyclic voltammetry for solid electrochemical systems (Fabry and Kleitz, 1979; Olmer et al., 1982; Schouler and Kleitz, 1987). It is worth pointing out that,

although the theory of cyclic voltammetry originally developed by Sevcik (1948), Randles (1948), Delahay (1954), and Srinivasan and Gileadi (1966) and lucidly presented by Bard and Faulkner (1980) is very well established and understood in aqueous electrochemistry, one must be cautious when applying this theory to solid electrolyte systems of the type described here, as some non-trivial refinements may be necessary.

Because of the geometric change at the working electrode due to the growth of the PEVD product, the results from a steady-state potentiostatic study are not applicable to stage I of PEVD. In this study, a solid electrolyte cyclic voltammetry (SECV) method was applied for two reasons:

- (a) It is possible to resolve complicated electrochemical reactions and qualitatively reveal the general current-overpotential behavior.
- (b) Both anodic and cathodic potentials are applied during a single scan, which is fast enough to minimize the working electrode change of a PEVD sample during testing.

6.5.1. Experimental Setup

During the SECV study, the PEVD system and all experimental parameters were similar to those in the steady-state potentiostatic work. The only difference was the external circuit, in which a CAS-100 system (Gamry, Inc.) was used to connect with a PEVD sample. This setup permits linear variation in time of the working electrode potential with respect to the reference electrode V_{WR} according to

$$\begin{aligned}
 V_{WR} &= V_{WR,1} + vt; & 0 < t \leq \frac{\tau}{2} \\
 V_{WR} &= V_{WR,2} - vt; & \frac{\tau}{2} < t \leq \tau \\
 \tau &= 2(V_{WR,2} - V_{WR,1})/v
 \end{aligned}
 \tag{6-25}$$

where $V_{WR,1}$ is the initial ($t = 0$) working electrode potential corresponding to the beginning of each cycle, $V_{WR,2}$ is the switching potential, τ is the time for one scan and v (V/s) is the sweep rate. The current I flowing between the working and the counter

electrode can be recorded simultaneously to reveal the rate of the PEVD reaction taking place on the working electrode.

6.5.2. Results and Discussion for Stage II of PEVD

The validity of the SECV method was first tested for a stage II PEVD sample at 550°C. Thus, the results from SECV and the steady-state potentiostatic method could be compared.

6.5.2.1. General Features of an SECV Spectrum

Figure 6-10 shows a three-dimensional SECV spectrum for a stage II PEVD system at 550°C. This spectrum can be projected to three planes, i.e., the working electrode overpotential – PEVD current ($V_{WR}-I$) plane, the PEVD current – time ($I-t$) plane and working electrode overpotential – time ($V_{WR}-t$) plane.

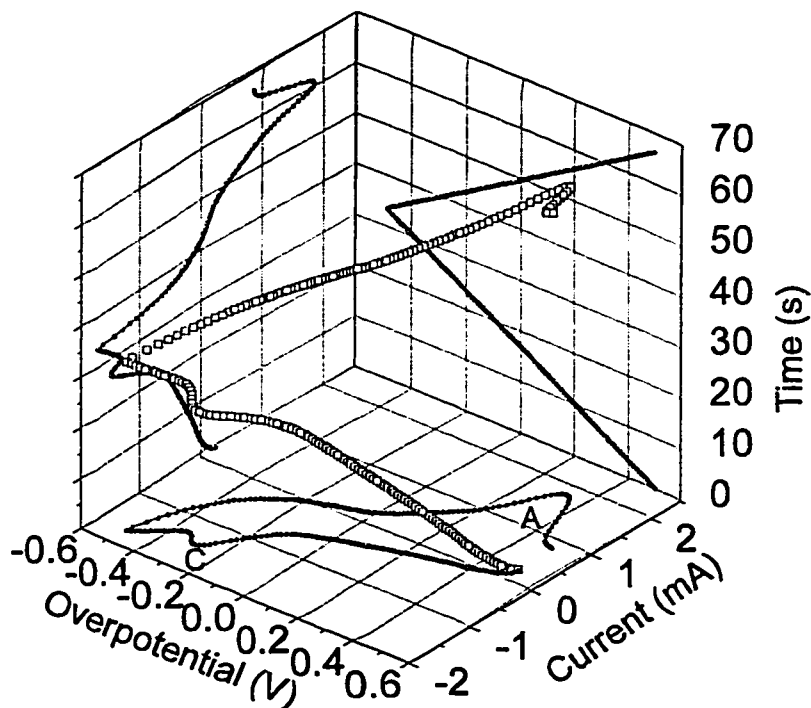


Figure 6-10. A three-dimensional SECV spectrum and its projection planes for a stage II PEVD sample at 550°C.

Traditionally, the most important projected curve, “cyclic voltammogram”, is the one on the V_{WR} - I plane. The peaks labeled C and A are the major features of the voltammogram. The cathodic peak C centered at $V_{WR} = -290$ mV corresponds to PEVD product (Na_2CO_3) formation at the working electrode; the anodic peak A at $V_{WR} = 320$ mV corresponds to Na_2CO_3 decomposition at the working electrode. The main reason that the current follows different paths on the $V_{WR} - I$ plane upon increasing and decreasing V_{WR} is due to the fact that part of the current is used to charge the solid electrolyte/electrode interface, which has a nonzero capacitance C_d . The “thickness” ΔI of the cyclic voltammogram is of the order of $2vC_d$. Thus ΔI decreases with decreasing sweep rate v and vanishes at $v = 0$, together with the cathodic peaks labeled C and the anodic peak labeled A (Wang and Nowick, 1979a, 1979b and 1981). At this limit the entire cyclic voltammogram collapses into a single curve between A and C. The electrochemical literature (Bard and Faulkner, 1980) provides a more detailed discussion.

The projected curve on the I - t plane indicates the change in PEVD current as well as the reaction rate as a function of time. Conventionally, $I < 0$ corresponds to cathodic currents, i.e., I/F expresses the rate of supply of Na^+ to the working electrode. The area of the cathodic current peak on the I - t plane is 0.02631 C, which corresponds via Faraday’s law to the reduction of 2.7×10^{-7} mol of Na to form 14 μg of Na_2CO_3 . According to the results from Chapter 4, this amount of Na_2CO_3 is equivalent to an increase of about 12.5 nm in product thickness during stage II PEVD. Thus, the change to the working electrode is insignificant during a single scan.

The projected curve on the V_{WR} - t plane records the change of the imposed working electrode overpotential waveform during the V_{WR} scan. An important parameter in cyclic voltammetric studies is the sweep rate v . The linear sweep rate for Figure 6-10 was 30 mV/s.

6.5.2.2. Effects of Sweep Rate

The cyclic voltammograms for various sweep rates at 550°C are reported in Figure 6-11. According to the theory of cyclic voltammetry (Bard and Faulkner, 1980), the peak

overpotential shift and peak current convey important information. A reversible redox reaction will not exhibit peak shifting with sweep rate change. In an aqueous electrochemical cell, the shift is generally caused by an irreversible redox reaction due to slow charge transfer compared with diffusion in the electrolyte. In such cases, the peak current I_p linearly increases with v (Bard and Faulkner, 1980). However, when the charge transfer reaction does not involve a chemisorbed reactant, then, in practically all other cases, I_p varies linearly with $v^{1/2}$. In this study, the current for both peaks is linearly related to $v^{1/2}$ as shown in Figure 6-12.

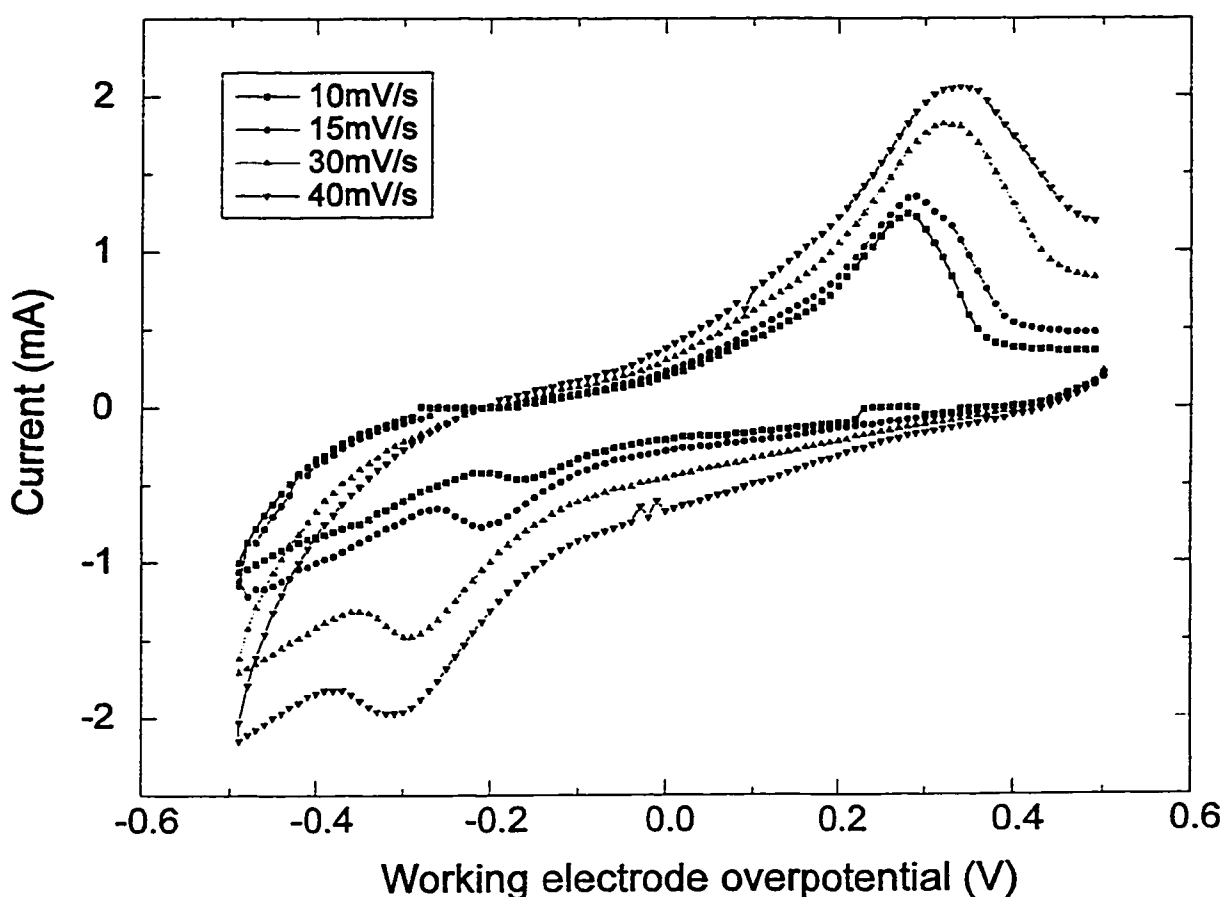


Figure 6-11. Cyclic voltammograms at various sweep rates during stage II PEVD (550°C).

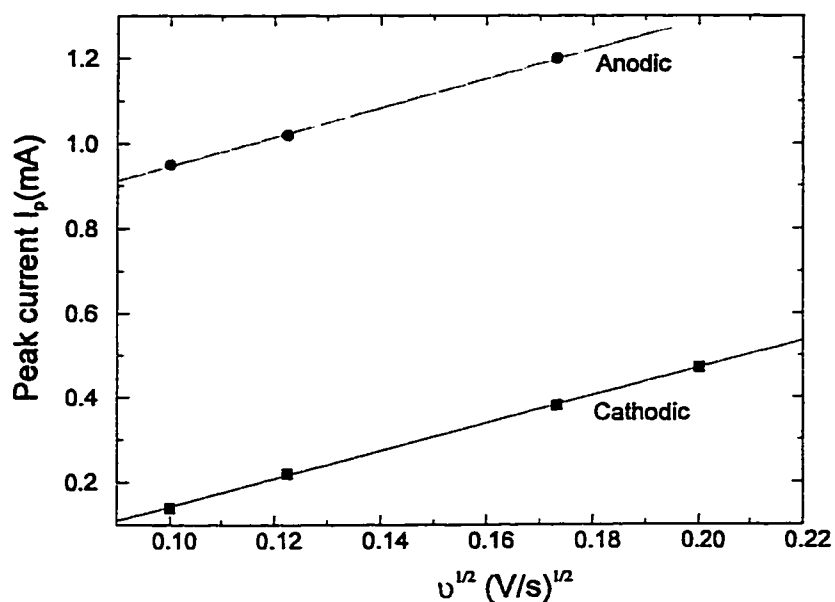


Figure 6-12. Cathodic and anodic peak currents in Figure 6-9 vs. the square root of the sweep rates.

Figure 6-11 also shows the effect of sweep rate ν on the cathodic peak potential $V_{WR,c}$. Increasing ν shifts $V_{WR,c}$ to more negative potentials. According to the theory of cyclic voltammetry, the magnitude of peak shift at various sweep rates permits direct computation of the cathodic transfer coefficient α_c :

$$\frac{dE_{p,c}}{d \ln \nu} = -\frac{RT}{\alpha_c F} \quad (6-26)$$

Figure 6-13 shows the usefulness of solid electrolyte cyclic voltammetry (SECV) for extracting transfer coefficients. The peak potentials are plotted against the logarithmic of the sweep rates. The α_c value can be obtained from the slope of the linear regression curve. It is calculated to be 0.63, which is close to the value, 0.59, obtained from the steady-state potentiostatic study.

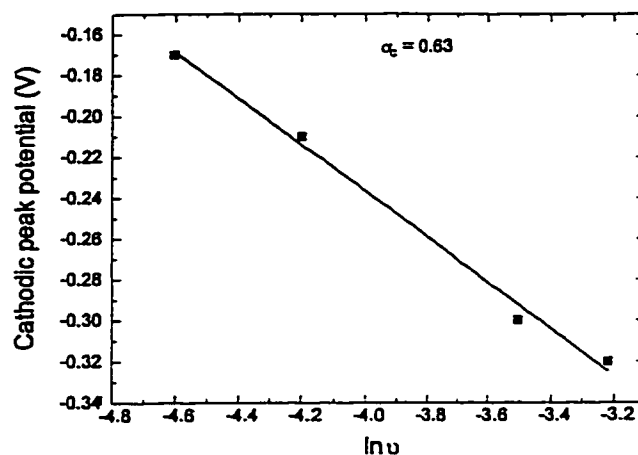


Figure 6-13. Linear regression of cathodic overpotential vs. logarithm of sweep rate.

Similarly, based on the equation for anodic peaks,

$$\frac{dE_{p,a}}{d \ln v} = \frac{RT}{\alpha_a F} \quad (6-27)$$

From the slope of the linear regression curve in Figure 6-14, the anodic transfer coefficient α_a is 1.

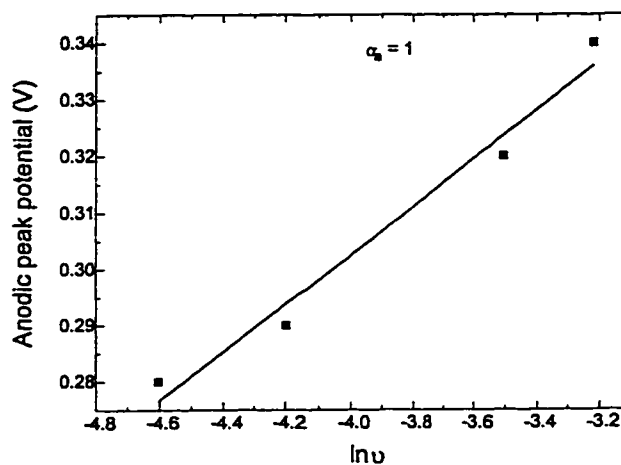


Figure 6-14. The linear regression of anodic overpotential vs. logarithm of sweep rate.

6.5.2.3. Effect of Holding Time

By holding the working electrode overpotential at 600 mV (anodic overpotential) for a period of time, then scanning to -1000 mV (cathodic overpotential), cyclic voltammograms are generated as shown in Figure 6-15. The cathodic peaks shift to lower (or more negative overpotentials) as the holding time increases. This indicates that the PEVD reaction is less limited by the higher overpotential limiting step. According to the results from steady-state potentiostatic studies (Table 6-2), the higher overpotential limiting step could be Step 3, Step 4 or Step 6. These experimental results indicate that Step 4 is more likely to be the higher overpotential limiting step, since Na_2CO_3 decomposes at the working electrode during the time of holding at an anodic overpotential. The longer the holding time, the more the decomposition proceeds. Step 3 and Step 6, gas phase diffusion and chemical reaction, respectively, will not be affected by this decomposition. On the other hand, surface diffusion of neutral reactants in Step 4 will be enhanced by the decomposition, since the products from decomposition are close to the reaction sites for formation. Thus, the limiting current for Step 4 will increase at the same working electrode overpotential. This delays the kinetic limitation step switch from Step 1 to Step 4. An interesting phenomenon is that the peak overpotential shift is linearly related to the holding time as shown in Figure 6-16.

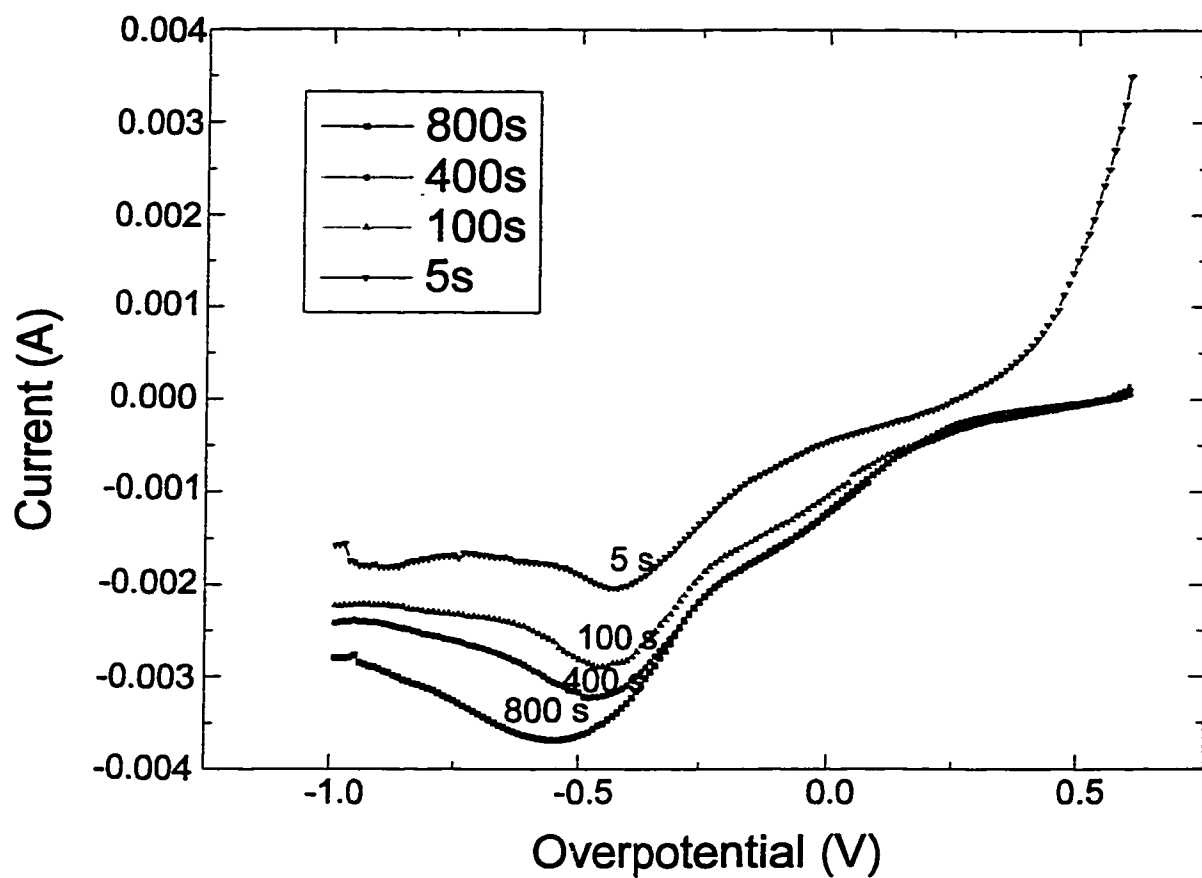


Figure 6-15. Cyclic voltammetric curves at various holding times.

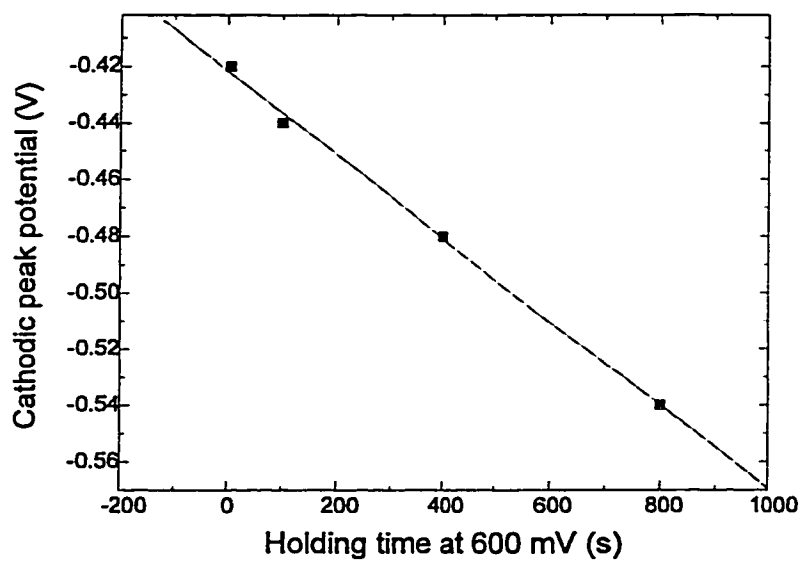


Figure 6-16. Cathodic peak shift at various holding times.

6.5.2.4. Summary

In this section, a number of SECV experimental methods have been applied for the first time to study a PEVD system. The results from a stage II PEVD sample not only confirm the capability of SECV to distinguish various PEVD reaction rate-limiting steps, but also offer complementary information to the steady-state potentiostatic studies. For instance, SECV results further indicate that the rate limiting step at higher temperatures and higher overpotentials is Step 4. Since very little product is deposited on the working electrode during a single scan, SECV is also applicable to study stage I PEVD behavior.

6.5.3. Application of SECV to the Study of Stage I of PEVD

A stage I PEVD sample was tested at 5 temperatures (450, 475, 500, 525 and 550°C).

6.5.3.1. Spectra at Lower Temperatures

Figures 6-17a, 6-18a and 6-19a are cyclic voltammograms for various sweep rates at 450°C, 475°C and 500°C, respectively. The voltammograms have similar features to those obtained from a stage II PEVD sample at higher temperature (550°C). Only one pair of cathodic and anodic peaks exists. The cathodic and anodic peaks shift to more negative and positive potentials at higher sweep rates, respectively. Accordingly, PEVD reaction rate-limiting steps under these conditions are the charge transfer reaction (Step 1) at lower working electrode overpotentials and surface diffusion of neutral reactants (Step 4) at higher working electrode overpotentials.

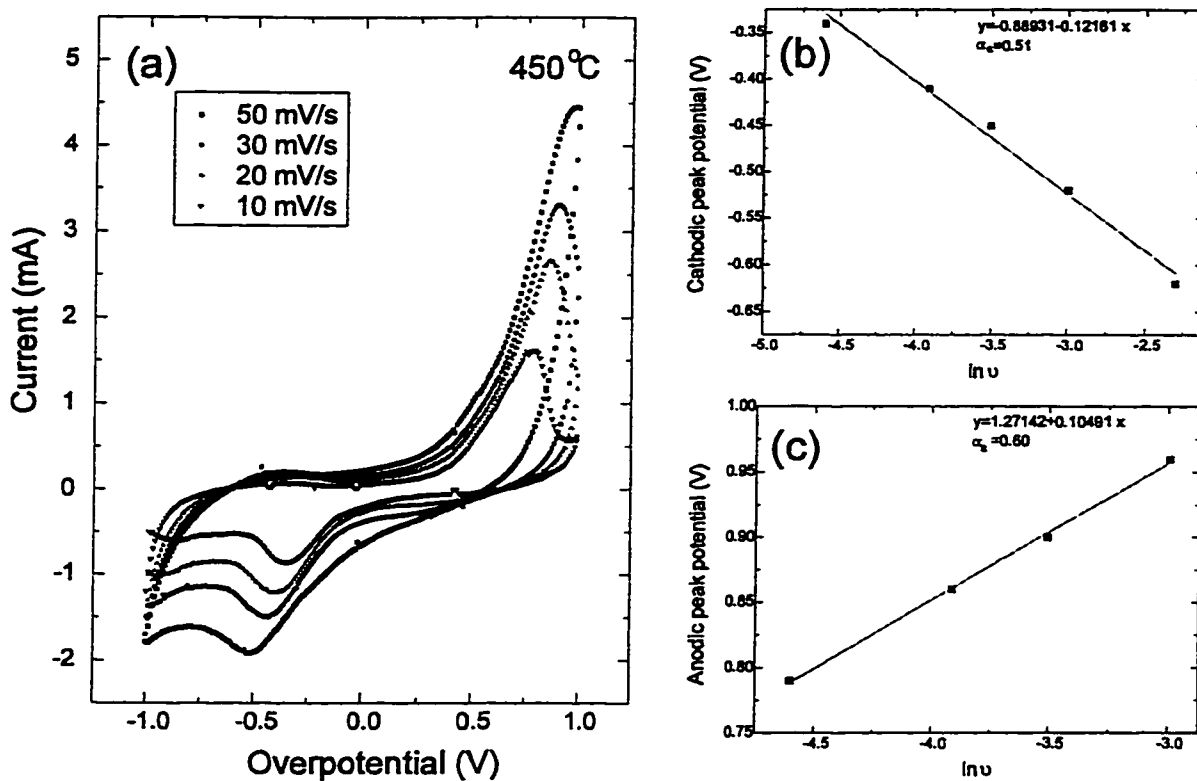


Figure 6-17. (a) Cyclic voltammetric curves at 450°C; (b) cathodic coefficient; (c) anodic coefficient.

Similar to the discussion for stage II, both cathodic and anodic transfer coefficients for the stage I PEVD sample can be obtained from the peak potential shifts resulting from changing sweep rates. The cathodic coefficients at each testing temperature are obtained by the peak overpotential vs. $\ln v$ plots in Figures 6-17b, 6-18b and 6-19b. Similarly, the anodic coefficients at each testing temperature are obtained by the peak overpotential vs. $\ln v$ plots in Figures 6-17c, 6-18c and 6-19c. The resulting α_c and α_a values are listed in Table 6-4, and are compared with those values from the stage II PEVD sample.

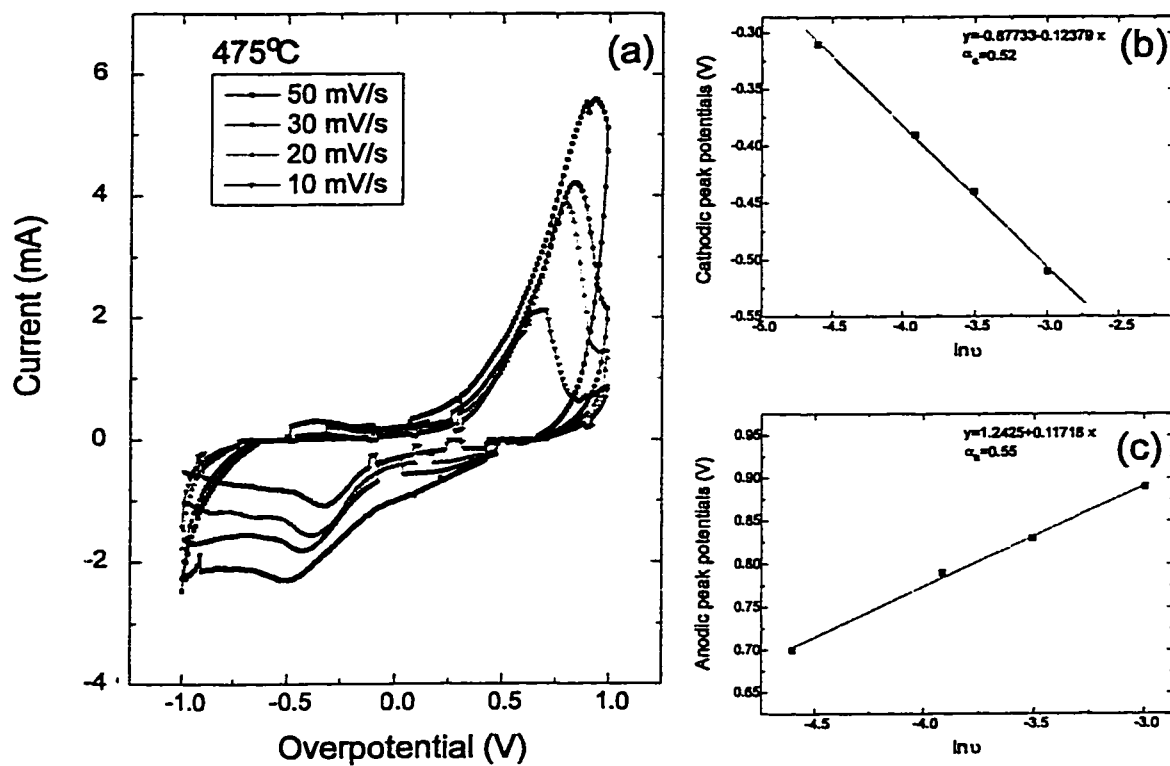


Figure 6-18. (a) Cyclic voltammetric curves at 475°C; (b) cathodic coefficient; (c) anodic coefficient.

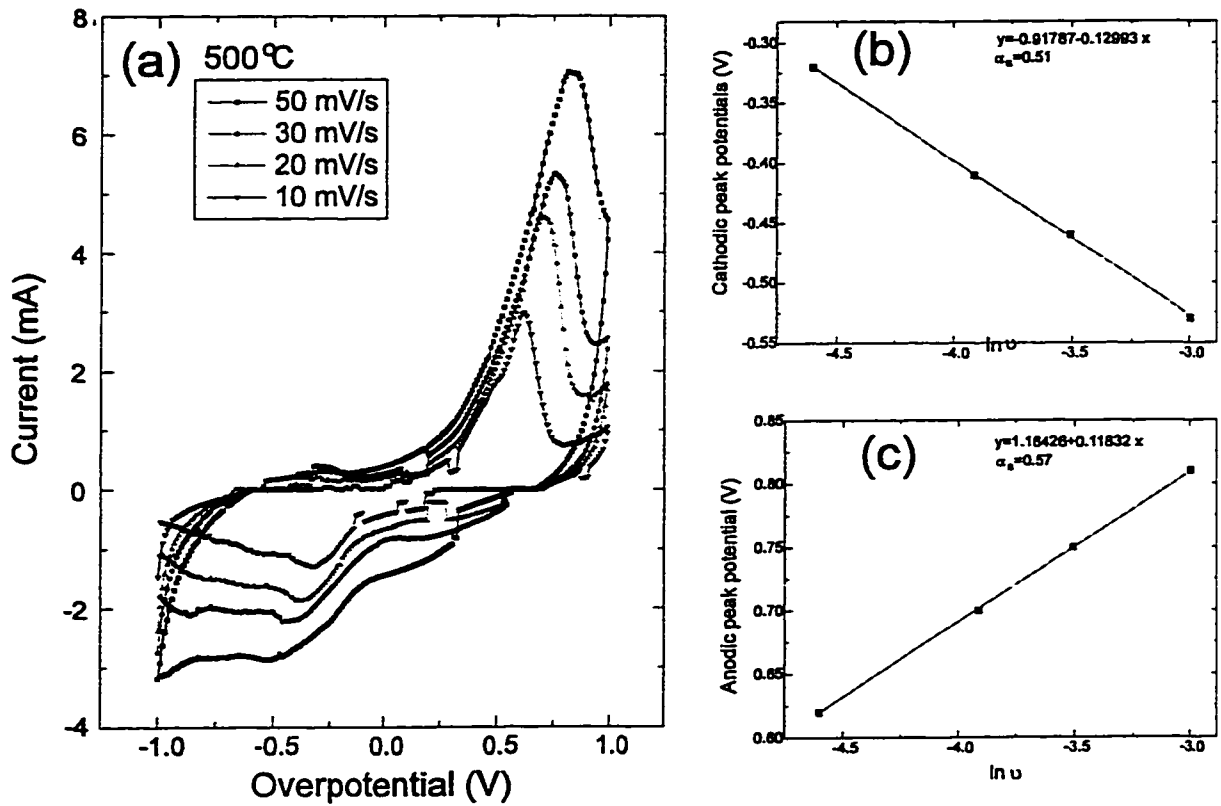


Figure 6-19. (a) Cyclic voltammetric curves at 500°C; (b) cathodic coefficient; (c) anodic coefficient.

Table 6-4. Comparison of the cathodic and anodic transfer coefficients from the two stages.

PEVD stage	Stage I			Stage II
	450°C	475°C	500°C	550°C
α_c	0.51	0.52	0.51	0.63
α_a	0.60	0.55	0.57	1

According to fundamental electrochemical theory, α_c and α_a should not change with processing temperature. The values for stage I are fairly constant. The significant increase in both coefficients from stage I to stage II is presumably due to the change in the solid electrolyte/working electrode interface during PEVD product (Na_2CO_3) formation. This indicates that the geometry of the auxiliary phase Na_2CO_3 at the working

electrode is also kinetically related to the charge transfer reaction at the working electrode. A PEVD process improves the solid electrolyte/electrode interface.

6.5.3.2. Spectra at Higher Temperatures

The cyclic voltammograms for stage I PEVD reactions at higher temperatures are more complicated. The voltammograms for various sweep rates at 525°C and 550°C are reported in Figures 6-20 and 6-21, respectively. Two pairs of peaks (labeled M and N for cathodic peaks, and M' and N' for anodic peaks) are distinguishable. Thus, extra PEVD reaction rate limiting steps must be involved under these conditions.

Generally speaking, the cathodic and anodic peaks exist as a pair, and each pair of peaks represents a redox reaction. The second pair of peaks could be due to an additional redox reaction other than the one in Eq.(6-17). However, a solid electrochemical system is usually very selective to only one mobile ionic species, which undergoes the charge transfer reaction. Previous investigation has found that double peaks could also result from different potential states in redox reactions for ionic species with higher valence (Vayenas et al., 1992; Jiang et al., 1993). For instance, during oxygen reduction, the oxygen has to obtain an electron twice to reduce to O^{2-} . In the current case, sodium ion is single valent. It is not likely to have two redox reaction potential states. Moreover, the shapes of the M peaks are different from those of redox reactions.

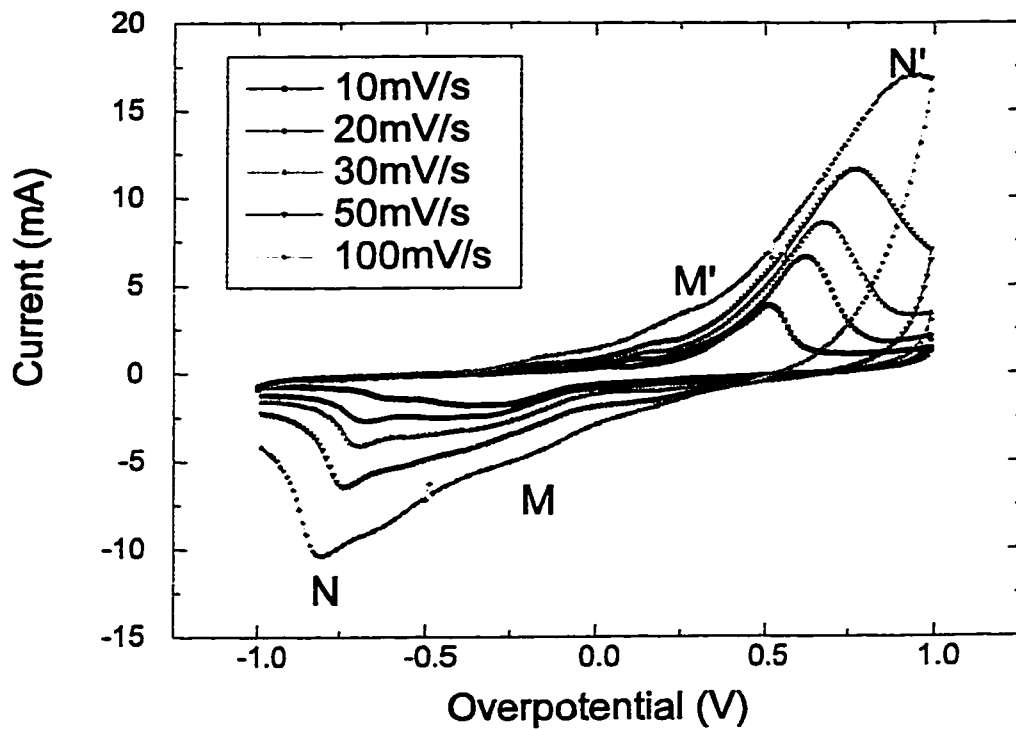


Figure 6-20. Cyclic voltammetric curves at 525°C.

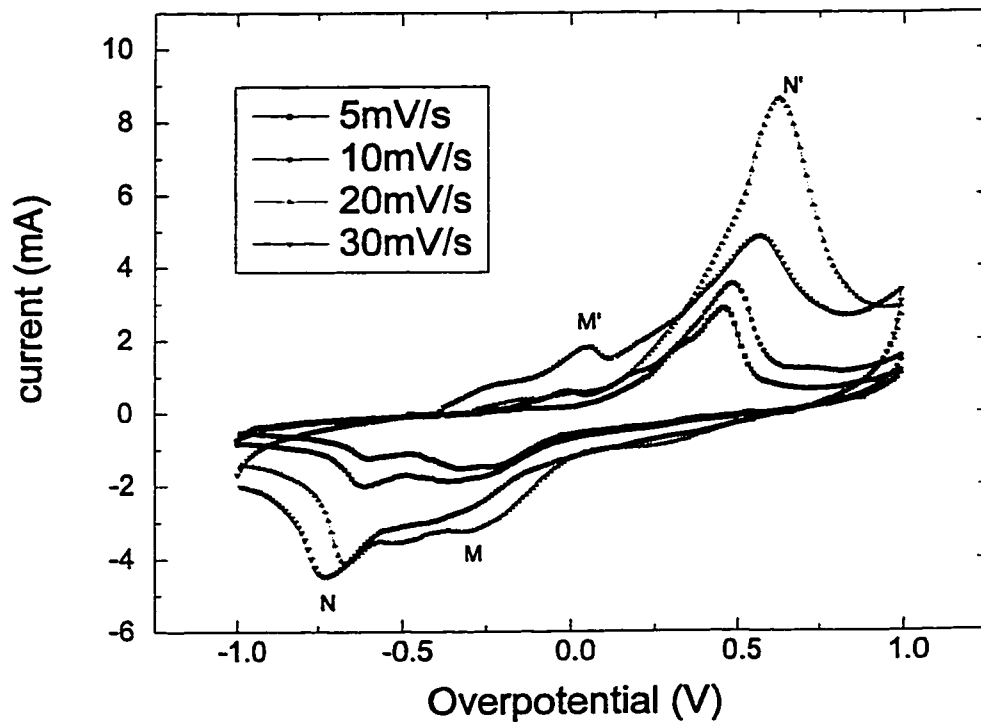


Figure 6-21. Cyclic voltammetric curves at 550°C.

According to fundamental cyclic voltammetry theory, a peak results when an overpotential related rate limiting step switches to another rate limiting step. In the case of the N peaks, the PEVD reaction rate limiting step switches from Step 1 to Step 4. As has been discussed previously, the diffusion of charged particles through the PEVD product is also a working electrode overpotential related step. Thus, it is possible that M peaks are due to a switch from Step 2a to Step 1 at certain working electrode overpotentials. Thus, a resistance overpotential is dominant at low working electrode overpotential. As a result, the PEVD current permitted by the charge transfer reaction is limited by the transport of Na^+ across the product under those PEVD conditions. It was also found that the repeatability of the M peaks in voltammograms was poor. The M peaks in these voltammograms do not have the same shape, peak overpotential and peak current under the same experimental conditions. This is possibly because M peaks are very sensitive to geometric factors at the working electrode of stage I PEVD samples during each SECV scan.

As shown in Figure 6-21, the cathodic M peaks are broader than the anodic M' peaks. The reason is that the PEVD processes for decomposition and formation at the working electrode are different. The broader M peak could result from diffusion of Na^+ across the product to form Na_2CO_3 in two steps,



When the process is limited by the diffusion of Na^+ inside the product, the first step will increase the electrochemical potential of the sodium ion at the surface of the PEVD product (location (III)). Thus, the thermodynamic driving force will decrease causing further transport of Na^+ in the product to pursue the second step. Two cathodic M peaks can indeed sometimes be resolved. The decomposition of Na_2CO_3 is a one step process.



The cause of the M peaks has been further confirmed with an SECV holding technique at 550°C. In this experiment, the V_{WR} was held at 600 mV for various times, then scanned negatively to -1000 mV at the cathodic side. The results are plotted in Figure 6-22. The longer the holding time, the more significant the M peaks vs. N peaks. As more decomposition of the product occurs, the Na^+ diffusion length decreases, and the PEVD current is less limited by Step 2a. The negative shift of the N peaks is a feature that has been discussed previously for a stage II PEVD sample.

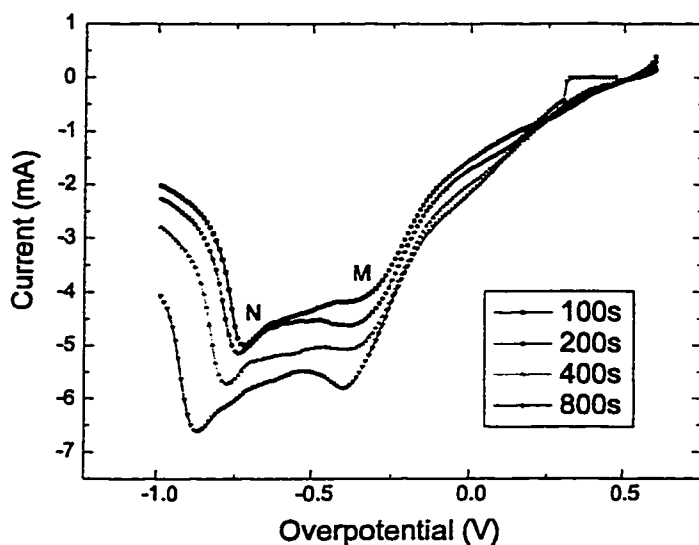


Figure 6-22. The effect of holding time on cyclic voltammetric curves during the first stage of PEVD at 550°C.

6.5.3.3. Summary

Although SECV studies are not able to give quantitative results for stage I PEVD behavior, PEVD reaction rate limiting steps are qualitatively revealed. At lower temperatures and working electrode overpotentials, the PEVD reaction rate limiting step is Step 1, the charge transfer reaction. At higher temperatures and lower working electrode overpotentials, the rate-limiting step is Step 2a, the diffusion of Na^+ across the product. At higher working electrode overpotentials for all temperatures, the rate-limiting step is Step 4, the surface diffusion of neutral reactants.

Chapter 7. Conclusions and Recommendations

During the last twenty years, we have witnessed the active development of solid state ionics associated with the study of ionic and electronic processes in solid state ionic materials. The investigation of energy converting applications to use ionic transport in solid state ionic materials is booming. The present availability of numerous types of solid state ionic materials allows for electrochemical reactions to be carried out with the surrounding vapor phase to form products of interest. This recent interfacing of vapor deposition and electrochemistry has led to the development of polarized electrochemical vapor deposition (PEVD) during the course of the current study.

The significance of this new technique is that PEVD applies solid state ionic techniques to modify the widely accepted CVD technique under controlled conditions in a solid electrochemical cell. Compared with other solid state ionic techniques, PEVD takes advantage of not only energy transformation but also material transport itself during ionic and electronic transport in solids to form desired products. Thus, PEVD has brought

Wagner's electrochemical tarnishing theory to a new field for making man-made products under well-defined thermodynamic and kinetic conditions.

PEVD holds promise for a wide range of potential applications for solid state ionic and electronic devices. During the course of the current thesis research, PEVD has been applied to fabricating two types of solid state ionic devices, i.e., potentiometric gaseous oxide sensors and solid oxide fuel cells. These applications have shown that PEVD is the most suitable technique to improve solid electrode / electrolyte contact and, consequently, the performance of these solid state ionic devices. Furthermore, the "active" use of material transport through the solid by PEVD offers interesting opportunities not only for forming deposition products but also for studying the physical properties of the products under well-defined thermodynamic and kinetic conditions.

It has been more than sixty years since Wagner's electrochemical tarnishing theory was developed. Finally, the two parallel suggestions of material transport and energy transformation in his theory overlap, and the newly developed PEVD technique will make solid state ionic devices to better serve today's ever-growing energy and environmental demands.

It should be pointed out that PEVD research and development is still in its very early stages. In the hope of promoting future research in this area, a few general recommendations are listed belows:

1. The future development of PEVD requires an interdisciplinary approach to cover topics such as ionic transport and electrochemical reaction kinetics in PEVD, solid and vapor phase electrochemical reactions and subsequent electro-crystallization behavior and thermodynamics of defects under PEVD conditions especially at solid-solid interfaces in PEVD systems.
2. As a promising new thin film deposition technique, the future development of PEVD should follow the course of other thin film deposition techniques with emphasis on each individual process for specific applications. For instance, based on the preliminary PEVD applications reported in the current thesis, more work needs to be done to fully develop the processes for potentiometric sensor auxiliary phase deposition and solid oxide fuel cell composite anode fabrication and, finally, to scale up for practical applications.

3. Like other processing techniques, the success of PEVD also relies on its application range. Foreseeable applications include other solid state ionic devices, such as ionistors, batteries and electrochromic displays. Since PEVD is compatible with other microelectronic processing techniques, PEVD could have applications in this area, such as the deposition of high quality oxides. Furthermore, PEVD could be applied to miniaturize solid state ionic devices, such as ionistors, batteries and sensors, such that they fit into integrated circuits (IC).
4. PEVD can also be applied to coat a thin continuous layer of protecting ceramic, such as ZrO_2 , on the top of a metallic component to form a unique cermet structure. This kind of cermet can be useful when high electrical conductivity, toughness and/or thermal shock resistance are required at the same time as high oxidation and/or corrosion resistance.

References

- Adachi, G. and Imanaka, N., in: Chemical Sensor Technology, vol.3, eds. Yamazoe et al., (Kodansha Ltd. Tokyo and Elsevier, Amsterdam, 1991) 131.
- Akila, R. and K. T. Jacob, Sensors and Actuators, 16, (1989) 311.
- Alcock, C. B., Electromotive Force Measurements in High Temperature Systems, (American Elsevier Publishing Company, Inc., New York, 1968).
- Alcock, C. B., Solid State Ionics, 53-56 (1992) 3.
- Aoustin, S., O. Tillement and M. Quarton, Mat. Res. Bull. 27 (1992) 1015.
- Appleby, A.J. and F.R. Faulkes, Fuel Cell Handbook. (Van Nostrand Reinhold, New York, 1989).
- Azad, A.M., S.A. Akbar, S.G. Mhaisalkar, L.D. Birkefield and K.S.Goto, J. Electrochem. Soc., 139 (1992) 3690.
- Balachandran, Y., S.E. Dorris, J.J. Picciola, R.B. Poeppel, C.C. McPheeters and N.Q. Minh, Proc. 1989 Intersociety Energy Conversion Engineering Conference, Vol. 3 (1989) 1553.

- Bard, A.J., and L.R. Faulkner, *Electrochemical Methods: Fundamentals and Applications*, (Wiley, New York, 1980).
- Bardeen, J. and C. Herring, in: *Atom Movements*, (Am. Soc. Met., Cleveland 1951) 87.
- Baumard, F. and Abelard, P., in: *Advances in Ceramics*, vol.12, eds. N. Claussen, M. Ruhle and H. Yanagida, (American Ceramic Society, Westerville, OH, 1988) 555.
- Baur, E. and H. Preis, *Z. Elektrochem.*, 43 (1937) 727.
- Bebelis, S. and C.G. Vayenas, *J. Catal.*, 118 (1989) 125.
- Beden, B., F. Kadirgan, C. Lamy and J.M. Leger, *J. Electroanal. Chem.*, 142 (1982) 171.
- Beevers, C.A. and M.A.S. Ross, *Z. Krist.* 97 (1937) 59.
- Bentzen, J.J., J.B. Bilde-Sorensen, B. Kindl and H.W. Poulsen, in: *Proc. of the 5th SSMS on New Materials and Processes*, eds., I.L.H. Hansson and H. Lilholt, (Copenhagen, 1989) 149.
- Bettman, M. and C.R. Peters, *J. Phys. Chem.* 73 (1969) 1174.
- Birks, N. and H. Rickert, *Ber. Bunsenges. Physik. Chem.*, 67 (1963) 97.
- Bockris, J.O'M. and A.K.N. Reddy, *Modern Electrochemistry*, Vol.2, (Plenum Press, New York, 1970).
- Bradley, J. N., and Green, P. D., *Trans. Faraday Soc.*, 63 (1967) 424.
- Bragg, W.L., Gottfried, C. and West, J., *Z. Kristallogr.* 77 (1931) 255.
- Brinkman, H.W. and A. J. Burggraaf, *J. Electrochem. Soc.*, 142 (1995) 3851.
- Brouwer, G., *Philips Res. Rept.*, 9 (1954) 366.
- Burley, G., *Acta Crystallogr.*, 23 (1967) 1.
- Butchereit, E., M. Schreiber and J. Schoonman, *Solid State Ionics* 69 (1994) 1.
- Carolan M.F. and J. N. Michaels, *Solid State Ionics*, 25 (1987) 207.
- Carolan, M.F. and J.N. Michaels, *Solid State Ionics*, 37 (1990a) 189.
- Carolan, M.F. and J.N. Michaels, *Solid State Ionics*, 37 (1990b) 197.
- Caspari, W.A., *Z. Physik. Chem.* 30 (1899) 89
- Choudhury, N.S. and J.W. Patterson, *J. Electrochem. Soc.*, 118 (1971) 1389
- Chu, W. F., D. Fischer, H. Erdmann, M. Ilgenstein, H. Koppen and V. Leonhard, *Solid State Ionics*, 53-56, (1992) 80.
- Cleaver, B. *Z. Physik. Chem. (Frankfurt)* 45 (1965) 346.

Cogan, S.F., T.D. Plante, R.S. McFadden and R.D. Rauh, *Solar Energy Mater.*, 16 (1987) 371.

Cote, R. et al., *J. Electrochem. Soc.*, 131 (1984) 63.

Couturier, G., J. Salardenne and C. Sribi and M. Rosso, *Solid State Ionics*, 9-10 (1983) 699.

Darken, L.S., *Trans. AIME*, 175 (1948) 184.

de Bethune, A.J., *J. Electrochem. Soc.*, 102 (1955) 288.

de Haart, L.G.J., Y.S. Lin, K.J. de Vries and A. J. Burggraaf, *J. Eur. Ceram. Soc.*, 8 (1991) 59.

Dees, D. W., T.D. Claar, T.E. Easler, D.C. Fee, and F.C. Mrazek, *J. Electrochem. Soc.*, 134, (1987) 2141.

Dees, D.W., U. Balachandran, S.E. Dorris, J.J. Heiberger, C.C. McPheeters and J.J. Picciolo, in: *Proceeding of the Symposium on Fuel Cells*, eds. R.E. White and A.J. Appleby. (The Electrochemical Society, Pennington, NJ, 1989) 130.

Dekker, J.P., N.J. kiwiet and J. Schoonman, in: *Solid Oxide Fuel Cells*, *The Electrochem. Soc. Proc. Ser.*, 89-11, (The Electrochemical Society, Pennington, NJ, 1989) 57.

Dekker, J.P., V.E.J. van Dieten and J. Schoonman, *Solid State Ionics*, 51 (1992) 143.

Delahay, P., *New Instrumental Methods in Electrochemistry*, (Interscience, New York, 1954).

Demott, D.S. and P. Hancock, *Proc. Brit. Ceram. Soc.*, 19 (1971) 193.

Detry, D., J. Drowart, P. Goldfinger, H. Keller and H. Rickert, *Z. Phys. Chem. N. F.*, 55 (1967) 314.

Dietrich, G. and W. Schafer, *Int. J. Hydrogen Energy*, 9 (1984) 747

Doklya, M., N. Sakai, T. Kawada and H. Yokokawa, in: *Proc. 1989 Intersociety Energy Conversion Engineering Conference*, Vol. 3 (1989) 1547.

Donner, D. and H. Rickert, *Z. Physik. Chem. N.F.*, 60 (1968) 11.

Drowart, J., P. Goldfinger, D. Detry, H. Rickert and H. Keller, in: *Advances in Mass Spectrometry, IV*, ed., E. Kendrick, (The Institute of Petroleum, London, 1968) 499.

Easler, T.E., B.K. Flandermeyer, T.D. Claar, D.E. Busch, R.J. Fousek, J.J. Picciolo, and R.B. Poppel, *Abstracts of the 1986 Fuel Cell Seminar*, Oct. 26-29, Tucson, AZ (1986) 72.

Eguchi, K., T. Setoguchi, H. Itoh and H. Arai, Extended Abstracts of 40th Meeting of International Society of Electrochemistry Kyoto, Japan (1989) 362.

Einstein, A., Ann. Phys. (4: Drude), 17 (1905) 549.

Erdey-Gruz, T. and M. Volmer: Z. physik. Chem. 150A, (1930) 203.

Etsell, T.H. and S.N. Flengas, Chemical Reviews, 70 (1970) 339.

Fabry, P. and M. Kleitz, J. Electrochem. Soc., 126 (1979) 2183.

Faraday, M., Ann Physik, 107 (1834) 241.

Fickett, A.P., in: Handbook of Batteries and Fuel Cells, ed. D. Linden (McGraw-Hill, New York, 1984) 41.

Fitterer, G.R., J. Metals, 18 (1966) 961.

Forlani, F., Sensors and Actuators B, 3, (1991) 165.

Fouletier, J., H. Seiner and M. Kleitz, J. Appl. Electrochem., 4, (1974) 305.

Fouletier, J. and G. Vitter, in: Applications of Solid Electrolytes, eds. T. Takahashi and A. Kozawa (JEC Press, Cleveland, OH, 1980) 108.

Frenkel, J., Z. Phys., 35 (1926) 652.

Gauthier, M. and A. Chamberland, J. Electrochem. Soc., 124 (1977a) 1579.

Gauthier, M. and A. Chamberland, A. Belanger and M. Poirier, J. Electrochem. Soc., 124 (1977b) 1584.

Gerisher, H., in: Proc. Electrode Processes in Solid State Ionics, NATO Adv. Study Inst. Ser. C, Ajaccio, eds., M. Kleitz and J. Dupuy (D. Reidel, Dordrecht/Boston, 1975) 277.

Goodenough, J.B. and A.K. Shukala, in: Proc. Intern. Sem. on Solid State Ionic Devices, eds. B.V.R. Chowdari and S. Radhakrishna (World Scientific, Singapore, 1988a) 573.

Goodenough, J.B. and A.K. Shukala, Proc. in: Intern. Sem. on Solid State Ionic Devices, eds. B.V.R. Chowdari and S. Radhakrishna (World Scientific, Singapore, 1988b) 663.

Gopel, W., Progress in Surface Sciences, 20 (1985) 9.

Gopel, W., Sensors and Actuators, 16, (1989) 167.

Gopel, W., Sensors and Actuators B, 18-19, (1994) 1.

Goto, K.S., Anal. Chem. Symp. Ser., 17 (1983) 338.

Green, J.E., C.E. Wickersham, J.L. Zilko, L.B. Walsh and F.R. Sofran, J. Vac. Sci. Technol., 13 (1976) 72.

Grove, W.R., Philos. Mag., 14, (1839) 127.

Guggenheim, E.A., *J. Phys. Chem.*, 33 (1929) 842.

Guggenheim, E.A., *J. Phys. Chem.*, 34 (1930) 1540.

Guggenheim, E.A., *Thermodynamics*, Fifth ed. (North-Holland, Amsterdam, 1967).

Gurevich, Y. Y., in: *III-V Compound Semiconductors and Semiconductor Properties of Superionic Materials*, eds. R.K. Willandson and A.C. Beer, (Academic Press, San Diego, 1988) 229.

Haaland, D.M., *J. Electrochem. Soc.*, 127 (1980) 796.

Hagemmuller, P. and W. van Gool, *Solid Electrolytes – General Principles, Characterization, Materials, Applications* (Academic Press, New York, 1980).

Hagemmuller, P., in: *Proc. Intern. Sem. on Solid State Ionic Devices*, eds. B.V.R. Chowdari and S. Radhakrishna (World Scientific, Singapore, 1988) 663.

Hamatani, H., T. Okada and T. Yoshida, in: *Proceedings of SOFC*, (Nagoya, 1989) 119.

Hammou, A., in: *Proc. Intern. Sem. on Solid State Ionic Devices*, eds. B.V.R. Chowdari and S. Radhakrishna (World Scientific, Singapore, 1988) 243.

Hebb, M.H., *J. Chem. Phys.*, 20 (1952) 185.

Heyne, L., in: *Mass Transport in Oxides*, eds. J.B. Wachtman and A.D. Franklin, (Natl. Bur. Stand. Spec. Publ. 1968) 149.

Heyne, L., in: *Fast Ion Transport in Solids*, ed. W. van Gool (North Holland, Amsterdam, 1973) 123.

Heyne L., in: *Topics in Applied Physics*, ed., S. Geler (Springer-Verlag, Berlin 1977) 169.

Heyne, L. and D. den Engelsen, *J. Electrochem. Soc.*, 124 (1977) 727.

Hladik, J., in: *Physics of Electrolytes*, ed. J. Hladik, (Academic Press, London, 1972) 35.

Hoshino, S., *Solid State Ionics*, 48 (1991) 179.

Hotzel, G. and W. Weppner, *Solid State Ionics*, 18/19 (1980) 1223.

Hotzel, G. and W. Weppner, in: *Proc. 6th Riso-Intern. Symp. on Transport-Structure Relations in Fast Ion and Mixed Conductor* (Riso Natl. Lab., Roskilde, 1985) 401.

Huang, K., W. Wu and Q. Liu, *Solid State Ionics*, 53-56 (1992) 24.

Ilschner-Gensch, C. and C. Wagner, *J. Electrochem. Soc.* 105 (1958) 198.

Inoue, T., K. Eguchi, T. Setoguchi and H. Arai, *Solid State Ionics*, 40-41 (1990) 407.

Isenberg, A.O., in: Proc. Symp. On Electrode Materials and Processes for Energy Conversion and Storage, Vol. 77-6, (Electrochemical Soc., Princeton, NJ, 1977) 572.

Isenberg, A.O., Thin film battery/fuel cell power generating system. Report ERDA. Contract EY-76-C-03-1197 (Westinghouse Electric Corporation, 1978).

Isenberg, A. O., Solid State Ionics, 3-4 (1981) 431.

Isenberg, A.O., Abstracts of the 1982 Fuel Cell Seminar, Newport Beach, CA, Nov. 14-18, (1982) 154.

Isenberg, A.O., US Patent 4,490,444 (Dec. 25, 1984)

Isenberg, A.O., Japanese Patent, Application no. S60-269217 (1985).

Isenberg, A.O. US Patent, 4,582,766 (Apr. 15, 1986a).

Isenberg, A.O. US Patent, 4,597,170 (Jul. 1, 1986b).

Isenberg, A.O., US Patent 4,728,584 (Mar. 1, 1988)

Ishigaki, T., S. Yamaguchi, K. Koshio, J. Misuzaki and K. Fueki, J. Solid State Chem., 73 (1988) 179.

Iwahara, H., et al., Solid State Ionics, 3-4 (1981) 359.

Jacob, K.T. and D.B. Rao, J. Electrochem. Soc., 126 (1979) 1842.

Jagannathan, K.P., S.K. Tiku, H.S. Ray, A. Ghosh and E.C. Subbarao, in: Solid Electrolytes and Their Applications, ed. E.C. Subbarao (Plenum Press, New York, 1980) 201.

Janata, J., Theory Design and Biomedical Applications of Solid State Chemical Sensors, (CRC Press, Boca Raton, 1978) 41.

Janata, J., Principles of Chemical Sensors (Plenum Press, New York, 1989).

Jensen, R.E., US Patent No. 4,971,830 (1990).

Jiang, Y., A. Kaloyannis and C.G. Vayenas, Electrochimica Acta, 38 (1993) 2533.

Joffe, A., Ann d. Phys., 72 (1923) 461.

Jones, S.D., J.R.Akridge, S.G.Humphrey, C.C. Liu and J. Saradin, Mat. Res. Soc. Symp. Proc. 210 (1991) 31.

Jost, W. and H. Schweitzer, Z. Phys. Chem., Abstr. B20, (1933) 118.

Jue, J.F., J. Jusko and A.V. Virkar, J. Electrochem. Soc., 139, (1992) 2458.

Kawada, T., N. Sakai, H. Yokokawa, M. Dokiya, M. Mori and T. Iwata, J. Electrochem. Soc., 137 (1990a) 3042.

- Kawada, T., N. Sakai, H. Yokokawa, M. Dokiya, M. Mori, and T. Iwata, *Solid State Ionics*, 40-41 (1990b) 402.
- Kiukkola, K. and C. Wagner, *J. Electrochem. Soc.*, 104 (1957a) 308.
- Kiukkola, K. and C. Wagner, *J. Electrochem. Soc.*, 104 (1957b) 379.
- Kleitz, M, P. Fabry and E. Schouler, in: *Proc. Electrode Processes in Solid State Ionics*, NATO Adv. Study Inst. Ser. C, Ajaccio, (D. Reidel Publ., Dordrecht, Holland,1975) 1.
- Kleitz, M. and E. Siebert, in: *Chemical Sensor Technology*, vol.2, ed. T. Seiyama, (Kodansha Ltd., Tokyo and Elsevier Science Publishers B.V., Amsterdam, 1989) 151.
- Kroger, F.A. and H.J. Vink, in: *Solid State Physics*, Vol.3, eds. F. Seitz and D. Turnbull, (Academic press, New York, 1956) 307.
- Kroger, F.A. and H.J. Vink, *J. Phys. Chem. Solids*, 5 (1958) 208.
- Kroger, F.A., *The Chemistry of Imperfect Crystals*, 2nd ed. (North-Holland, Amsterdam 1974).
- Kummer, J.T., *Prog. Solid State Chem.* 7 (1972) 141.
- Ladas, S, S. Bebelis and C.G. Vayenas, *Surf. Sci.*, 251-252 (1991) 1062.
- Lamy-Pitara, E., L. Lghouzouani, Y. Tainon and J. Barbier, *J. Electroanal. Chem.*, 260 (1989) 157.
- Leclaire, A. D., in: *Physical Chemistry 10*, ed. W. Jost, (Academic, New York, 1970) 261.
- Leonhard, V., et al., Comparison of thin- and thick-film CO₂ sensors, *Sensors and Actuators B*, 13-14 (1993) 530.
- Lessing, P.A., L.W. Tai and K.A. Klemm, in: *Solid Oxide Fuel Cells*, the Electrochemical Society, 89-11 (Electrochemical Soc., Princeton, NJ, 1989) 337.
- Lidiard, A.B., in: *Handbook of Physics*, vol.20, ed., S. Flugge (Springer-Verlag, Berlin, 1957) 246.
- Lin, Y.S., K.J. de Vries, and A.J. Burggraaf, *J. de Phys.*, Colloque C5, 50 (1989a) 861.
- Lin, Y.S., L.G.J. de Haart, K.J. de Vries and A.J. Burggraaf, in: *Solid Oxide Fuel Cells*, The Electrochem. Soc. Proc. Ser., 89-11 (Electrochemical Soc., Princeton, NJ, 1989b) 67.
- Lin, Y.S., L.G.J. de Haart, K.J. de Vries and A.J. Burggraaf, *J. Electrochem. Soc.*, 137 (1990) 3960.

- Lin, Y.S., K.J. de Vries, H.W. Brinkman and A.J. Burggraaf, *J. of Membrane Sci.*, 66 (1992) 211.
- Littlewood, R., *Can. Met. Quart.*, 5 (1966) 1.
- Liu, C., H.G.K. Sunder and A. Angell, *Mat. Res. Bull.* 20 (1985) 525.
- Livage, J., P. Barboux, M. Nabavi and P. Judeinstein, *Mat. Res. Soc. Symp. Proc.* 135 (1988) 131.
- Madou, M. J. and S. R. Morrison, *Chemical Sensing with Solid State Devices*, (Academic Press, Inc., Boston, 1989).
- Maier, J., *Solid State Ionics*, 28-30 (1988) 1073.
- Maruyama, T., X. Ye and Y. Saito, *Solid State Ionics*, 24, (1987a) 281.
- Maruyama, T., S. Sasaki, and Y. Saito, *Solid State Ionics*, 23 (1987b) 107
- Maruyama, T., *Materials Science and Engineering A*, 146, (1991) 81.
- Minami, T., *J. Non-Crystalline Solids* 73 (1985) 273.
- Minh N. Q., C.R. Horne, F. Liu, P.R. Staszak, T.L. Stillwagon and J.J. van Ackeren, in: *Solid Oxide Fuel Cells, The Electrochemical Society Proc. Ser.*, 89-11 (The Electrochemical Society, Princeton, NJ, 1989) 307.
- Minh, N.Q., *J. Am. Ceram. Soc.*, 76 (1993) 563.
- Mitoff, S.P., *J. Chem. Phys.*, 36 (1962) 1383.
- Miura, N., S. Yao, Y. Shimizu and N. Yamazoe, *J. Electrochem. Soc.*, 139, (1992a) 1384.
- Miura, N., S. Yao, Y. Shimizu and N. Yamazoe, *Sensors and Actuators B*, 9 (1992b) 165.
- Miura, N., S. Yao, Y. Shimizu, and N. Yamazoe, *Sensors and Actuators B*, 13-14 (1993) 387.
- Miura, N., Y. Yan, M. Sato, Y. Shimizu, and N. Yamazoe, *Chem. Lett.*, 1994 (1994) 393.
- Miysmura, M., S. Tomura, A. Inai and S. Inomata, *Solid State Ionics*, 3-4 (1981) 149.
- Morf, W.E., *The Principles of Ions-Selective Electrodes and of Membrane Transport* (Elsevier, Amsterdam, 1981).
- Mott, N.F. and R.W.Gurney, *Electronic Processes in Ionic Crystals*, 2nd. Ed., (Oxford, 1948).
- Mrowec, S. and H. Rickert, *Z. Physik. Chem.*, 28 (1961) 422.
- Mrowec, S. and H. Rickert, *Ber. Bunsenges. Physik. Chem.*, 66 (1962) 14.

Murakami, S., Y. Akiyama, N. Ishida, Y. Miyake, M. Nishida, Y. Itoh, T. Saito and N. Furukawa, *Denki Kagaku*, 59 (1991a) 320.

Murakami, S., N. Akiyama, N. Ishida, T. Yasuo, T. Saito and N. Furukawa, in: *Proc. Second Intern. Symp. on SOFC*, eds. F. Grosz, P. Zegers, S.C. Singhal and O. Yamamoto (The Commission of European Communities, 1991b) 561.

Negishi, A., K. Nozaki and T. Ozawa, *Solid State Ionics*, 3-4 (1981) 443.

Neophytides, S. and C.G. Vayenas, *J. Catal.*, 118 (1989) 147.

Nernst, W., *Z. Phys. Chem.*, 2 (1888) 613.

Nernst, W., *Z. Electrochem.*, 6 (1899) 41.

Newman, J., in: *Advances in Electrochemistry and Electrochemical Engineering*, V, eds. C.W. Tobias, (Interscience, New York, 1967) 129.

Ogumi, Z., T. Ioroi, Y. Uchimoto, Z. Takehara, T. Ogawa and K. Toyama, *J. Am. Ceram. Soc.*, 78 (1995) 593.

Okazaki, H., *J. Phys. Soc. Japan*, 23 (1967) 355.

Olmer, L. J., J.C. Viguie and E.J.L. Schouler, *Solid State Ionics*, 7 (1982) 23.

Pal, U.B. and S.C. Singhal, in: *Proc. Sixth (IUPAC) Internat. Conf. High Temperature-Chemistry of Inorganic Materials*. (Gaithersburg, MD, 1989).

Pal, U.B. and S.C. Singhal, *J. Electrochem. Soc.*, 137 (1990a) 2937.

Pal, U. B. and S. C. Singhal, *High Temp. Sci.*, 27 (1990b) 251.

Pal, U.B., *Solid State Ionics*, 52 (1992) 227.

Papoutsis, A., J. M. Leger and C. Lamy, *J. Electroanal. Chem.*, 234 (1987) 315.

Park, J.M. and R.N. Blumenthal, *J. Electrochem. Soc.*, 136 (1989) 2867.

Patterson, J.W., *J. Electrochem. Soc.*, 118 (1971) 1033.

Patterson, J.W., in: *Electrical Conductivity in Ceramics and Glass*, part B, ed. N. M. Tallan, (Marcel Dekker, Inc., New York, 1974) 453.

Patterson, J.W., in: *Corrosion Chemistry*, ACS Symposium Series, eds., G.R. Brubaker and B.P. Phipps, (1989) 96.

Peters, H. and H. Mobius, *Z. Phys. Chem.* 209 (1958) 298.

Peters, H. and H. Mobius, *Z. Electrochem.* 63 (1959) 244.

Pilling, N.B. and R.E., Bedworth, *J. Inst. Met.*, 29 (1923) 529.

Pretzel, F. E., et al., *J. Phys. Chem. Solids*, 16 (1960) 10.

- Przyluski, J. and W. Wieczorek, *Solid State Ionics*, 36 (1989) 371.
- Raleigh, D. O., in: *Progress in Solid State Chemistry*, Vol. 3, (Macmillan, New York, 1966) 83.
- Raleigh, D. O., *J. Electrochem. Soc.*, 114 (1967) 493.
- Raleigh, D. O. and H.R. Crowe, *J. Electrochem. Soc.*, 116 (1969) 40.
- Raleigh, D. O., in: *Proc. Electrode Processes in Solid State Ionics*, NATO Adv. Study Inst. Ser. C, Ajaccio, eds., M. Kleitz and J. Dupuy, (D. Reidel, Dordrecht/Boston, 1975) 119.
- Ramastry, C. and Y.V.G.S. Murti, *Proc. Roy. Soc.*, A305 (1968) 441.
- Randles, J.E.B., *Trans. Faraday Soc.*, 44 (1948) 327.
- Rankin, G.A. and H.E. Merwin, *J. Am. Chem. Soc.*, 38 (1916) 3568.
- Rapp, R.A. and D.A. Shores, in: *Physicochemical Measurements in Metals Research*, part 2, ed. R.A. Rapp, (Interscience, New York, 1970) 123.
- Ratchford, R.J. and H. Rickert, *Z. Electrochem.*, 66 (1962) 497.
- Ribes, M., D. Ravaine, J.L. Souquet and M. Maurin, *Rev. Chim. Miner.* 16 (1979) 339.
- Rickert, H., *Z. Physik. Chem. N.F.*, 23 (1960) 356.
- Rickert, H., *Ber. Bunsenges. Physik. Chem.*, 65 (1961) 463.
- Rickert, H. and C. Wagner, *Z. Physik. Chem. N.F.*, 31 (1962) 32.
- Rickert, H. and C.D. O'Briain, *Z. Physik. Chem. N.F.*, 31 (1962) 71.
- Rickert, H., in: *Condensation and Evaporation of Solids*, eds., E. Rutner, P. Goldfinger, and J. P. Hirth, (Gordon and Breach Publ., New York, 1962) 201.
- Rickert, H., in: *Electromotive Force Measurements in High-Temperature Systems*, ed. C.B. Alcock (Inst. Min. Metall. Publ., London, 1968a) 59.
- Rickert, H., *Werkstoffe und Korrosion*, 19 (1968b) 869.
- Rickert, H., *Angew. Chem., Int. Engl. Ed.*, 17 (1978) 37.
- Rickert, H., *Electrochemistry of Solids*, (Springer-Verlag, Berlin, 1982).
- Robertson, N. L. and J.N. Michaels, *J. Electrochem. Soc.*, 137 (1990) 129.
- Ruka, R. and J. Weisbart, *J. Electrochem. Soc.*, 109 (1962) 723.
- Saito, Y., K. Kobayshi and T. Maruyama, *Solid State Ionics*, 3-4 (1981) 393.
- Saito, Y., T. Murayama and K. Kobayashi, *Solid State Ionics*, 14 (1984a) 265.

- Saito, Y., T. Murayama, Y. Matsumoto, K. Kobayashi and Y. Yano, *Solid State Ionics*, 14 (1984b) 273.
- Sammes, N.M., M.S. Brown and R. Ratnaraj, *Journal of Materials Science Letters*, 13 (1994) 1124.
- Sato, H., in: *Topics in Applied Physics*, ed. S. Geler, (Springer-Verlag, Berlin 1977) 3.
- Schmalzried, H., *Z. Phys. Chem. (Frankfurt)*, 38 (1963) 87.
- Schmalzried, *Thermodynamics*, Vol.1, IAEA, Vienna, (1966) 97.
- Schoonman, J., J.L. De Roo, C.W. De Kreuk and A. Mackor, *Proc. 2nd Intern. Meeting on Chemical Sensors, Bordeaux* (1986) 319.
- Schoonman, J., in: *Proc. Intern. Sem. on Solid State Ionic Devices*, eds. B.V.R. Chowdari and S. Radhakrishna, (World Scientific, Singapore, 1988) 697.
- Schoonman, J., J.P. Dekker, J.W. Broers and N.J.Kiwiet, *Solid State Ionics*, 46 (1991) 299.
- Schottky, W., *Z. Phys. Chem. B*, 29 (1935) 335.
- Schouler, E.J.L. and M. Kleitz, *J. Electrochem. Soc.*, 134 (1987) 1045.
- Schulz, H., in: *Annual Rev. Mat. Sci.*, Vol.12 (Ann. Rev. Inc., Palo Alto, California, 1982) 351.
- Setohuchi, T., H. Ito, M. Sawano, K. Eguchi, H. Arai, in: *Proceedings for SOFC, Nagoya* (1989) 105.
- Setogichi, T., K. Okamoto, K. Eguchi and H. Arai, *J. Electrochem. Soc.*, 139 (1992) 2875.
- Sevcik, A., *Collec. Czech. Chem. Commun.*, 13 (1948) 349.
- Shimizu, Y., Y. Okamoto, S. Yao, N. Miura, and N. Yamazoe, *Denki Kagaku*, 59 (1991) 465
- Short, J. and R. Roy, *J. Phys. Chem.*, 67 (1963) 1860.
- Singhal, S.C., *Interconnection material development for solid oxide fuel cells*, DOE contract no. DE-AC21-84MC21184, Final report (1985).
- Singhal, S.C., in: *Proceedings of the Second International Symposium on Solid Oxide Fuel Cells*, Athens, Greece, July 2-5, 1991. (Commission of the European Communities, Luxembourg, 1991) 25.
- Souquet, J.L., *Solid State Ionics*, 28-30 (1988) 1073.

- Sridhar, S. and U.B. Pal, *Powder Technology*, 88 (1996) 173.
- Srinivasan, S. and Gileadi, E., *Electrochim. Acta*, 11 (1966) 321.
- Stark, G. *Solid State Ionics*, 28-30 (1988) 1773.
- Steele, B.C. and C.B. Alcock, *Trans. Met. Soc., AIME*, 233 (1965) 1359.
- Steele, B.C.H., in: *Proc. Electrode Processes in Solid State Ionics*, NATO Adv. Study Inst. Ser. C, Ajaccio, eds., M. Kleitz and J. Dupuy, (D. Reidel, Dordrecht/Boston, 1975) 367.
- Stevens, R. and J.G.P. Binner, *J. of Materials Sci.*, 19 (1984) 695.
- Stevens, R., *An Introduction to Zirconia*, (Magnesium Elektron, London, U.K., 1986).
- Stranski, I.N., *Z. Physik. Chem.*, 136 (1928) 259.
- Stroock, L.W., *Z. Phys. Chem.*, B25 (1934) 441.
- Stroock, L.W., *Z. Phys. Chem.* 31 (1936) 132.
- Subbarao, E.C., *Solid Electrolytes and their Applications* (Plenum Press, New York, 1980).
- Subbarao, E.C. and Maiti, H.S., *Solid State Ionics*, 11 (1984) 317.
- Suzuki, M., H. Sasaki, S. Ootoshi, A. Kajimura and M. Ippommatsu, *Solid State Ionics*, 62 (1993) 125.
- Sverdrup, E.F., C.J. Warde and R.L. Eback, *Ener. Conv.*, 13 (1973) 129.
- Takahashi, T., in: *Superionic Solids and Solid Electrolytes*, *Materials Sciences Series*, eds, A.L. Laskar and S. Chandra, (Academic Press, New York 1989) 1.
- Tammann, G., *Z. anorg. Chem.* 111 (1920) 78.
- Tang, E.Z., T.H. Etsell and D.G. Ivey, *Solid State Ionics*, 91 (1996a) 213.
- Tang, E.Z., T.H. Etsell and D.G. Ivey, in: *Ceramic Sensors III*, PV96-27, *The Electrochemical Society Proceeding Series*, (The Electrochemical Society, Pennington, NJ, 1996b) 131.
- Tang, E.Z., T.H. Etsell and D.G. Ivey, in: *Electrochemical Deposited Thin Film III*, PV96-19, *The Electrochemical Society Proceeding Series*, (The Electrochemical Society, Pennington, NJ, (1996c) 71.
- Tang, E. Z., T. H. Etsell and D. G. Ivey, *Sensors and Actuators B*, 45/2 (1997a) 21.
- Tang, E.Z., D.G. Ivey and T.H. Etsell, *Micron*, in press (1997b).

Tang, E.Z., T.H. Etsell and D.G. Ivey, High Temperature Materials Processing, (1998) submitted.

Tanner, C.W., J.F. Jue and A.V. Virkar, J. Electrochem. Soc., 140 (1993) 1073.

Tanner, C.W. and A.V. Virkar, J. Electrochem. Soc., 141 (1994a) 1262.

Tanner, C.W. and A.V. Virkar, J. Am. Ceram. Soc., 77 (1994b) 2209.

Tillement, O, J. Angenault, J.C. Couturier and M. Quarton, Solid State Ionics, 53-56 (1992) 391

Tillement, O, Solid State Ionics, 68 (1994) 9.

Tubandt, C. and F. Lorenz, Z. Phys. Chem., 87 (1914) 513.

Tubandt, C., H. Reinhold and G. Liebold, Z. Anorg. Allgem. Chem., 197 (1931) 225.

Tubandt, C., Handbook for Experimental Physics, vol. 12, pt. 3, (Akademische Verlagsgesellschaft, Leipzig, 1932) 383.

Ure, R.W. Jr., J. Chem. Phys., 26 (1957) 1363.

van Herle, J. and K. R. Thampi, Journal of Applied Electrochemistry, 24 (1994) 970.

Vayenas, C.G., S. Bebelis and S. Neophytides, J. Phys. Chem., 92 (1988) 5083.

Vayenas, C.G., S. Bebelis and S. Ladas, Nature (London), 343 (1990) 625.

Vayenas, C.G. and S. Neophytides, J. Catal., 127 (1991) 645.

Vayenas, C.G., A. Ioannides and S. Bebelis, J. Catal., 129 (1991) 67.

Vayenas, C. G., S. Bebelis, I.V. Yentekakis and H.G. Lintz, Catalysis Today, 11 (1992) 303.

Veonhard, V., D. Fischer, H. Erdmann, M. Ilgenstein and H. Koppen, Sensors and Actuators B, 13-14, (1993) 530.

Vetter, K.J., Electrochemical Kinetics – Theoretical and Experimental Aspects, (Academic Press, New York, 1967).

Wagner, C., Z. Phys. Chem., B11 (1930) 139.

Wagner, C. and W. Schottky, Z. Phys. Chem. B, 11 (1930) 163.

Wagner, C., Z. Phys. Chem. B 21 (1933) 25.

Wagner, C., Phys. Z., 36 (1935) 721.

Wagner, C., in: Atom Movements, (Cleveland, Am. Soc. Met., 1951) 153.

Wagner, C., J. Chem.Phys., 21 (1953) 1819.

Wagner, C., in: Proc. Intern. Comm. Electrochem. Therm. Kinetics (CITCE), 7th meeting Lindau, 1955 (Butterworth Scientific Publ., London, 1957) 361.

Wagner, C., Adv. Catalysis, 21 (1970) 323.

Wagner, C., Prog. Solid State Chem., 10(1) (1975) 3.

Wagner, J.B. and C. Wagner, J. Chem. Phys., 26 (1957) 1597.

Wagner, J.B., in: Electrode Processes in Solid State Ionics, Proc. NATO Adv. Study Inst., Ajaccio, eds. M. Kleitz and J. Dupuy, (D. Reidel, Dordrecht/Boston, 1975) 185.

Wang, D.Y. and A.S. Nowick, J. Electrochem. Soc., 126 (1979a) 1155.

Wang, D.Y. and A.S. Nowick, J. Electrochem. Soc., 126 (1979b) 1166.

Wang, D.Y. and A.S. Nowick, J. Electrochem. Soc., 128 (1981) 55.

Weber, W.J., C.W. Griffin and J.L. Bates, J. Am. Ceram. Soc., 70 (1987) 265.

Weissbart, J. and R. Ruka, in: Fuel Cells, Vol. II, ed. G.J. Young, (Reinhold, New York, 1963) 37.

Weppner, W. and R.A. Huggins, J. Electrochem. Soc., 124 (1977) 1569.

Weppner, W., Electrochem. Acta, 22 (1977a) 721.

Weppner, W., J. Solid State Chem., 20 (1977b) 305.

Weppner, W. and R.A. Huggins, Ann. Rev. Mater. Sci., 8 (1978) 269.

Weppner, W., German Patent DF 2926172 C2 (June 28, 1979).

Weppner, W., Solid State Ionics, 3/4 (1981) 1.

Weppner, W., in: Proc. 2nd Int. Meeting on Chemical Sensors (1986) 59.

Weppner, W., Sensors and Actuators, 12 (1987a) 107.

Weppner, W., in: Proc. Science and Technology of Fast Ion Conductors, eds. H.L. Tuller and M. Balkanski (1987b) 293.

Weppner, W., Solid State Ionics, 40/41 (1990) 369.

White, J.H., E.A. Needham, R.L. Cook and A.F. Sammells, Solid State Ionics, 53-56 (1992) 149.

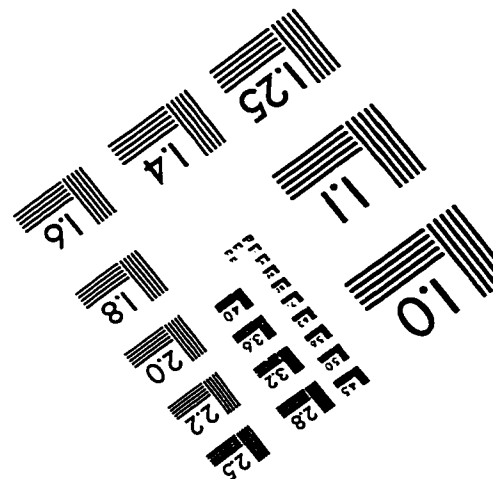
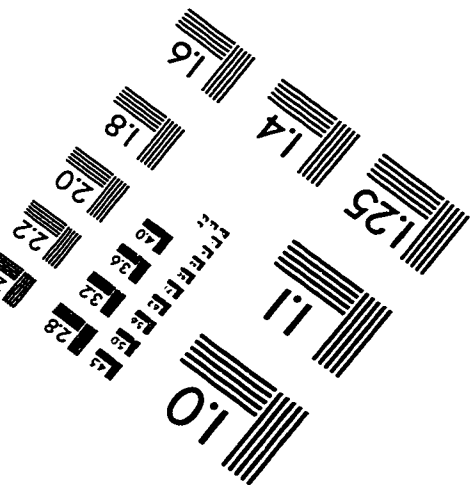
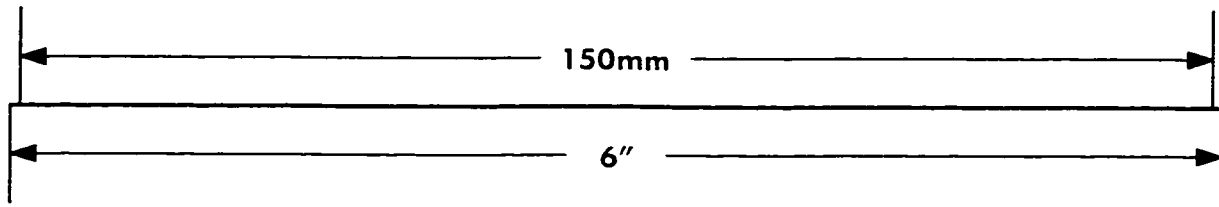
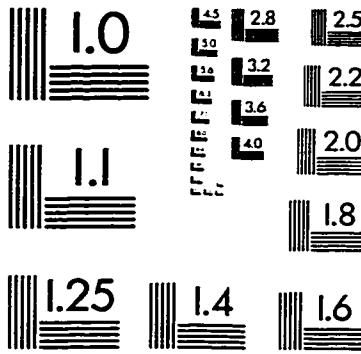
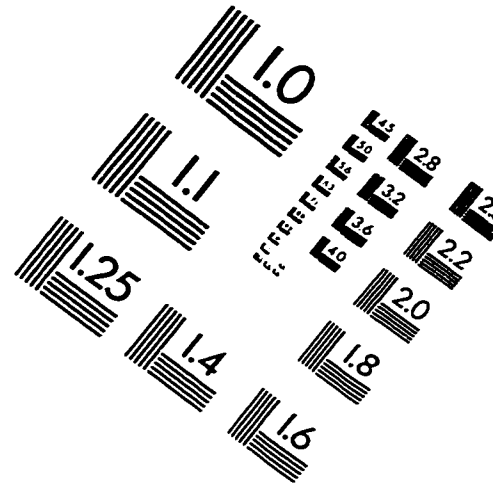
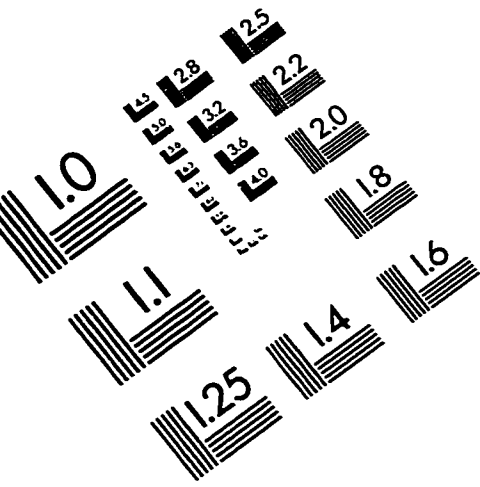
Williams, D.E. and McGeehin, P., Electrochemistry, 9 (1984) 246.

Worrell, W.L., V.B. Tare and F.J. Bruni, in: High Temperature Technology, IUPAC, (Butterworths, London, 1969) 503.

Worrell, W.L. and J. Hladik, in Physics Electrolytes, ed. J. Hladik, (Academic press, London, 1972) 747.

- Worrell, W.L., *Am. Ceram. Soc. Bull.*, 53 (1974) 425.
- Worrell, W. L. and Q.G. Liu, *J. Electroanal. Chem.*, 124 (1977) 1579
- Worrell, W.L. and Q.G. Liu, *Sensors and Actuators*, 2 (1982) 385.
- Yamazoe, N. and N. Miura, *Sensors and Actuators B*, 20 (1994) 95.
- Yamazoe, N. and N. Miura, *IEEE Transactions on Components, Packaging, and Manufacturing Technology*, part A, 18 (1995) 252.
- Yan, Y., Y. Shimizu, N. Miura, and N. Yamazoe, *Chem. Lett.*, 1992 (1992) 635.
- Yao, S., S. Hosohara, Y. Shimizu, N. Miura, H. Hutata, and N. Yamazoe, *Chem. Lett.*, 1991 (1991) 2069.
- Yao, S., Y. Shimizu, N. Miura, and N. Yamazoe, *Chem. Lett.*, 1992 (1992) 587.
- Yao, Y.F.Y. and J.T. Kummer, *J. Inorg. Nucl. Chem.*, 29 (1967) 2453.
- Yentekakis, I.V. and C.G. Vayenas, *J. Catal.*, 111 (1988) 170.
- Yokota, I, *J. Phys. Soc. Japan*, 21 (1966) 420.

IMAGE EVALUATION TEST TARGET (QA-3)



APPLIED IMAGE, Inc
1653 East Main Street
Rochester, NY 14609 USA
Phone: 716/482-0300
Fax: 716/288-5989

© 1993, Applied Image, Inc., All Rights Reserved